Thèse présentée pour obtenir le diplôme

D'HABILITATION A DIRIGER DES RECHERCHES

DE L'UNIVERSITE PIERRE ET MARIE CURIE

spécialité : PHYSIQUE

par

Frédéric FLEURET

Optimisation du calorimètre électromagnétique de l'expérience ATLAS.

Identification et reconstruction des électrons auprès de l'expérience DØ.

Table des matières

Curriculum Vitae **5**

Liste des Publications **6**

Résumé de la thèse **12**

Résumé **13**

I Optimisation du calorimètre électromagnétique de l'expérience ATLAS **14**

1 Introduction **15**
1.1 Le détecteur ATLAS 16
1.2 Le calorimètre électromagnétique d'ATLAS 17
1.2.1 Généralités 17
1.2.2 Segmentation du calorimètre électromagnétique 18
1.2.3 Les absorbeurs du calorimètre électromagnétique 19

2 Optimisation du calorimètre électromagnétique **21**
2.1 Simulation d'un module du calorimètre 21
2.2 Méthodes d'appariement des plaques de plomb 23
2.3 Performances de la procédure d'appariement 24

3 Conclusion **26**

II Identification et reconstruction des électrons auprès de l'expérience DØ **28**

1 Introduction **29**
1.1 Le détecteur DØ 30
1.2 Le détecteur de traces 30

1.3 Le détecteur de pied de gerbe 31
1.4 Le calorimètre électromagnétique de DØ 31
1.4.1 Généralités 32
1.4.2 Calorimètre central 33

2 Recherche de candidats électrons **35**
2.1 Recherche de *pré-clusters* électromagnétiques 36
2.2 SEMReco : recherche de candidats trace-tour 36
2.2.1 Appariemment trace-*cluster* du détecteur de pied de gerbe 37
2.2.2 Appariemment trace-tour du calorimètre électromagnétique 37
2.2.3 Rejet du bruit de fond 37

3 Reconstruction des électrons **39**
3.1 Généralités 39
3.2 Sélection des candidats 39
3.3 Construction du *cluster* électromagnétique final 40
3.4 Performances du programme de reconstruction 40
3.4.1 Régions «fiducielles» 41
3.4.2 Mesure des efficacités 42

4 Conclusion **45**

Perspectives **47**

A Notes ATLAS **49**
A.1 Correction of Lead Plates Thickness Fluctuation Effect on the Energy of the EM Accordion Calorimeter. *F. Fleuret, B. Laforge, P. Schwemling.* ATL-LARG-2000-001 (ATL-COM-LARG-99-022). 49
A.2 Constant Term Evolution with Lead Plate Thickness Fluctuations in EM Module 0. *F. Fleuret, B. Laforge, P. Schwemling.* ATL-LARG-2000-002 (ATL-COM-LARG-99-021). 49
A.3 Lead Matching and Consequences on the EM Module 0 Constant Term. *F. Fleuret, B. Laforge, P. Schwemling.* ATL-LARG-99-014 (ATL-COM-LARG-99-020). 49

B Notes DØ **50**
B.1 Energy Restoration of Edge Electrons in the DØ Central Calorimeter. *F. Fleuret.* DØ note 3739. 50
B.2 Low Energy Electron Identification in DØ. *F. Fleuret.* DØ note 3870. . . . 50
B.3 The DØ Soft Electron Reconstruction Package SEMReco. *F. Fleuret, F. Beaudette, S. Protopopescu.* DØ note 3872. 50
B.4 The DØ Electron/Photon Analysis Package EMAnalyze. *F. Fleuret.* DØ note 3888. 50

Table des figures

1.1 *Potentiel de découverte du boson de Higgs* 15
1.2 *Le détecteur ATLAS.* 16
1.3 *Le système calorimétrique d'ATLAS.* 17
1.4 *La structure plomb - argon - électrode.* 18
1.5 *Structure en accordéon du calorimètre électromagnétique* 19

2.1 *Simulation d'une gerbe d'électron de 20 GeV dans un module du calorimètre électromagnétique.* 22
2.2 *Schéma d'une plaque de plomb* 24

1.1 *Le détecteur DØ.* 30
1.2 *Calorimètre à argon liquide de l'expérience DØ.* 31
1.3 *Schéma des tours projectives du calorimètre.* 32
1.4 *Régions non-instrumentées du calorimètre* 33

2.1 *Schéma de principe de la recherche d'électrons au moyen de la méthode trace-tour.* 37

3.1 *Régions fiducielles de la partie centrale du détecteur.* 42
3.2 *Efficacités de reconstruction.* 43
3.3 *Isolation des clusters électromagnétiques.* 44

4.1 *Résolution sur la mesure de l'impulsion pour le détecteur de traces.* 47

Liste des tableaux

2.1 *Fluctuation d'épaisseur et contribution au terme constant de la résolution en énergie pour le module 0 du calorimètre électromagnétique.* 23
2.2 *Fluctuation d'épaisseur et contribution au terme constant de la résolution en énergie pour le module 0 avec et sans appariement des plaques de plomb.* 24

1.1 *Segmentation $\Delta\eta \times \Delta\phi$ et longueurs de radiation $X_\circ$ pour les différentes couches du calorimètre central.* 32

2.1 *Performances obtenues, hors efficacité de reconstruction des traces, pour des traces appariées à un cluster du détecteur de pied de gerbe et à une tour du calorimètre électromagnétique* 38

3.1 *Régions fiducielles du détecteur de traces, du détecteur de pied de gerbe (CPS) et du calorimètre* 41
3.2 *Efficacité de reconstruction.* 43

FREDERIC FLEURET

Date de naissance : 18 décembre 1968
Chargé de Recherche de 1ère classe

LPNHE-Paris
4 Place Jussieu, 75252 Paris
Téléphone : 01.44.27.22.33
Mél : fleuret@in2p3.fr

Emploi et formation

Depuis 1997 : Chargé de recherche au CNRS/IN2P3, LPNHE-Paris.

1994 - 1997 : Thèse au LPNHE-Ecole Polytechnique, Palaiseau.

1993 - 1994 : Service Militaire.

1992 - 1993 : DEA de Physique des particules, Luminy, Marseille.

Expériences professionnelles

août 1999 - sept. 2001 :
Expérience DØ : développement et implémentation du programme d'analyse de la reconstruction des électrons.
Expérience DØ : participation à l'adaptation du programme global de reconstruction des électrons.
Expérience DØ : développement et implémentation du programme de reconstruction des électrons non-isolés.

oct. 1997 - août 1999 :
Expérience DØ : étude sur la mesure des électrons déposant tout ou partie de leur énergie dans les régions non-instrumentées du détecteur.
Expérience ATLAS : étude et optimisation de la résolution en énergie du calorimètre électromagnétique.

sept. 1994 - mai 1997 :
Expériences NA38, NA51 et NA50 : recherche du plasma de quark et de gluon par l'étude des mésons J/ψ et ψ' dans les collisions d'ions Pb et de protons ultrarelativistes sur divers noyaux.

Autres expériences

depuis Nov. 2001 : Membre nommé de la commission de spécialistes de la 29ème section de l'Université Pierre et Marie Curie.

août 1999 - juil. 2001 : Séjour au laboratoire Lawrence Berkeley (LBNL), Berkeley, Californie, Etats-Unis.

mars 1998 - juil. 1998 : Encadrement d'un stagiaire (Rachid Guernane) du DEA de physique subatomique de Strasbourg (expérience ATLAS).

fév. 1998 - mai 1999 : Co-fondateur et président de l'association des doctorants de l'Ecole Polytechnique.

1) Liste des notes

Expérience DØ :

- **The DØ Electron/Photon Analysis Package EMAnalyze.** *F. Fleuret.* DØ note 3888 (2001).
- **The DØ Soft Electron Reconstruction Package SEMReco.** *F. Fleuret, F. Beaudette, S. Protopopescu.* DØ note 3872 (2001).
- **Low Energy Electron Identification in DØ.** *F. Fleuret.* DØ note 3870 (2001).
- **Energy Restoration of Edge Electrons in the DØ Central Calorimeter.** *F. Fleuret.* DØ note 3739 (2000).

Expérience ATLAS :

- **Correction of Lead Plates Thickness Fluctuation Effect on the Energy of the EM Accordion Calorimeter.** *F. Fleuret, B. Laforge, P. Schwemling.* ATL-LARG-2000-001 (ATL-COM-LARG-99-022).
- **Constant Term Evolution with Lead Plate Thickness Fluctuations in EM Module 0.** *F. Fleuret, B. Laforge, P. Schwemling.* ATL-LARG-2000-002 (ATL-COM-LARG-99-021).
- **Lead Matching and Consequences on the EM Module 0 Constant Term.** *F. Fleuret, B. Laforge, P. Schwemling.* ATL-LARG-99-014 (ATL-COM-LARG-99-020).

2) Liste des principales publications

- **J/ψ, ψ' and Drell-Yan production in S-U interactions at 200-GeV per nucleon**, M. C. Abreu *et al.* [NA38 Collaboration], Phys. Lett. B **449**, 128 (1999).
- **Charmonia production in 450-GeV/c proton induced reactions**, M. C. Abreu *et al.* [NA38 Collaboration], Phys. Lett. B **444**, 516 (1998).
- **J/ψ, ψ' and Drell-Yan production in p-p and p-d interactions at 450-GeV/c**, M. C. Abreu *et al.* [NA51 Collaboration], Phys. Lett. B **438**, 35 (1998).
- **Anomalous J/ψ suppression in Pb-Pb interactions at 158 GeV/c per nucleon**, M. C. Abreu *et al.* [NA50 Collaboration], Phys. Lett. B **410**, 337 (1997).
- **J/ψ and Drell-Yan cross-sections in Pb-Pb interactions at 158 GeV/c per nucleon**, M. C. Abreu *et al.* [NA50 Collaboration], Phys. Lett. B **410**, 327 (1997).

3) Liste des publications

Expérience DØ :

- **The inclusive jet cross-section in p-$\overline{\mathbf{p}}$ collisions at $\sqrt{s}$ = 1.8-TeV using the k(T) algorithm**,V. M. Abazov *et al.* [D0 Collaboration], arXiv :hep-ex/0109041.
- **Subjet multiplicity of gluon and quark jets reconstructed with the k(T) algorithm in p-$\overline{\mathbf{p}}$ collisions**, V. M. Abazov *et al.* [D0 Collaboration], arXiv :hep-ex/0108054.
- **A search for the scalar top quark in p-$\overline{\mathbf{p}}$ collisions at $\sqrt{s}$ = 1.8-TeV**, V. M. Abazov *et al.* [D0 Collaboration], arXiv :hep-ex/0108018.
- **Measurement of the ratio of differential cross sections for W and Z boson production as a function of transverse momentum in p-$\overline{\mathbf{p}}$ collisions at $\sqrt{s}$ = 1.8-TeV**, V. M. Abazov *et al.* [D0 Collaboration], Phys. Lett. B **517**, 299 (2001) [arXiv :hep-ex/0107012].
- **A study of multiple jet production at transverse energy near 20-GeV**, V. M. Abazov *et al.* [D0 Collaboration], arXiv :hep-ex/0106072.
- **Search for leptoquark pairs decaying to nu nu + jets in p-$\overline{\mathbf{p}}$ collisions at $\sqrt{s}$ = 1.8-TeV**, V. M. Abazov *et al.* [D0 Collaboration], arXiv :hep-ex/0106065.
- **Search for single top quark production at D0 using neural networks**, V. M. Abazov *et al.* [D0 Collaboration], Phys. Lett. B **517**, 282 (2001) [arXiv :hep-ex/0106059].
- **Search for new physics using QUAERO : A general interface to D0 event data**, V. M. Abazov *et al.* [D0 Collaboration], arXiv :hep-ex/0106039.
- **Measurement of the ratio of the differential cross sections for W and Z boson production as a function of transverse momentum in p-$\overline{\mathbf{p}}$ collisions at $\sqrt{s}$ = 1.8-TeV**, V. M. Abazov *et al.* [D0 Collaboration], arXiv :hep-ex/0106027.
- **The inclusive jet cross section in p-$\overline{\mathbf{p}}$ collisions at $\sqrt{s}$ = 1.8-TeV using the k(T) algorithm**, V. M. Abazov *et al.* [D0 Collaboration], arXiv :hep-ex/0106032.
- **The ratio of the isolated photon cross sections at $\sqrt{s}$ = 630-GeV and 1800-GeV**, V. M. Abazov *et al.* [D0 Collaboration], arXiv :hep-ex/0106026.
- **Improved D0 W boson mass determination**, V. M. Abazov *et al.* [D0 Collaboration], arXiv :hep-ex/0106018.
- **Search for first-generation scalar and vector leptoquarks**, V. M. Abazov *et al.* [D0 Collaboration], Phys. Rev. D **64**, 092004 (2001) [arXiv :hep-ex/0105072].
- **Search for heavy particles decaying into electron positron pairs in p-$\overline{\mathbf{p}}$ collisions**, V. M. Abazov *et al.* [D0 Collaboration], Phys. Rev. Lett. **87**, 061802 (2001) [arXiv :hep-ex/0102048].
- **Direct search for charged Higgs bosons in decays of top quarks**, V. M. Abazov *et al.* [D0 Collaboration], arXiv :hep-ex/0102039.
- **High-p(T) jets in $\overline{\mathbf{p}}$-p collisions at $\sqrt{s}$ = 630-GeV and 1800-GeV**, B. Abbott *et al.* [D0 Collaboration], Phys. Rev. D **64**, 032003 (2001) [arXiv :hep-ex/0012046].
- **A quasi-model-independent search for new high p(T) physics at D0**, B. Abbott *et al.* [D0 Collaboration], Phys. Rev. Lett. **86**, 3712 (2001) [arXiv :hep-ex/0011071].

- **A quasi-model-independent search for new physics at large transverse momentum**, B. Abbott *et al.* [D0 Collaboration], Phys. Rev. D **64**, 012004 (2001) [arXiv :hep-ex/0011067].
- **Inclusive jet production in p-$\overline{\mathbf{p}}$ collisions**, B. Abbott *et al.* [D0 Collaboration], Phys. Rev. Lett. **86**, 1707 (2001) [arXiv :hep-ex/0011036].
- **Differential cross section for W boson production as a function of transverse momentum in p-$\overline{\mathbf{p}}$ collisions at $\sqrt{s}$ = 1.8-TeV**, B. Abbott *et al.* [D0 Collaboration], Phys. Lett. B **513**, 292 (2001) [arXiv :hep-ex/0010026].
- **Measurement of the angular distribution of electrons from W $\rightarrow$ e nu decays observed in p-$\overline{\mathbf{p}}$ collisions at $\sqrt{s}$ = 1.8-TeV**, B. Abbott *et al.* [D0 Collaboration], Phys. Rev. D **63**, 072001 (2001) [arXiv :hep-ex/0009034].
- **Ratios of multijet cross sections in p-$\overline{\mathbf{p}}$ collisions at $\sqrt{s}$ = 1.8-TeV**, B. Abbott *et al.* [D0 Collaboration], Phys. Rev. Lett. **86**, 1955 (2001) [arXiv :hep-ex/0009012].
- **The ratio of jet cross sections at $\sqrt{s}$ = 630-GeV and 1800-GeV**, B. Abbott *et al.* [D0 Collaboration], Phys. Rev. Lett. **86**, 2523 (2001) [arXiv :hep-ex/0008072].
- **Search for large extra dimensions in dielectron and diphoton production**, B. Abbott *et al.* [D0 Collaboration], Phys. Rev. Lett. **86**, 1156 (2001) [arXiv :hep-ex/0008065].
- **Search for electroweak production of single top quarks in p-$\overline{\mathbf{p}}$ collisions**, B. Abbott *et al.* [D0 Collaboration], Phys. Rev. D **63**, 031101 (2001) [arXiv :hep-ex/0008024].
- **Cross section for b jet production in $\overline{\mathbf{p}}$-p collisions at $\sqrt{s}$ = 1.8-TeV**, B. Abbott *et al.* [D0 Collaboration], Phys. Rev. Lett. **85**, 5068 (2000) [arXiv :hep-ex/0008021].
- **Search for new physics in e muon X data at D0 using Sherlock : A quasi model independent search strategy for new physics**, B. Abbott *et al.* [D0 Collaboration], Phys. Rev. D **62**, 092004 (2000) [arXiv :hep-ex/0006011].
- **Search for R-parity violation in multilepton final states in p-$\overline{\mathbf{p}}$ collisions at $\sqrt{s}$ = 1.8-TeV**, B. Abbott *et al.* [D0 Collaboration], Phys. Rev. D **62**, 071701 (2000) [arXiv :hep-ex/0005034].
- **A search for dilepton signatures from minimal low-energy supergravity in p-$\overline{\mathbf{p}}$ collisions at $\sqrt{s}$ = 1.8-TeV**, B. Abbott *et al.* [D0 Collaboration], Phys. Rev. D **63**, 091102 (2001).
- **Spin correlation in t anti-t production from p-$\overline{\mathbf{p}}$ collisions at $\sqrt{s}$ = 1.8-TeV**, B. Abbott *et al.* [D0 Collaboration], Phys. Rev. Lett. **85**, 256 (2000) [arXiv :hep-ex/0002058].
- **A measurement of the W $\rightarrow$ tau nu production cross section in p-$\overline{\mathbf{p}}$ collisions at $\sqrt{s}$ = 1.8-TeV**, B. Abbott *et al.* [D0 Collaboration], Phys. Rev. Lett. **84**, 5710 (2000) [arXiv :hep-ex/9912065].
- **Hard single diffraction in $\overline{\mathbf{p}}$-p collisions at $\sqrt{s}$ = 630-GeV and 1800-GeV**, B. Abbott *et al.* [D0 Collaboration], arXiv :hep-ex/9912061.
- **Limits on anomalous W W gamma and W W Z couplings from W W / W Z $\rightarrow$ e nu j j production**, B. Abbott *et al.* [D0 Collaboration], Phys. Rev. D **62**, 052005 (2000) [arXiv :hep-ex/9912033].

- **Probing BFKL dynamics in the dijet cross section at large rapidity intervals in p-$\overline{\mathbf{p}}$ collisions at $\sqrt{s}$ = 1800-GeV and 630-GeV**, B. Abbott *et al.* [D0 Collaboration], Phys. Rev. Lett. **84**, 5722 (2000) [arXiv :hep-ex/9912032].
- **Limits on quark compositeness from high-energy jets in $\overline{\mathbf{p}}$-p collisions at 1.8-TeV**, B. Abbott *et al.* [D0 Collaboration], Phys. Rev. D **62**, 031101 (2000) [arXiv :hep-ex/9912023].
- **The isolated photon cross-section in p-$\overline{\mathbf{p}}$ collisions at $\sqrt{s}$ = 1.8-TeV**, B. Abbott *et al.* [D0 Collaboration], Phys. Rev. Lett. **84**, 2786 (2000) [arXiv :hep-ex/9912017].
- **Search for second generation leptoquark pairs in $\overline{\mathbf{p}}$-p collisions at $\sqrt{s}$ = 1.8-TeV**, B. Abbott *et al.* [D0 Collaboration], Phys. Rev. Lett. **84**, 2088 (2000) [arXiv :hep-ex/9910040].

Expériences NA38, NA50 et NA51 :

- **Study of J/ψ suppression in Pb Pb collisions at the CERN SPS**,. M. C. Abreu *et al.* [NA50 Collaboration],
- **Summary of J/ψ suppression data and preliminary results on multiplicity distributions in Pb Pb collisions from the NA50 experiment**,. M. Abreu *et al.* [NA50 Collaboration],
- **Charmonium production in Pb Pb collisions**, M. Abreu *et al.* [NA50 Collaboration], Nucl. Phys. A **663**, 765 (2000).
- **Strangeness measurements in NA50 experiment with Pb projectiles**, M. Abreu *et al.* [NA50 Collaboration], Nucl. Phys. A **663**, 721 (2000).
- **Results on J/ψ suppression**, M. C. Abreu *et al.* [NA50 Collaboration], *In *Trento 1999, Understanding deconfinement in QCD* 291-302.*
- **Dimuon enhancement in nucleus nucleus ultrarelativistic interactions**, M. C. Abreu *et al.* [NA38/NA50 Collaborations], Nucl. Phys. A **661**, 538 (1999).
- **Φ, ρ and ω production in Pb - Pb collisions at 158-GeV/c**2 per nucleon**, M. C. Abreu *et al.* [NA50 Collaboration], Nucl. Phys. A **661**, 534 (1999).
- **The elliptic flow of neutral transverse energy in heavy ion interactions at SPS energies**, M. C. Abreu *et al.* [NA50 Collaboration], Nucl. Phys. A **661**, 345 (1999).
- **Fission of lead projectiles in Pb nucleus collisions at the SPS**, M. C. Abreu *et al.* [NA50 Collaboration], Nucl. Phys. A **661**, 321 (1999).
- **Latest results from NA50 on J/ψ suppression in Pb Pb collisions**, M. C. Abreu *et al.* [NA50 Collaboration], Nucl. Phys. A **661**, 93 (1999).
- **Dimuon and charm production in nucleus nucleus collisions at the CERN-SPS**, M. C. Abreu *et al.* [NA38 Collaboration], Eur. Phys. J. C **14**, 443 (2000).
- **Onset of the anomalous J/ψ suppression in Pb + Pb collisions**, M. C. Abreu *et al.* [NA50 Collaboration], *Prepared for Workshop on Quarkonium Production in Relativistic Nuclear Collisions, Seattle, Washington, 11-15 May 1998.*
- **Results on charmonium states in Pb Pb interactions**, C. Baglin *et al.* [NA50 Collaboration], *Prepared for 29th International Conference on High-Energy Physics*

(ICHEP 98), Vancouver, British Columbia, Canada, 23-29 Jul 1998.

- **Intermediate mass dimuons in NA38/NA50**, M. C. Abreu *et al.* [NA50 Collaboration], *Prepared for 29th International Conference on High-Energy Physics (ICHEP 98), Vancouver, British Columbia, Canada, 23-29 Jul 1998.*
- **Low mass dimuon production in proton and ion induced interactions at the SPS**, M. C. Abreu *et al.* [NA38 and NA50 Collaborations], Eur. Phys. J. C **13**, 69 (2000).
- **J/ψ and ψ' production in p, O and S induced reactions at SPS energies**, M. C. Abreu *et al.*, Phys. Lett. B **466**, 408 (1999).
- **J/ψ suppression**, M. C. Abreu *et al.* [NA50 Collaboration], *Prepared for International Conference on Hadron Structure (HS 98), Stara Lesna, Slovakia, 7-13 Sep 1998.*
- **Observation of a threshold effect in the anomalous J/ψ suppression**, M. C. Abreu *et al.* [NA50 Collaboration], CERN-EP-99-013.
- **Φ, ρ and ω production in collisions induced by deuteron and heavy ions at 200-A-GeV/c**, M. C. Abreu *et al.* [NA38 and NA50 Collaborations], Heavy Ion Phys. **4**, 155 (1996).
- **Observation of fission in Pb Pb interactions at 158-A-GeV**, M. C. Abreu *et al.* [NA50 Collaboration], Phys. Rev. C **59**, 876 (1999).
- **Intermediate mass muon pair continuum in Pb Pb collisions at 158-GeV/c**, E. Scomparin *et al.* [NA50 Collaboration], Nucl. Phys. A **610**, 331C (1996).
- **Anomalous J/ψ suppression in Pb + Pb collisions at 158-A-GeV/c**, M. Gonin *et al.* [NA50 Collaboration], Nucl. Phys. A **610**, 404C (1996).
- **A new measurement of the J/ψ production rate in lead lead interactions at 158-GeV/c per nucleon**, M. C. Abreu *et al.* [NA50 Collaboration], *Given at International Europhysics Conference on High-Energy Physics (HEP 97), Jerusalem, Israel, 19-26 Aug 1997.*
- **Intermediate mass dimuons in NA38/NA50**, M. C. Abreu *et al.* [NA50 Collaboration], J. Phys. G **25**, 235 (1999).
- **NA38/NA50 results on the low mass dimuon spectra**, M. Abreu *et al.* [NA38 and NA50 Collaborations], Nucl. Phys. A **638**, 487 (1998).
- **Φ, ρ and ω production in collisions induced by deuteron and heavy ions around 200-GeV per nucleon**, M. C. Abreu *et al.* [NA50 and NA38 Collaborations], Nucl. Phys. A **638**, 483 (1998).
- **Charmonium production in Pb Pb interactions at 158-GeV/c per nucleon**, M. C. Abreu *et al.* [NA50 Collaboration], Nucl. Phys. A **638**, 261 (1998).
- **J/ψ suppression**, M. C. Abreu *et al.* [NA50 Collaboration], Nucl. Phys. Proc. Suppl. **71**, 279 (1999).
- **Transverse momentum of J/ψ, ψ' and mass continuum muon pairs produced in S-32 U collisions at 200-GeV/c per nucleon**, M. C. Abreu *et al.* [NA38 Collaboration], Phys. Lett. B **423**, 207 (1998).
- **A 4-dimensional deconvolution method to correct NA38 experimental data**, M. C. Abreu *et al.* [NA38 Collaboration], Nucl. Instrum. Meth. A **405**, 139 (1998).

- **Anomalous J/ψ suppression in 158-GeV/c Pb Pb collisions at the CERN SPS**, C. Baglin *et al.* [NA50 Collaboration], LAPP-EXP-97-04 *Talk given at 6th Conference on the Intersections of Particle and Nuclear Physics (CIPANP 97), Big Sky, MT, 27 May - 2 Jun 1997.*
- **Anomaly in charmonium suppression in Pb + Pb collisions : Final results**, M. Gonin *et al.*, PRINT-97-208 *Presented at 3rd International Conference on Physics and Astrophysics of Quark Gluon Plasma (ICPAQGP 97), Jaipur, India, 17-21 Mar 1997.*
- **Anomaly in charmonium suppression in Pb + Pb collisions**, M. Gonin *et al.*, PRINT-97-209 *Presented at 25th International Workshop on Gross Properties of Nuclei and Nuclear Excitation : QCD Phase Transitions (Hirschegg 97), Hirschegg, Austria, 13-18 Jan 1997.*
- **Evidence of strong J/ψ and ψ' suppression in high-energy Pb-Pb interactions**, M. C. Abreu *et al.* [NA50 Collaboration], LIP-96-04 *Invited talk at 26th International Symposium on Multiparticle Dynamics (ISMD 96), Faro, Portugal, 1-5 Sep 1996.*
- **J/ψ and ψ' production in lead-lead collisions at 158 x A-GeV/c**, M. C. Abreu *et al.* [NA50 Collaboration], PRINT-97-210 *Presented at 8th International Conference on Nuclear Reaction Mechanisms, Varenna, Italy, 9-14 Jun 1997.*
- **The Evolution of cross-section ratio ψ' / J/ψ from p A to S U interactions : Direct photon emmission in correlation with Φ and J/ψ**, S. Ramos *et al.* [NA38 Collaboration], Nucl. Phys. A **590**, 117C (1995).

Résumé de la thèse

Recherche du plasma de quarks et de gluons par l'étude des mésons J/ψ et ψ' dans les collisions d'ions Pb et de protons ultrarelativistes sur divers noyaux.

Dans le cadre de la recherche du plasma de quarks et de gluons, nous avons étudié la production des mésons J/ψ et ψ' dans les collisions p-p, p-d (expérience NA51), p-C, p-Al, p-Cu, p-W (expérience NA38) et Pb-Pb (expérience NA50).

Les résultats des analyses proton-noyau fournissent une valeur de référence pour l'étude des interactions noyau-noyau. Ils permettent de montrer une continuité dans l'évolution de la production du J/ψ qui peut être comprise par l'absorption des *charmonia* par la matière nucléaire des noyaux projectiles et cibles, des collisions p-p aux collisions S-U (expériences NA38 et NA51). les résultats de l'analyse des données Pb-Pb (expérience NA50) mettent en évidence une production anormalement supprimée du J/ψ en comparaison avec la valeur attendue et extrapolée à partir du comportement observé pour les systèmes plus légers. Cette suppression est d'autant plus importante que la centralité de la collision augmente.

L'étude de la production du ψ' dans les collisions proton-noyau permet de mettre en évidence une suppression supplémentaire dans les interactions noyau-noyau par rapport au modèle d'absorption. Le comportement obtenu pour les collisions Pb-Pb s'inscrit dans la continuité de la forte suppression déjà observée pour le système S-U.

Résumé

Ce rapport présente les activités effectuées de 1997 à 2001 auprès des expériences ATLAS et DØ.

Nous nous sommes intéressés à la problématique de la reconstruction des électrons dans des expériences fonctionnant auprès de collisionneurs. Nous avons, dans un premier temps, concentré nos activités sur les aspects mécaniques d'un calorimètre électromagnétique en participant à l'optimisation de celui de l'expérience ATLAS. Puis, nous avons abordé les problèmes d'identification et de reconstruction d'électrons. Ce dernier travail a été effectué auprès de l'expérience DØ.

Les activités effectuées auprès de l'expérience ATLAS ont porté sur le développement d'un algorithme d'appariemment des absorbeurs qui entrent dans la composition du calorimètre électromagnétique, avec pour objectif de réduire la contribution de leurs inhomogénéités d'épaisseur au terme constant de la résolution en énergie.

Les activités effectuées auprès de l'expérience DØ ont, quant à elles, couvert les différents aspects de la reconstruction des électrons : nous avons développé et implémenté un nouvel algorithme d'identification et de reconstruction des électrons non-isolés, participé à l'adaptation du programme global de reconstruction des électrons et développé un programme d'analyse destiné à évaluer les performances des programmes de reconstruction des électrons.

Ce rapport sera donc séparé en deux parties : la première, consacrée aux activités d'optimisation du calorimètre électromagnétique de l'expérience ATLAS ; la seconde, à la reconstruction des électrons auprès de l'expérience DØ.

Première partie

Optimisation du calorimètre électromagnétique de l'expérience ATLAS

Chapitre 1

Introduction

Le détecteur ATLAS sera mis en œuvre, à l'horizon 2006, auprès du collisionneur proton-proton LHC (Large Hadron Collider), installé au CERN près de Genève, qui fonctionnera de manière nominale à une énergie de 14 (7+7) TeV dans le centre de masse de la collision. Le LHC succèdera au LEP et, dans l'absence de signal, au Tevatron, pour la recherche du boson de Higgs. Le LHC, accédant à des domaines d'énergie jamais atteints jusqu'alors, sera aussi consacré à la recherche de physique au-delà du modèle standard et à l'étude des quarks top et bottom.

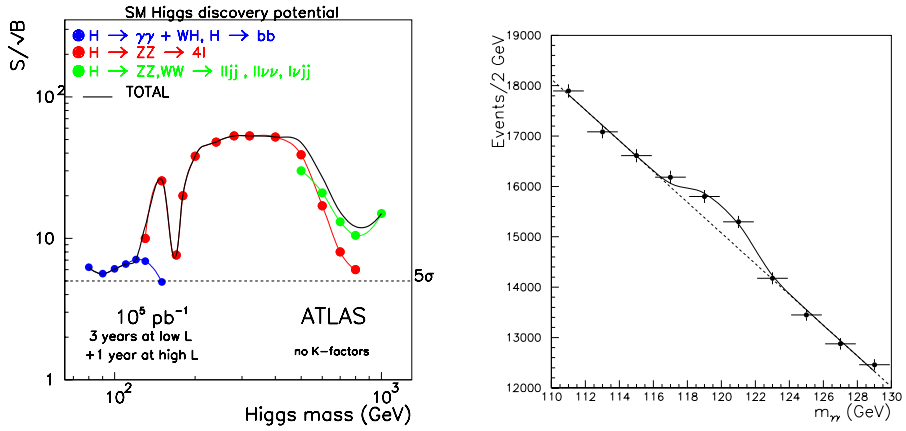

FIG. 1.1 – *Gauche : le canal de désintégration en photons permet de sonder les régions de basse masse (de l'ordre de 120 GeV). Droite : spectre de masse invariante des paires de photons reconstruites dans le calorimètre électromagnétique dans l'hypothèse d'un Higgs de 120 GeV.*

Dans le cadre de la recherche du boson de Higgs, le canal H$\longrightarrow \gamma\gamma$ joue un rôle essentiel puisqu'il permet de tester les régions de basse masse, comme montré sur la figure 1.1. Ce canal requiert de hautes performances du calorimètre électromagnétique et a guidé l'établissement de ses spécifications.

Dans la suite de cet exposé, nous présentons rapidement la structure du détecteur

ATLAS, les caractéristiques du calorimètre électromagnétique pour finalement aborder le problème de son optimisation lors de la phase d'assemblage.

1.1 Le détecteur ATLAS

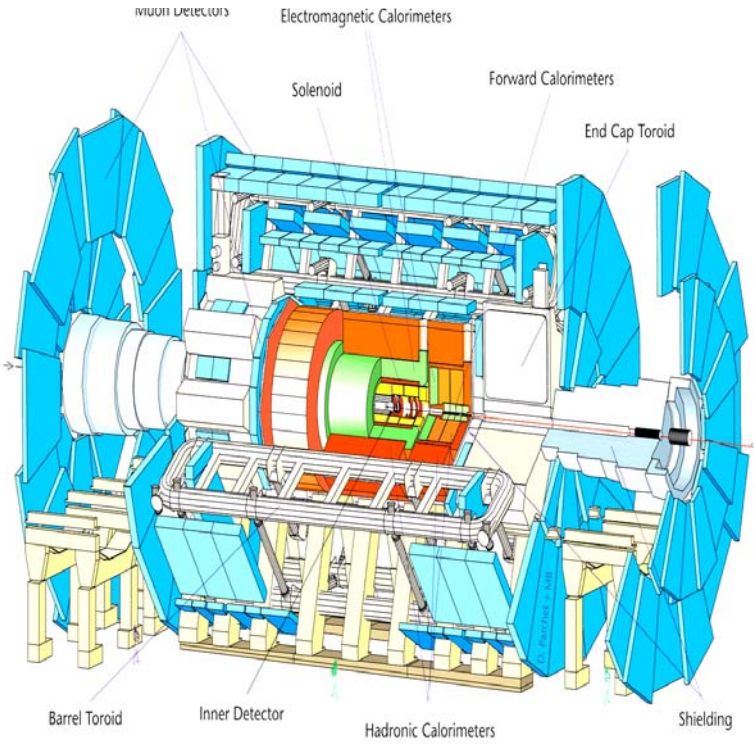

FIG. 1.2 – *Le détecteur ATLAS.*

Le détecteur ATLAS (figure 1.2) est l'un des quatre détecteurs qui seront mis en fonctionnement auprès du LHC. Une description détaillée peut en être trouvée dans [1]. Le détecteur est composé de trois ensembles de détection et de deux aimants. Du centre, c'est à dire depuis l'axe du faisceau, vers l'extérieur, on trouve :

- le détecteur interne (SCT + pixel + TRT),
- l'aimant solénoïdal,
- l'ensemble calorimétrique (calorimètre électromagnétique + calorimètre hadronique),
- le détecteur de muons et l'aimant toroïdal.

1.2 Le calorimètre électromagnétique d'ATLAS

1.2.1 Généralités

Dans cette partie, nous nous limitons à la présentation de la partie centrale du calorimètre électromagnétique.

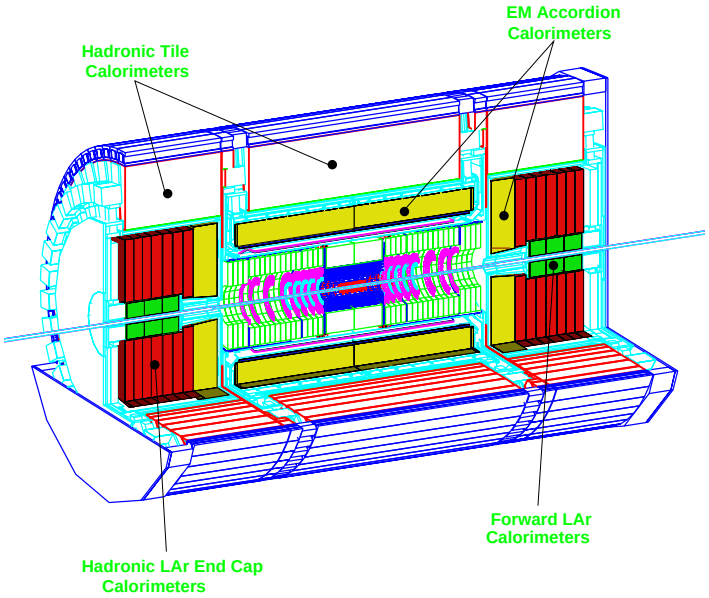

FIG. 1.3 – *Le système calorimétrique d'ATLAS.*

Le calorimètre électromagnétique de l'expérience ATLAS (figure 1.3) est un calorimètre à échantillonnage utilisant l'argon liquide comme milieu actif et le plomb comme milieu absorbant. Les avantages de cette technique, utilisée dans de nombreuses expériences, sont :

- la stabilité au cours du temps et uniformité du signal,
- la résistance aux radiations.

Le calorimètre électromagnétique a été conçu suivant une structure en accordéon. Cette géométrie, illustrée sur les figures 1.4 et 1.5, offre une couverture azimuthale homogène tout en maintenant constant (en ajustant les angles de pliage) le rapport d'échantillonnage pendant tout le développement de la gerbe.

Le calorimètre central est constitué de deux parties identiques de 3,15 m de long ($z>0$ et $z<0$). Chacune des parties est composée de 16 modules couvrant chacun 22,5°

dans le plan azimuthal et regroupant 64 absorbeurs.

1.2.2 Segmentation du calorimètre électromagnétique

Les cellules physiques du calorimètre sont composées d'une plaque d'absorbeur et de deux espaces (*gaps*) d'argon liquide de même épaisseur, séparés par une électrode de lecture. Cette structure est représentée sur la figure 1.4.

Les électrodes sont des circuits imprimés composés de trois couches de cuivre. Les deux couches externes sont à un potentiel de 2000 volts et servent à créer le champ électrique (les absorbeurs sont reliés à la masse) permettant la dérive des charges dans l'argon liquide. La couche interne recueille le signal par couplage capacitif.

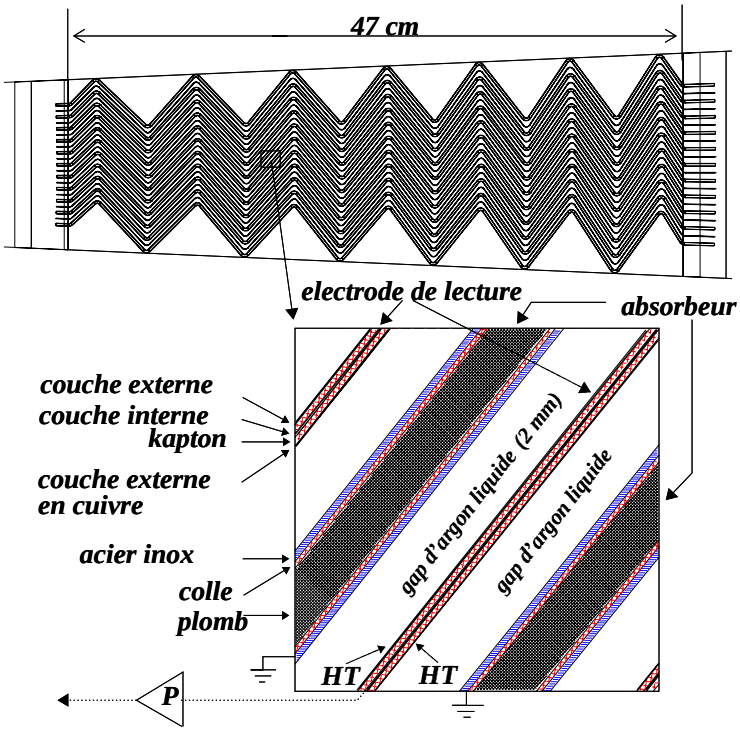

FIG. 1.4 – *La structure plomb - argon - électrode.*

La gravure des électrodes en pavés de lecture permet d'obtenir une segmentation longitudinale (granularité en η) et radiale (en profondeur, le calorimètre électromagnétique est divisé en trois compartiments). Dans le plan azimuthal, le regroupement de plusieurs électrodes définit une cellule de lecture. La granularité des cellules de lecture dépend du compartiment considéré comme suit :

– le premier compartiment est équipé de cellules très fines en η (voir figure 1.5),

notamment pour permettre la séparation γ/π^0. Sa granularité est $\Delta\eta \times \Delta\varphi = 0.003 \times 0.1$. Il représente 4,3 longueurs de radiation.

- le second compartiment a pour rôle la mesure de l'énergie de la gerbe. Il représente 16 longueurs de radiation. La segmentation de ce compartiment est adaptée à la taille des gerbes électromagnétiques : $\Delta\eta \times \Delta\varphi = 0.025 \times 0.025$.

- le troisième compartiment représente 2 longueurs de radiation et vient compléter la mesure de l'énergie : $\Delta\eta \times \Delta\varphi = 0.05 \times 0.025$.

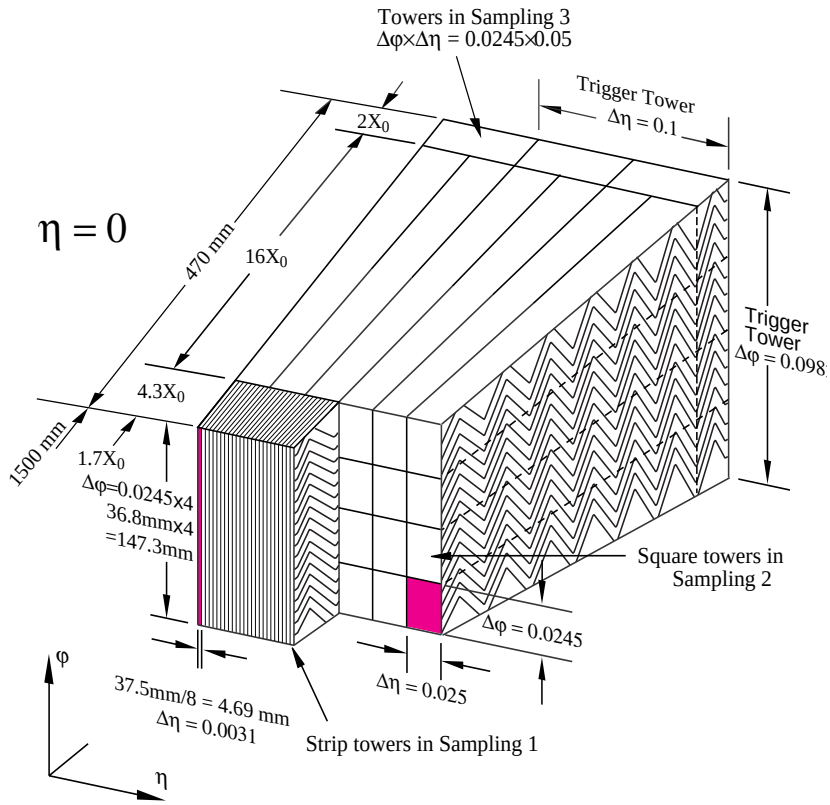

FIG. 1.5 – *Structure en accordéon du calorimètre électromagnétique. Sont représentées, les longueurs de radiation et segmentation $\eta \times \varphi$ des trois compartiments.*

1.2.3 Les absorbeurs du calorimètre électromagnétique

Les absorbeurs, reliés à la masse, sont constitués d'une plaque de plomb de 1,53 mm d'épaisseur (1,13 pour $|\eta| > 0,8$) en sandwich entre deux plaques d'inox de 0,2 mm. Une couche de colle de 0,13 mm (0,33 pour $|\eta| > 0,8$) entre les plaques complète la structure de l'absorbeur. Les plaques d'inox sont nécessaires pour assurer le maintien mécanique

de la structure. La diminution de l'épaisseur des plaques de plomb pour $|\eta| > 0.8$ permet d'augmenter la fraction d'échantillonnage et compense ainsi la détérioration de la résolution en énergie due à la diminution avec la rapidité η de la fréquence d'échantillonnage.

Considérant les spécifications des absorbeurs du calorimètre, le terme d'échantillonnage de la résolution en énergie ne doit pas excéder $10\%/\sqrt{E}$. Quant au terme constant, il ne doit pas excéder 0,7% avec une composante liée aux uniformités mécaniques inférieure à 0,3%. Cette dernière composante provient, en partie, des variations d'épaisseur des plaques de plomb apparaissant lors de la phase de laminage des feuilles de plomb qui ont été utilisées pour produire les absorbeurs.

Dans la suite de cet exposé, nous présentons la méthode qui est utilisée pour réduire les inhomogénéités dues aux variations d'épaisseur des plaques de plomb. Considérant qu'une gerbe électromagnétique voit, en moyenne, cinq absorbeurs, il est possible, en appariant des absorbeurs d'épaisseur différente, de maintenir constante l'épaisseur moyenne de plomb vue par une gerbe.

Chapitre 2

Optimisation du calorimètre électromagnétique

Le calorimètre électromagnétique de l'expérience ATLAS a été dessiné pour que le terme constant de la résolution en énergie n'excède pas 0,7% [2] ; la composante liée aux non-uniformités mécaniques, dans laquelle interviennent les non-uniformités provenant des variations d'épaisseur des plaques de plomb par rapport à l'épaisseur nominale, ne doit pas excéder 0,3%.

Afin de réduire cette contribution et ainsi répondre aux exigences expérimentales, nous avons développé un programme d'appariement des plaques de plomb qui, en moyenne sur 5 plaques, minimise les fluctuations d'épaisseur.

Nous présentons, dans un premier temps, le programme de simulation que nous avons utilisé afin de tester, d'optimiser et de valider l'algorithme d'appariement. Puis, nous détaillons le principe de l'algorithme, pour finir sur ses performances.

2.1 Simulation d'un module du calorimètre

Afin de pouvoir tester et valider le programme d'appariement utilisé pour optimiser le calorimètre électromagnétique, nous avons développé, à l'aide du programme GEANT, une géométrie détaillée d'un module du calorimètre central. Nous nous sommes appuyés sur une description déjà existante, mais insuffisamment précise pour nos besoins. En effet, cette géométrie intégrait les éléments «plomb+inox+colle» des absorbeurs dans un seul et même volume et considérait des absorbeurs d'épaisseur constante.

Nous avons développé une géométrie adaptée intégrant les éléments «plomb» et «inox+colle» dans des objets différents et permettant de prendre en compte les épaisseurs réelles des plaques de plomb. La figure 2.1 montre le développement, dans le module simulé, d'une gerbe d'électron de 20 GeV.

Le détail de cette implémentation peut être trouvé dans l'annexe A.2. Cette nou-

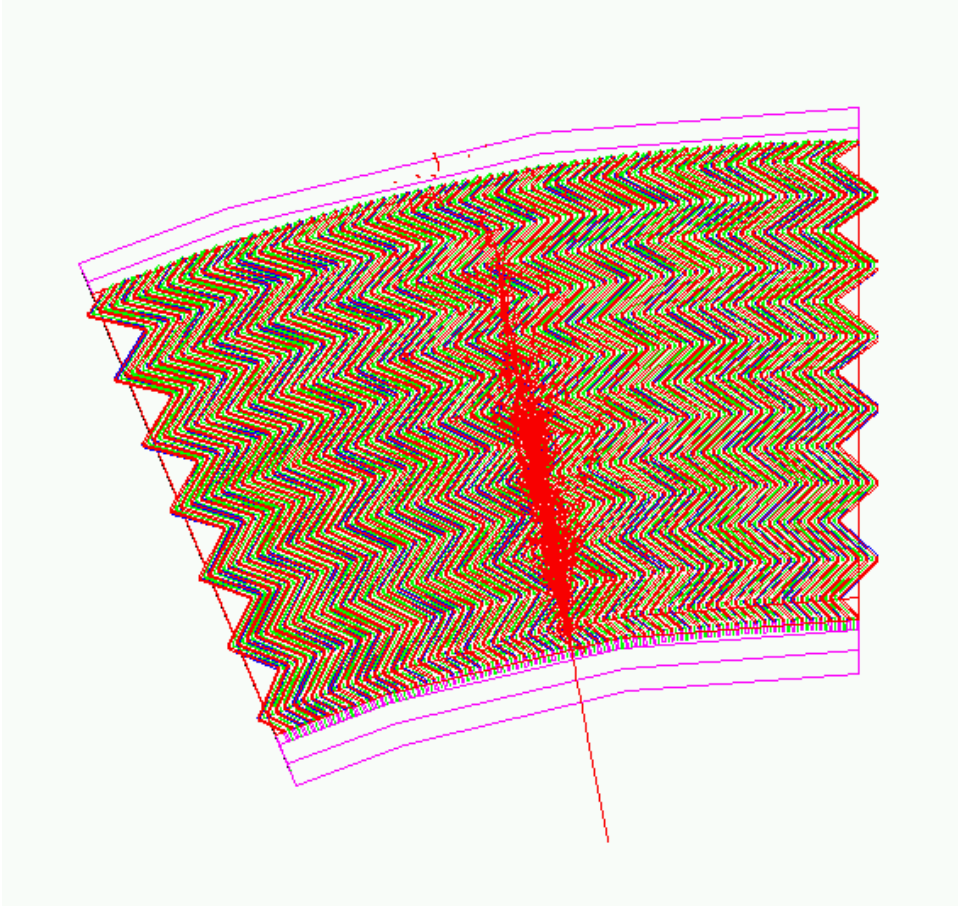

FIG. 2.1 – *Simulation d'une gerbe d'électron de 20 GeV dans un module du calorimètre électromagnétique.*

velle description nous a permis d'évaluer la contribution des fluctuations d'épaisseur des plaques de plomb au terme constant de la résolution en énergie. Pour ce faire, nous avons construit un estimateur qui calcule les fluctuations d'épaisseur en moyenne sur cinq plaques[1] :

$$\frac{\sigma_e^{(5)}}{e} = \frac{RMS[e_i^{(5)} - e_{th}]}{e_{th}} \tag{2.1}$$

où $e_i^{(5)}$ est l'épaisseur de la plaque i moyennée avec l'épaisseur des deux plaques les plus proches de part et d'autre de i, et où e_{th} est l'épaisseur théorique des plaques de plomb.

Utilisant notre programme de simulation, nous avons pu montrer (voir annexe A.2)

[1] Le choix du nombre (5) de plaques a été guidé par des considérations physiques puisqu'une gerbe électromagnétique possède, en moyenne, une taille transverse de 1,67 *gap* ; par conséquent, 4,3 (5,5) plaques contiennent 99 (99,9) % de l'énergie d'une gerbe (voir annexe A.3).

	1,13 mm	1,53 mm
fluctuation d'épaisseur $\frac{\sigma_e^{(5)}}{e_{th}}$	$7,4.10^{-3}$	$2,3.10^{-3}$
contribution au terme constant C_e (%)	0,33	0,12

TAB. 2.1 – *Fluctuation d'épaisseur et contribution au terme constant de la résolution en énergie pour le module 0 du calorimètre électromagnétique.*

que la contribution des fluctuations d'épaisseur au terme constant de la résolution en énergie s'exprime de la manière suivante :

$$C_{1,53}(\%) \simeq 0,53\frac{\sigma_{1,53}^{(5)}}{e_{1,53}} \qquad\qquad C_{1,13}(\%) \simeq 0,44\frac{\sigma_{1,13}^{(5)}}{e_{1,13}} \tag{2.2}$$

où $C_{1,53}$ ($C_{1,13}$) est la valeur du terme constant provenant des fluctuations d'épaisseur des plaques de plomb pour l'épaisseur nominale $e_{1,53} = 1,53$ mm ($e_{1,13} = 1,13$ mm), et $\sigma_{1,53}^{(5)}$ ($\sigma_{1,13}^{(5)}$) est la déviation standard de l'épaisseur des plaques, moyennée sur cinq plaques.

Afin d'évaluer la contribution des fluctuations d'épaisseur au terme constant dans des conditions réelles, nous avons utilisé les mesures d'épaisseur prises sur les plaques de plomb utilisées pour la fabrication du module 0 du calorimètre (ce module, du même type que les 32 modules qui constitueront le calorimètre électromagnétique a été construit pour les tests en faisceau). Le tableau 2.1 donne les valeurs obtenues dans le cas où aucun appariement des plaques est effectué. Utilisant les équations 2.2, on en déduit les valeurs de la contribution au terme constant provenant des fluctuations d'épaisseur, dans les deux cas 1,13 et 1,53 mm (voir tableau 2.1).

2.2 Méthodes d'appariement des plaques de plomb

Afin de réduire la valeur du terme constant provenant des fluctuations d'épaisseur des plaques de plomb, nous avons développé un programme qui effectue l'appariement des plaques avec pour objectif de minimiser les variations d'épaisseur moyennées sur cinq plaques. Ce programme utilise les informations fournies par une table à ultra-sons effectuant sur chaque plaque environ 470 mesures (au total pour les deux plaques, 63 longitudinalement $\times$ 15 radialement) avec une précision de quelques microns. La figure 2.2 montre une vue schématique de cette matrice de mesure. Pour chaque tranche de

η, nous avons calculé la valeur moyenne des mesures ; cette valeur sera utilisée par le programme d'appariement.

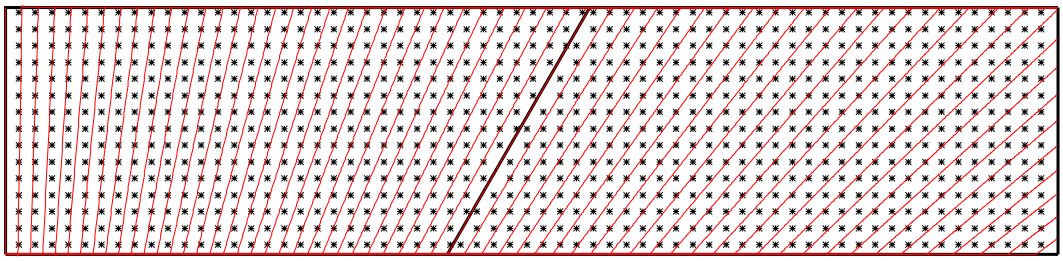

FIG. 2.2 – *Schéma d'une plaque de plomb. Chaque étoile correspond à un point de mesure effectué par la machine à ultra-sons. Les lignes délimitent les celllules en η des électrodes.*

On définit e_{ij} l'épaisseur de la plaque j pour la tranche i en η. La fonction de choix des plaques est la suivante :

$$\sum_{i \in cell.} | \sum_{j \in plaque} w_j (e_{ij} - e_{th}) | \tag{2.3}$$

où w_j vaut respectivement 1 et 2 pour les deux plaques (de la plus éloignée à la plus proche) déjà installées dans le module, 3 pour la plaque à installer, et 2, 1 (de la plus proche à la plus éloignée) pour les deux plaques suivantes[2] ; e_{th} est la valeur nominale (1,13 ou 1,53 selon le cas) de l'épaisseur. La plaque à installer est choisie après minimisation de la fonction de choix.

2.3 Performances de la procédure d'appariement

	$\frac{\sigma^{(5)}_{1,13}}{e_{1,13}}$	$C_{1,13}(\%)$	$\frac{\sigma^{(5)}_{1,53}}{e_{1,53}}$	$C_{1,53}(\%)$
sans appariement	$7,4.10^{-3}$	0,33	$2,3.10^{-3}$	0,12
avec appariement	4.10^{-3}	0,18	$2,2.10^{-3}$	0,12

TAB. 2.2 – *Fluctuation d'épaisseur et contribution au terme constant de la résolution en énergie pour le module 0 avec et sans appariement des plaques de plomb.*

Le tableau 2.2 présente les performances de l'appariement des plaques de plomb dans le cas du module 0. Dans le cas des plaques de 1,13 mm d'épaisseur on observe une

[2] L'installation d'une plaque contraint donc l'installation des deux plaques suivantes.

réduction de l'ordre de 40% de la valeur du terme constant provenant des fluctuations d'épaisseur ; dans le cas des plaques de 1,53 mm d'épaisseur, la réduction est beaucoup plus modeste. Notons qu'en raison des tolérances qui sont en valeur absolue du même ordre pour 1,13 et 1,53, les variations d'épaisseur relatives sont plus faibles pour les plaques de 1,53 mm que pour celles de 1,13 mm. Ceci conduit à une contribution au terme constant plus faible dans la région 1,53 que dans la région 1,13.

Chapitre 3

Conclusion

Les principaux travaux effectués auprès de l'expérience ATLAS et présentés dans ce rapport portent sur l'optimisation du calorimètre électromagnétique pendant la phase d'assemblage des absorbeurs.

Nous avons développé un algorithme d'appariement des absorbeurs dans le but de minimiser les fluctuations d'épaisseur moyennées sur cinq plaques.

Afin de tester et de mettre au point cet algorithme, nous avons adapté le programme de simulation du détecteur à nos besoins en remplaçant, plaque à plaque, l'épaisseur théorique par des épaisseurs variables. Nous avons ainsi pu évaluer l'évolution de la contribution des fluctuations d'épaisseur au terme constant de la résolution en énergie.

Nous avons, de plus, pu évaluer les performances du programme d'appariement dans des conditions réelles, puisque nous avons établi l'appariement du module 0 du calorimètre, module construit pour les tests en faisceau. Cette procédure d'appariement est aujourd'hui utilisée de manière systématique dans la construction des modules qui vont entrer dans la composition du calorimètre électromagnétique d'ATLAS.

Bibliographie

[1] ATLAS : Detector and Physics Performance Technical Design Report, CERN/LHCC/99-14.

[2] ATLAS Liquid Argon Calorimeter Technical Design Report, 15 December 1996.

Deuxième partie

Identification et reconstruction des électrons auprès de l'expérience DØ

Chapitre 1

Introduction

Le détecteur DØ est mis en œuvre auprès du collisionneur proton-antiproton Tevatron (au laboratoire Fermilab dans la banlieue de Chicago) qui fonctionne de manière nominale à une énergie de 2 (1+1) TeV dans le centre de masse de la collision. Le Tevatron succède au LEP pour la recherche du boson de Higgs, mais il est aussi consacré à la recherche de physique au-delà du modèle standard et à l'étude du quark top avant la mise en œuvre du LHC.

Les sujets de physique étudiés par l'expérience DØ peuvent être classés en cinq grandes catégories :
- la physique des quarks top et bottom,
- les études des paires de bosons W et Z,
- les études des interactions QCD,
- la recherche du boson de Higgs,
- la recherche de physique au-delà du modèle standard.

Pour l'ensemble de ces domaines, l'identification et la reconstruction des électrons jouent un rôle majeur. En termes de détection, il est possible d'identifier deux grandes familles d'électrons dans les états finaux vus par le détecteur : les électrons de grande énergie (de l'ordre d'une quarantaine de GeV), issus, par exemple, des désintégrations des Z et W, et les électrons de faible énergie (quelques GeV) issus des désintégrations semi-leptoniques des quarks b ou des résonances de faible masse.

Au niveau du calorimètre électromagnétique, la détection d'un objet «électromagnétique» passe, traditionnellement, par la localisation d'un *cluster* (amas) d'énergie nettement isolé des autres dépots d'énergie, ce qui est le cas pour la majeure partie des électrons de grande énergie. En revanche, les électrons de faible énergie sont pour la plupart émis à proximité d'un jet et l'énergie qu'ils déposent dans le calorimètre est difficilement dissociable de l'énergie déposée par le jet associé. Le calorimètre n'est plus alors un outil suffisant pour identifier de tels électrons et il convient d'utiliser aussi les informations provenant du détecteur de pied de gerbe et du système de mesure des traces.

Dans la suite de cet exposé, nous présentons rapidement la structure du détecteur

DØ, puis nous passons en revue les caractéristiques du calorimètre électromagnétique pour finalement nous concentrer sur l'identification et la reconstruction des électrons.

1.1 Le détecteur DØ

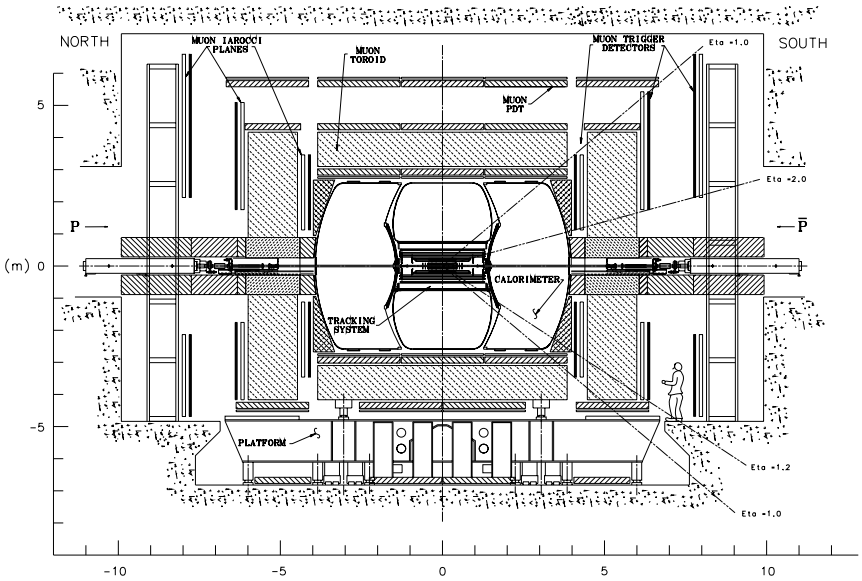

FIG. 1.1 – *Le détecteur DØ.*

Le détecteur DØ ([1], [2]) est composé de trois ensembles de détection et de deux aimants. Du centre, c'est à dire depuis l'axe du faisceau, vers l'extérieur, on trouve :

- le détecteur central (détecteur de vertex [3] + détecteur de traces [4]),
- l'aimant solénoïdal,
- l'ensemble calorimétrique (détecteur de pied de gerbe + calorimètre à argon liquide),
- le détecteur de muons et l'aimant toroïdal.

La figure 1.1 présente une vue schématique du détecteur DØ.

1.2 Le détecteur de traces

Le détecteur de traces CFT (Central Fiber Tracker) est situé entre le détecteur de vertex et l'aimant solénoïdal et ne couvre que la région centrale du détecteur ($|\eta| < 2$). Il participe, avec le détecteur de vertex à la reconstruction des particules chargées.

Ce détecteur est composé de huit compartiments cylindriques (CFT1 à CFT8), chacun comportant deux doublets de fibres scintillantes parallèles à l'axe du faisceau.

La résolution sur la position des traces est de l'ordre de 90 μm et la résolution sur l'impulsion de l'ordre de 8% pour un p_T de 50 GeV/c.

1.3 Le détecteur de pied de gerbe

Le détecteur de pied de gerbe est situé entre l'aimant solénoïdal et le cryostat du calorimètre. Il a pour but de compenser la perte d'énergie dans le solénoïde et d'améliorer l'identification des électrons en fournissant notamment une mesure précise des directions des particules incidentes.

Le détecteur est constitué de trois couches de scintillateurs extrudés contenant les fibres de lecture. Il est précédé d'une plaque d'absorbeur en plomb totalisant deux longueurs de radiation.

La résolution sur la position des traces est de l'ordre de 550 μm.

1.4 Le calorimètre électromagnétique de DØ

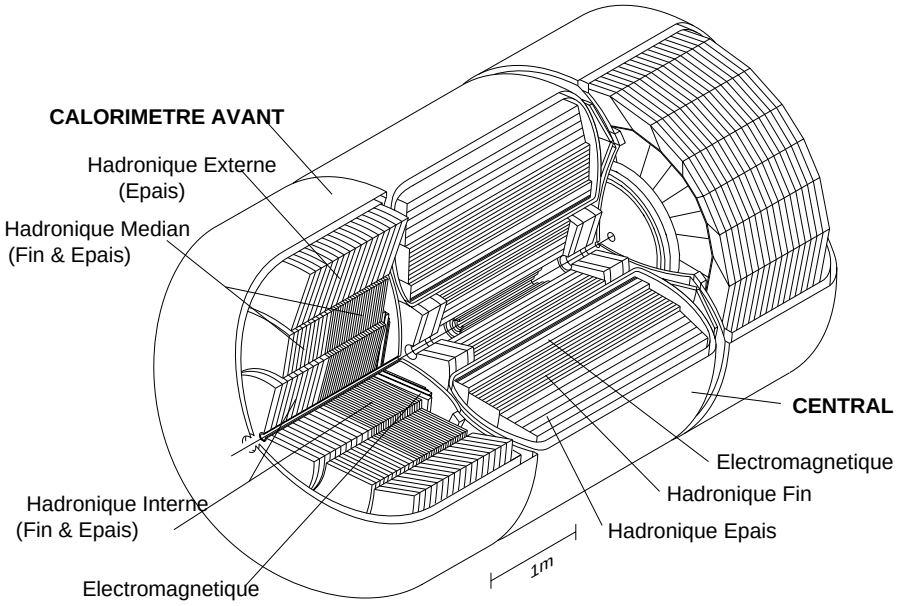

FIG. 1.2 – *Calorimètre à argon liquide de l'expérience DØ.*

Le calorimètre de l'expérience DØ (figure 1.2) est, de même que celui de l'expérience ATLAS, un calorimètre à échantillonnage qui utilise la technique argon liquide. A la différence d'ATLAS, le milieu absorbant utilisé par l'expérience DØ est l'uranium.

1.4.1 Généralités

Le calorimètre est composé de trois éléments : le calorimètre central qui couvre la région en rapidité $|\eta| < 1,1$ et les deux calorimètres bouchons couvrant les régions $1,4 < |\eta| < 4,0$. Le calorimètre électromagnétique est segmenté radialement en quatre compartiments de détection dont les caractéristiques sont résumées dans le tableau 1.1. L'ensemble des cellules qui possèdent le même η et ϕ constituent une tour, comme schématisé sur la figure 1.3.

Compartiment	$\Delta\eta \times \Delta\phi$	$X_\circ$(g/cm^2)
EM1	$0,1 \times 0,1$	1.95
EM2	$0,1 \times 0,1$	1.95
EM3	$0,05 \times 0,05$	6.83
EM4	$0,1 \times 0,1$	9.75
FH1	$0,1 \times 0,1$	38.40

TAB. 1.1 – *Segmentation ($\Delta\eta \times \Delta\phi$) et longueurs de radiation $X_\circ$ pour les différentes couches du calorimètre central (le premier compartiment hadronique, FH1, a été ajouté pour comparaison).*

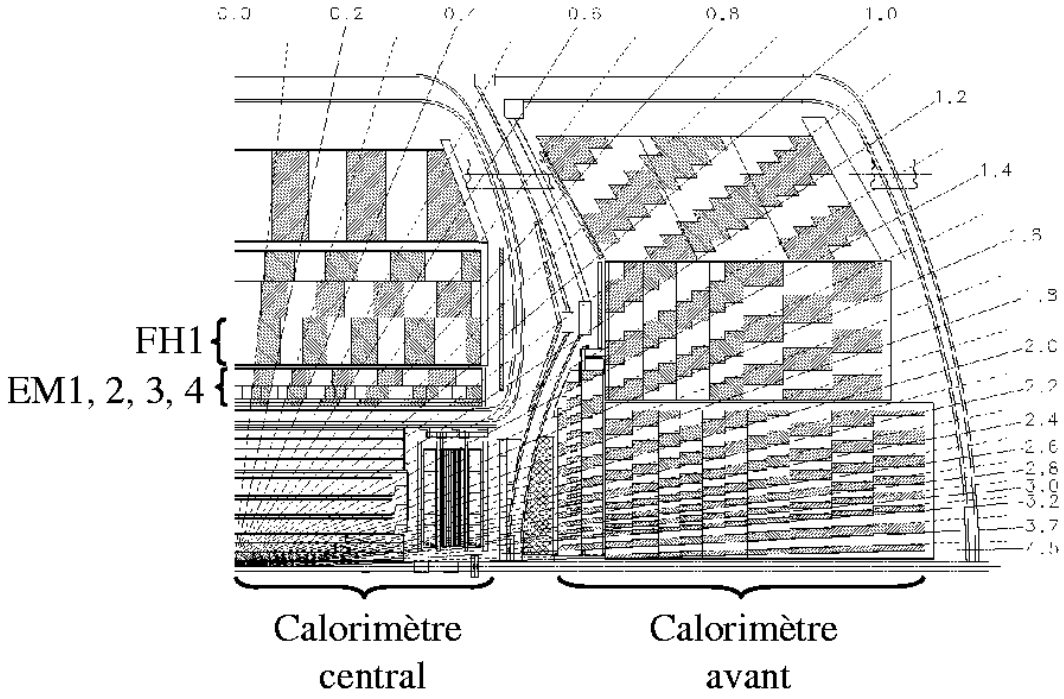

FIG. 1.3 – *Schéma des tours projectives du calorimètre.*

1.4.2 Calorimètre central

A la différence du calorimètre central de l'expérience ATLAS, le calorimètre central de DØ suit une géométrie à plaques planes. Il est constitué de 32 modules séparés par des régions non-instrumentées. Ainsi, les électrons déposant leur énergie dans une région de 0,01 à 0,02 radians autour des espaces non-instrumentés ne sont généralement pas inclus dans les analyses de physique, conduisant à une perte de 10 à 20 % de la statistique disponible.

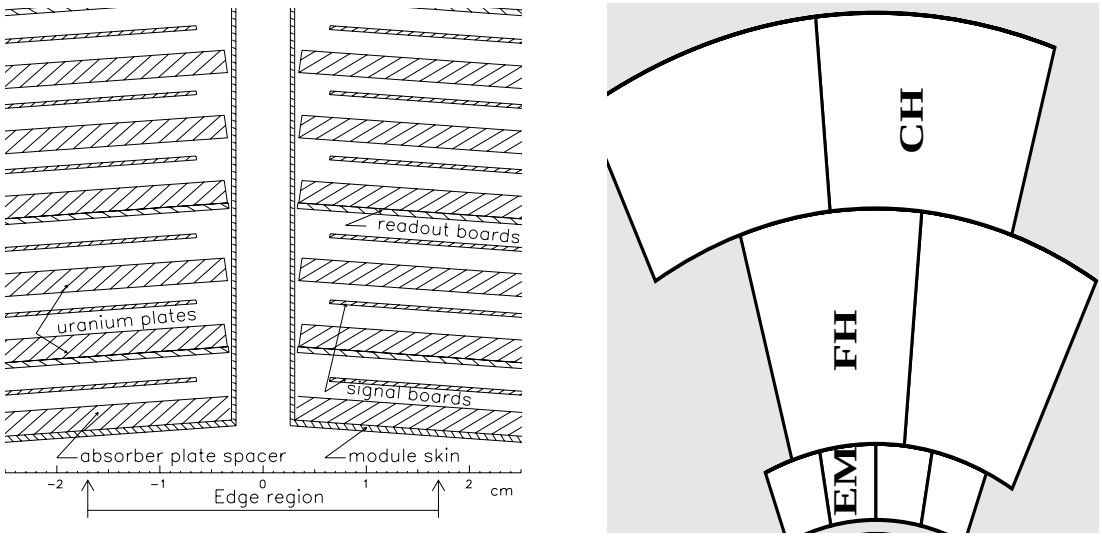

FIG. 1.4 – *Gauche : schéma des régions non-instrumentées du calorimètre ; droite : décalage azimuthal entre le calorimètre électromagnétique (EM) et le calorimètre hadronique (FH).*

Il est toutefois possible de tirer partie de la présence du compartiment hadronique FH1 situé immédiatement à l'arrière du dernier compartiment électromagnétique. Les modules du FH1 offrent une couverture, dans le plan azimuthal, deux fois plus grande que celle fournie par les modules du calorimètre électromagnétique et sont, de plus, décalés azimuthalement de telle manière que leurs régions non-instrumentées ne coïncident pas avec celles du calorimètre électromagnétique (voir figure 1.4).

L'annexe B.1 met en évidence, pour les électrons interagissant au voisinage des espaces non-instrumentés, deux catégories de dépôts d'énergie qui correspondent à deux configurations d'interaction des électrons avec le calorimètre :

- la première catégorie est représentative des électrons interagissant sur le bord d'un module, développant une gerbe standard, mais déposant moins d'énergie en raison de l'absence d'instrumentation,
- la seconde catégorie contient des électrons passant entre deux modules électromagnétiques, développant une gerbe non standard et déposant de l'énergie dans le premier compartiment hadronique (FH1).

Il est montré, dans B.1, qu'une coupure sur la fraction d'énergie électromagnétique permet de séparer les deux populations, et, qu'en utilisant des corrélations appropriées, il est possible de restaurer l'énergie perdue par les électrons dans les régions non-instrumentées.

Chapitre 2

Recherche de candidats électrons

Comme il a été dit dans l'introduction, les électrons traversant le détecteur peuvent être classés en deux grandes catégories : les électrons isolés et les électrons non-isolés. Les électrons isolés sont aisément identifiables, mais nécessitent des algorithmes raffinés pour bien mesurer leur énergie. *A contrario*, les électrons non-isolés sont aisément mesurables, mais plus difficilement identifiables. Il convient donc, dans le programme de reconstruction et d'identification des électrons, de tenir compte des contraintes respectives de ces deux catégories.

Afin de prendre en compte les difficultés techniques que représente la détection des électrons non-isolés (essentiellement de basse énergie), l'algorithme d'identification des électrons a été séparé en deux sous-algorithmes, l'un destiné à la recherche d'électrons isolés, l'autre, à la recherche d'électrons non-isolés. La procédure de regroupement de ces deux lots en un lot d'objets électrons est effectuée dans un troisième temps, décrit dans le chapitre suivant.

Nous allons, ici, passer en revue les deux algorithmes qui permettent de produire les lots de candidats électrons. Le premier hérite directement des algorithmes mis en place et développés pour analyser les données acquises lors du Run I du Tevatron. Il s'appuie sur les informations provenant du calorimètre électromagnétique. Le second tire avantage des nouvelles spécificités du détecteur après son amélioration. En effet, l'apport d'une bobine produisant un champ magnétique sinusoïdal de 2T permet d'obtenir des informations précises sur les traces et sur la charge des particules qui leur sont associées.

2.1 Recherche de *pré-clusters* électromagnétiques

L'algorithme de recherche de *pré-clusters*, actuellement le plus utilisé par la collaboration est l'algorithme «simple cone», issu des études et analyses du Run I. Il peut être résumé comme suit :

parcourant la liste des tours, classées dans l'ordre des impulsions transverses décroissantes (de la tour de plus grand P_T à celle de plus petit P_T),

1. on recherche la première tour telle que P_T(tour)>P_T(seuil), où P_T(seuil) est un paramètre de l'algorithme (par défaut, P_T(seuil) = 0,5 GeV),
2. si P_T(tour) > P_T(seuil), on démarre un *pré-cluster* autour de cette tour «graine»,
   (a) on parcoure la liste des tours restantes et on calcule la valeur : $R^2 = (\eta_{graine} - \eta_{tour})^2 + (\phi_{graine} - \phi_{tour})^2$,
   (b) si $R^2 < R^2(seuil)$, où $R^2(seuil)$ est un paramètre de l'algorithme (par défaut, $R(seuil)$ = 0,4), on ajoute la tour dans le *pré-cluster*.
3. si P_T(*pré-cluster*)>$P_T(min)$, où $P_T(min)$ est un paramètre de l'algorithme (par défaut, $P_T(min)$ = 1 GeV), le *pré-cluster* est ajouté dans la liste des candidats et les tours associées sont retirées de la liste des tours. Dans le cas contraire, le *pré-cluster* est rejeté.

Pour chaque *pré-cluster* sélectionné, on calcule «l'isolation» de la manière suivante :

$$isolation = \frac{E_{tot} - E_{core}}{E_{core}} \tag{2.1}$$

où E_{tot} est l'énergie totale (électromagnétique + hadronique) contenue dans le cône $R^2 < R^2(seuil)$ (pour la définition de R^2, voir ci-dessus), et où E_{core} est l'énergie électromagnétique dans le cône $R^2 < R^2(core)$ (par défaut, $R(core)$=0,2). Par la suite, est considéré isolé, tout *pré-cluster* tel que $isolation < isoratio$ (par défaut, $isoratio = 0,2$).

L'algorithme produit une liste de candidats qui seront utilisés (voir chapitre 3) par le programme global de reconstruction pour produire les objets électrons.

2.2 SEMReco : recherche de candidats trace-tour

L'algorithme que nous allons présenter ici est décrit, en détail, dans les annexes B.2 et B.3. Nous ne ferons donc qu'en énoncer le principe ainsi que les performances obtenues à partir d'événements simulés $Z \to b\overline{b}$.

La figure 2.1 illustre le principe de l'algorithme. Il s'agit de considérer l'ensemble des traces reconstruites d'impulsion transverse supérieure à une valeur seuil (par défaut 1,5 GeV/c), d'extrapoler leur trajectoire jusque dans le calorimètre et de rechercher des dépôts d'énergie dans le détecteur de pied de gerbe et dans le calorimètre au voisinage immédiat de la trajectoire.

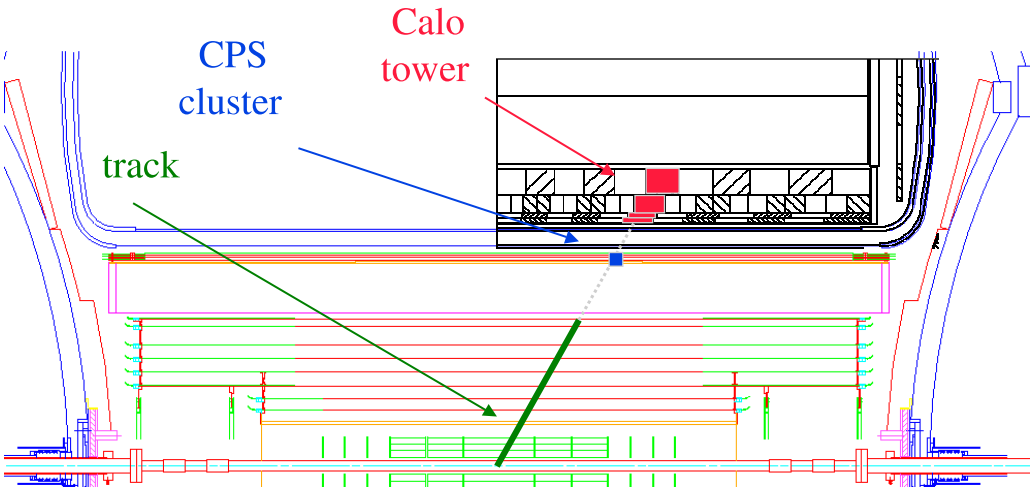

FIG. 2.1 – *Schéma de principe de la recherche d'électrons au moyen de la méthode trace-tour.*

2.2.1 Appariemment trace-*cluster* du détecteur de pied de gerbe

L'appariemment trace-*cluster* est effectué dans une fenêtre $\Delta\eta \times \Delta\phi$ où $\Delta\eta = \eta_{cluster} - \eta_{trace}$ et $\Delta\phi = \phi_{cluster} - \phi_{trace}$.
Une trace est considérée associée à un *cluster* du détecteur de pied de gerbe si :

- $\Delta\eta < 0,025$
- $\Delta\phi < 0,03$

Les valeurs de ces coupures ont été ajustées à l'aide d'électrons simulés dans une gamme d'impulsion transverse allant de 3 à 20 GeV/c et reconstruits dans le détecteur, de telle manière qu'environ 95% des électrons soient effectivement sélectionnés.

2.2.2 Appariemment trace-tour du calorimètre électromagnétique

L'appariemment trace-tour du calorimètre électromagnétique est effectué de la même manière que précédemment : une trace est considérée associée à une tour du calorimètre électromagnétique si :

- $\Delta\eta < 0,05$
- $\Delta\phi < 0,045$

Dans ces conditions, au moins 95% des électrons sont effectivement sélectionnés.

2.2.3 Rejet du bruit de fond

Afin d'étudier les performances de cet algorithme, nous avons utilisé un échantillon d'événements simulés $Z \to b\bar{b}$ pour lesquels les électrons, issus des désintégrations semi-leptoniques des quarks b, sont majoritairement non-isolés.

On définit l'efficacité

$$\varepsilon = \frac{N_e^{T+PS+CAL}}{N_e} \tag{2.2}$$

où N_e est le nombre d'électrons simulés et $N_e^{T+PS+CAL}$ est le nombre d'électrons simulés, reconstruits possédant une trace associée et appariée à un *cluster* du détecteur de pied de gerbe et à une tour du calorimètre électromagnétique,

la pureté

$$\Pi = \frac{N_e^{T+PS+CAL}}{N_{tot}^{T+PS+CAL}} \tag{2.3}$$

où $N_{tot}^{T+PS+CAL}$ est le nombre total de traces appariées à un *cluster* du détecteur de pied de gerbe et à une tour du calorimètre électromagnétique,

et le taux de mauvaise identification

$$misID = \frac{N_{bdf}^{T+PS+CAL}}{N_{bdf}} \tag{2.4}$$

où N_{bdf} est le nombre de traces reconstruites autres que des électrons et $N_{bdf}^{T+PS+CAL}$ est le nombre de traces reconstruites, autres que des électrons, appariées à un *cluster* du détecteur de pied et à une tour du calorimètre électromagnétique.

Le tableau 2.1 donne les résultats obtenus hors efficacité de reconstruction des traces qui, dans notre cas, est de l'ordre de 75%. La première colonne fournit les résultats après appariemment des traces avec un *cluster* du détecteur de pied de gerbe et une tour du calorimètre, montrant une efficacité d'identification des électrons proche de 95%. Le tableau montre aussi que l'application d'une coupure sur la fraction d'énergie électromagnétique vue par la tour appariée permet de réduire le taux de mauvaise identification et d'améliorer la pureté, tout en affectant peu les résultats sur l'efficacité.

	trace+PS+EM no EM frac.	trace+PS+EM 0.5 EM frac.	trace+PS+EM 0.8 EM frac.	trace+PS+EM 0.99 EM frac.
$\varepsilon(\%)$	$96\pm^{4}_{5}$	$96\pm^{4}_{5}$	94 ± 5	67 ± 4
$\Pi(\%)$	55 ± 2	62 ± 2	68 ± 2	85 ± 2
$misID(\%)$	16 ± 6	12 ± 1	9 ± 1	2.3 ± 0.3

TAB. 2.1 – *Performances obtenues, hors efficacité de reconstruction des traces, pour des traces appariées à un cluster du détecteur de pied de gerbe et à une tour du calorimètre électromagnétique, dans les cas suivants (de gauche à droite) : sans coupure sur la fraction d'énergie électromagnétique, 50% de l'énergie provient du calorimètre électromagnétique, 80% de l'énergie provient du calorimètre électromagnétique, 99% de l'énergie provient du calorimètre électromagnétique.*

Chapitre 3

Reconstruction des électrons

Dans cette partie, nous présentons la structure du programme de reconstruction qui utilise, comme informations de départ, les listes des candidats électrons construites durant les deux étapes indépendantes mentionnées dans 2.1 et 2.2.

3.1 Généralités

Un des enjeux essentiels dans la mise au point de cette étape cruciale de la reconstruction des électrons est d'arriver à préserver et utiliser les informations complémentaires que fournissent les deux méthodes de recherche de candidats électrons tout en évitant le problème du double comptage. En effet, si l'algorithme SEMReco permet de trouver des électrons de faible énergie, il permet, *a fortiori*, de trouver des électrons de grande énergie qui sont identifiés par les algorithmes de *pré-clustering*.

Par conséquent, construire des objets électrons en ajoutant les candidats des deux listes reviendrait à construire, dans certains cas, deux fois le même électron. Par ailleurs, puisque les deux méthodes s'appuient sur des concepts opposés, il est important d'utiliser toutes les informations mises à notre disposition. Cette tâche est effectuée par le programme de reconstruction EMReco qui est chargé d'utiliser les informations provenant, à la fois, de SEMReco et des algorithmes de *pré-clustering*, et de produire, *in fine*, une liste d'objet électrons, les EMparticles.

3.2 Sélection des candidats

La sélection des candidats est discutée en détail dans l'annexe B.4. Il s'agit d'utiliser les deux listes de candidats produites en amont et de construire une liste unique de candidats électrons. Comme il a été dit précédemment, un électron détecté peut donner naissance à la fois à un *pré-cluster* électromagnétique et une SEMparticle (candidat électron produit par SEMReco) ; afin d'éviter un double comptage, on cherche, pour

chaque *pré-cluster*, une SEMparticle appariée dans une fenêtre $(\Delta R)^2 = (\Delta\eta)^2 + (\Delta\phi)^2 < 0,01$. La liste des candidats est ensuite construite de la manière suivante :

1. chaque *pré-cluster* isolé (pour la définition de l'isolation, voir section 2.1) ou ayant une SEMparticle associée est ajouté dans la liste des candidats et sera utilisé comme «graine» pour construire le *cluster* électromagnétique final,
2. chaque SEMparticle restante est ajoutée dans la liste des candidats électrons et sera utilisée comme «graine» pour construire le *cluster* électromagnétique final.

3.3 Construction du *cluster* électromagnétique final

Partant de la liste des candidats (voir section 3.2), EMReco construit, pour chaque candidat, un *cluster* électromagnétique (voir annexe B.4) et lui associe un identifiant caractéristique des propriétés du *cluster*. On distingue quatre grandes familles de *cluster* électromagnétiques :

1. graine = *pré-cluster* ; satisfait le critère d'isolation et possède une SEMparticle associée. Qualitativement, cette catégorie contient les électrons les mieux identifiés.
2. graine = *pré-cluster* ; satisfait le critère d'isolation et ne possède pas de SEMparticle ou de trace associée. Les photons se rangent dans cette catégorie.
3. graine = *pré-cluster* ; ne satisfait pas le critère d'isolation et possède une SEMparticle associée. Electron proche d'un jet
4. graine = SEMparticle ; ne satisfait pas le critère d'isolation. Electron proche ou dans un jet.

Après avoir formé un *cluster* électromagnétique, EMReco complète l'information sur l'objet électron en intégrant les informations issues du détecteur de pied de gerbe et du détecteur de traces (voir annexe B.4) si elles existent. Là encore, toute l'information provenant des SEMparticles associées est utilisée. Si il n'y a pas de SEMparticle associée, ou si SEMparticle ne contient pas de *cluster* du détecteur de pied de gerbe, un algorithme de recherche de *cluster* dans le détecteur de pied de gerbe et/ou de trace associés entre en jeu (voir annexe B.4).

3.4 Performances du programme de reconstruction

Dans cette partie, nous présentons les performances obtenues avec le programme de reconstruction EMReco. Ce programme a été testé avec des événements simulés $Z \to e^+e^-$.

On considère qu'un objet électron est parfaitement reconstruit si lui sont associés, dans le détecteur, un *cluster* électromagnétique, un *cluster* dans le détecteur de pied de gerbe et une trace dans le système de détection des traces. L'étude que nous avons faite sur l'efficacité du programme de reconstruction se décompose donc en trois étapes :

1. mesure de l'efficacité de la reconstruction des *clusters* dans le calorimètre,

2. mesure de l'efficacité de la reconstruction des *clusters* dans le détecteur de pied de gerbes,
3. mesure de l'efficacité de la reconstruction des traces.

Par ailleurs, afin de tester de manière pertinente le programme de reconstruction, il convient d'étudier l'efficacité dans des régions où le détecteur offre son plein potentiel de détection, régions qui sont différentes selon que l'on considère le calorimètre électromagnétique, le détecteur de pied de gerbe ou le système de mesure des traces. Nous avons donc défini des régions «fiducielles», régions géométriques couvertes par les différents détecteurs.

Nous nous limiterons ici aux résultats obtenus dans la région centrale du détecteur.

3.4.1 Régions «fiducielles»

La région «fiducielle» centrale peut être décomposée en trois sous-régions correspondant au trois sous-détecteurs, le calorimètre, le détecteur de pied de gerbe et le détecteur de traces. Le tableau 3.1 donne les valeurs utilisées pour chacun des sous-détecteurs. Ne sont utilisées dans les analyses que les particules (simulées et/ou reconstruites) traversant ces régions «fiducielles».

Détecteur	longueur du détecteur $\lvert z_{max}\rvert$ (cm)	longueur de la région «fiducielle» $\lvert z_{fid}\rvert$ (cm)	η «fiduciel»
CFT1	83,1	74,8	2,02
CFT2	83,1	74,8	1,81
CFT3	126,0	113,4	2,04
CFT4	126,0	113,4	1,89
CFT5	126,0	113,4	1,77
CFT6	126,0	113,4	1,66
CFT7	126,0	113,4	1,56
CFT8	126,0	113,4	1,53
CPS	120,6	108,5	1,19
Calorimètre	129,9	116,9	1,06

TAB. 3.1 – *Régions fiducielles du détecteur de traces, du détecteur de pied de gerbe (CPS) et du calorimètre. Les CFT1 à CFT8 correspondent aux huit compartiments qui composent le détecteur de traces. |z max| est la longueur du détecteur par rapport à la position du point d'interaction, |z «fiduciel»| est la longueur choisie pour la région «fiducielle» et η «fiduciel» est la valeur maximale de la rapidité dans la région «fiducielle».*

La figure 3.1 illustre les coupures appliquées. Les traits signalés par des flèches correspondent aux régions fiducielles. Les variations sur la position du vertex de l'interaction (0± 56 cm, soit deux écarts standards) sont aussi représentées.

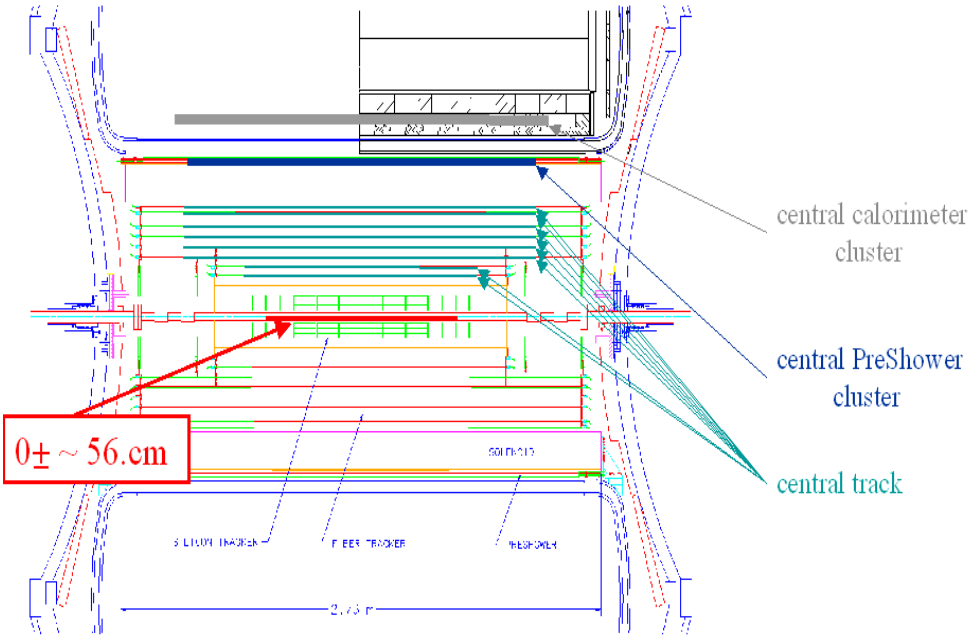

FIG. 3.1 – *Régions fiducielles de la partie centrale du détecteur. Une particule incidente est considérée comme traversant la région «fiducielle» du détecteur de traces si elle traverse les huits compartiments CFT1 à CFT8.*

3.4.2 Mesure des efficacités

Comme il a été dit précédemment, nous avons mesuré trois efficacités différentes auxquelles sont associées trois régions «fiducielles» différentes (correspondant aux régions couvertes par les trois sous-détecteurs). La figure 3.2 montre les distributions en impulsion transverse pour chacun des cas :

1. région «fiducielle» du calorimètre électromagnétique :
   a) électrons simulés (nombre de particules = N_{MC}^{Calo}).
   b) électrons simulés et reconstruits. *Cluster* calorimétrique associé (nombre de particules = N_{EM}^{Calo}).
2. Région «fiducielle» du détecteur de pied de gerbe :
   c) électrons simulés et reconstruits. *Cluster* calorimétrique associé (nombre de particules = N_{EM}^{PS}).
   d) électrons simulés et reconstruits. *Cluster* calorimétrique + *cluster* PS (détecteur de pied de gerbe) associés (nombre de particules = N_{EM+PS}^{PS}).
3. Région «fiducielle» du détecteur de traces :
   e) électrons simulés et reconstruits. *Cluster* calorimétrique + *cluster* PS associés (nombre de particules = N_{EM+PS}^{TRK}).
   f) électrons simulés et reconstruits. *Cluster* calorimétrique + *cluster* PS + trace associés (nombre de particules = $N_{EM+PS+TRK}^{TRK}$).

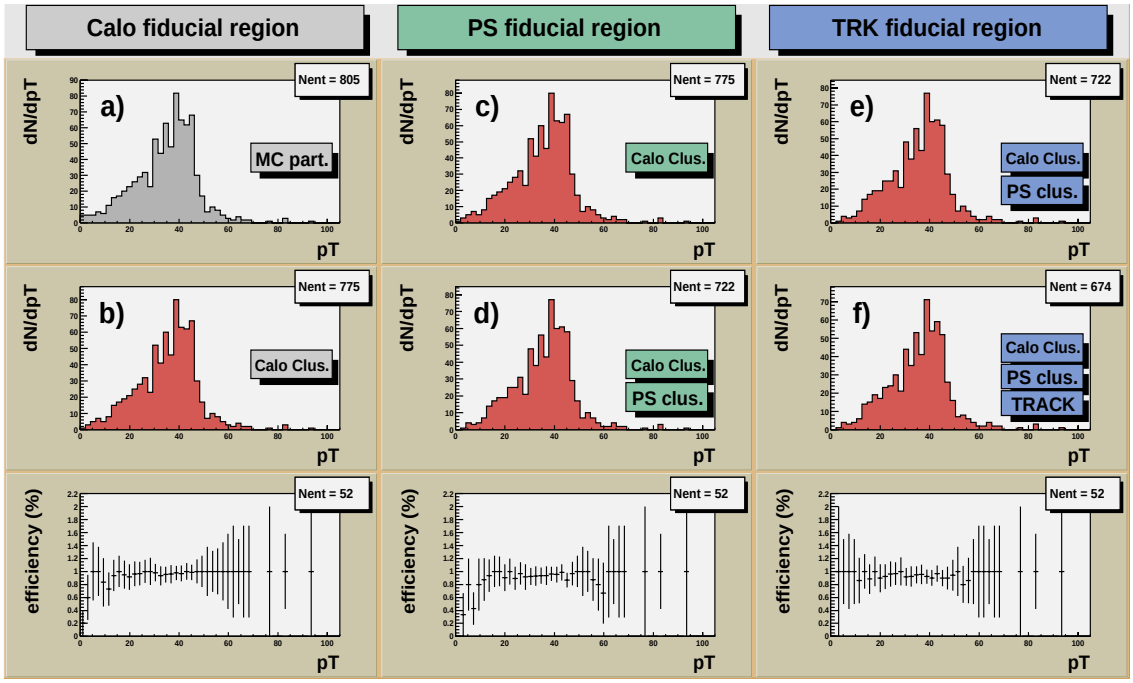

FIG. 3.2 – *Efficacité de reconstruction. De gauche à droite : efficacité de reconstruction des clusters calorimétriques, efficacité de reconstruction des clusters du détecteur de pied de gerbe, efficacité de reconstruction des traces.*

Les trois efficacités sont définies comme suit :

$$\varepsilon_{Calo} = \frac{N_{EM}^{Calo}}{N_{MC}^{Calo}} \qquad \varepsilon_{PS} = \frac{N_{EM+PS}^{PS}}{N_{EM}^{PS}} \qquad \varepsilon_{TRK} = \frac{N_{EM+PS+TRK}^{TRK}}{N_{EM+PS}^{TRK}} \tag{3.1}$$

où ε_{Calo} est l'efficacité de reconstruction des *clusters* électromagnétiques, ε_{PS} est l'efficacité de reconstruction des *clusters* du détecteur de pied de gerbe et ε_{TRK} est l'efficacité de reconstruction des traces. Numériquement, les résultats obtenus sont résumés dans

	calorimètre électromagnétique	détecteur de pied de gerbe	détecteur de traces
efficacité (en %)	96^{+3}_{-3}	93^{+3}_{-3}	93^{+4}_{-4}

TAB. 3.2 – *Efficacité de reconstruction. De gauche à droite : efficacité de reconstruction des clusters calorimétriques, efficacité de reconstruction des clusters du détecteur de pied de gerbe, efficacité de reconstruction des traces.*

le tableau 3.2 et montrent de bonnes efficacités de reconstruction. La figure 3.3 montre

les distributions en impulsion transverse des *clusters* reconstruits dans le calorimètre électromagnétique. Comme attendu (pour des événements $Z \to e^+e^-$), la grande ma-

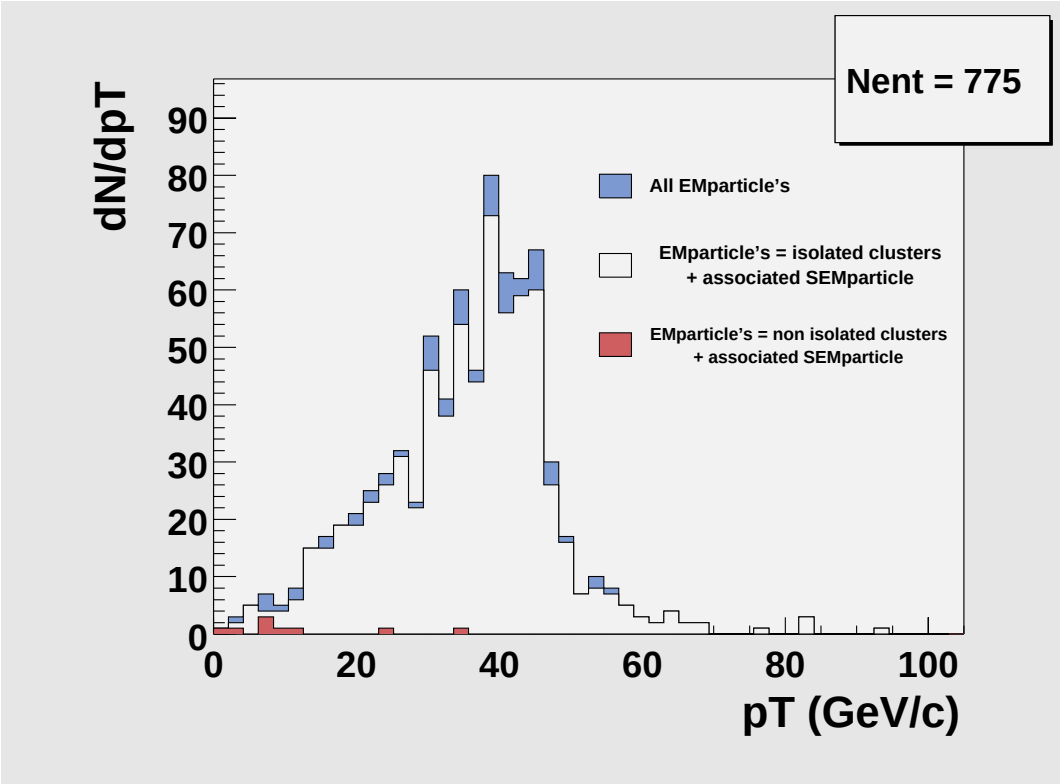

FIG. 3.3 – *Isolation des clusters électromagnétiques. La courbe bleue correspond à l'ensemble des clusters reconstruits ; la courbe blanche montre l'ensemble des clusters reconstruits, isolés et possédant une SEMparticle associée ; la courbe rouge représente l'ensemble des clusters non-isolés.*

jorité des clusters sont isolés. Notons qu'environ 90% des clusters isolés possèdent une SEMparticle associée (correspondant à l'efficacité de reconstruction des traces), justifiant *a posteriori* l'importance de construire une liste unique de candidats électrons comme mentionné dans la section 3.2.

Chapitre 4

Conclusion

Les principaux travaux effectués auprès de l'expérience DØ et présentés dans ce rapport portent sur les programmes d'identification et de reconstruction des électrons.

Nous avons développé et implémenté un algorithme d'identification d'électrons s'appuyant sur les informations provenant du détecteur de traces dans un premier temps, puis sur les informations provenant du détecteur de pied de gerbe et du calorimètre électromagnétique.

Par la suite, nous avons participé à l'adaptation du programme global de reconstruction afin qu'il prenne en compte les listes de candidats produits par ce nouvel algorithme et qu'il exploite et fournisse toute l'information disponible.

Enfin, nous avons développé et implémenté un programme d'analyse utilisant les informations issues des programmes d'identification et de reconstruction et permettant d'en tester les efficacités. Nous avons, de plus, rédigé une documentation qui présente le détail du programme global de reconstruction et qui, à l'heure actuelle, constitue le seul document de référence sur ce sujet.

Pour être complet, nous avons effectué des tests au moyen de données simulées. Ces tests montrent une bonne efficacité des programmes de reconstruction qui sont actuellement validés et améliorés au moyen des données réelles, en cours d'acquisition par l'expérience DØ.

Bibliographie

[1] Collaboration DØ, Nucl. Instrum. Meth. A **338** (1994) 185.

[2] Collaboration DØ, Nucl. Instrum. Meth. A **408** (1998) 103.
Collaboration DØ, *The DØUpgrade, The Detector and its physics*, DØnote (1996).

[3] R. Lipton, Nucl. Instrum. Method. A **418** (1998) 85.
M. T. Roco, Nucl. Instrum. Meth. A **418** (1998) 91.
J. Ellison, Nucl. Instrum. Meth. A **342** (1994) 33.
Collaboration DØ, *DØSilicon Tracker Technical Design Report*, DØnote 2169 (1994).

[4] M. R. Wayne, Nucl. Instrum. Meth. A **387** (1997) 278.
M. Adams *et al.*, Nucl. Instrum. Meth. A **366** (1995) 263.
A. Bross *et al.*, Nucl. Instrum. Meth. A **394** (1997) 87.
B. Baumbaugh *et al.*, Nucl. Instrum. Meth. A **345** (1994) 271.
Collaboration DØ, *The DØupgrade central fiber tracker Technical Design Report, DØnote* (1997).

Perspectives

Les travaux et études effectués auprès de l'expérience DØ ont montré l'importance du critère d'isolation pour l'identification et la reconstruction des électrons. S'appuyant sur ce critère, nous avons adapté le programme de reconstruction de l'expérience pour qu'il permette l'identification des électrons sur une grande gamme d'énergie. Ce travail a été accompli au cours de l'année 2001.

Le travail que nous avons présenté a été effectué à l'aide de données simulées et l'ensemble des paramètres utilisés dans les algorithmes nécessitent donc une optimisation à partir de données réelles, actuellement en cours d'acquisition.

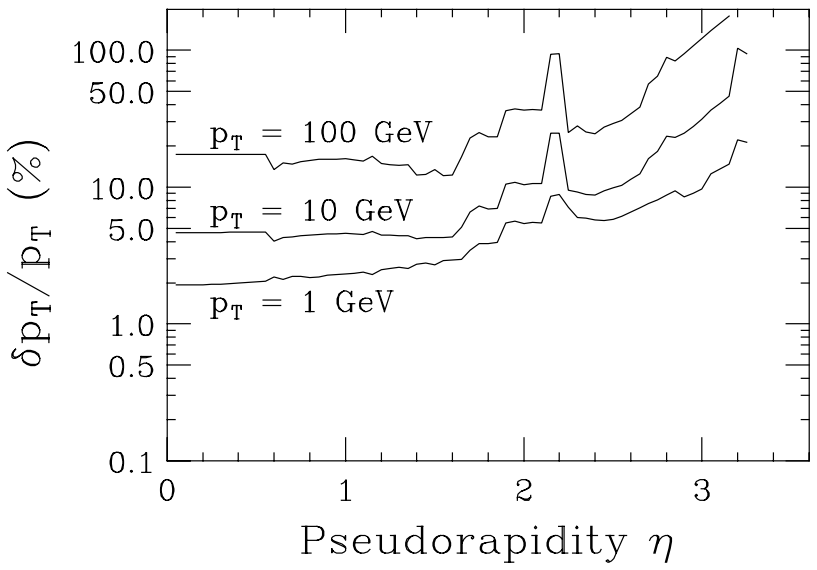

FIG. 4.1 – *Résolution sur la mesure de l'impulsion pour le détecteur de traces.*

Par ailleurs, le travail d'optimisation de la mesure de l'énergie et de la position des candidats électrons identifiés par le programme de reconstruction reste à être effectué. Comme nous l'avons dit précédemment, un candidat électron est caractérisé par un dépôt d'énergie dans le calorimètre électromagnétique, la présence d'une trace associée à ce dépôt d'énergie et éventuellement un *cluster* dans le détecteur de pied de gerbe. Il est donc possible d'utiliser les informations provenant à la fois du calorimètre électroma-

gnétique et du détecteur de traces pour mesurer de manière précise l'énergie des électrons.

La figure 4.1 montre la résolution accessible par le détecteur de traces sur la mesure de l'impulsion d'une particule. Les trois courbes correspondent à trois valeurs différentes de l'impulsion transverse de la particule mesurée. En comparant à la résolution attendue pour le calorimètre électromagnétique (de l'ordre de 15 à 20 $\%/\sqrt{E}$), on peut en déduire que, dans la région centrale, la mesure de l'énergie d'un électron est obtenue de manière plus précise avec le détecteur de traces pour des électrons d'impulsion transverse inférieure à 10–15 GeV et par le calorimètre électromagnétique pour des énergies plus élevées. Il serait, par conséquent, extrêmement utile d'utiliser conjointement les informations provenant des deux détecteurs afin d'obtenir des résolutions effectives plus faibles. Il semble, par exemple, intéressant de moyenner les deux mesures en les pondérant par la résolution attendue pour chacun des détecteurs.
De telles études seront entreprises, dans les mois à venir, au sein de la collaboration.

L'expérience ATLAS est, quant à elle, actuellement en phase de construction. L'algorithme d'appariemment que nous avons développé est utilisé de manière systématique dans l'assemblage des 32 modules qui viendront constituer la partie centrale du calorimètre électromagnétique. Du point de vue de la reconstruction des électrons, un grand travail reste à être entrepris sur les algorithmes d'identification et de reconstruction des électrons. Considérant les similitudes entre les expériences ATLAS et DØ, il serait profitable pour l'expérience ATLAS d'utiliser les compétences et l'expérience acquises auprès de l'expérience DØ et de s'appuyer sur l'architecture et les méthodes utilisées par celle-ci pour mettre en place son programme de reconstruction des électrons.

Annexe A

Notes ATLAS

A.1 Correction of Lead Plates Thickness Fluctuation Effect on the Energy of the EM Accordion Calorimeter. *F. Fleuret, B. Laforge, P. Schwemling*. **ATL-LARG-2000-001 (ATL-COM-LARG-99-022).**

A.2 Constant Term Evolution with Lead Plate Thickness Fluctuations in EM Module 0. *F. Fleuret, B. Laforge, P. Schwemling*. **ATL-LARG-2000-002 (ATL-COM-LARG-99-021).**

A.3 Lead Matching and Consequences on the EM Module 0 Constant Term. *F. Fleuret, B. Laforge, P. Schwemling*. **ATL-LARG-99-014 (ATL-COM-LARG-99-020).**

Annexe B

Notes DØ

B.1 Energy Restoration of Edge Electrons in the DØ Central Calorimeter. *F. Fleuret*. **DØ note 3739.**

B.2 Low Energy Electron Identification in DØ. *F. Fleuret*. **DØ note 3870.**

B.3 The DØ Soft Electron Reconstruction Package SEMReco. *F. Fleuret, F. Beaudette, S. Protopopescu*. **DØ note 3872.**

B.4 The DØ Electron/Photon Analysis Package EMAnalyze. *F. Fleuret*. **DØ note 3888.**

September 22, 1999

ATL-LARG-2000-001
15/02/2000

Correction of lead plates thickness fluctuation effect on the energy of the EM accordion calorimeter

F. Fleuret, B. Laforge, Ph. Schwemling

LPNHE-Paris, Universités Paris 6-7, and IN2P3-CNRS

Abstract

We present in this note a method to construct a correction function of the EM accordion calorimeter energy to take into account the lead plates inhomegeneous thickness distribution. After having derived the method, the results of the analysis of the real Module 0 plates distribution are presented and discussed. We show that the knowledge of the lead plate thickness can be used to correct the reconstructed energy such as the residual constant term due to lead thickness fluctuation can be reduced. We show that the connection between two modules with two different mean thickness can be also very well corrected resulting in a very small constant term contribution.

1 Introduction

The challenge of the EM accordion calorimeter is to measure the energy of electromagnetic showers with a global constant term of about $C_{tot} \sim 0.5‰$ as quoted in [1]. As previously shown in [2], the lead plates actually put in the ATLAS accordion calorimeter have a thickness which can fluctuate around the nominal value within a range $\pm 0.6\%$ of the nominal value. These fluctuations lead to an increase of the energy constant term as studied in [3]. This contribution has to be smaller than 0.3 % if we want to be able to study the channel $h \rightarrow \gamma\gamma$ and have a chance to discover a very light Higgs boson.

In order to reduce the effects of lead thickness fluctuation on the energy resolution, a pairing process based on the fact that an electromagnetic shower deposits its energy within 5 lead plates has been developped. This procedure reduces by almost a factor two the contribution to the constant term coming from lead thickness inhomogeneities. Nevertheless, the produced modules have a residual plate to plate thickness fluctuation.

The ideas and the method presented below intend to show that this residual effect on the constant term can be highly reduced from the knowledge of lead plate thicknesses measured in the hall IN2P3 at Orsay during the construction process.

2 Principles of the correction method

The leading idea is to take into account two basic physical effects :

- Five plates are seen by a single electromagnetic shower,
- the signal loss due to an increase by 1% of the lead thickness is respectively 0.59%/0.47% of the nominal signal for a nominal lead thickness of 1.53 mm/1.13 mm.

The last statement is coming from the simulation of the EM barrel Module 0 made in Paris [4]. We have dedicated a special production of 4050 simulated EM showers with a "perfect" module but with a lead thickness 1% uniformely above the nominal value. "Perfect" module is to be understood as a module with no fluctuation at all in its mechanics structure i.e. every absorber is the same, every gap is the same, every cell sees the same high voltage, etc... We have used 4050 showers initiated by 50 GeV electrons in that configuration and 4050 other coming from a simulation of a perfect module with the nominal lead thickness $1.5mm$. These electrons have been

shot at $\eta = 0.3$ and in the ϕ range $[0.1; 0.3]$. Figure (2) shows the reconstructed energy in both cases. Using the mean values of the distributions or the mean values coming from a gaussian fit made on these distributions lead to an estimation of the energy loss of $\epsilon_A = -0.59\% \pm 0.01\%$.

The same study has also been done in the 1.13 mm lead thickness part at $\eta = 1.1$ as shown figure (2) showing in that region a weaker dependance $\epsilon_B = -0.44\% \pm 0.01\%$.

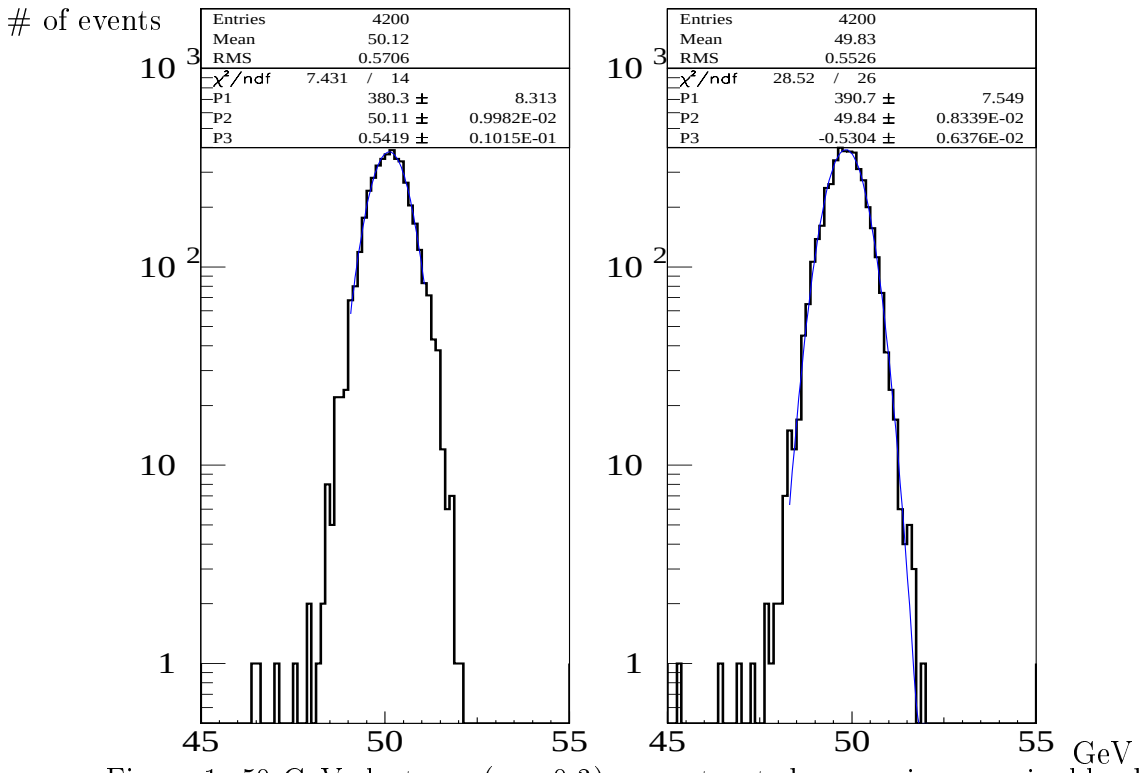

Figure 1: 50 GeV electrons ($\eta = 0.3$) reconstructed energy in a nominal lead thickness module (right) and in a module with lead thickness 1% above the nominal value (left).

The available information that we can use to correct the lead fluctuation effect is a precise measurement of lead plates which is available as a map of about 70×15 points per absorber.

The method applied to correct for lead thickness fluctuation has three steps :

1. the local lead thickness averaged over 5 plates is computed,
2. the obtained distribution is normalised to the nominal value,
3. the correction function is computed taking into account the local difference between the lead thickness and the nominal value.

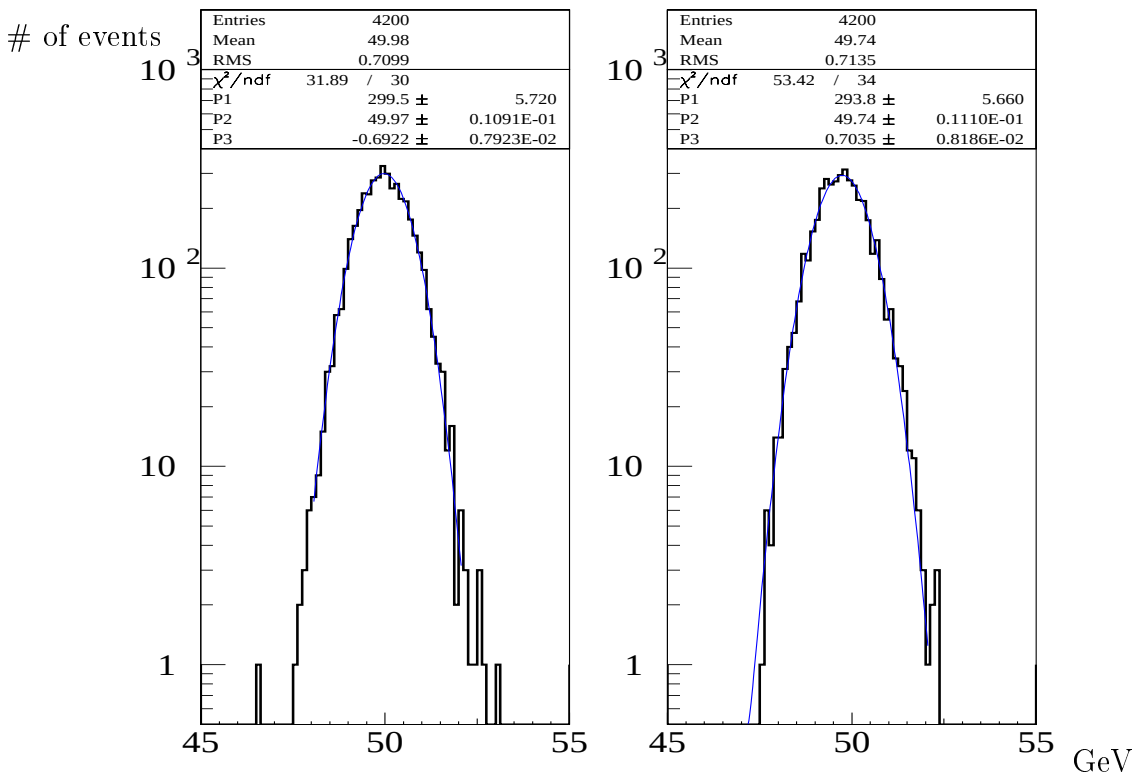

Figure 2: 50 GeV electrons ($\eta = 1.1$) reconstructed energy in a nominal lead thickness module (right) and in a module with lead thickness 1% above the nominal value (left).

3 Construction of the correction function

In order to study the power of this correction procedure, we have used a set of simulation files with 4050 50 GeV electrons interacting in a module with a determined lead plate distribution shown in figure (3.a) corresponding to a flat distribution with a relative width $\frac{\Delta e}{e_0} = 10\%$ where $e_0 = 1.53$ mm is the nominal thickness.

This very large fluctuation has been made in order to have a very large effect on the recontructed energy distribution. All the electrons have been generated at a fixed $\eta = 0.3$ and in the ϕ range [0.1;0.3] to avoid energy leakage due to the fact that we have a single module in the simulation.

The reconstructed energy fluctuation induced by this lead thickness distribution is shown in figure (4.a) as a function of the generated ϕ angle of the electrons.

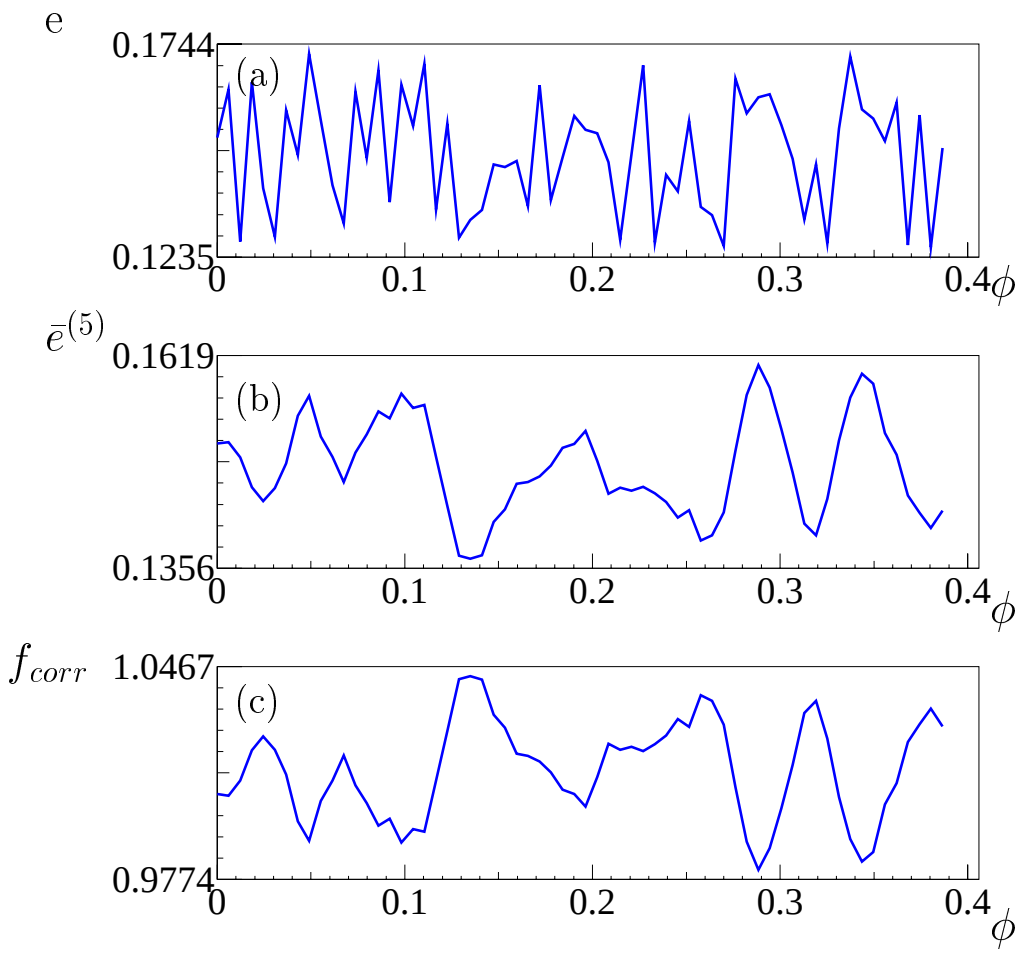

Figure 3: (a) Plot of lead plate thickness put in the simulation versus ϕ ($\phi_n = \frac{2\pi}{1024} * n$ where n is the plate indice in the module ; $n \in [1, 64]$) in the calorimeter, (b) Plot of mean lead plate thickness over 5 plates (computed as explained in the text) versus n, (c) correction function versus ϕ

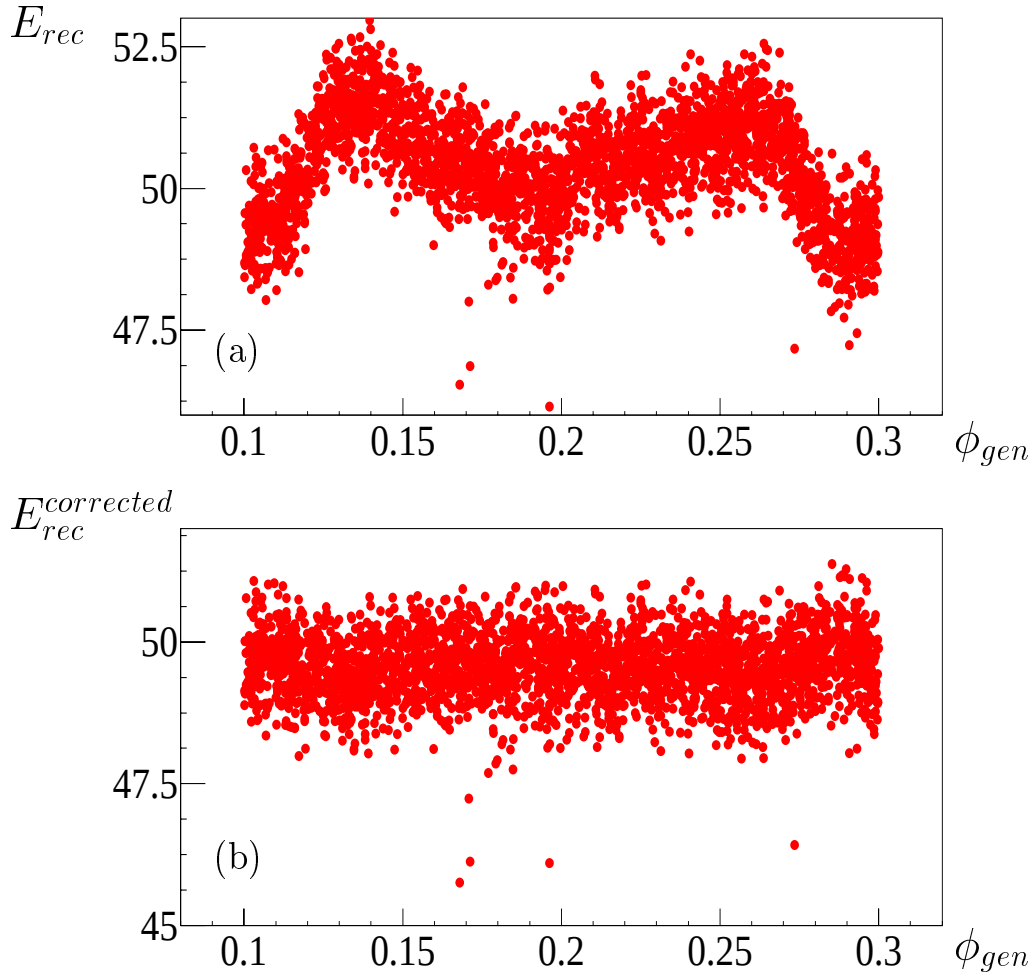

Figure 4: (a) Scatter plot of the reconstructed energy versus ϕ_{gen} for 50 GeV electrons (b) Scatter plot of the corrected reconstructed energy versus ϕ_{gen} for 50 GeV electrons

We construct the correction function following 4 steps :

1. We define an array $e(n)$ (n=1,..,64) containing all the individual lead plate thicknesses

2. From $e(n)$, an array $\bar{e}^{(5)}(n)$ of the mean thickness over 5 plates is computed using a dedicated weighting for each of the 5 plates using the formula :

$$\bar{e}^{(5)}(n) = \frac{\sum_{i=n-2}^{n+2} w_i \, e(i)}{\sum_{i=n-2}^{n+2} w_i}$$

with 3 options (if $n \pm i$ (with $i = 1, 2$) is not in the range [1,64], $w_i = 0$):

A- $w_{n-2} = 0$, $w_{n-1} = 0$, $w_n = 1$, $w_{n=1} = 0$, $w_{n+2} = 0$

B- $w_{n-2} = 1$, $w_{n-1} = 2$, $w_n = 3$, $w_{n=1} = 2$, $w_{n+2} = 3$

C- $w_{n-2} = e^{\frac{-2}{2\sigma^2}}$, $w_{n-1} = e^{\frac{-1}{2\sigma^2}}$, $w_n = 1$, $w_{n=1} = e^{\frac{-1}{2\sigma^2}}$, $w_{n+2} = e^{\frac{-2}{2\sigma^2}}$

where $\sigma = 1.67$ is the sigma in number of gaps (or equivalently of plates) obtained from a gaussian fit of the EM energy deposited in the accordion calorimeter for electrons shot at a given (η, ϕ) point as explained in [3].

3. We compute the correction function $f_{corr}(\phi_n)$ for each ϕ_n with the following formula :

$$f_{corr}(\phi_n) = \frac{1}{(\frac{\bar{e}^{(5)}(n)}{e_0} - 1) \times \epsilon_A + 1}$$

For a random ϕ, we determine n such as $\phi_n < \phi < \phi_{n+1}$ and we make a linear interpolation of $f_{corr}(\phi)$ between $f_{corr}(\phi_n)$ and $f_{corr}(\phi_{n+1})$.

Figures (3.b) and (3.c) present respectively $\bar{e}^{(5)}$ and the correction function in the (C) case obtained from the lead plate thickness distribution used in the simulation. The corrected energy is then presented figure (4.b), showing a very good correction of the ϕ inhomogeneities. The corrected energy is obtained with the following formula :

$$E_{rec}^{corrected} = \frac{E_{rec}}{f_{corr}}$$

Here, E_{rec} is already corrected from the usual ϕ modulation as explained in the reference [4].

4 Application to the Module 0 lead plate distribution

In order to validate the method and to evaluate the effect on a realistic lead plate distribution, we have simulated a module with the effective plate thickness of the real Module 0. The plate distribution that we used is presented figure (5.a) as a function of the ϕ angle.

We have triggered 4050 electrons in that simulation at a fixed $\eta = 0.3$ and in the ϕ range $\phi \in [0.1, 0.3]$. We have then applied the same procedure as explained in [4] to extract a relevant evaluation of the sampling and constant

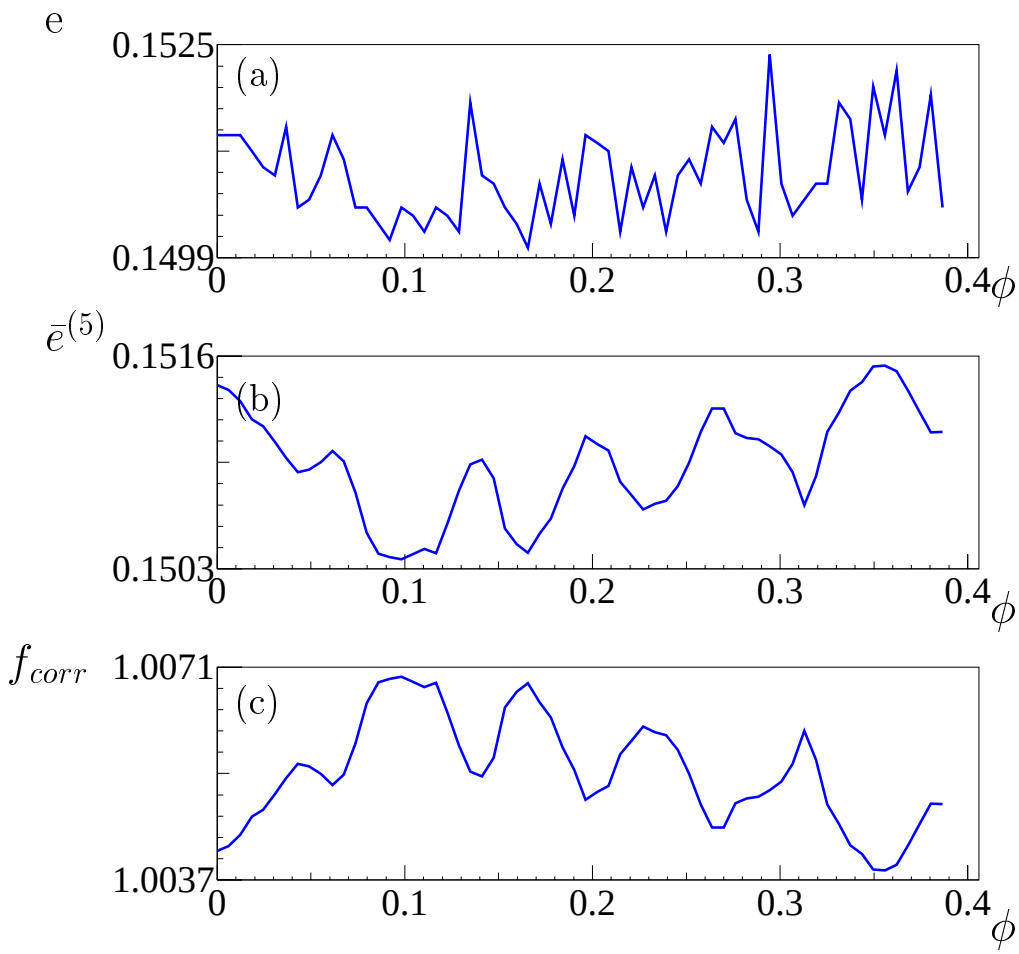

Figure 5: (a) Plot of lead plate thickness put in the simulation versus ϕ ($\phi_n = \frac{2\pi}{1024} * n$ where n is the order indice in which they are put in the module and is in the range $[1, 64]$) in the calorimeter, (b) Plot of mean lead plate thickness over 5 plates (computed as explained in the text) versus n, (c) correction function versus ϕ. This lead plate thickness distribution is the one of the Module 0 built up in Orsay last year.

term of the module 0 taking into account the residual usual ϕ modulation and the lead plate thickness modulation.

Figure (6.a) shows the results obtained when only the usual ϕ modulation correction is applied. We end with a constant term of $2.9‰ \pm 0.2‰$ and a sampling term of $7.76\% \pm 0.08\%$.

Figures (6.b), (6.c) and (6.d) show the results obtained when a correction taking respectively into account :

- thickness of lead plate which is the closest to the generated direction of the electron (option A),
- thickness of the 5 plates with a triangle shower shape (option B)
- thickness of the 5 plates with a gaussian shower shape (option C).

One can see that as soon as one of these corrections is applied the constant term is highly reduced below $3.‰$ and that the sampling term stays the same ($7.76\% \pm 0.08\%$) within the statistical errors of the perfect case.

Option C gives the best constant term as expected but the difference between option A,B and C is not large and stays in the error bar. Nevertheless, as all these plots correspond to the same initial distribution of events, the different plots are highly correlated. Thus we can infer that the improvement of the constant term from option A to C is real. This is confirmed also by the evolution of the χ^2 of the different fits which favors undoubtly option C.

The best result that we obtain is then a sampling term of $7.76\% \pm 0.08\%$ and a constant term of $2.8‰ \pm 0.2‰$.

This result must be compared to the case of a perfect module with no lead fluctuation. This case has been studied in great details in the reference [4] where the constant term is found to be $C_{perfect} = 2.5‰ \pm 0.17‰$ whereas the sampling term is $A_{perfect} = 7.89\% \pm 0.08\%$.

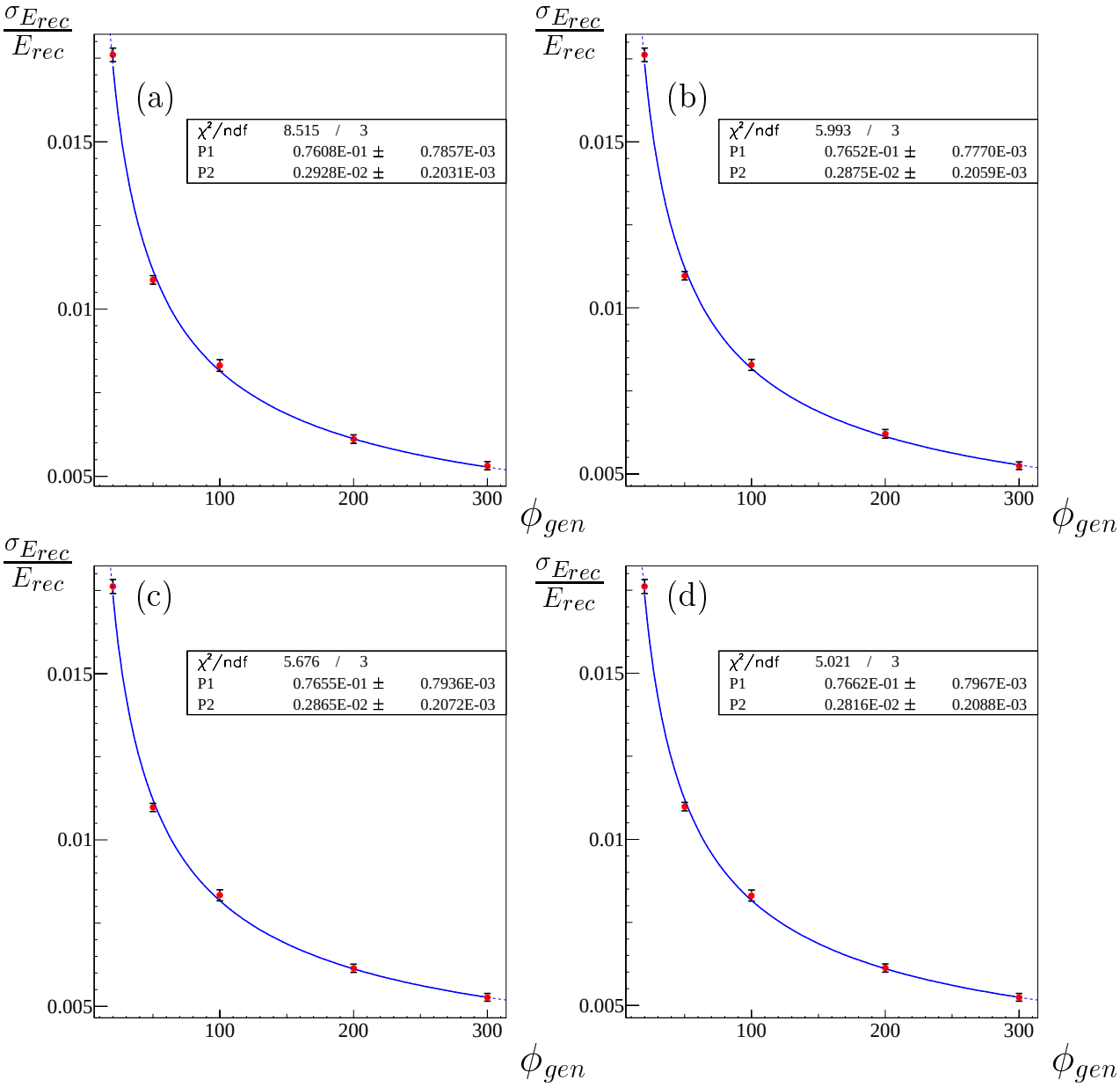

Figure 6: (a) Extraction of the constant term with no correction of lead thickness fluctuation, (b) Extraction of the constant term with the correction function with option A, (c) Extraction of the constant term with the correction function with option B, (d) Extraction of the constant term with the correction function with option C. P1 is the sampling term and P2 the constant term.

5 Correction of a thickness step in the barrel calorimeter

The pairing program has been designed to perform a continuous pairing over the full half barrel. Nevertheless if an unfortunate event would destroy the homogeneity of the mean thickness, we would have a step function in the calorimeter of small amplitude due to the high quality lead used.

In order to test our capability to correct for such an effect, we have designed a toy distribution with a thickness step just in the middle of the simulated module ($\phi = 0.2$). The thickness of the first 32 plates is 1.520 mm whereas the thickness of the last 32 plates is 1.540 mm as shown figure (7). This figure shows also the corresponding correction function computed as explained above.

Figure (8) shows the fit of $\frac{\sigma_{E_{rec}}}{E_{rec}}$ versus ϕ_{gen} in two cases. The first (a) plot corresponds to the situation where no correction for lead thickness fluctuation is applied, the correspond constant term is found to be $0.34 \pm 0.02\%$. Corrected with the function corresponding to option C, the constant term is drastically reduced to $0.26 \pm 0.02\%$ almost at the level of the constant term of a perfect module i.e. without any lead thickness fluctation (as shown in reference [4], $C_{perfect} = 0.25 \pm 0.017\%$).

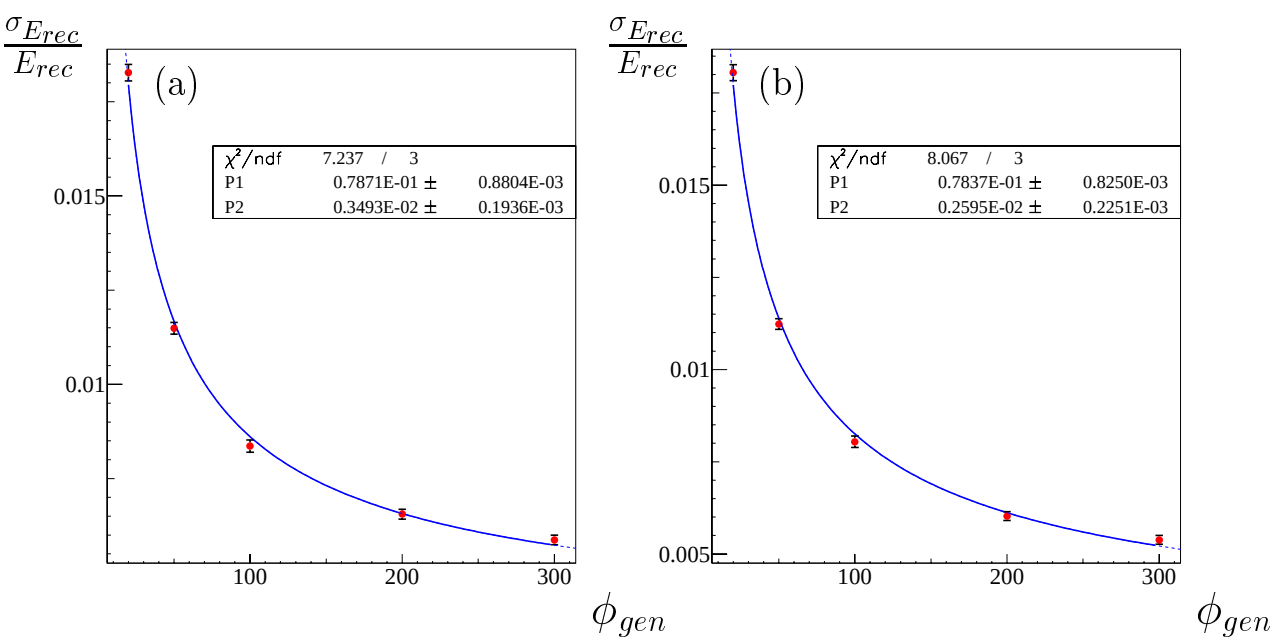

Figure 8: (a) Extraction of the constant term with no correction of lead thickness fluctuation, (b) Extraction of the constant term with the correction function with option C.

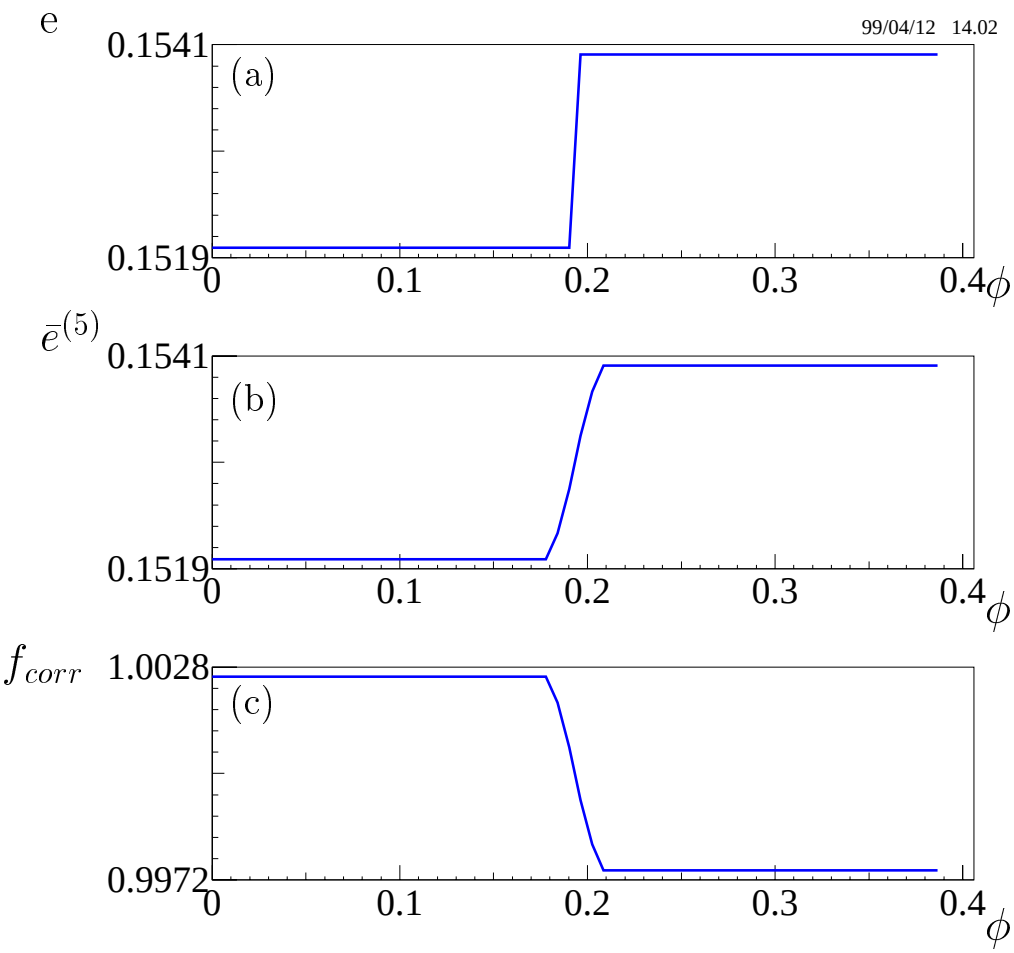

Figure 7: (a) Plot of lead plate thickness put in the simulation versus ϕ in the calorimeter, (b) Plot of mean lead plate thickness over 5 plates (computed as explained in the text) versus n, (c) correction function versus ϕ.

6 Conclusion

We have shown that the knowledge of the local thickness of each lead plate put in the calorimeter can be used to correct the reconstructed energy in the calorimeter from lead plate fluctuations. We have described the method used and we have presented an evaluation of the efficiency of this correction method using a simulation of a module with a realistic lead plate distribution taken from Module 0 construction data. We obtain a sampling term of $7.767\% \pm 0.08\%$ and a constant term of $2.8‰ \pm 0.2‰$. This constant is to be compared to $2.5‰ \pm 0.17‰$ which was obtained from the simulation of a perfect module as reported in [4].

The total constant term is the sum of different terms coming from independant sources of inhomogeneities among which the more important are :

- the ϕ asymetry coming from the non exact compensation of X_0 depth around the bends in the accordion shape,
- the lead plates thickness fluctuations coming from the finite resolution of the laminating process ($\sigma \sim 10\ \mu m$),
- the intercalibration between modules,
- the electronic inhomogeneities of each channel

So the constant term can be written :

$$C_{tot} = C_{accordion} \oplus C_{lead} \oplus C_{electrodes} \oplus C_{electronics} \oplus C_{intercalibration} \oplus \ldots$$

In the present note, we investigate the relation between the first two terms. All the other terms were put to 0 in the simulation. From the "total" constant term of $2.8‰ \pm 0.2‰$ obtained, we can quote a value coming from the lead thickness fluctuation :

$$C_{lead} = 1.2‰$$

Even the improbable contribution from a step of the lead thickness has been investigated and has been found to be easily corrected to a residual value which should not be seen in the data.

7 Acknowledgements

We take the opportunity of thanking B. Mansoulié for fruitful discussions and suggestions along that work.

References

[1] ATLAS Liquid Argon Calorimeter Technical Design Report, 15 December 1996.

[2] B. Canton et al., Analysis and Results of the measurements of the plate thickness, done at the factory, during the production of the lead for the module 0 of the Barrel and End-Cap ATLAS electromagnetic calorimeter. ATLAS Internal note LARG-76

[3] F. Fleuret, B. Laforge, P. Schwemling, *"Lead Matching and Consequences on the EM Module 0 Constant Term"*, ATLAS Internal Note, to be published.

[4] F. Fleuret, B. Laforge, P. Schwemling, *"Constant Term Evolution with Lead Plate Thickness fluctuations in EM Module 0"*, ATLAS Internal Note, to be published.

September 22, 1999

ATL-LARG-2000-002
15/02/2000

Constant Term Evolution with Lead Plate Thickness fluctuations in EM Module 0

F. Fleuret, B. Laforge, Ph. Schwemling

LPNHE-Paris, Universités Paris 6-7, and IN2P3-CNRS

Abstract

We report on the results of the Monte Carlo simulation of the module 0 electromagnetic barrel calorimeter. The impact of the thickness variations of the lead plates, which enter in the construction of the module 0, on the energy resolution constant term is presented. Using the real lead plates thickness data which have been used to build the module 0 we find, at $\eta = 0.3$ and $\eta = 1.1$, a constant term $C < 0.3\%$. The contribution to the constant term coming from lead thickness fluctuations is found to be respectively $C_{\text{lead fluctuation}} = 0.53\frac{\sigma^{(5)}}{e_{th}}$ and $C_{\text{lead fluctuation}} = 0.44\frac{\sigma^{(5)}}{e_{th}}$ at $\eta = 0.3$ and $\eta = 1.1$, where $\sigma^{(5)}$ is the standard deviation of the mean lead thickness averaged over 5 plates and e_{th} is the nominal thickness of a single lead plate.

Introduction

The thickness measurement of the lead plates, which enter in the construction of the electromagnetic barrel calorimeter module 0, exhibits small relative variations as we compare real thickness and nominal value [1]. This contributes to increase the constant term value of the energy resolution of the calorimeter. In order to reduce this contribution, a mathematical algorithm has been used to sort and pair the lead plates during the construction of the module 0 [2].
In this note, we estimate, by using a simulation of the module 0 (using DICE), the impact of the lead plate thickness variations on the constant term value of the electromagnetic barrel calorimeter energy resolution. We also estimate the lead plates thickness variations contribution to the constant term value of the module 0.
In the first section, we present our module 0 simulation (using DICE) which is largely based on the program written by G. Parrour and P. Petroff hereafter referred as "Parrour-Petroff" description and intended for module 0 simulation. Our main modification was, in order to take into account the effect of the lead plates variations, the modification of the absorber description.
In a second section we present the "dead material" and ϕ-modulation studies for an "ideal" calorimeter (*i.e.*, without lead plates thickness fluctuations).
In the third section, we present the simulation context and the different samples we consider in our analysis.
Finaly, in the last section, we point out our results on the study of the constant term evolution as a function of the lead plates thickness fluctuations. We also show the results for the module 0 using the real map of the lead plates thickness.

1 Module 0 design and implementation

In this section, we present the test beam experimental setup implementation in DICE as it was done in the Parrour-Petroff description; we have used the same implementation for our study. We also present the differences between the calorimeter module description made by G. Parrour and P. Petroff and our description.

1.1 Test beam experimental setup design and implementation in DICE

The experimental setup used for the module 0 simulation (see figure 1) was designed by G. Parrour and P. Petroff. It takes into account all the volumes which enter in the test beam setup, *i.e.*, the aluminum walls of the cryostat, the foam which is used to reduce the liquid argon thickness seen by incident particles, the preshower detector and the calorimeter module. Figure 2 shows the implementation diagram of all these volumes, and table 1 gives their descriptions as they were specified by the authors.

1.2 Calorimeter module description for GEANT simulation

The Parrour-Petroff geometry is a precise description of all the volumes which enter in the composition of the module 0. The calorimeter structure and the volumes descrip-

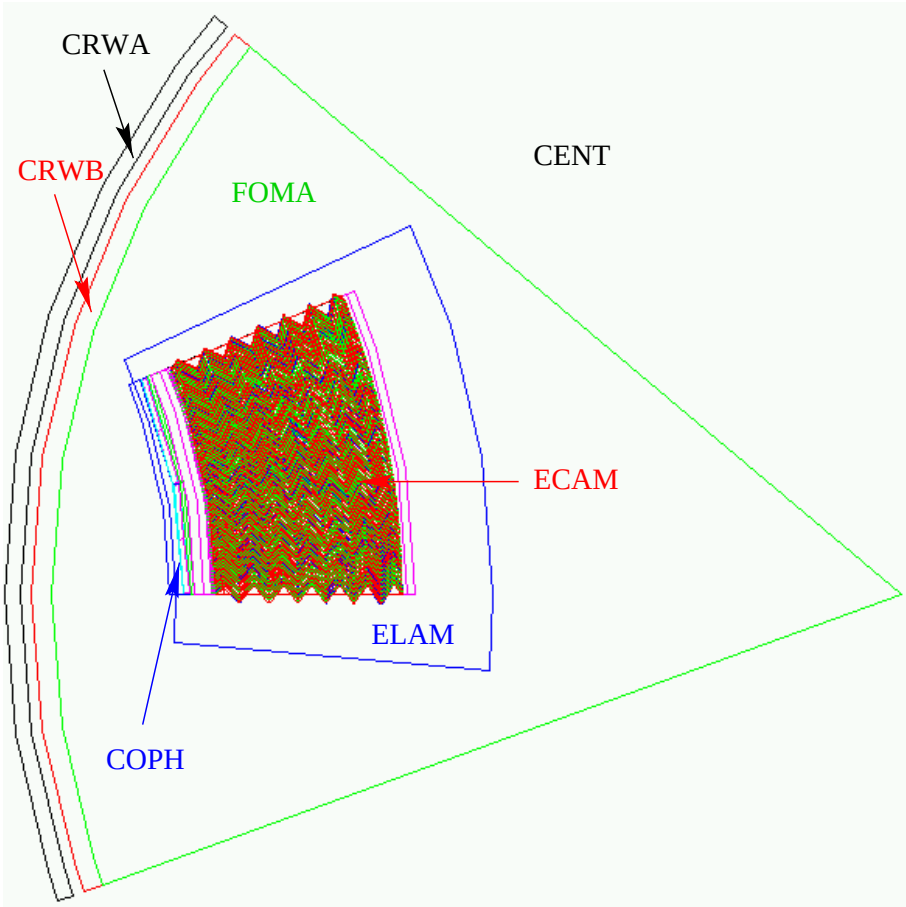

Figure 1: experimental setup layout as simulated in DICE

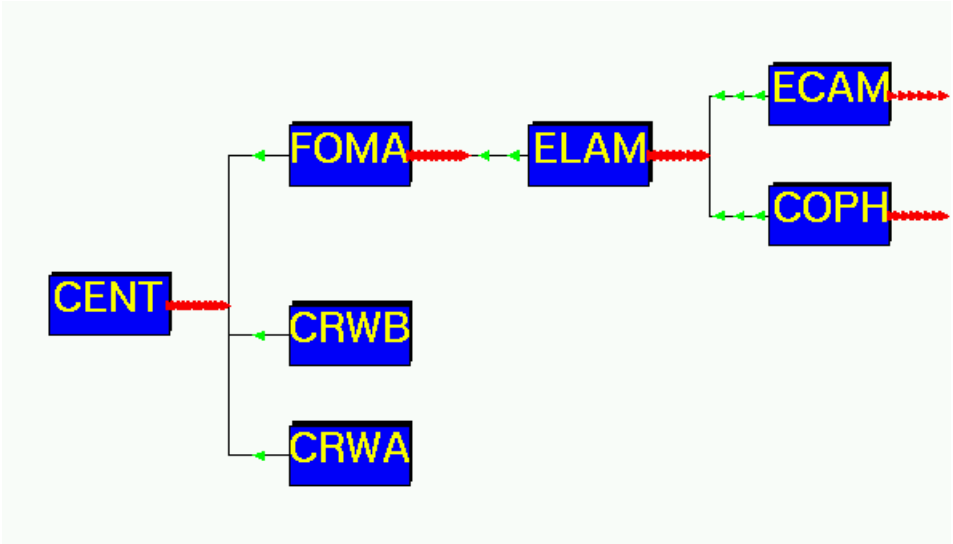

Figure 2: experimental setup implementation in DICE

tion are given in appendix 1; the ACCG bank which gives all the parameters entering in the calorimeter description is described in appendix 2. In this geometry, absorbers are designed as individual volumes made of a mixture, "thinabs" (for thin lead plates) or "thickabs" (for thick lead plates), which is a mixing of lead, stainless steel and glue.

volume name	volume description	volume material
CENT	Calorimeters Mother volume	Vacuum
FOMA	foam volume	foam
ELAM	LAr mother volume for presampler and accordion	liquid argon
ECAM	accordion volume with electronics, g10 frame, ...	liquid argon
COPH	half of COPS but is ok for modul0	liquid argon
CRWB	volume of cryostat cold wall	aluminum
CRWA	warm wall of cryostat	aluminum

Table 1: experimental setup in the Parrour-Petroff volumes description

In our description, in order to take into account the lead plate thickness fluctuations,

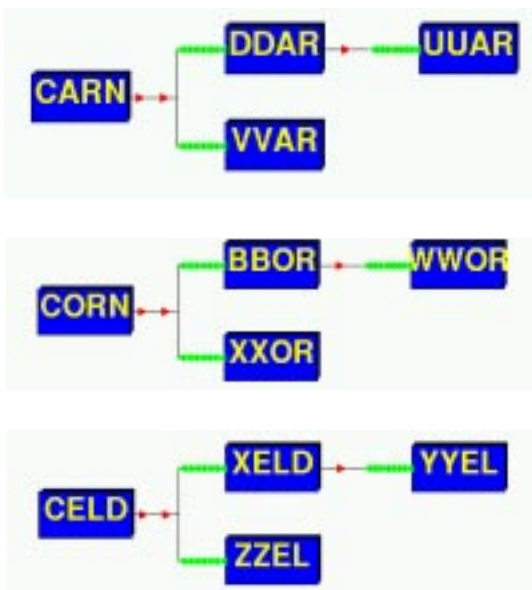

Figure 3: Absorbers corners and plates description in our geometry :

absorbers are described as an addition of two different volumes. Figure 3 shows this structure: lead plates (VVAR for 1.1 mm thick lead plates; UUAR for 1.5 mm) are inserted into "prep" boxes (CARN for 1.1 mm thick lead plates; DDAR for 1.5 mm) which are made of stainless steel and glue. The densities of these boxes mixtures depend of the theoretical lead plates thickness as it is shown in table 2. Then, for a thick lead plate, the density of the "glue+stainless steel" boxes is bigger than for a thin lead plate (due to the relative higher amount of stainless steel in the mixture).
The positioning order has been done, for the CARN volume (for example), as follow:

1. put DDAR in CARN (the volume occupied by DDAR is made of thinprep)
2. put VVAR in CARN (the volume occupied by VVAR is made of lead)
3. put UUAR in DDAR (the volume occupied by UUAR is made of lead)

The positioning for the CORN and CELD volumes was made in the same way. Using

volume name	volume description	volume material	material components	materia density
64×CARN	round corner upper glue+stainless steel	thikprep	H + C + O + Fe	3.705
DDAR	upper round corner thick absorber	thinprep	H + C + O + Fe	5.235
UUAR	1.5 mm Pb corner	lead	Pb	11.35
VVAR	1.1 mm Pb corner	lead	Pb	11.35
64×CORN	round corner down absorber	thikprep	H + C + O + Fe	3.705
BBOR	down round corner thin glue+stainless steel	thinprep	H + C + O + Fe	5.235
WWOR	1.5 mm Pb corner	lead	Pb	11.35
XXOR	1.1 mm Pb corner	lead	Pb	11.35
64×CELD	glue+stainless steel box	thikprep	H + C + O + Fe	3.705
XELD	innermost glue+stainless steel trap	thinprep	H + C + O + Fe	5.235
YYEL	1.5 mm Pb plate	lead	Pb	11.35
ZZEL	1.1 mm Pb plate	lead	Pb	11.35

Table 2: Absorbers corners and plates volumes description in our geometry.

this positioning order, we are ensured that the volumes get the right material in the right place.

With this simulation we are able to study the "perfect module" with no lead fluctuation. In that model, as the total absorber thickness is set, increading the lead thickness is equivalent to decrease the stainless steel plate thickness and not only the glue thickness. So, to study the lead thickness fluctuation, we adapted this simulation using 3 volumes instead of two to describe lead, prepreg and stainless steel. Using this geometry, we are able to modify the lead thickness, leaving constant the absorber thickness and the gap thickness.

2 Setup detailed study

We discuss here a radiation length (X_0) and absorption length (λ_I) detailed study of the simulated setup. We first compare the Parrour-Petroff geometry description, then we look at the contribution of the "dead matter" in front of the calorimeter. In a last part, we discuss the several calibration corrections we have to apply to the measured energy.

2.1 Comparison with Parrour-Petroff description

In order to check for any bias in our geometry description, we made, in a first step, a comparison between the Parrour-Petroff geometry and our description where all lead plates are 1.5 mm and 1.1 mm thick. Figure 4 shows a comparison between both descriptions. The results point out no major difference between both distributions. Figures 4.c and 4.d give $\Delta X_0 = 0.04$ and $\Delta\lambda_I = 0.012$. The fact that absorbers are not homogeneous volumes in our description where incident particles see much more density materials when they cross the lead plates can certainly explain the observed differences.
After this check, we believe in our geometrical description and then, in the following, all the distributions shown will be obtained with our geometrical description.

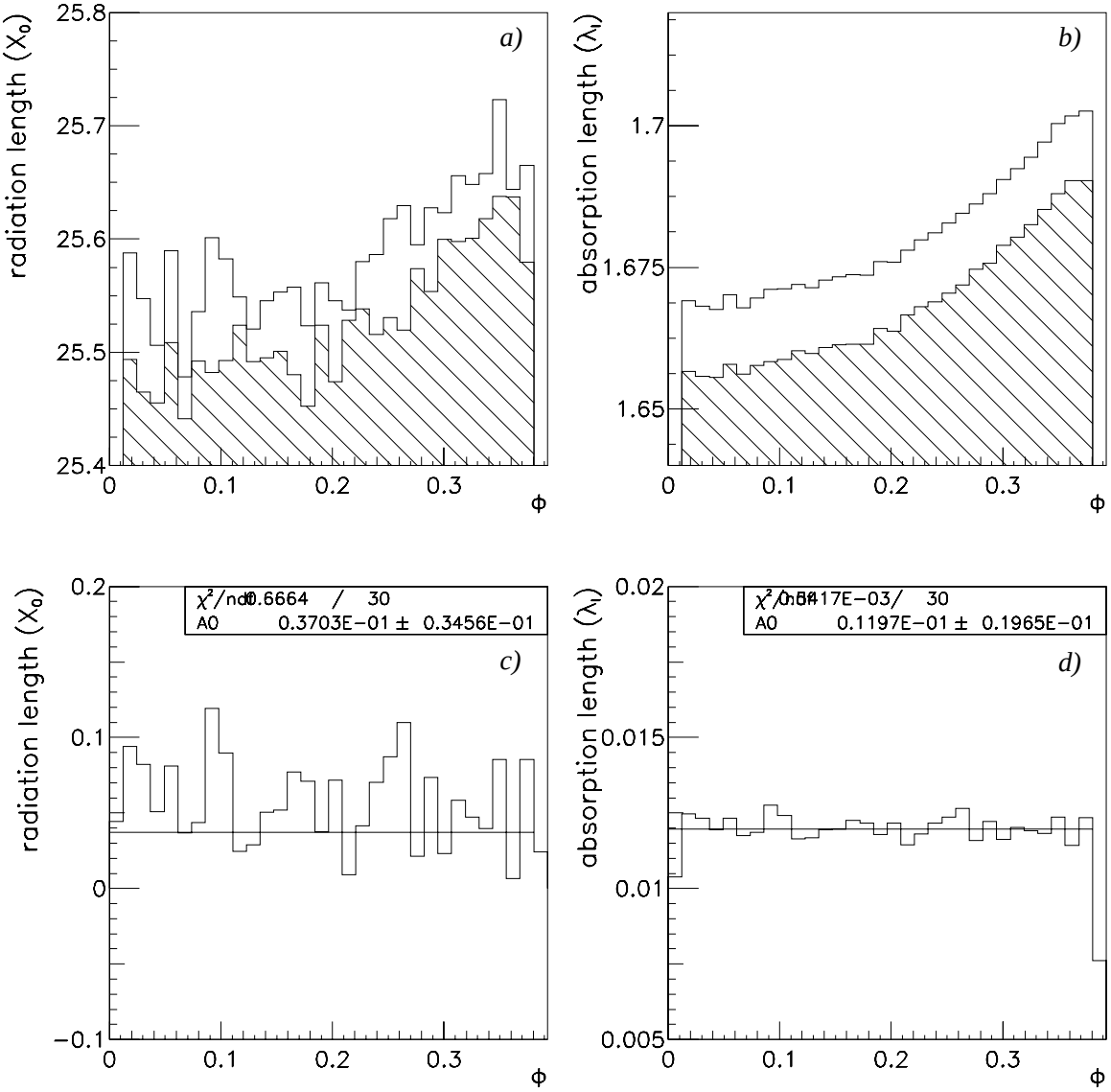

Figure 4: Comparison between Parrour-Petroff geometry and our description; top: radiation length a) and absorption length b) in Parrour-Petroff description (dashed surface) and our description (undashed) at $\eta = 0.3$; bottom : difference between both descriptions for radiation length c) and absorption length d).

2.2 Setup contribution to the radiation length

In this section, we estimate the radiation length (and the absorption length) contribution coming from the setup design, in order to point out a Φ-dependence of the correction we will have to apply to the data.

In the setup implementation, three different volumes can contribute to the increase of the calorimeter radiation length: the two aluminum walls of the cryostat and the foam volume in front of the calorimeter.

In section 2.2.1, 2.2.2 and 2.2.3 we present the contribution respectively of the walls, of the foam and all together. In order to do this, we had to sligthly modify the experimental setup as it is shown in appendix 3. The main result is the observation of a Φ-dependence of the X_0 amount coming from the "dead matter" in front of the calorimeter.

2.2.1 Aluminum walls contribution to the radiation length and to the absorption length

In this section, we present the contribution which comes from the aluminum walls. Figure 5 shows the radiation length and the absorption length seen by incident particles with and without the two aluminum walls.

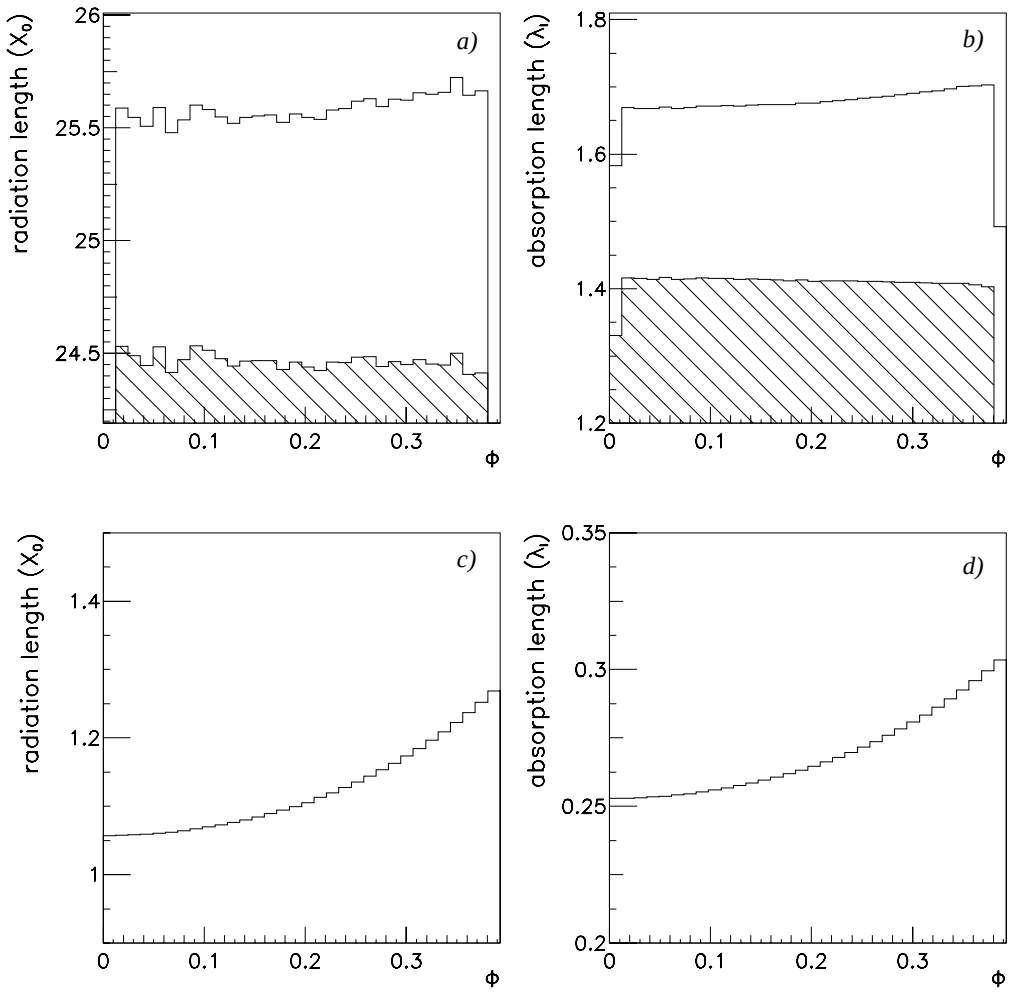

Figure 5: Comparison between experimental setups with and without the two aluminum walls; top: radiation length a) and absorption length b) in the "without walls" configuration (dashed surface) and the "with walls" setup (undashed) at $\eta = 0.3$; bottom : difference between both configurations for radiation length c) and absorption length d).

Figure 5 shows a large contribution (between 1.1 and 1.3 X_0, and between 0.25 and 0.3 λ_I) coming from aluminum walls. Due to geometrical effects, this contribution increases with Φ.

2.2.2 Foam contribution to the radiation length and to the absorption length

In this section, we present the X_0 and λ_I contributions coming from the foam volume. Figure 6 shows the radiation length and the absorption length seen by incident particles with and without the foam volume.
Figure 6 shows a smaller additive amount of X_0 coming from the foam volume when one

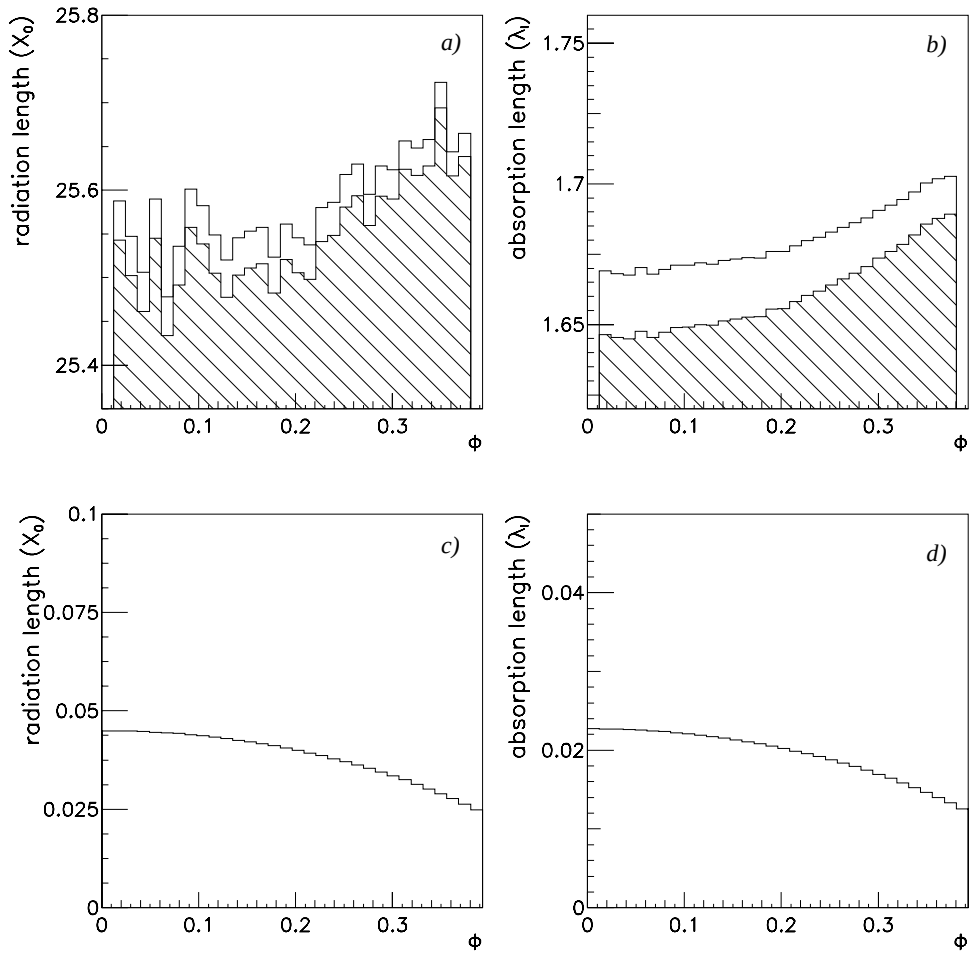

Figure 6: Comparison between experimental setups with and without the foam volume (without aluminum walls for both); top: radiation length a) and absorption length b) in the "without foam" configuration (dashed surface) and the "with foam" setup (undashed) at $\eta = 0.3$; bottom : difference between both configurations for radiation length c) and absorption length d).

compares it with the one coming from aluminum walls contribution. Added X_0 at $\Phi = 0$. is a factor 1.3 bigger than at $\Phi = 0.4$. This Φ-dependence is shown in figures 6.c and 6.d.

2.2.3 Foam + walls contribution

In the two precedent sections, we have seen the "dead material" contribution (to the total absorption length and radiation length) coming from aluminum walls and foam volume individually.
In fact, we are interested in looking at the whole "dead material", *i.e.* aluminum walls and foam volume together. This is the purpose of the present section.
Figure 7 shows the radiation length and the absorption length with and without dead material in the front of the calorimeter.

As it could be expected, we observe a large Φ-dependent contribution coming essentially from the aluminum walls.
Looking at figure 7.c, we observe $X_0(\Phi \simeq 0.4)/X_0(\Phi \simeq 0.1) \simeq 1.3$. Such a result should be observed on the data energy distribution.

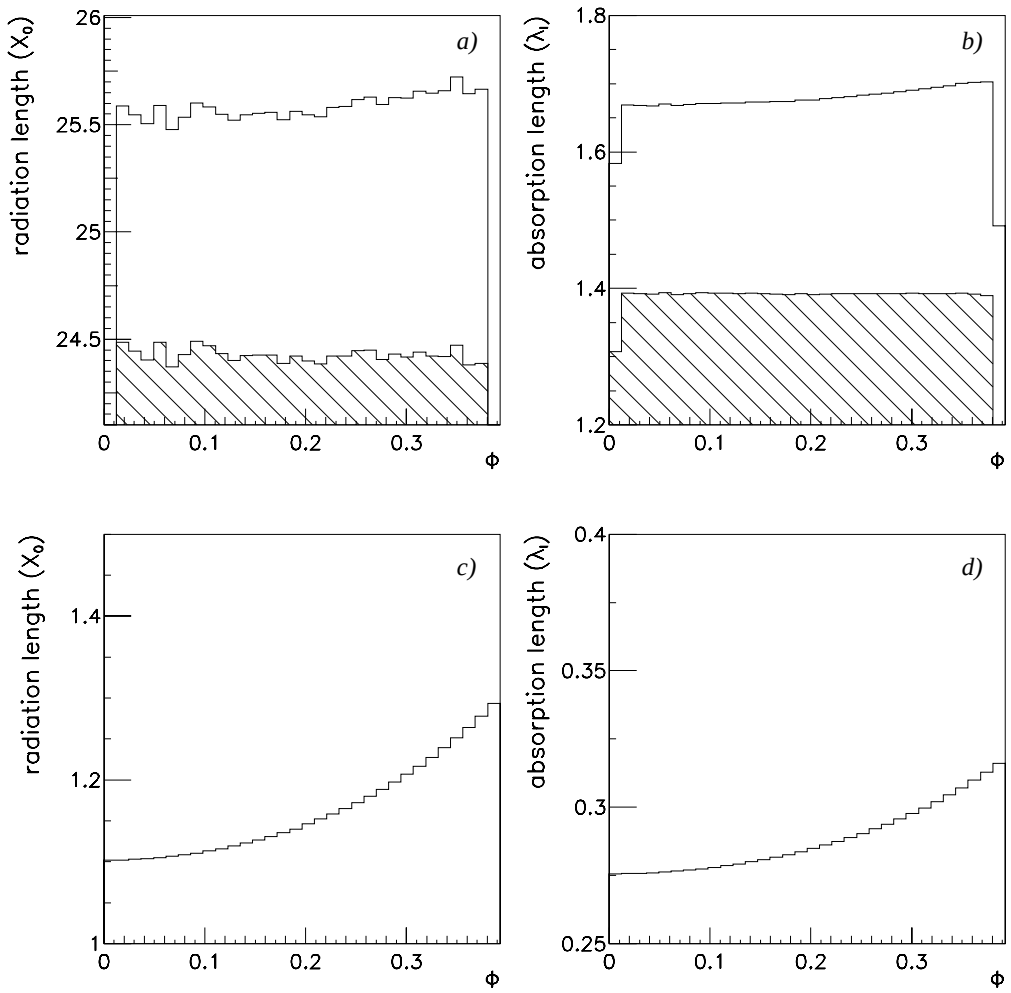

Figure 7: Comparison between experimental setups with and without foam+walls; top: radiation length a) and absorption length b) in the "without foam+walls" configuration (dashed surface) and the "with foam+walls" setup (undashed) at $\eta = 0.3$; bottom : difference between both configurations for radiation length c) and absorption length d).

2.3 Lead thickness dependence of the calorimeter response

As in the rest of this paper, we will be interested by the effect of lead fluctuation, we want first to remind the global effect of a change in the lead thickness. Using the simulation program for different lead thicknesses, it has been found that the signal loss due to an increase by 1% of the lead thickness is respectively 0.59%/0.47% of the nominal signal for a nominal lead thickness of 1.53 mm/1.13 mm. This study is described in details in [3].

3 Simulation and analysis procedure

In order to achieve the studies of dead materials in the Test Beam set up, we have studied within ATLSIM the structure of volumes implemented in order to identify the possible dead materials. Using ATLSIM, we have profiled the ϕ distribution of X_0 for different dead materials. Then, using the DICE framework we have generated several data files with or without the main dead material, i.e. the aluminum wall of the cryostat. We have simulated at 50 GeV two samples with respectively 4000 events with the wall and 3500 without it.

After the dead material effect analysis, we have begun the study of lead thickness fluctuations. The simulation program used to simulate the lead fluctuation effect has a true description of volumes present in the EM Accordion calorimeter, namely one stainless steel volume, one prepreg volume and two lead volumes (one for each lead thickness). This simulation program was fully tested within the ATLSIM framework. As the real high precision data, coming from measurement of lead plate thickness achieved at Hall IN2P3 at Orsay [2], is showing thickness distributions with non-gaussian shape, we choose to implement in our simulation lead plates distributed using an uniform law. This law is well adapted to the Module 0 lead plate distribution which is presented on the figure 8. With that approach, our results enable to quote a conservative bound on the contribution of lead thickness fluctuations to the energy constant term of the EM calorimeter.

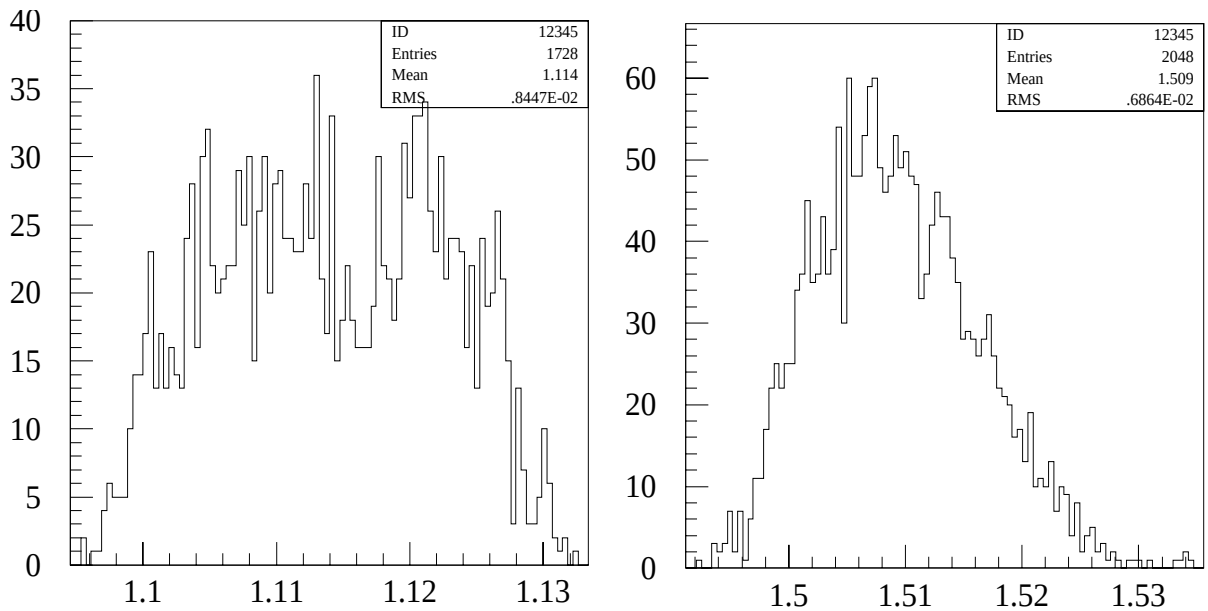

Figure 8: Module 0 lead plates thickness distributions for both (a) 1.13 mm and (b) 1.53 mm regions. These distributions are not gaussian and are well approximated by a uniform

In order to achieve detailed studies of thickness fluctuations, we have simulated large samples of events for different energies and different amplitudes of thickness fluctuation. We used 5 energies, 20, 50, 100, 200 and 300 GeV and 5 fluctuation amplitudes, $\frac{\sigma^5}{e_{th}} =$ 0%, 1.118 %, 2.236 %, 3.354 % 4.472 %,where $\frac{\sigma^5}{e_{th}}$ is the fluctuation of the mean thickness calculated over 5 consecutive plates. The number of 5 plates was determined because it is the number of plates over which an electromagnetic shower spreads most of its energy in the EM calorimeter. The fluctuation amplitude on the lead thickness is about 0.6% in

the real data acquired with the ultra-sound system implemented in Orsay and used when lead plates are stacked before being used in the calorimeter.

We have chosen to use large fluctuations to be able to extract the contribution of lead thickness fluctuation to the constant term from the total constant term itself with a limited statistics of few thousand events. For each $\frac{\sigma^5}{e_{th}}$ configuration, we have simulated about **12500** events given in the following table :

Energy (GeV)	20	50	100	200	300
# of events	4000	4050	1600	1600	1122

These events were simulated with $\phi \in [0.1; 0.3]$ at $\eta = 0.3$ which is in the 1.53 mm thickness region of the calorimeter. In fact, we have also done the same analysis scheme done at $\eta = 1.1$ which is the 1.13 mm thickness region. We won't describe this second analysis in details here as we followed the same way as for the $\eta = 0.3$ case. Nevertheless, we will quote the results in the dedicated section. The number of simulated events decreases with energy because the higher the energy the more secondary particles to be simulated, so the more CPU consumption. These events were produced by batches of 80 to 250 events each. For each batch, the plate distribution was changed in order to have a representative idea of what could be the constant term over the whole calorimeter made of 32 modules.

On top of these events, we simulated **8200 events** with the perfect geometry within a very restricted ϕ ([0.2; 0.225]) domain to study the ϕ modulation and obtain the correction function which is periodical over the full calorimeter. All together, we have simulated about **130 000** electromagnetic showers to make all the studies presented in this note. We used electrons as incoming particles. The simulation was done using the CCPN/IN2P3 computing power.

3.1 Data corrections

Before doing a fine analysis on the contribution of lead thickness fluctuations, we have to be able to reconstruct the energy as better as possible in the calorimeter. As we wanted to extract a very precise physical effect, we used the setting of the Module 0 DICE simulation where the energy is distributed accordingly to the true lost energy given by *GEANT* i.e. without using current maps around the electrodes to describe the true migration of electrical charges produced in the liquid argon to the kapton electrodes.

Our files were simulated without electronic noise and we worked without clustering. As we had one EM shower by event, we considered the sum of all the cells of the module to be the energy of the incoming particle. As we did not use any clustering, we used the ϕ of the incoming particle given by the GEANT KINE bank.

3.1.1 "Dead matter" contribution correction

Using ATLSIM, we have shown that the bigger contribution to energy resolution coming from dead material should come from the aluminum wall of the cryostat. We have analysed carefully how this contribution of dead material could be seen at the reconstructed energy level. The main result of this analysis is that the wall should give a very light asymetry in ϕ in the test beam data. In the simulation, we have observed a relative normalisation

of effect of about $1.5\,10^{-3}$. The phi distribution of $\frac{E_{rec}}{E_{gen}}$ is shown for electrons of 50 GeV with and without the aluminum wall of figure 9. The vertical scale is expanded since the whole scale of the plot is between $\pm 5‰$. We see that the wall enlarges the shower initiation and so produces some lateral energy loss at the order of $0.2‰$. Morevover, after a careful check, we conclude that the effect in the real Test Beam set up should be even smaller because the actual wall is slightly thinner than in the simulation model.

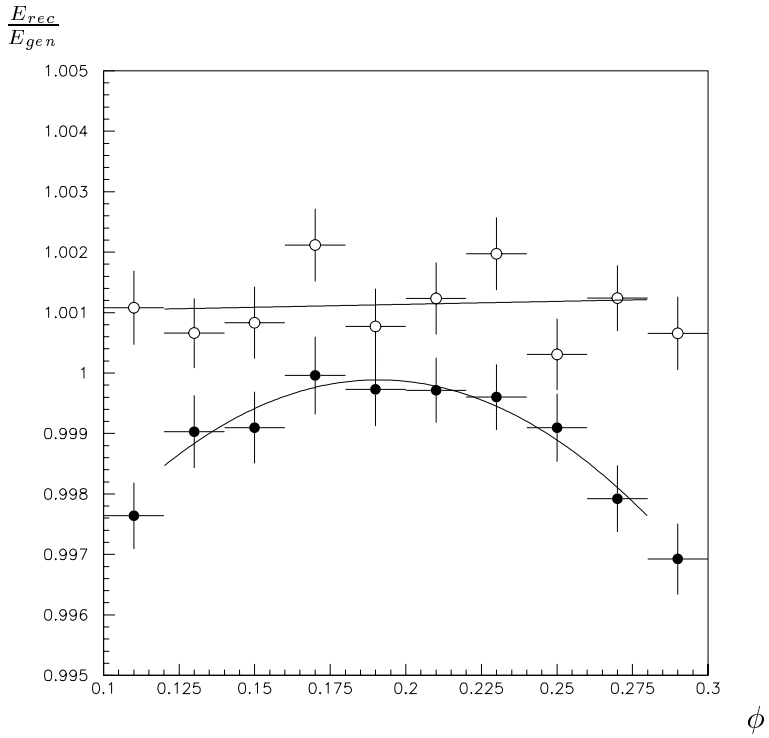

Figure 9: ϕ distribution of $\frac{E_{rec}}{E_{gen}}$ for (open circle) the module 0 without the cryostat wall and for (closed circle)the module 0 with the wall. The observed effect can reasonably be interpreted as follows : the wall opens slightly the showers when they are initiated in it and so the shape that is observed with the wall shows a very small leakeage effect that is not present without the wall. The ϕ dependence of the reconstructed energy is then insentitive to the inhomogeneities of cryostat wall matter and we are only sensitive to an earlier showering due to the wall existence. This effect of the order of $1‰$ is very small and should be hardly seen in the test beam data.

3.1.2 ϕ-modulation correction

The accordion shape was designed to have a perfect ϕ symetry. But because of the impossibility to make very sharp bends with the lead, the compensation between the different lead thicknesses is not perfect and varies with ϕ. Since the non compensation pattern is periodical over the whole calorimeter, we have restricted the initial electrons to be in the range $\phi \in [0.2; 0.225]$ which corresponds to about 4 consecutive absorbers which is enough to see the periodical pattern. So we could have quite a large statistics per ϕ bin without simulating a huge number of events. Figure 10 shows the ϕ modulation of the integrated argon thickness along a small ϕ range. Figure 11 shows in the upper left plot the residual ϕ modulation of the radiation length over all the Module 0.

The middle left plot shows the ratio $\frac{E_{rec}}{E_{gen}}$ as a function of ϕ. The comparison with the previous plot exibits the correlation between the two shapes. The $\frac{E_{rec}}{E_{gen}}$ asymetry can be well fitted by the function :

$$\begin{aligned}\frac{E_{corr.}}{E_{meas.}} &= f(\phi) = 1 + \mathbf{a} + \mathbf{b}\sin(1024\phi + \phi_{\mathbf{0}}) \\ &\quad + \sum_{i=0}^{63} \mathbf{A} \exp\left(-\frac{1}{2\sigma^2}\left[\phi - \frac{1}{1024}\left(\phi_{\mathbf{0}} - \frac{\pi}{2} + 2i\pi\right)\right]^2\right)\end{aligned}$$

The fit parameters that we obtained for a $\chi^2 = 1.3$ (for 48 points fitted) are :

$\mathbf{a} = -0.17445 \times 10^{-1} \pm 0.15197 \times 10^{-3}$ $\quad$ $\mathbf{b} = -0.69112 \times 10^{-2} \pm 0.22459 \times 10^{-3}$

$\phi_{\mathbf{0}} = 1.5446 \pm 0.13561 \times 10^{-1}$ $\quad$ $\mathbf{A} = -0.80117 \times 10^{-2} \pm 0.50344 \times 10^{-3}$

$\sigma = -0.37543 \times 10^{-3} \pm 0.22050 \times 10^{-4}$

Discussing the geometry of the simulation, we have seen previously that the description of the absorber as a single volume with an average mixing of stainless steel, prepreg and lead was not giving the same number of X_0 than the description with several volumes describing individually the lead plates and the prepreg+stainless steel plates. We used in the simulation the calibration constant coming from an analysis with the first configuration of volumes with electrons of 50 GeV. Thus, it was predictable that these calibration constants would not be precisely the good ones.

As the calibration constant are only depending on η and as we shoot electrons only at $\eta = 0.3$, this appears on our data as an overall calibration constant that is taken care of by parameter **a**. So our ϕ-modulation correction function corrects also for the calibration.

We did not use 20 GeV electrons to extract the modulation correction function because as it can be observed on figure 12, the linearity is not good for low energies. Using 20 GeV energy would have lead to a bad estimation of the normalisation factor of the correction factor discussed above. This reflects the fact that the setting of the calorimeter calibration was made to have the best energy resolution around 50-100 GeV as there is an interplay between the linearity at low energies and the constant term around 50 GeV.

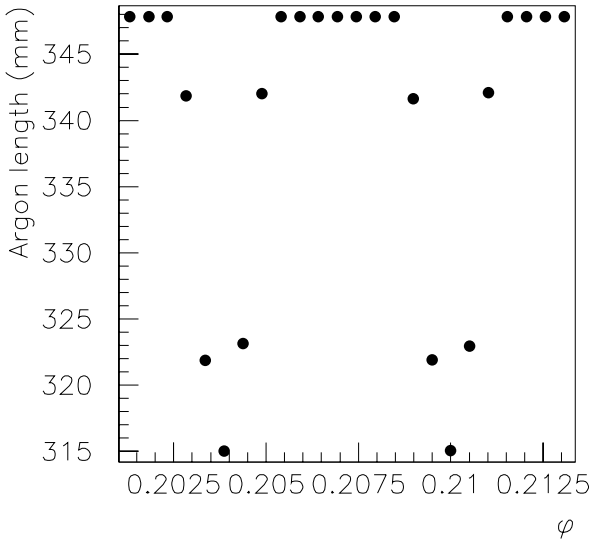

Figure 10: ϕ modulation of the liquid argon integrated thickness. Comparing this plot with fig. 11 shows a nice correlation. The small shift in the ϕ angle between the two plots is due to the fact that the present plot was derived from a technical drawing of a module for which it was not easy to define $\phi = 0$ in the same way as in the simulation program.

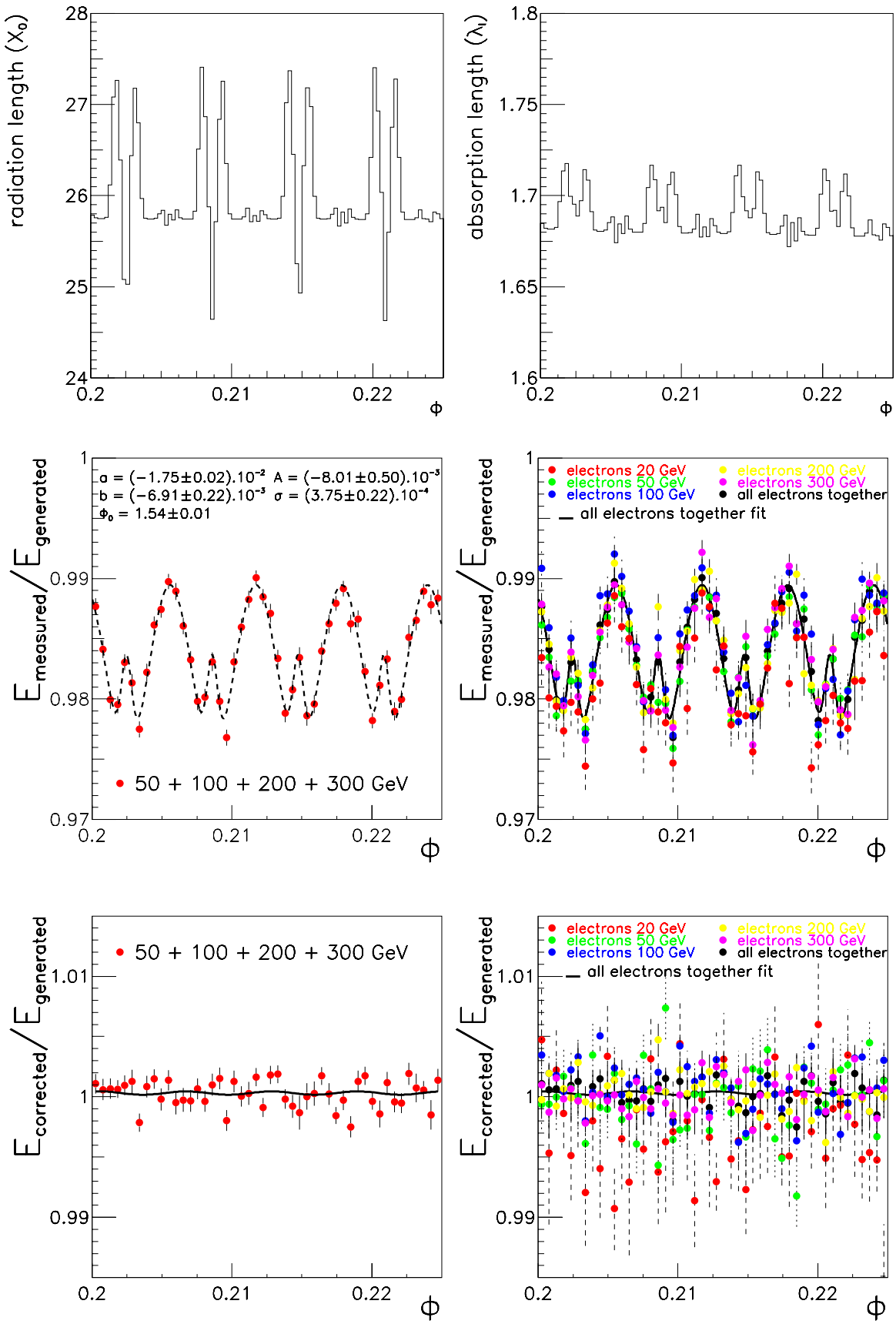

Figure 11: ϕ modulation of radiation length in a part of a module. The top plots show respectivly the modulation of the radiation length and absorption length as a function of ϕ. The middle plots show the energy response as a function of ϕ for different energies of incoming electrons. The bottom plots show the remaining modulation after energy correction.

3.2 "Ideal" calorimeter study

As a first step, we have investigated the constant term of the energy resolution for the module 0 with a perfect geometry, i.e. without any fluctuation of lead plate thickness.

3.2.1 Results : constant term evolution

The aim is to have a constant term smaller than 5 ‰ [4]. First we study the value of the physical constant (i.e. without any clustering) coming from inexact compensation of the phi modulation.

We used electrons of 20, 50, 100, 200 GeV to extract the constant term. Indeed, 300 GeV electrons give an EM shower which leaks into the hadronic calorimeter. In our simulation of the module 0, we have no hadronic system, so it was not possible to correct for this leakage. Using these events would then lead to an overestimation of the constant term.

The result plot of the analysis is shown on figure 12. The extraction of the constant term was done in three steps :

1. Correction of the phi modulation,
2. for each energy, gaussian fit of the E_{rec} distribution to determine $\frac{\sigma_{E_{rec}}}{E_{rec}}$,
3. fit of $\frac{\sigma_{E_{rec}}}{E_{rec}}$ versus E_{gen} with a 2-parameters function :

$$\frac{\sigma_{E_{rec}}}{E_{rec}} = \sqrt{\left(\frac{A}{\sqrt{E_{gen}}}\right)^2 + \left(C\right)^2}$$

where A is the sampling term and C the constant term.

The sampling term and the constant term for the "ideal" module were found to be $A = 7.89 \pm 0.08$ % and $C = 0.26 \pm 0.02$% for $\chi^2 = 1.02$.

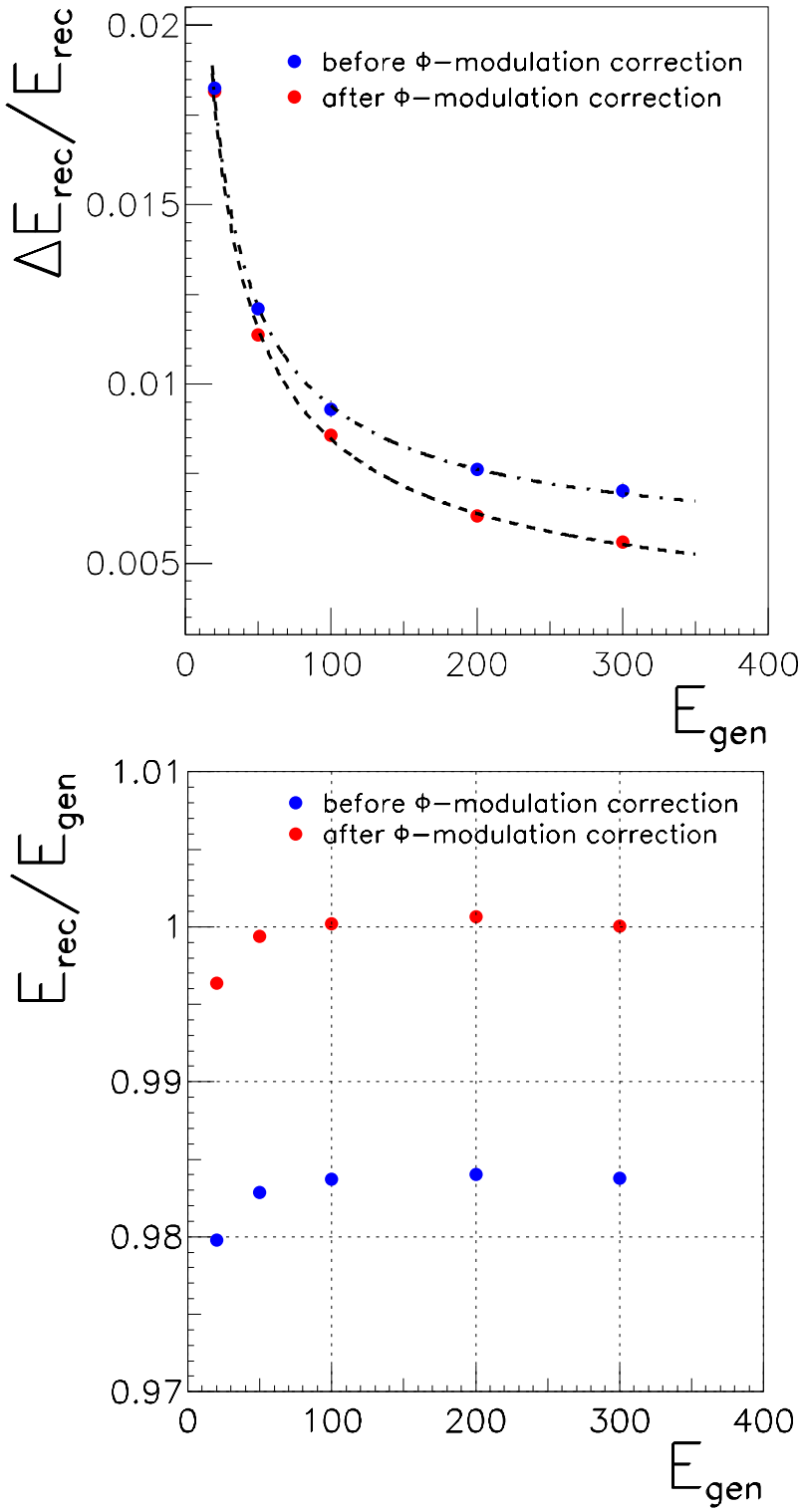

Figure 12: energy resolution as a function of energy (left) for a module without lead plate thickness fluctuations; linearity (right) of the response as a function of energy

4 Study of samplings with lead plates thickness fluctuations

The final goal of this note is to study the evolution of the calorimeter energy resolution constant term as a function of the lead plate thickness fluctuations. As explained in

([2],[1]), the correlation between the lead thickness fluctuation and the constant term C is very useful. We are interested in the evolution of C as a function of $\frac{\sigma^{(5)}}{e_{th}}$ where $\sigma^{(5)}$ is the standard deviation of the mean lead thickness averaged over 5 plates. e_{th} is the nominal thickness of a single lead plate. We used the 5 following settings of fluctuation $\frac{\sigma^{(5)}}{e_{th}} = 0\%,\ 1.118\,\%,\ 2.236\,\%,\ 3.354\,\%\ 4.472\,\%$.

4.1 Correlation between constant term and fluctuations

To reach this result, we have done for each value of $\frac{\sigma^{(5)}}{e_{th}}$ the same analysis than the one explained for the "ideal" calorimeter (i.e. without lead fluctuations) except that we did the fit of $\frac{\sigma_{E_{rec}}}{E_{rec}}$ as a function of E_{gen} with only one parameter (the constant term C). The sampling term is taken to be the one obtained from the "ideal" case.
Figure 13 shows one example of fit corresponding to a thickness fluctuation of 1.118 % whereas figure (14) presents the results obtained for the constant term evolution when different energy corrections are applied. The upper left plot shows the evolution of the constant term with the full analysis described applied. The upper right plot shows the result of the same analysis for which we just applied a sine correction function (of the same type as the one described in [5]) i.e. with no exponential correction. The bottom plot presents the result obtained when no energy correction is applied.

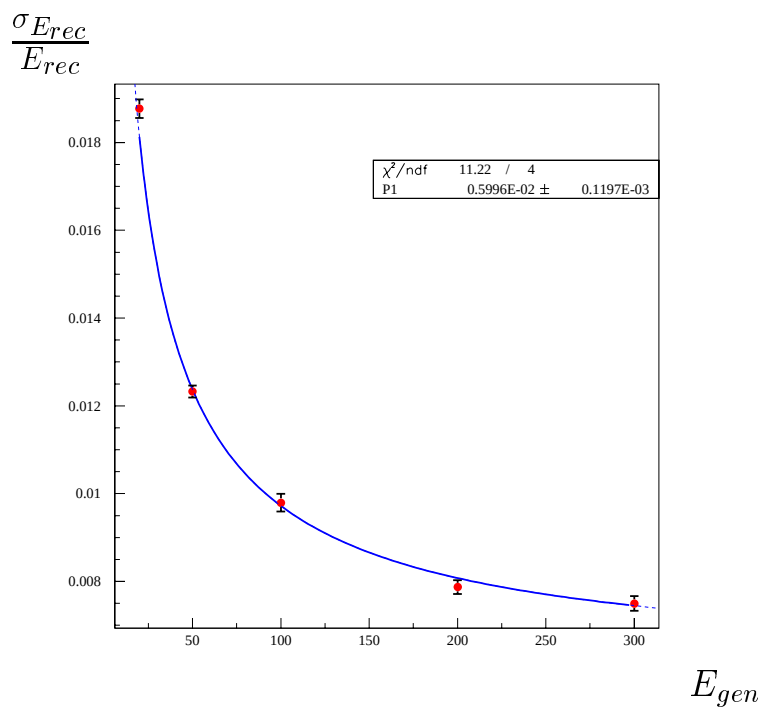

Figure 13: Example of fit corresponding to a thickness fluctuation of $\frac{\sigma^{(5)}}{e_{th}} = 1.118\,\%$

Each curve was fitted using the function :

$$C\ (\%) = \sqrt{\left(a\ \frac{\sigma^{(5)}}{e_{th}}\ (\%)\right)^2 + \left(b\right)^2}$$

which is the expected error on a random variable which is a function of two uncorrelated random variables. This function fits the data well in each case. As far as the energy cor-

rection is better, the b parameter is decreasing as expected but the slope given by the a parameter is not modified within the errors. This shows that fluctuations of lead thickness and the residual constant term coming from a non perfect compensation of ϕ-modulation are two uncorrelated sources of the energy resolution. The values of the parameters found in the different cases are at $\eta = 0.3$:

	Energy Correction		
	No	Sinus	Sinus+Gaussian
a (%)	0.534	0.531	0.530
δa (%)	$3. \times 10^{-3}$	$3. \times 10^{-3}$	$3. \times 10^{-3}$
b (%)	0.462	0.319	0.26
δb (%)	1.5×10^{-2}	1.9×10^{-2}	1.7×10^{-2}

The results quoted above correspond to the use of 300 GeV events for which a part of the energy is leaking outside the EM-Calorimeter. Moreover, this effect is bigger than expected in our simulation made within the Module 0 test beam set up because there is no coil in front of the module, so electrons see about 2 X_0 less than in the real atlas set-up. If we use only energies from 50 to 200 GeV, the results are a bit better : $a = 0.23$ and $b = 0.53$ with errors of the same order as quoted above and a $\chi^2 = 0.97$.

At $\eta = 1.1$, the same analysis lead to a term $b = 0.44 \pm 0.01$ whereas the sampling term is found to be 10.5%. This is a nice feature that the lead thickness fluctuation contribution is smaller in the 1.13 mm lead thickness region than in the 1.53 mm region because the laminating process gives the same tolerance on laminated lead thickness unrespective of the nominal thickness. So the relative lead thickness fluctuations are bigger in the 1.13 mm region ($\eta \in [0.8, 1.4]$) than in the 1.53 mm ($\eta \in [0., 0.8]$).

4.2 Conclusion

First, the effect of dead material in the EM barrel test beam set up has been studied showing that no significant effect should be observed in the test beam data. Second, we have established the relation between the constant term and the lead thickness fluctuation which was found to be at $\eta = 0.3$:

$$C(\%) \simeq \sqrt{\left(0.53\ \frac{\sigma^{(5)}}{e_{th}}(\%)\right)^2 + \left(0.26\right)^2}$$

The contribution from lead fluctuation at $\eta = 1.1$ (1.13 mm thickness region) is found to be 0.44 instead of 0.53 at $\eta = 0.3$ (1.53 mm region). Using these figures and the available thickness data taken at Orsay, the Module 0 constant term can be computed and we find that the contribution coming from lead thickness variations should be less than 0.3 %[2]. The contribution of lead plate thickness fluctuation to the constant term is in good agreement with an analytical calculation presented in [6].

5 Acknowledgements

We want to thank G.Parrour and P.Petroff who helped us to use the detailled simulation of the Module 0. We also want to thank S.Simion for his help to cross-check some of our

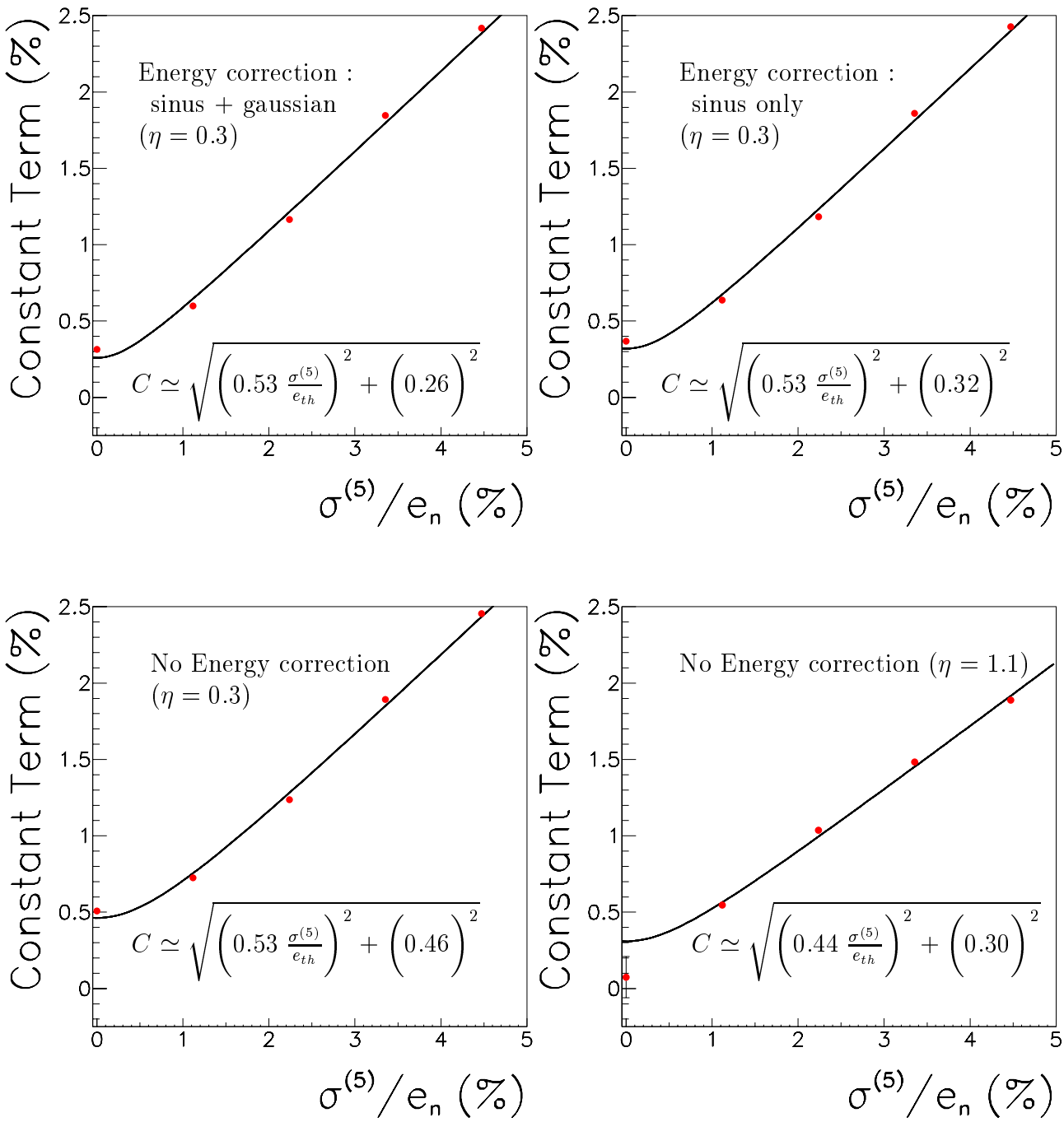

Figure 14: Evolution of lead thickness fluctuation contribution and residual contribution to the constant term for different energy correction. As expected, the less corrected energy, the bigger residual constant term. Nevertheless, the contribution coming from lead thickness fluctuation is constant in each case showing that this effect is uncorrelated from the other one. The right-bottom plot correspond to $\eta = 1.1$ with no energy correction. The three other plots correspond to $\eta = 0.3$.

simulation results. Finally, we take the opportunity of thanking B. Mansoulié for fruitful discussions and suggestions along that work.

References

[1] B. Canton *et al.*, ATLAS Internal Note 076, 1997.

[2] F. Fleuret, B. Laforge, P. Schwemling, *"Lead Matching and Consequences on the EM Module 0 Constant Term"*, ATLAS Internal Note ATL-LARG-99-???.

[3] F. Fleuret, B. Laforge, P. Schwemling, *"Correction of lead plates thickness fluctuation effect on the energy of the EM accordion calorimeter"*, ATLAS Internal Note ATL-LARG-99-???.

[4] Technical Design Report on Calorimeter Performance, ATLAS Collaboration, p. 62, 1997.

[5] V. Tisserand, *"Optimisation du détecteur ATLAS pour la recherche du boson de Higgs se désintégrant en deux photons au LHC."*, Thèse de l'Université Paris-Sud (Orsay), 1997, LAL 97-01.

[6] B. Mansoulié, ATLAS Internal Note ATL-LARG-98-099, *"Non-uniformity of lead plates and gap : Analytical estimates of the shower averaging effect."*, 1998.

Appendix 1 : The Parrour-Petroff description

In this section we present the calorimeter structure (see figure 15) as it was defined by G. Parrour and P. Petroff for their module 0 geometry description. In our geometry description, we have taken the same structure except for the CARN, CORN, CELD elements and their daughter volumes.

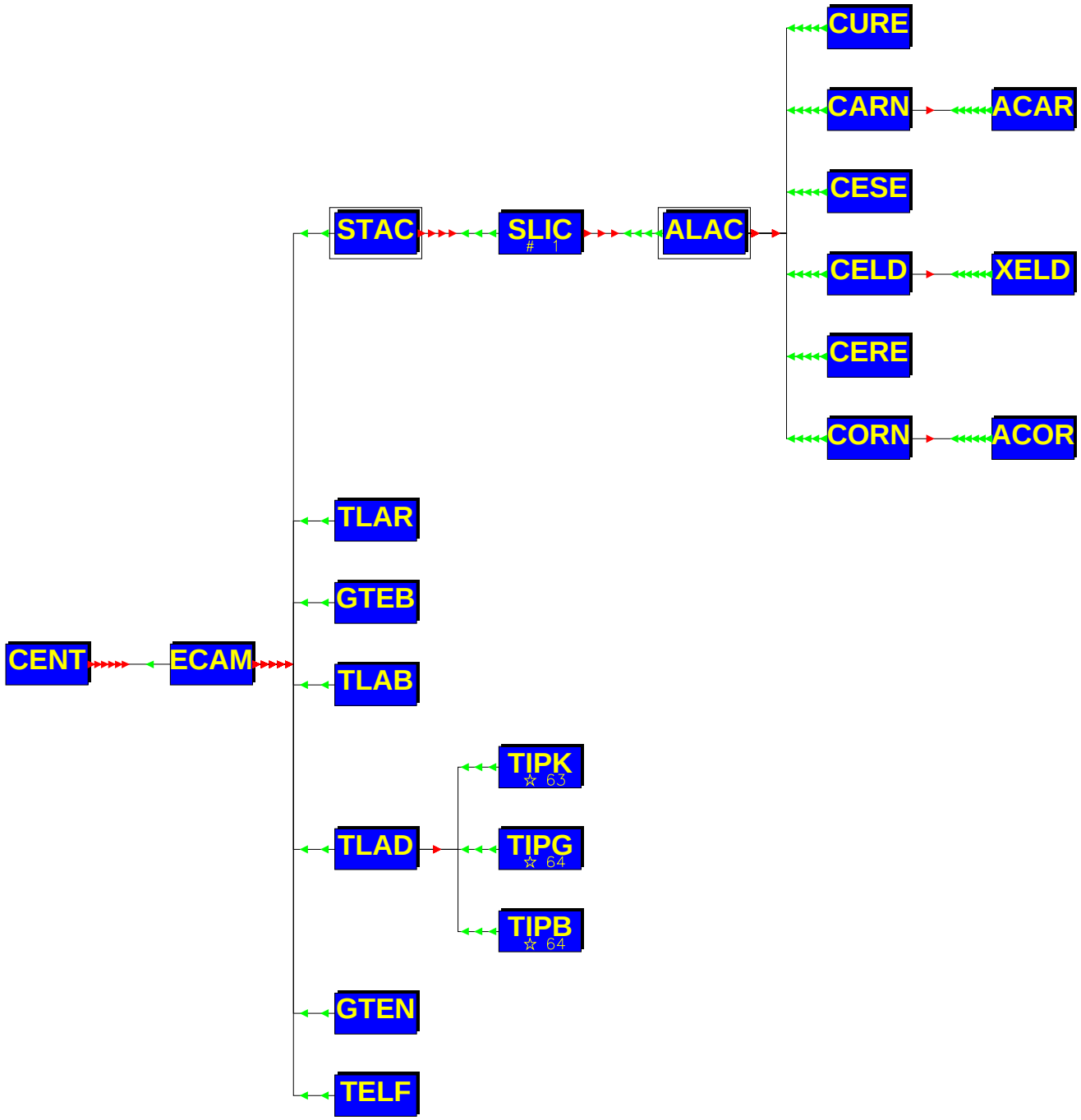

Figure 15: Barrel Ecal tree struture in the Parrour-Petroff geometry description.

Tables 3 and 4 give the description and the materials used for each volume which enter in the calorimeter structure. Again, in our calorimeter description, we have used the same description except for the CARN, CORN, CELD elements and their daughter volumes.

volume name	volume description	volume material
ECAM	accordion volume with electronics, g10 frame, ...	liquid argon
TELF	Electronics layer in front of crocodile	lar elect
GTEN	contains all frontal g10 bars	GTEN
TLAD	nose filled with liquid argon	liquid argon
64×TIPK	extra piece of Kapton	kapton
64×TIPG	added piece of G10	GTEN
64×TIPB	first piece of absorber	thinabs
TLAB	back nose filled with liquid argon	liquid argon
GTEB	contains all g10 bars at back	GTEN
TLAR	Crown (tube) filled with Liquid between eta=1.4 and 1.48	liquid argon
STAC	filled with liquid mother for absorbers and electrodes	liquid argon
SLIC	Crowns sliced in nsli slices in PHI direction	—
14×ALAC	crown - a kind of a cell	—
64×CURE	round corner upper electrode	kapton
64×CARN	round corner upper absorber	thinabs
ACAR	upper round corner thick absorber	thikAbs
64×CESE	flat part of an odd electrode	kapton
64×CELD	absorber box	thinabs
XELD	innermost absorber trap	thikabs
64×CERE	round corner down electrode	kapton
64×CORN	round corner down absorber	thinabs
ACOR	down round corner thick absorber	thikAbs

Table 3: barrel volumes description

material name	material components	material density
liquid argon	Ar	1.4
lar elect	CH^2Ar	1.28
GTEN	$C^8H^{14}O^4$	1.8
kapton	H + C + O + Cu	3.854
thinabs	H + C + O + Pb + Fe	7.598
thikabs	H + C + O + Pb + Fe	9.481

Table 4: barrel materials description

Appendix 2 : the ACCG data bank

In this section, we present the ACCG bank which gives all the parameters entering in the Parrour-Petroff calorimeter description.

```
fill  ACCG   ! geometry definitions
      version = 1                 ! version number
      NBRT    = 14                ! number of zigs+1
      NCELMX  = 1024              ! NCELMX nb of physical phi cells
      IDELFI  = 4                 ! IDELFI electronic phi cell size
      NSTAMX  = 3                 ! NSTAMX nb of samplings in depth
      IRUNC   = icour+1                ! IRUNC run cond. 1/2 = energy/current
      ETACUT  = 1.475             ! ETACUT barrel max eta acceptance
      PHIGAP  = 0.667             ! PHIGAP total gap thickness (PHI_view)
      XCLA    = 0.0               ! XCLA LAr clearance backward
      DELETA  = 0.0250            ! DELETA cell size in eta
      ETACU1  = 0.8               ! ETACU1 1rst cut in eta
      GAMMA   = 1.430             ! GAMMA overlapping para. for geometry
      NCEL_SL = nint(accg_NCELMX /16)  ! un module = 22.5 degrees
      ALFA    = 360./accg_NCELMX ! ALFA angular aperture of a phi cell
      PSI     = accg_NCEL_SL*accg_ALFA  ! elementary phi slice for geometry
      THCU    = 0.011             ! THCU electrode copper thickness
      THFG    = 0.021             ! THFG electrode kapton thickness
      RINT    = 0.278             ! RINT neutral fiber radius (absorber)
      RCF     = 0.278             ! RCF  neutral fiber radius (electrode)
      ZMIN    = 0.5               ! ZMIN   z min position
      ZMAX    = 315.0             ! ZMAX   z max position
      RMIN    = 144.70            ! RMIN   mini radius for mother 1rst elec.
      RMAX    = 200.35            ! RMAX   maxi radius for mother
      XLA1    = 0.0               ! XLA1   inactive LAr layer in copsgeo now
      XLA2    = 1.0               ! XLA2 straight part of the massles gap
      XEL1    = 2.3               ! XEL1   inner electronics
      XEL2    = 0.0               ! XEL2   outer electronics in cryogeo now
      XG10    = 2.0               ! XG10   G10 support bars in
      XTAL    = 1.3               ! XTAL   LAr gap tail
      XGSB    = 2.0               ! XGSB   G10 support bars out
      XTIP_PB = 0.2               ! lead tip thickness
      XTIP_GT = 0.8               ! G10  tip thickness
      RHOMIN  = 148.1934          ! RHOMIN
      RHOMAX  = 198.6387          ! RHOMAX
      PHIIXT1 = -0.565761         ! PHIIXT(1)
      PHIIXT2 = -0.603661         ! PHIIXT(2)
      RCUT12  = 159.39            ! RCUT12 end of the first compartment tap.
      RCUT23  = 186.61            ! RCUT23 end of the second compartment no tap.
      COEP    = 1.266             ! COEP  tapering coef at eta>etacu1
      ISEGME  = 8                 ! ISEGME eta segmentation (D1 design)
      IFIGEM  = 4                 ! IFIGEM D1phi cell (i.e. nb. of elec.cell)
      MDETA   = 4                 ! MDETA U_V eta segmentation
      NDETA   = 2                 ! NDETA U_V natural granu. subdivision
```

```
IWGEM   = 3                 ! IWGEM 1/2/3  1D/UV/both
PACHAM  = 0.01              ! PACHAM pas des cartes courant (cm)
THPB    = 0.150             ! THPB thin absorber lead thickness
THGL    = 0.026             ! THGL thin absorber glue thickness
THFE    = 0.04              ! THFE thin absorber iron thickness
TGPB    = 0.110             ! TGPB absorber lead thickness
TGGL    = 0.066             ! TGGL absorber glue thickness
TGFE    = 0.04              ! TGFE absorber iron thickness
TAPER_1 = 6.0               ! TAPER_1 strips tapered at 6 X0
TAPER_2 = 24.0              ! TAPER_2 2-nd compartment tapered at 24 X0
RIN_AC  = 150.0024          ! RIN_AC radius at which strips starts
ROUT_AC = 197.0482          ! ROUT_AC outer radius of active accordion
X0_INFRACC = 1.7            ! X0_INFRACC number of X0 in front of strips
RDIST_res = 0.7             ! RDIST_res radial distance for resor
DMIN_SEC3 = 2.0             ! DMIN_SEC3 minimal depth of 3-rd compartment
TOT1_X0 = 23.74             ! TOT1_X0 number of X0 for high density part
TOT2_X0 = 19.177            ! TOT2_X0 number of X0  for LOW density part
DENS_STEP = 0.8             ! DENS_STEP eta at which density changes
DENS_H = 2.137              ! DENS_H cm/X0 in high density region
DENS_L = 2.695              ! DENS_L cm/X0 in low density region
BEND1  = 152.1000           ! BEND1 radius of first accordion bend
BEND2  = 155.9659           ! BEND2 radius of second accordion bend
BEND3  = 159.7202           ! BEND3 radius of third accordion bend
Rhocen  = {150.0024, 152.1000, 155.9659, 159.7202, 163.4566,
           167.1019, 170.7433, 174.3067, 177.8757, 181.3753,
           184.8873, 188.3362, 191.8024, 195.2099, 197.0482} _
                          ! R coordinates for the centers of curavture
PHICEN  = {+0.10619, +0.56959, -0.57320, +0.57653, -0.57970,
           +0.58265, -0.58547, +0.58812, -0.59066, +0.59306,
           -0.59538, +0.59757, -0.59969, +0.60171, +0.08083}   _
                          ! phi coordinates for the centers of curvature
DELTA   = { 46.2025, 45.0574, 43.3446, 42.4478, 40.9436,
            40.2251, 38.8752, 38.2915, 37.0608, 36.5831,
            35.4475, 35.0556, 33.9977, 33.6767, 0.}        _
                          !   delta angle of zigs
```

Appendix 3 : the testing geometry

In order to study radiation length and absorption length, we have used geantinos, GEANT's particles which return the number of X_0 and λ_I they see when they cross matter. When using the Parrour-Petroff setup description, geantinos see all the matter which enter in the composition of the calorimeter plus the foam in its back. In order to cancel this unexpected contribution to the X_0 and λ_I we had a new volume NFOA made of vacuum as it can be seen in figure 16.

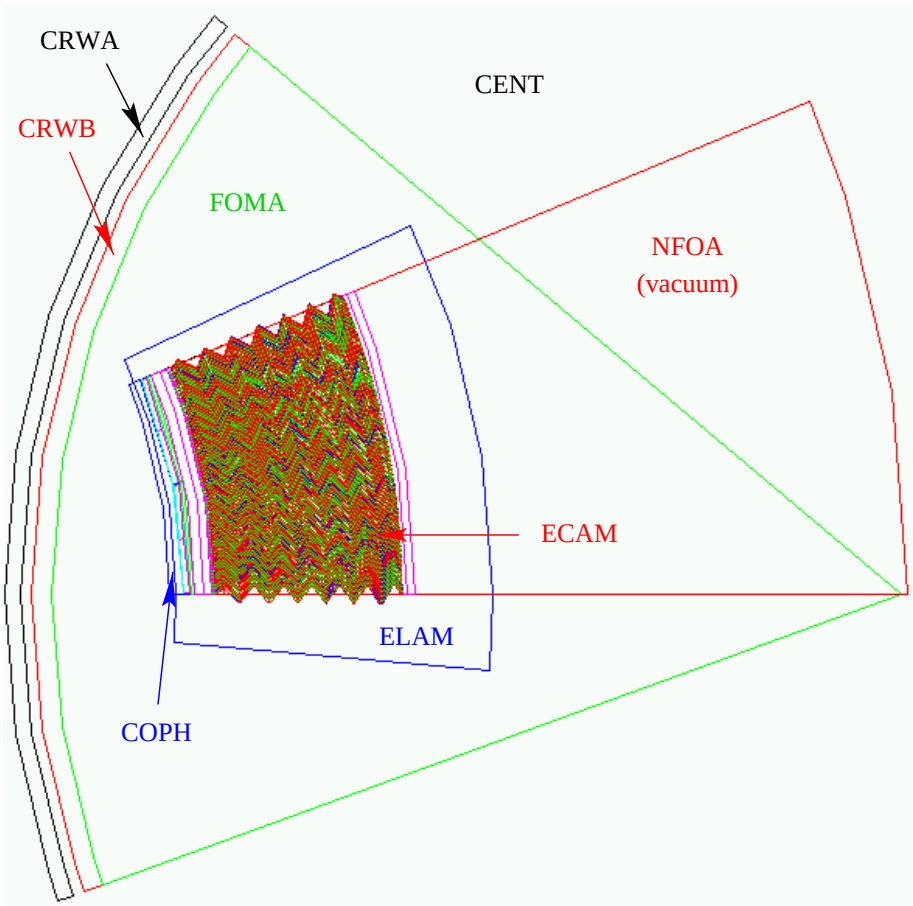

Figure 16: experimental setup layout as simulated in DICE to get correct radiation length and absorption length

Appendix 4 : the datacards (rundice.sh)

```
*********************************************
* INPUT file created by script rundice.sh :
* ----------------------------------------
*********************************************
C------DATACARD FILE for DICE version---
C
C ------------------------------------------------------------
C ------ Run number will be  999                 -------------
C     [1-2146] [1-999999]  Combined to give single integer to ranlux
C RNDM      999  945944
RNDM      999  $seed
RUNG      999
C
LIST
C  ----- TRAP handling has been added into SLUG -------------
TRAP  0  3  10 10  1 0 10 1 4 10
C  ----- Monitoring report on monitor file (random numbers)      -----
MONI  2
C ------ number of triggers to be processed and part. generation -----
TRIG $1
C
C GENERATE event: kine(2): electron=11, mu=13, pi=211 g=22 pi0=111
C    PDG code  EMin-Max    EtaMin-Max  PhiMin-Max   E/Pt
KINE  0  $3    $4   $5       $6   $7     $8   $9     0.
VERT  0.  0.   0.
C*NEWV 'P' 10
C
C  ----- SLUG/GEANT debugging parametrs/modes -------------
TIME 2=10. 3=1
DEBU 0 0 1
C DEBU 1 1 1
SWIT 0 2
C
C ----  digitization and simulation and analysis status
SIMULATION    1
DIGITIZATION  1
RECONSTR      1
ANALYSIS      1
OUTP          1
*BKIO 'O' 'RUNT'
*BKIO 'O' 'EVNT'
*BKIO 'O' 'KINE'
*BKIO 'O' 'HITS'
*BKIO 'O' 'DIGI'
C
C ------- GEANT TRACKING CARDS -----------------
AUTO 0
OPTI 2
DCAY 1
MULS 2
```

```
PFIS 1
MUNU 1
LOSS 3
PHOT 1
COMP 1
PAIR 1
BREM 1
DRAY 1
ANNI 1
HADR 4
ABAN 0
C
C  100 keV as a first speed compromize
CUTS 1=.0001 2=.0001 3=.0001 4=.0001 5=.0001
C  10 keV as a second speed compromize
C  CUTS 1=.00001 2=.00001 3=.00001 4=.00001 5=.00001
CUTS 6=.001  7=.001  8=.001  9=.001
CUTS 11=100.E-9
C--- SLUG filter etc...
C  *TFLT 'ETAP' -2.5 2.5
C  *DREV 'SLUG'    3   1    0.  0.  0.   1.0
C
C SIMU=1 for TRAC means save part of stack on KINE
*MODE 'TRAC' 'SIMU' 1 'HIST' 0 'PRIN' 0 'DEBU' 0 'RAND' 1
C Define:    process     Rmax    Zmax Emin(parent) Emin(daughters)
*DETP 'TRAC' 2='DCAY'   3=110.  4=340.    5=10.       6=0.0
*DETP 'TRAC' 7='PAIR'   8=110.  9=340.   10=10.      11=0.0
*DETP 'TRAC' 12='BREM' 13=110. 14=340.   15=10.      16=1.0
C-----------------------------------------------------------------------C
C----GEOMETRY DEFINITION OF ATLAS  (FULL LAR + COIL IN FRONT+ AIR T)----C
C-----------------------------------------------------------------------C
*MODE 'INIT' 'PRIN' 0
*MODE 'GEOM' 'PRIN' 1
*MODE 'DOCU' 'PRIN' 1
*MODE 'CLOS' 'PRIN' 1
*MODE 'DIGI' 'PRIN' 1 'RAND' 1
*MODE 'RECO' 'PRIN' 1
*MODE 'CONS' 'PRIN' 0
*MODE 'GENE' 'PRIN' 1 'RAND' 1
*MODE 'INPU' 'PRIN' 0
C  Magnetic field
*MODE 'MFLD' 'GEOM' 0 'MFLD' 0 'PRIN' 0
C  the atlas geometry
*MODE 'ATLS' 'GEOM' 1 'PRIN' 1 'GRAP' 0 'MFLD' 0 'DEBU' 1
*MODE 'PIPE' 'GEOM' 0 'PRIN' 1 'GRAP' 0 'MFLD' 1 'SIMU' 1
*MODE 'CRYO' 'GEOM' 1 'PRIN' 1 'GRAP' 0 'MFLD' 0 'SIMU' 1 'DIGI' 0 'RECO' 0
*MODE 'COIL' 'GEOM' 0 'PRIN' 1 'GRAP' 0 'MFLD' 1 'SIMU' 1 'DIGI' 0 'RECO' 0
C      Inner tracker - version 95-1 on   (Morges layout)
*MODE 'PIXB' 'GEOM' 0 'PRIN' 1 'GRAP' 0 'MFLD' 1 'SIMU' 1 'DIGI' 0 'RECO' 0
*MODE 'PIXE' 'GEOM' 0 'PRIN' 1 'GRAP' 0 'MFLD' 1 'SIMU' 1 'DIGI' 0 'RECO' 0
*MODE 'SCTT' 'GEOM' 0 'PRIN' 1 'GRAP' 0 'MFLD' 1 'SIMU' 1 'DIGI' 0 'RECO' 0
*MODE 'ZSCT' 'GEOM' 0 'PRIN' 1 'GRAP' 0 'MFLD' 1 'SIMU' 1 'DIGI' 0 'RECO' 0
```

```
*MODE 'XTRT' 'GEOM' 0 'PRIN' 1 'GRAP' 0 'MFLD' 1 'SIMU' 1 'DIGI' 0 'RECO' 0
*MODE 'INAF' 'GEOM' 0 'PRIN' 1 'GRAP' 0 'MFLD' 1
C      calorimetry
*MODE 'CALO' 'GEOM' 1 'PRIN' 1 'RECO' 1
*MODE 'COPS' 'GEOM' 1 'PRIN' 1 'GRAP' 0 'MFLD' 0 'SIMU' 1 'DIGI' 1 'RECO' 1
*MODE 'ACCB' 'GEOM' 1 'PRIN' 1 'GRAP' 0 'MFLD' 0 'SIMU' 1 'DIGI' 1 'RECO' 1
*MODE 'ENDE' 'GEOM' 0 'PRIN' 1 'GRAP' 0 'MFLD' 0 'SIMU' 1 'DIGI' 1 'RECO' 1
*MODE 'HEND' 'GEOM' 0 'PRIN' 1 'GRAP' 0 'MFLD' 0 'SIMU' 1 'DIGI' 1 'RECO' 1
*MODE 'TILE' 'GEOM' 0 'PRIN' 1 'GRAP' 0 'MFLD' 0 'SIMU' 1 'DIGI' 1 'RECO' 1
*MODE 'FWDC' 'GEOM' 0 'PRIN' 1 'GRAP' 0 'MFLD' 0 'SIMU' 0 'DIGI' 0 'RECO' 1
C      muons
*MODE 'WBTO' 'GEOM' 0 'PRIN' 1
*MODE 'WFTO' 'GEOM' 0 'PRIN' 1
*MODE 'MUCH' 'GEOM' 0 'PRIN' 1 'GRAP' 0 'MFLD' 1 'SIMU' 1 'DIGI' 0 'RECO' 0
*MODE 'FMUC' 'GEOM' 0 'PRIN' 1 'GRAP' 0 'MFLD' 1 'SIMU' 1 'DIGI' 0 'RECO' 0
*MODE 'TGCC' 'GEOM' 0 'PRIN' 1 'GRAP' 0 'MFLD' 1 'SIMU' 1 'DIGI' 0 'RECO' 0
*MODE 'RPCH' 'GEOM' 0 'PRIN' 1 'GRAP' 0 'MFLD' 1 'SIMU' 1 'DIGI' 0 'RECO' 0
*MODE 'FCSC' 'GEOM' 0 'PRIN' 1 'GRAP' 0 'MFLD' 1 'SIMU' 1 'DIGI' 0 'RECO' 0
STOP
STOP
```

ATL-LARG-99-014
27/09/99

September 22, 1999

Lead Matching and Consequences on the EM Module 0 Constant Term

F. Fleuret, B. Laforge, Ph. Schwemling

LPNHE-Paris, Universités Paris 6-7, and IN2P3-CNRS

Abstract

We present in this note the mathematical algorithms that have been used to sort and pair the lead plates during the construction of the Module 0 of the Liquid Argon barrel calorimeter. This pairing is done to reduce as much as possible the contribution to the constant term that arises from lead thickness inhomogeneities. It is planned to use similar algorithms also during the construction of the complete detector, for the same reason. In addition to the pairing itself, we describe the physical considerations that have led us to the choice of a particular class of algorithms. At the end, we show how the chosen algorithm performs using the thickness data available for the lead plates that have been used for the construction of module 0.

1 Introduction

The constraints that the expected performance of the Liquid Argon calorimeter places on the constant term are very stringent. From the Technical Design Report [1], the goal is to have a total constant term amounting to 0.7%, with the contribution of the mechanics (due to local non-uniformities of various origins : lead thickness variations, shape changes from one absorber to its neighbours, gap variations appearing during the assembly of the absorbers, etc.) less than 0.3%. Most of the constant term due to these mechanical causes is expected to be due to the lead thickness non-homogeneities, due to the high variation induced locally on the collected charge by a local variation of the lead thickness : an increase of 1% in the lead thickness translates into a 0.59% decrease of the induced signal [3].

In practice, it is extremely difficult to produce lead with 1% tolerance on the thickness. A 1% tolerance, given the lead thicknesses we use (1.13 mm and 1.53 mm), represents a tolerated thickness variation of 10 to 15 microns. No lead provider is technically able to produce lead with such small tolerances ; the company which is the closest to this number achieves only 3% with no special equipment. This appears at first largely insufficient, however, it is possible by using thickness informations, plate by plate, to cope with the fact that the manufacturer cannot reach a tolerance of 1% on the lead thickness. The main idea is to take advantage from the fact that the electric charge generated by an electromagnetic shower is the sum of the charges generated in the vicinity of several absorbers. In other words, if at some place of the calorimeter there is an absorber whose lead is too thin, the variation this would induce on the collected charge can be largely compensated by placing close to this "thin" absorber an other one that is too thick.

2 Thickness shape of the lead plates

The production process of the lead plates has been largely documented elsewhere [4]. We will simply recall that the lead is laminated from lead blocks of about 1 to 2.3 tons each and wound on big rolls, called "coils".

The final thickness is obtained after several (typically 7) passes. Since the roller is an alternating, reversible system, the lead always passes through the same rolls, whose separation is progressively reduced as the lead thickness decreases. Since the lead is soft and the thickness decrease during the last pass is of the order of 0.4 mm, i.e. much bigger than the highest thickness variation along the whole roll, the force applied ($\simeq 1\ MN$) is sufficient to resorb all the inhomogeneities that have been created before, so we are left

only with the ones created during the last pass. Thickness is measured on the fly using an on-line X-ray measurement system during this last pass. Thickness measurements [4] and visual observation of the operation of the roller have shown that thickness variations are due to :

- ellipticity of the rolls. This effect is more or less pronounced, depending upon the temperature (the effect decreases when the rolls get hotter) and upon the relative phase of the rolls. This phase is unfortunately random at the start of the processing of each roll and cannot be changed. This leads to an oscillating thickness pattern of period $\simeq 50\pi\ cm$ with an amplitude varying from a few μm to $\simeq 40\ \mu m$.
- instabilities of the hydraulic sytem used to control the speed and torque of the winding and unwinding rolls. This has been seen to lead also to thickness oscillations of various periods and amplitudes but usually less striking than the previous ones.
- parallelism defects in the positionning of the axes of the rolls with respect to each other. This leads to an inclined thickness profile in the r-profile of the plates, whereas the two previous causes only affect the η-profiles. This effect is typically of the order of a few microns along the whole radius span of the calorimeter.

3 Implementation of the pairing system in the IN2P3 hall

After being laminated, lead is cut into plates which are stored by boxes of about 40 plates. The X-ray measurement made during the laminating process gives information about the average thickness of plates within a box. After this step, boxes are sent to IN2P3 hall in Orsay where they are stored.

Ideally, one could think of unpacking all the plates and building the absorbers by always choosing for the nth absorber the plates that "best match" the absorbers previously built. By "best match", we mean "that will produce the most uniform local response". This criterion will be explicited more precisely in the next sections.

Due to space limitations, only 8 heaps are possible (+2 heaps containing the plates ready for absorber production. See figure-1 which shows the practical organisation of hall IN2P3). Furthermore, the total plate weight (80 t) is so large that it is not possible to unpack them all and stack them at once over the 9 available heaps. The challenge is then to always supply lead with

the most constant mean thickness as possible. For the module 0, this is not a problem due to the limited number of plates needed to build it (2×64), so that the storing system could load them all at the same time, its total capacity being about 2 modules. For the production, the X-ray information will be used to select which box must be unpacked in order to constitute the heaps, so as to ensure a lead supply of long range constant average thickness.

When a plate is unpacked, its ultra-sound measurement is done. This information is then put into a database which will be used for the pairing process. After this measurement, the plate is stacked using a vacuum lift mounted on a mobile deck.

4 General description of the pairing method

Despite a reasonable accuracy of the lead plate thickness achieved in the laminating process (30 μm), plate to plate thickness fluctuations cannot be neglected. Reaching a contribution to the constant term as small as possible (below 0.3% as required in the ATLAS TDR [1]) requires the build-up of a plate to plate correlation able to smooth out the average thickness calculated over the number of plates seen by an electromagnetic shower.

As soon as we have established this effective number of lead plates seen by a shower, we have elaborated a way of pairing the plates based on a minimization principle taking into account the extremely constrained conditions of lead manipulation in the hall IN2P3. Basically, as we can't move plates except to use them to build an absorber, we have 9 possibilities for each kind of plate (1.13 mm and 1.53 mm) to choose one. Thus, the pairing scheme consists of the calculation of a choice function for each heap. At this step, the work remaining to be done is to decide what is the best choice function. This implies to contruct an estimator to test the different choice functions we could think about. The choice function has to be chosen to ensure the most possible constant response.

As we cannot take the thickness measurements to put them into GEANT and choose the combination that gives the most constant response (due to obvious computing time limitations) we have to design choice functions and a "response constantness evaluation function" that are more easily calculable, as described in the next section.

The data we can use to contruct a choice function are the ultra-sound measurements of each lead plate. These constitute a matrix of about 460 (63 in z $\times$ 15 in r) local thickness measurements taken over the whole surface of

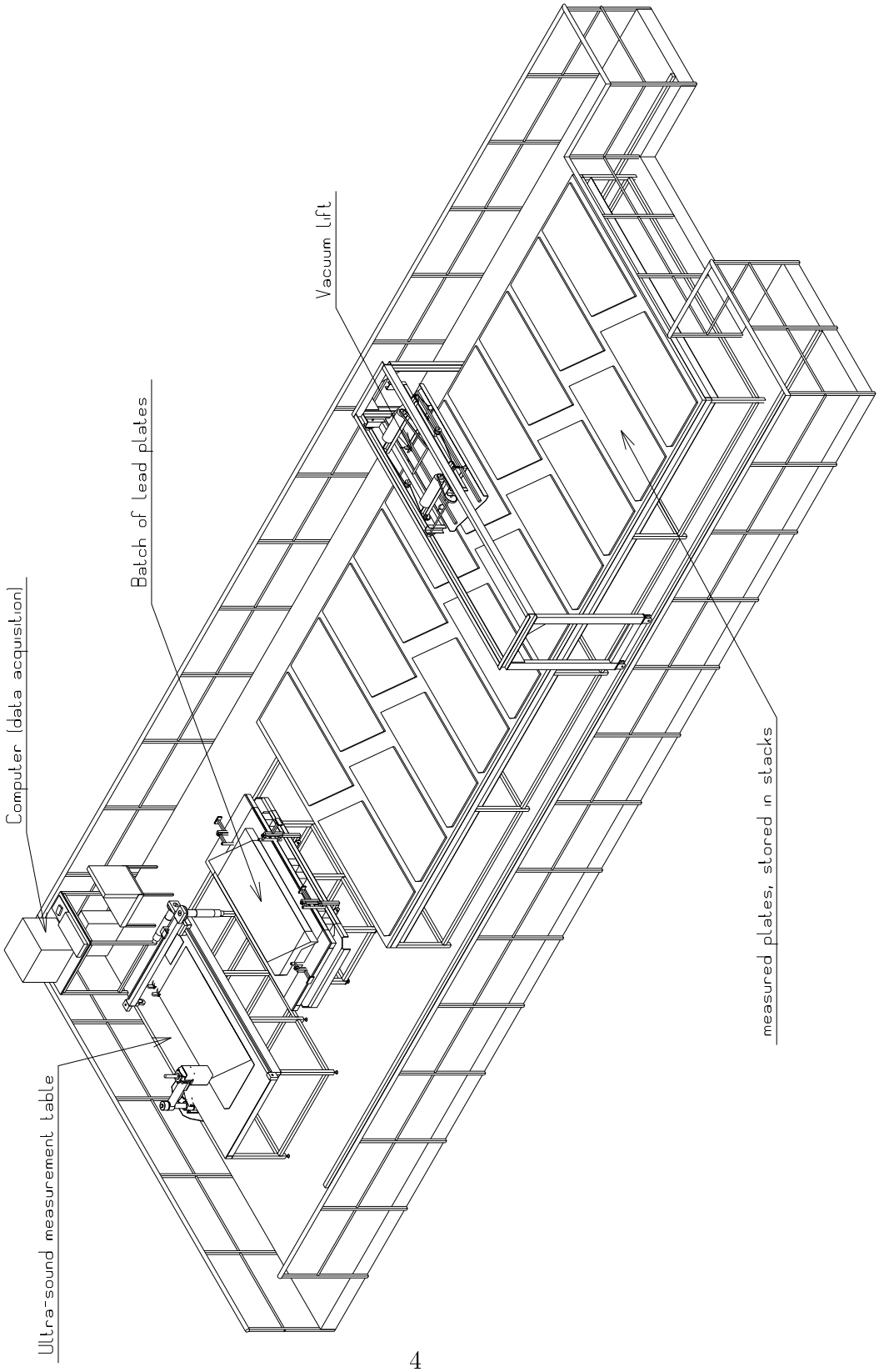

Figure 1: Schematic of the technical design of lead plates heaps in the IN2P3 hall. On the right hand side is represented the ultra-sound measurement system. There are actually 10 heaps present ; the 10th is used as an intermediate storing place, before placing the plates in their final stack.

the plate for each of them. A schematic of the measurement matrix is shown figure 2.

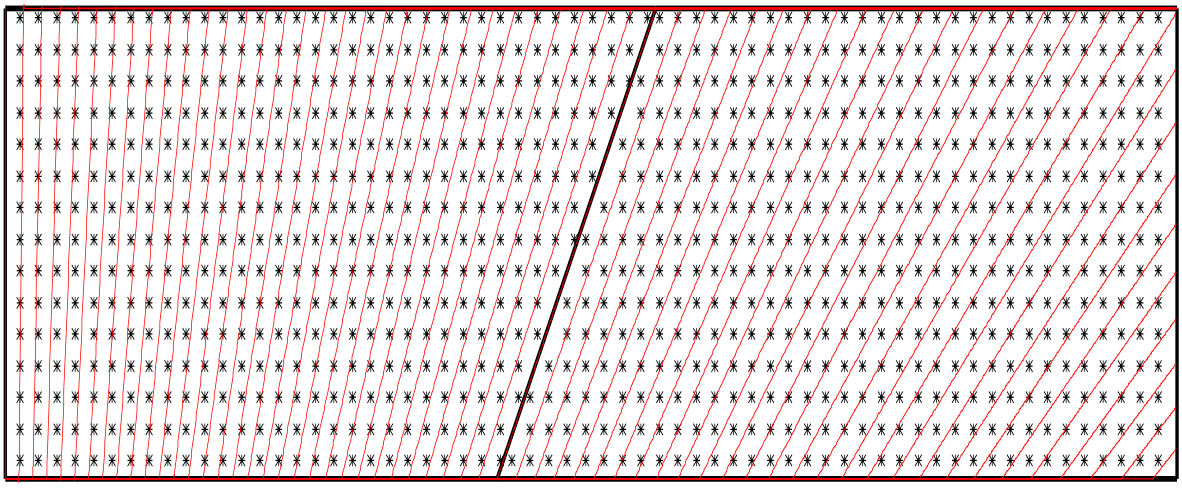

Figure 2: Schematic of the measurement matrix available on each absorber lead plates. The dashed lines delimit the 60 η-cells.

5 Actual implementation of the method

5.1 Number of plates seen by an electromagnetic shower

The build-up of the correlation that is supposed to ensure constant response needs first the knowledge of the number of consecutive plates (absorbers) over which the correlation has to be effective, i.e. the number of plates over which an electromagnetic shower develops. The determination of the average number of lead plates seen by an electromagnetic shower requires the use of a detailed simulation of a module. We have used the dedicated version of DICE done especially to simulate the Module 0 of the EM barrel done by G. Parrour and P. Petroff. We have adapted this program in order to get the energy deposited in each liquid Argon gap by a shower [3].

Looking at the distribution of this energy as a function of the gap number, we can get the effective number of gaps over which a certain fraction of the shower energy is deposited. We have studied both electron and photon showers for energies between 10 to 100 GeV. We did not simulate higher energy showers because above 100 GeV, leakage begins to be sizeable and because the most strigent requirements on the calorimeter resolution come from

physical processes that involve photons or electrons of energies of $\simeq$ 100 GeV or less ($H \to \gamma\gamma$, $H \to e^+e^-e^+e^-$).

In order to get a robust result, we have changed in our simulation several parameters that are likely to have an effect on the shower width. We have studied also the effect of the pre-shower detector and established that it has almost no effect at the level of precision we required. We have simulated showers both in the 1.13 mm and 1.53 mm lead region. We also tested the effect of the ϕ inhomogeneities, shooting particles in between two absorbers or directly in the "foot" of an absorber, i.e. in the G10 bar. None of these effects were found to have a big effect on the shower shape. In each case, using a gaussian fit of the energy profile of the obtained electromagnetic shower, we obtained a $\sigma_{N_{gap}}$, the standard width of a shower, located between 1.60 and 1.68 gap. The corresponding plots are presented on figures 3 to 4. We simulated 10 events for each case in order to save CPU time. However, we checked that simulating 100 events does not change the result by more than 5%. As we are interested in determining an integer effective number of plates, the precision that we obtained this way is large enough for our purpose.

According to the previous fit, we can deduce that the main part of a shower energy is roughly deposited over 5 plates. This number of plates is also the one which can be deduced from calculations made in [2]. We choose then to make the matching in order to reduce fluctuation of the mean thickness over 5 plates.

5.2 Estimator of the pairing quality

As the final result we want to achieve is a smoothing of the mean thickness over 5 plates, the natural estimator we can think about to evaluate the constantness of the calorimeter response is the variance of this quantity calculated along the whole module 0 using a sliding mean thickness calculation over 5 plates since, at first order, the response is linearly dependent over the thickness. This estimator can be written :

$$\sigma^{(5)} = RMS\left\{\bar{e}_i - e_n\right\}_{\text{all cells}}$$

where e_n is the nominal thickness of the lead plates and $\bar{e}_i$ is the mean thickness over 5 plates of a defined cell i. This mean thickness is computed from ultra-sound measurements of all points in the cell over the 5 plates. The number of cells we have used is 60 as represented on figure 2. We have used this estimator in all the studies presented here.

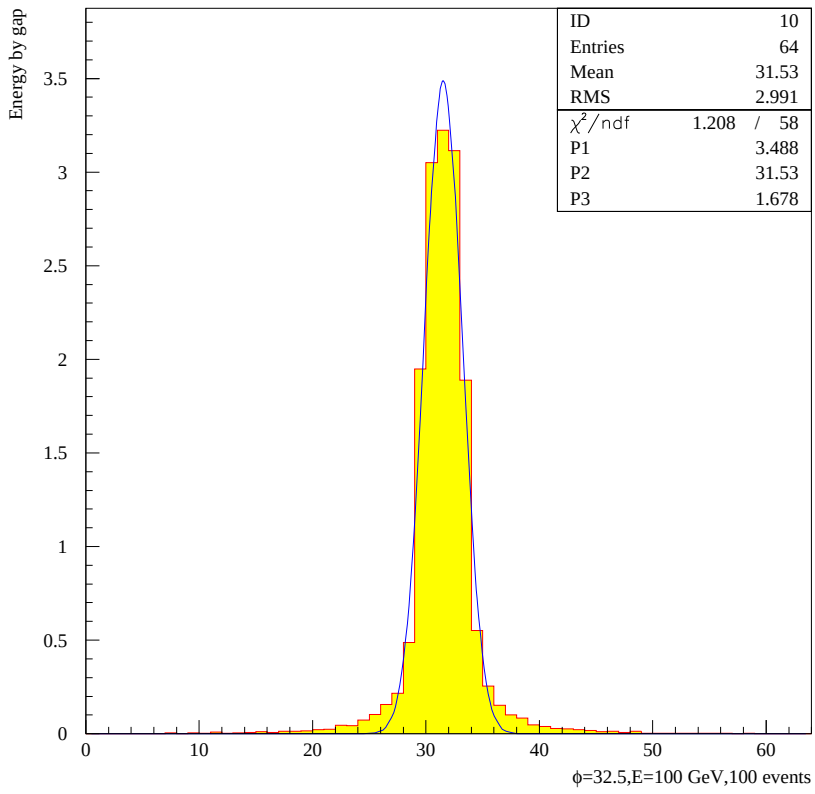

Figure 3: Energy deposited in each gap of the module 0 for a photon of 100 GeV emitted at $\Phi = 0.2$ and $\eta = 0.3$ as a function of the gap number (1 to 64). The sigma obtained with a gaussian fit is 1.67 gap.

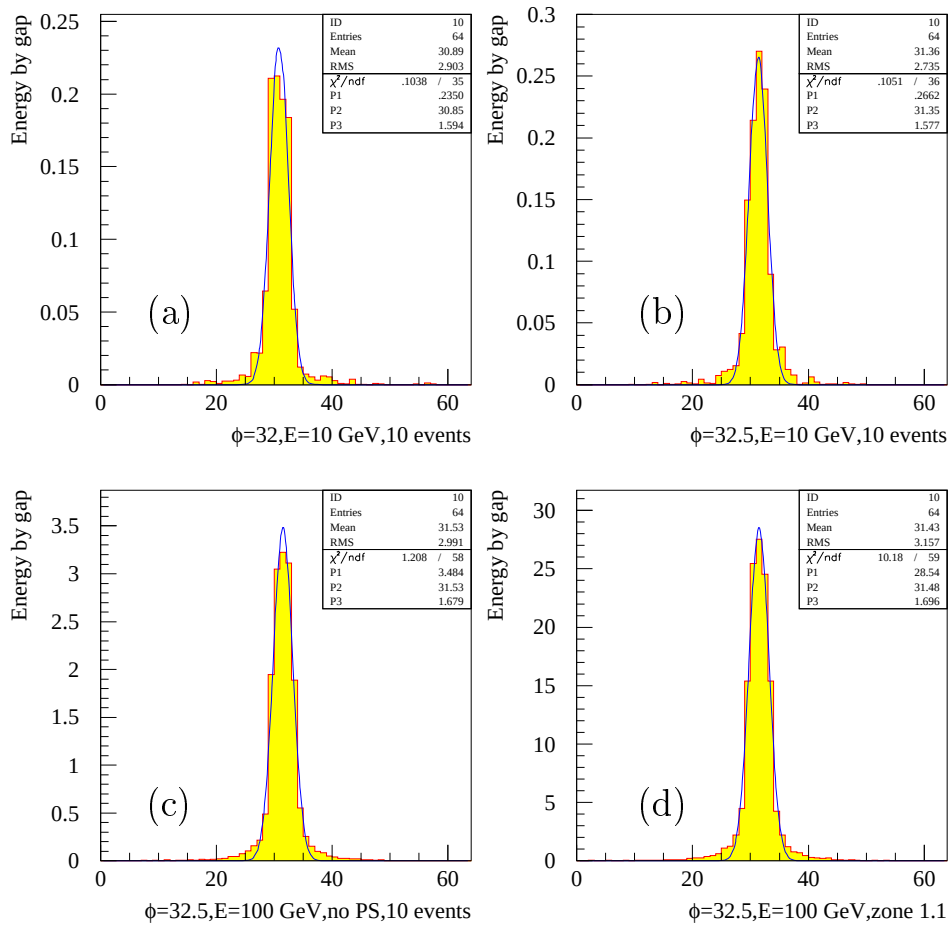

Figure 4: Energy in Gev deposited in each gap of the module 0 for (a) a electron of 50 GeV, (b) a photon of 100 GeV, (c) a photon of 50 GeV without the pre-shower detector. All these particles were emitted at $\Phi = 0.2$ and $\eta = 0.3$ as a function of the gap number (1 to 64). (d) Same distribution for a photon of 50 GeV emitted in the 1.13 mm thickness part. On each of these plots is given the fitted sigma value in number of gaps.

5.3 Test of Choice functions

The knowledge of the lead plate thickness over their all surface allows to compute choice functions giving both information on the local and global fluctuation of each plate thickness.

Having built n absorbers in a module, the most naive choice function to pick up a lead plate which can be thought about is based on each top plate. We can, for instance, take the plate whose average thickness is the nearest to the nominal value. But doing that, we don't use the available information coming from the existing absorbers already put in the module nor the information based on the structure of the lead plates still in the heaps available to make the next absorbers. As the number of plates seen by an electromagnetic shower is five, we decided to use information from 2 plates from the 2 last already built absorbers and from 3 plates available on the heaps. Each of these three plates corresponds to a plate which would be on top of a heap after we would have picked up the previous one. In other words, we use information on plates which can be buried in the heaps at a maximum depth of 3 plates.

Global shape information are obtained from averages over a large domain of a plate whereas local information is given from few measurements located close to each other. The most global information over a 5 plates configuration is then the mean thickness computed from every single measurement from every plate. The most local information is the mean over the 5 plates of the thickness measurements taken at the same point. We have to find a compromise between the long and the short range information to compute a choice function. Indeed, on one hand, using only long range quantities can be very inefficient as global compensation can occur. As an illustration of that fact, imagine a plate with half of it being 20 μ thinner than the nominal thickness and the second half being 20 μ thicker, globally the mean thickness would be the nominal value. Therefore, choosing such a plate without further consideration can create a very bad fluctuation in the local response of the detector. On the other hand, short range criteria could reject a very good plate because of a very local default. As we choose a whole plate each time, both kinds of information must be used.

A convenient estimator of the local plate thickness quality is the difference to the nominal thickness : $e_i - e_n$. Thus, we will naturally construct the choice functions with this quantity.

As the fluctuation in the r direction is much smaller than the one in the

z direction, we decided to use local information on the z structure of the lead plates. More precisely, we defined 60 cells in η as represented on fig. 2. Because of the large number of η cells, this segmentation is roughly equivalent to a z segmentation.

Then, we naturally define choice functions with the functional form :

$$\sum_{i \in cell} \left| \sum_{j \in plate} w_j \left(e_i - e_n\right) \right|^{\alpha}$$

where α is a certain power and w_j a weight factor. These weight factors are respectively 1 and 2 for the two plates already in the module and 3, 2, 1 for the three plates used to compute the choice function. This procedure cancels any degenerated solutions space (with no weight, we could find situations where taking plates in reverse orders would give the same value of the choice function) and gives a predominance to the plate to be chosen in the choice function value. Moreover, a natural idea is to attribute weights relatively to the fraction of the shower seen by each plate. The weights that we have applied are an approximation of the shower tranverse energy density distribution in order to have a physically motivated weighting.

5.4 Respect of technical constraints

The algorithms that we wrote and tested are meeting two key-points imposed by the organisation of the production process. The first one is due to the very delicate manipulation of lead plates which is done with a system based on a vacuum pump and an armada of succion pads. In order not to damage the plates, each of them should not be moved except to be used in the module being built. The second technical constraint taken into account is the difference of thickness between the 1.53 mm plate and the 1.13 mm plate at the interface of each absorber. We took into account the constraint :

$$|e_{1.53} - e_{1.13}| = 0.4 \pm 0.02$$

around a region of 20 cm around the $\eta = 0.8$ cut line. This constraint is supposed to avoid bubbles when the absorber is built up.

5.5 The final configuration

Using real data, we tested different values of the power α given in the previous equation, trying to minimize the value of our estimator. It turned out that the best exponent sits around 1. Therefore, the module 0 matching will be

done using an exponent exactly equal to 1. The final choice function is then :

$$\sum_{i \in cell} \left| \sum_{j \in plate} w_j \, (e_i - e_n) \right|$$

6 Simulation results on toy thickness distributions

In order to test our ideas and methods, we used different 'toy' distributions of lead plate thickness. As a first try, we used plates with distributed thickness but without local inhomogeneities. We used equiprobable distributions and gaussian distributions. We also investigated the consequences of heaps constitution. We especially tested a distribution of plates whose thickness increased gradually in order to see how our algorithms could make vanish a very strong plate to plate correlation intendedly put in the heaps. These simulations showed that we could even in this case decrease the fluctuation of the thickness averaged over 5 plates by 50 % compared to the one obtained with an uncorrelated distribution whose plates would have been chosen in the heaps order.

7 Results on real thickness distribution

The different algorithms were also tested with the real distribution of plates as it was available in the hall IN2P3 at Orsay. We compared our algorithm to the case where the plates were chosen in the order of the heap (1st of the 1st heap, 2nd of the 1st heap, ... ,last of the last heap) and with the "orthogonal" order (1st of 1st heap, 1st of 2nd heap, ... , last of last heap). Depending upon the way heaps were built, one mode corresponds to constructing absorbers with a succession of plates having the same fluctuation dependence as the one produced by the laminating process and the other to a large breaking of this correlation. The second case can roughly be considered as being equivalent to an uncorrelated distribution of plates because all plate to plate correlation is broken by the dealing procedure. In that case, correlations between plates being on top of a heap are almost null since these plates were produced either from a different lead roll or at a non-adjacent place on the same roll.

We did the analysis both for 1.13 mm plates and 1.53 mm. As the laminating production process is roughly the same for both kind of thickness, the σ on the thickness (e) of the two kind of plates is the same. Consequently, $\sigma^{(5)}_{1.1}/e_{1.1}$ (for 1.13 plates) is bigger than $\sigma^{(5)}_{1.5}/e_{1.5}$ (for 1.53 plates). We give below the obtained results on the 1.13 and 1.53 plates for the three cases discussed above :

Matching method	$\sigma^{(5)}_{1.1}/e_{1.1}$	$\sigma^{(5)}_{1.5}/e_{1.5}$
In the order of heap	$7.4\,10^{-3}$	$2.3\,10^{-3}$
In the orthogonal order	$5.48\,10^{-3}$	$2.3\,10^{-3}$
Our Matching	$4.\,10^{-3}$	$2.2\,10^{-3}$

It turns out that for 1.13 plates, our weighting procedure induces a subtantial gain whereas for the 1.53, the gain is smaller. This is due to the fact that the 1.53 plate distribution was already of good quality. Figure 5 shows the map of the Module 0 actually built (60 η-cells $\times$ 64 plates). Figure 6 shows the η profiles of the Module 0 for both 1.13 mm and 1.53 mm parts. Figure 7 shows the distribution of η-cell thickness for each individual plate or averaged over 5 plates. These distributions were used to extract the thickness fluctations quoted in the previous table. Figure 7.(b) exhibits a small peak around 1.13 mm. This peak is due to the last 4 plates of the modules which were chosen by the pairing program at a time when there were very few remaining plates on the 1.13 mm heaps and consequently a limited choice. Figure 8 shows the same distribution than figure 7.(b) but with the last 4 plates of the modules removed showing clearly the origin of the bump. During the series production such an effect should not occur since heaps will be repeatedly loaded with new plates.

As the relation between $\sigma^{(5)}/e$ and the constant term C was determined from a simulation to be about (see figure 9) :

$$C \simeq \sqrt{\left(0.53\,\frac{\sigma^{(5)}}{e}\right)^2 + 0.25^2}$$

and

$$C \simeq \sqrt{\left(0.44\,\frac{\sigma^{(5)}}{e}\right)^2 + 0.3^2}$$

respectively at $\eta = 0.3$ and $\eta = 1.1$ [3], we can quote constant term contributions from lead inhomogeneities to be : $C_{1.1} = 1.8 \times 10^{-3}$ and $C_{1.5} = 1.17 \times 10^{-3}$.

8 Conclusion

Finally, we have reached the goal for Module 0 and achieved a contribution from lead thickness inhomogeneities to the constant term smaller than 0.3 %. We can quote constant term contributions from lead inhomogeneities should be for the Module 0 :

$$C_{1.1} = 1.8 \times 10^{-3} \quad \text{and} \quad C_{1.5} = 1.17 \times 10^{-3}$$

This will be checked in the coming beam tests.

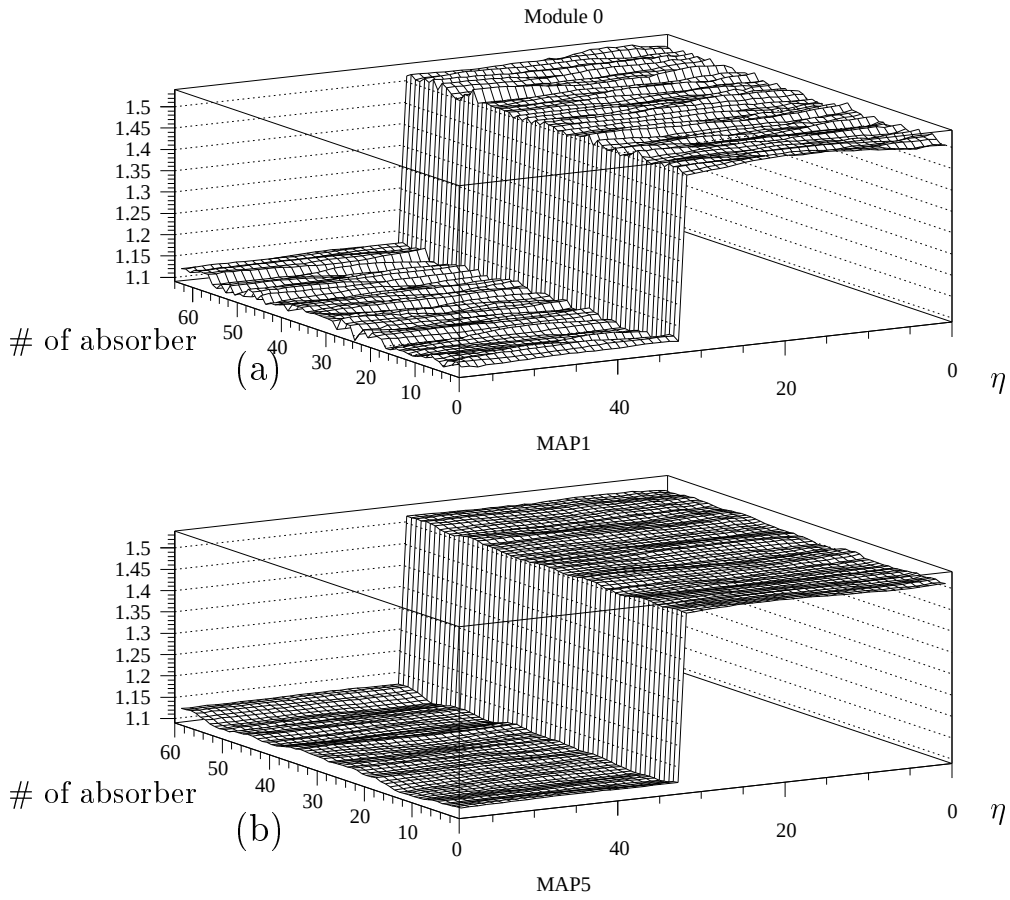

Figure 5: (a) Individual thickness map of Module 0 (60 η-cells $\times$ 64 absorbers). (b) Averaged over 5 absorbers thickness map of module 0

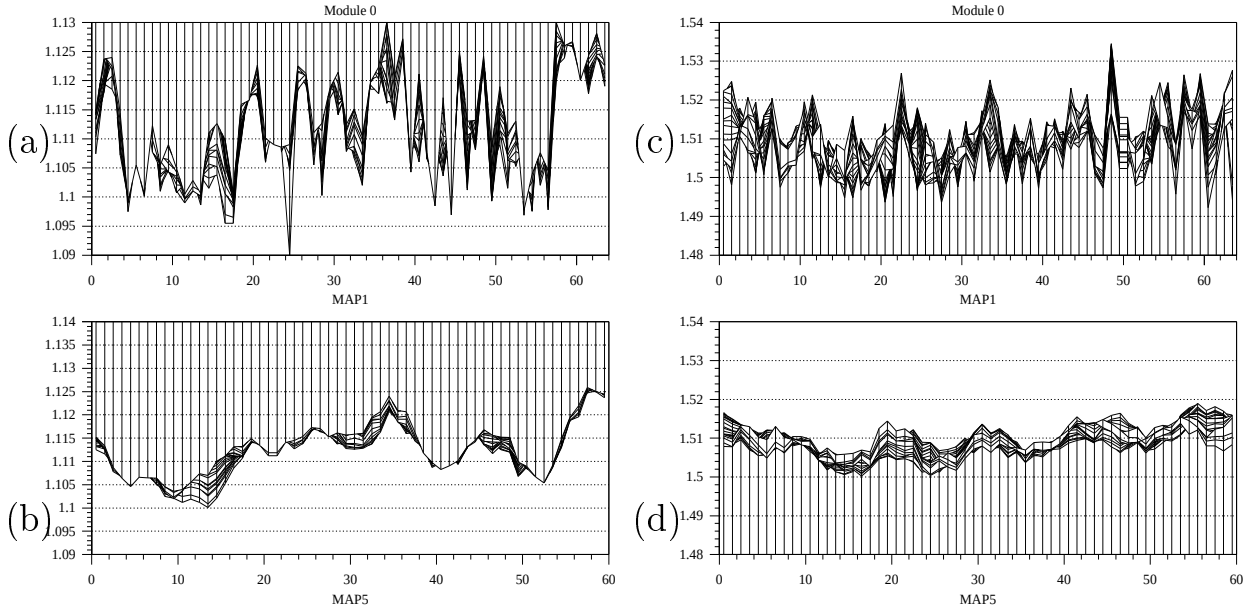

Figure 6: (a) Individual thickness η-profile of the 1.13 mm part of the Module 0. (b) Averaged (over 5 plates) thickness η-profile of the 1.13 mm part of the Module 0. (c) Individual thickness z-profile of the 1.53 mm part of the Module 0. (d) Averaged (over 5 plates) thickness η-profile of the 1.53 mm part of the Module 0. The multiple lines which are observed reflect the projection on the η-axis of the 2D-map of the Module 0 (60 η-cells $\times$ 64 absorbers).

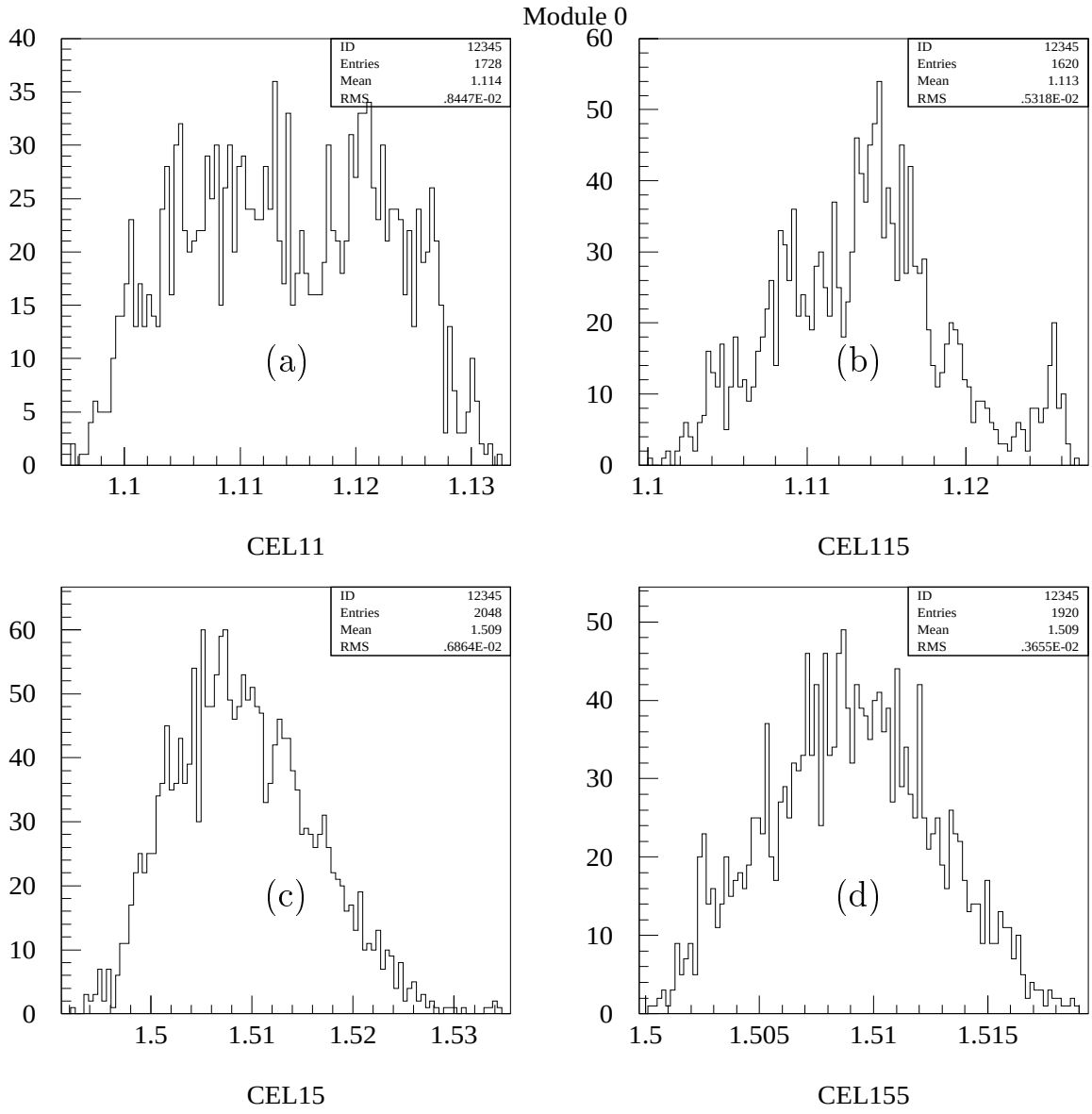

Figure 7: Module 0 characterization : (a) individual cell thickness distribution in the 1.13 mm (b) η-cell averaged (over 5 plates) thickness distribution in the 1.13 mm (c) η-cell individual thickness distribution in the 1.53 mm (d) η-cell averaged (over 5 plates) thickness distribution in the 1.53 mm

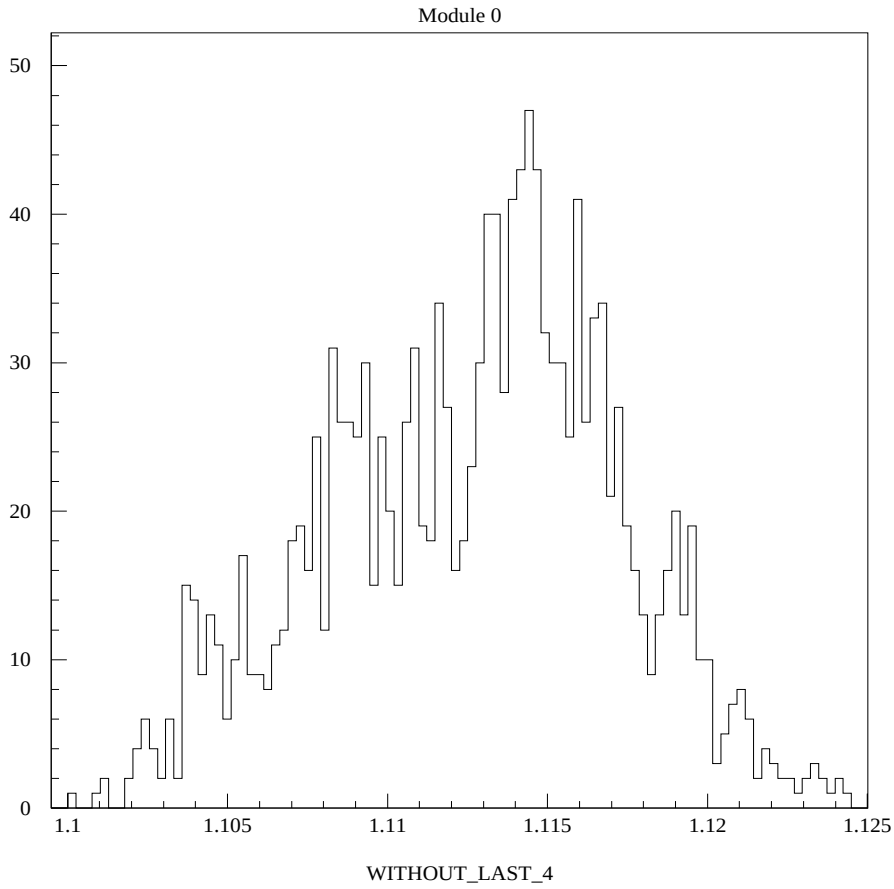

Figure 8: Same distribution as figure 7.b but without the last four 1.13 plates. The peak around 1.13 mm has disapeared. This peak reflects the small number of available plates at the end of the construction of the Module 0. This effect should not occur during the series production since heaps will be continuously loaded.

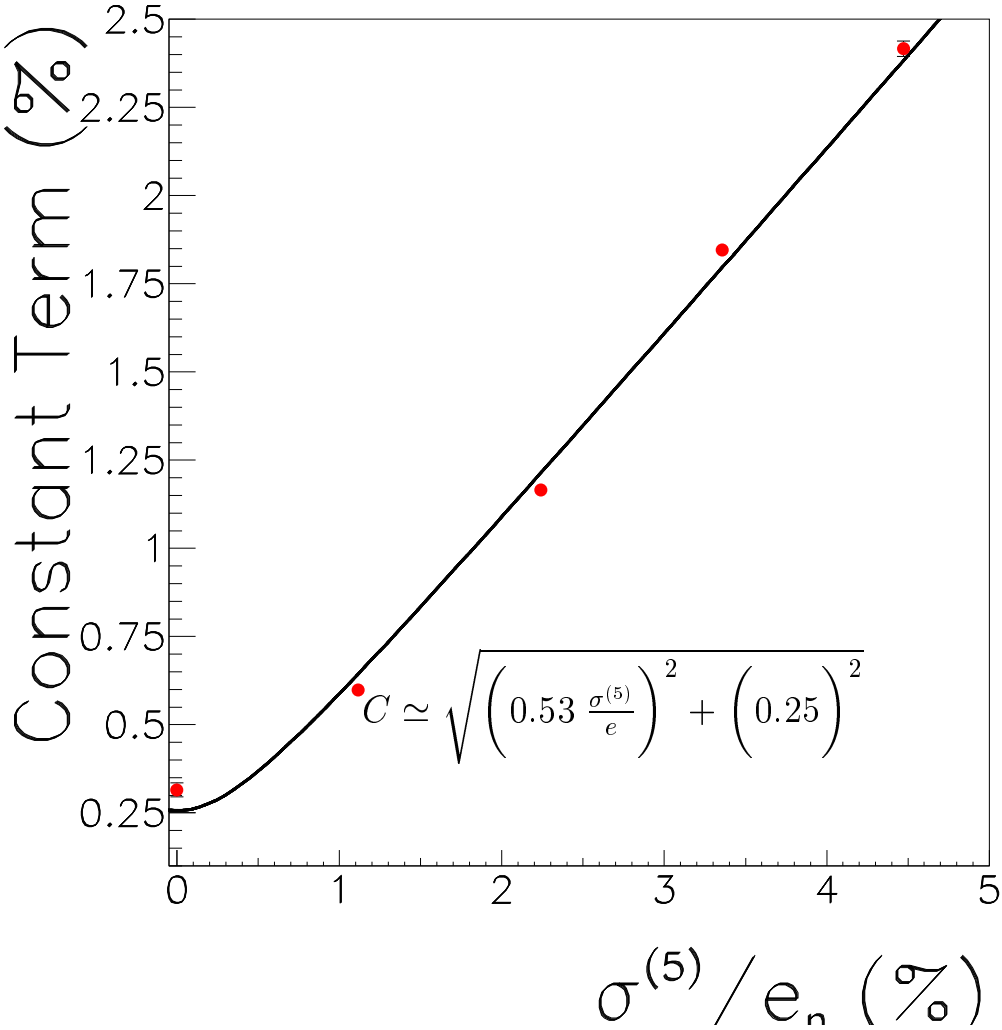

Figure 9: Evolution of the constant term as a function of the ratio of the fluctuation of the mean thickness over 5 plates divided by the nominal thickness of the lead plates.

9 Acknowledgements

We take the opportunity of thanking B. Mansoulié for fruitful discussions and suggestions along that work.

References

[1] ATLAS Liquid Argon Calorimeter Technical Design Report, 15 December 1996.

[2] B. Mansoulié, ATLAS Internal Note ATL-LARG-98-099, *"Non-uniformity of lead plates and gap : Analytical estimates of the shower averaging effect."*, 1998.

[3] F. Fleuret, B. Laforge et Ph. Schwemling, *Constant Term Evolution with Lead Plate Thickness fluctuations in EM Module 0*, ATL-LARG-99-???.

[4] B. Canton et al., *"Analysis and Results of the measurements of the plate thickness, done at the factory, during the production of the lead for the module 0 of the Barrel and End-Cap ATLAS electromagnetic calorimeter"*. ATLAS Internal note LARG-76

Energy Restoration of Edge Electrons in the D0 Central Calorimeter

F. Fleuret
Laboratoire de Physique Nucléaire et de Hautes Energies, Paris, FRANCE
Lawrence Berkeley National Laboratory, CA, USA

March 28, 2000

Abstract

A new method for the energy restoration of edge electrons in the D0 Central Electromagnetic Calorimeter is presented. This method uses the correlations between measured electromagnetic and hadronic energies. The resolution obtained with such a method varies from $37\%/\sqrt{E}$ to $47\%/\sqrt{E}$ for 50 GeV electrons between η=0.05 and η=0.95, and from $31\%/\sqrt{E}$ to $83\%/\sqrt{E}$ for electrons between 20 and 200 GeV.

1 Introduction

The D0 Central Electromagnetic Calorimeter consists of 32 azimuthal modules. Because energy is lost in the uninstrumented region by the azimuthal edges, electrons within 0.01 – 0.02 radians of the azimuthal edges are usually not included in physics analyses, leading to a loss of 10–20% of electrons.

In the following, after having presented the samples we used and a few less efficient global correction methods, we present a method based on electromagnetic and hadronic energy correlations which can restore the energy of most of these edge electrons with a resolution better than the one gets with the central tracker system for electrons greater than 20-30 GeV.

2 Data Samples

This analysis has been made using the RunII software implemented on a Linux machine in LPNHE-Paris. Using the Preshower and calorimeter energy calibration weights optimized for RunII, we produced several samples of single electrons from 20 GeV to 200 GeV, and from η=0.05 to η=0.95.

2.1 Simulation and reconstruction

The samples used in this analysis were created by running D0GSTAR (version P01.00.02) and D0reco (version t00.53.00) both in LPNHE-Paris. We have used in D0reco the energy calibration weights given in D0note 3716 [1]. The Preshower and Electromagnetic Calorimeter weights were optimized to get the best energy resolution for 50 GeV electrons, and the Hadronic Calorimeter weights were optimized to get the best energy resolution for 50 GeV pions (using the previous Preshower and Electromagnetic Calorimeter calibration weights). Table 1 gives the calibration weights used in D0reco as they appear in D0note 3716.

detector	calibration weights
Central Preshower	12.32738
Electromagnetic layer 1	17.87720
Electromagnetic layer 2	13.24849
Electromagnetic layer 3	13.21898
Electromagnetic layer 4	13.86140
Fine Hadronic layer 1	20.67801

Table 1: Calibration weights used in D0reco as they appear in d0note 3716

To compute the reconstructed electron energies we used the calorimeter response at the cell level (equivalent to the GEANT deposited energy) without threshold, clustering or electronic noise.

2.2 Data samples as a function of η and energy

For this study, we generated single electron samples at several energies and several η values. Table 2 shows the energy value, η value, the number of

events, the ϕ range [1] and the Z vertex [2] for each generated file.

energy	η value	number of events	ϕ range (degree)	Z vertex
50 GeV	0.05	5000	[8.59:25.79]	0.0 $\pm$ 0.0
50 GeV	0.25	5000	[8.59:25.79]	0.0 $\pm$ 0.0
50 GeV	0.55	5000	[8.59:25.79]	0.0 $\pm$ 0.0
50 GeV	0.75	5000	[8.59:25.79]	0.0 $\pm$ 0.0
50 GeV	0.95	5000	[8.59:25.79]	0.0 $\pm$ 0.0
20 GeV	0.05	2500	[8.59:25.79]	0.0 $\pm$ 0.0
100 GeV	0.05	2500	[8.59:25.79]	0.0 $\pm$ 0.0
200 GeV	0.05	2500	[8.59:25.79]	0.0 $\pm$ 0.0
50 GeV	0.05	2500	[8.59:25.79]	0.0 $\pm$ 28.0 cm

Table 2: Data samples as a function of energy and η

After the reconstruction stage, the Central Preshower, Electromagnetic Calorimeter and Fine Hadronic Calorimeter energies are stored separately for our analysis. Figure 1 shows the energy distributions for non-edge 50 GeV electrons [3] at η=0.05 for these detectors. In that case, 3.6% of the energy is seen by the Central Preshower, 95.9% by the Electromagnetic Calorimeter and 0.5% by the Hadronic Calorimeter. The edge effects can be seen on the reconstructed energy *versus* ϕ plots: the Electromagnetic Calorimeter energy strongly decreases in the edge region; on an other hand, the Hadronic Calorimeter energy increases.

[1] The ϕ range was determined to cover two inter-module regions.
[2] There is no X or Y vertex smearing for any events.
[3] Electrons not within 0.025 radians of the azimuthal edges.

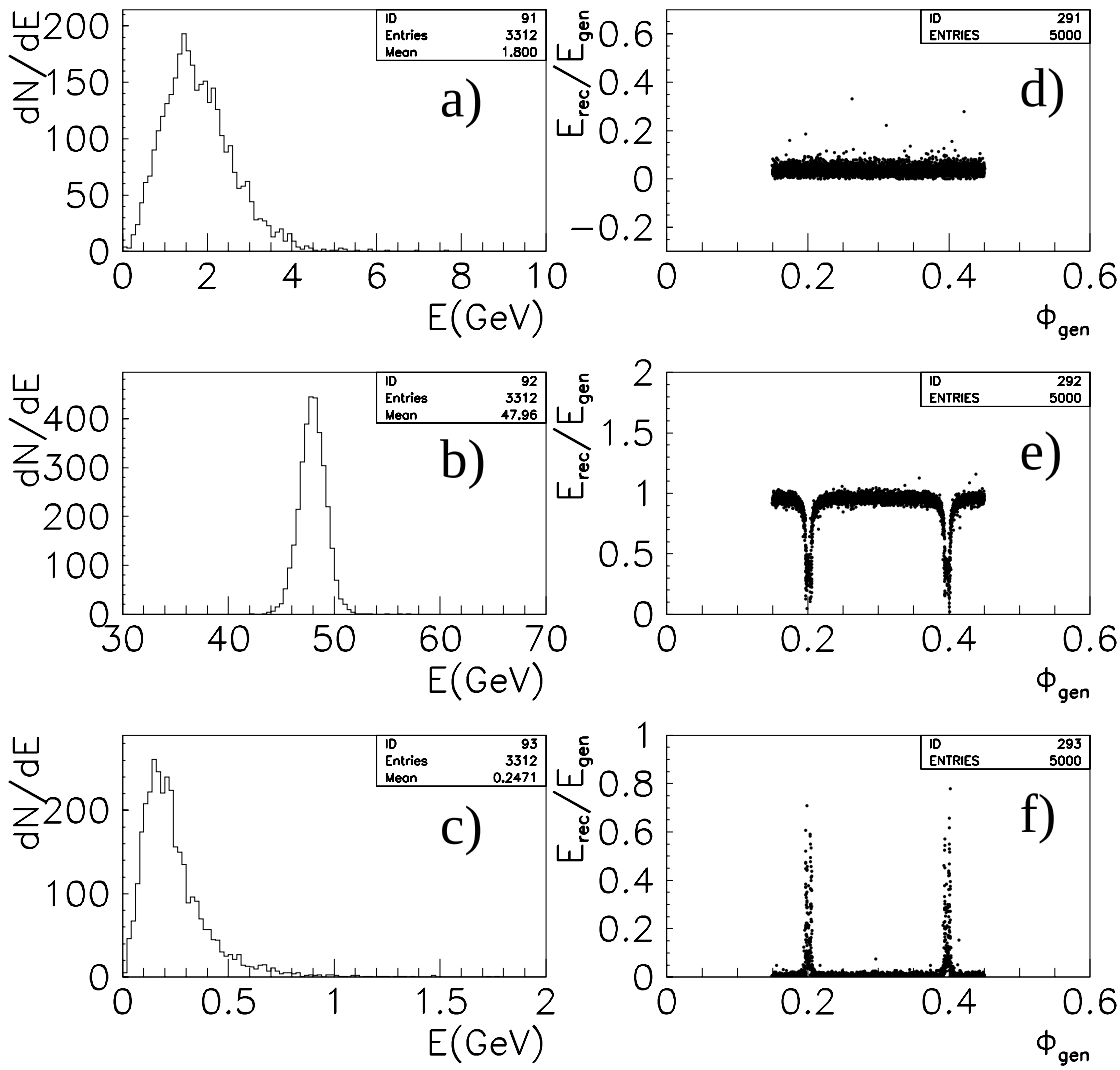

Figure 1: Energy distribution for a) Central Preshower, b) Electromagnetic Calorimeter and c) fine Hadronic Calorimeter for 50 GeV electrons not within 0.025 radians of the azimuthal edges; Reconstructed energy normalized to the generated energy (50 GeV in this case) as a function of ϕ_{gen} for d) Central Preshower, e) Electromagnetic Calorimeter and f) fine Hadronic Calorimeter.

3 Analysis method

In this section, we will investigate several "global correction" methods for the restoration of the energy of electrons near the central Electromagnetic Calorimeter edges, and one "correlation method" (using the correlations between the electromagnetic and hadronic calorimeter energies); the best results will be obtained with this last method. We will not use the generated ϕ information except to determine what we are calling the "edge events".

All the plots shown in this section have been made using 50 GeV electrons generated at $\eta = 0.05$, and in the following, we will call E_{EM} the reconstructed energy in the Central Preshower plus the reconstructed energy in the Electromagnetic Calorimeter, E_{HA} the reconstructed energy in the Fine Hadronic Calorimeter, and "edge events" all the events for which the ϕ generated value is contained in a $\Delta\phi = \pm 0.025$ radians window around the inter-module center.

3.1 Electromagnetic fraction of the energy

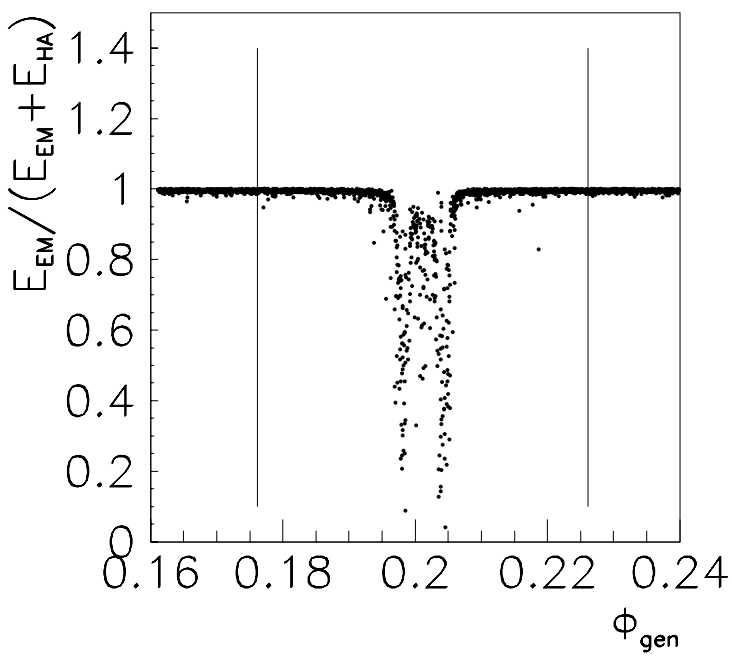

Figure 2: Electromagnetic fraction of the energy as a function of generated ϕ.

One important feature for the indentification of electromagnetic objects is the electromagnetic fraction of the total deposited energy. Figure 2 shows the

electromagnetic fraction of the energy as a function of generated ϕ in a window $\Delta\phi = \pm 0.04$ around the inter-module center. The window $\Delta\phi = \pm 0.025$ is represented by the two vertical lines. In this last window, only 14.4% of the events have an electromagnetic fraction smaller than 0.9. Because the $\Delta\phi = \pm 0.025$ window represents 25.5% of the 2π azimuthal coverage in the whole detector, only 25.5% $\times$ 14.4% = 3.7% have an electromagnetic fraction smaller than 0.9 due to edge effects. In a real analysis, one would apply this cut and then lose 3.7% of the events, but in our analysis, in order to understand all the effects, we will keep all the events.

3.2 Global method

A first approach, based on the fact that the calorimeter is compensated, is to compute the total electron energy as the sum of the subdetector energies, namely:

$$\mathrm{E}_{total} = \mathrm{E}_{EM} + \mathrm{E}_{HA}$$

where E_{EM} is the reconstructed energy in the Central Preshower plus the reconstructed energy in the Electromagnetic Calorimeter, and E_{HA} is the reconstructed energy in the Fine Hadronic Calorimeter. Such a method does not restore the entire energy as it can be seen on Figure 3c, meaning that part of the energy is definitely lost in the edge region.

In order to restore the lost energy, one can compute the total electron energy as the sum of the subdetectors energies multiplied by a global calibration factor:

$$\mathrm{E}_{total} = \alpha \times (\mathrm{E}_{EM} + \mathrm{E}_{HA})$$

where α is computed in such a way that the average total energy in the $\Delta\phi = \pm 0.025$ window around the inter-module center is equal to the average energy out of this window. In the present case, $\alpha = 1.12$. However, looking at Figure 3d, one can see that such a method does not restore correctly the lost energy.

Finaly, one can use the Hadronic Calorimeter energy only in order to restore the lost energy, meaning multiplying the Hadronic Calorimeter energy by a scaling factor. The total energy then becomes :

$$\mathrm{E}_{total} = \mathrm{E}_{EM} + \alpha \times \mathrm{E}_{HA}$$

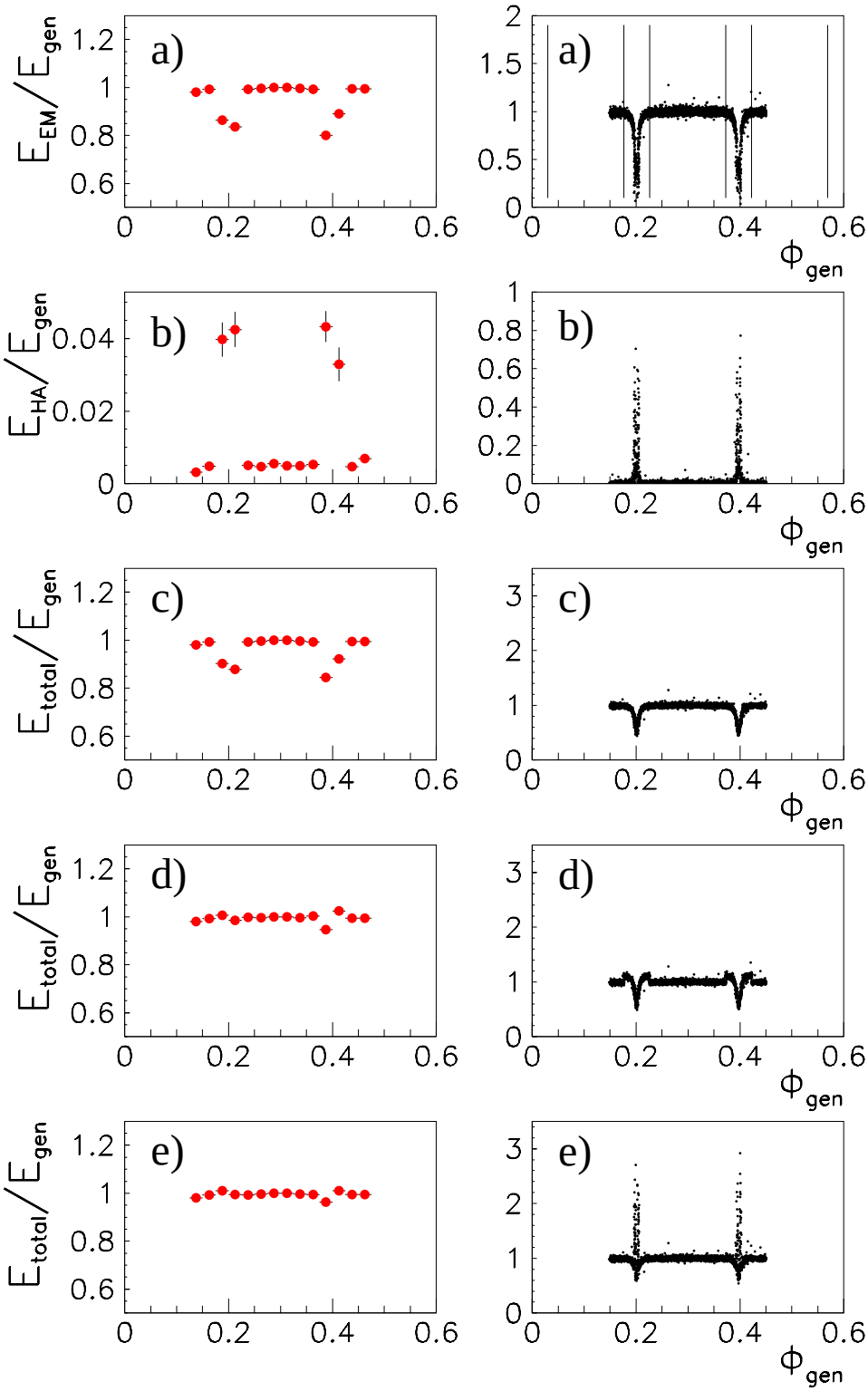

Figure 3: Normalized reconstructed energy a) E_{EM}, b) E_{HA}, c) E_{total}=E_{EM} + E_{HA}, d) E_{total}=1.12×(E_{EM}+E_{HA}), e) E_{total}=E_{EM}+3.73×E_{HA}; left plots are profile histograms, right plots are scatter plots.

The result of such correction can be seen in Figure 3e. By applying a scaling factor of 3.73, one can restore on average the initial electron energy, but, looking at the reconstructed energy *versus* ϕ distribution, one can see large fluctuations of the E_{total} energy, up to a factor 2.5 bigger than the correct value.

3.3 Correlation method

The results presented in the last section point out a complicated scenario for the energy deposition near edges. To figure out this scenario, one has to look at several correlations between "missing", electromagnetic and hadronic energies.

Figure 4a shows the correlation between the normalized missing energy (E_{miss}/E_{gen})[4] and the normalized hadronic energy (E_{HA}/E_{gen}). The line corresponds to the correction we have used in the previous section ($E_{gen} \equiv E_{total} = E_{EM}+3.73\times E_{HA}$). The points distributed around the line explain clearly why we get large fluctuations in Figure 3e. Figure 4a also exhibits three types of events:

- The first type (E_{HA}/E_{gen} close to 0) corresponds to the electrons which are interacting on the border of the Electromagnetic Calorimeter modules and develop a shower as standard electrons but deposit less energy in the sensitive regions.
- The second type of events (large value of E_{HA}/E_{gen}) correspond to electrons which are going through the edge region and develop a shower abnormaly [5].
- The third type of events is a mixture of the above two types of events.

In order to confirm these hypothesis and to apply the appropriate correction for each sample of events, we have used the generated ϕ information and looked at the E_{miss}/E_{gen} *versus* E_{HA}/E_{gen} energy distributions for the first two cases:

1. Events with a generated ϕ contained in the window $0.007 < |\Delta\phi| < 0.025$ (region (1) in Figure 4b; edge electrons which are interacting on the border of the Electromagnetic Calorimeter)
2. Events with a generated ϕ contained in the window $0.004 > |\Delta\phi|$ (regions (2) in Figure 4b; pure edge events).

[4] where E_{miss}=E_{gen}-E_{EM}

[5] Abnormaly means, as an example, showers which deposit most of their energy in the fourth electromagnetic layer

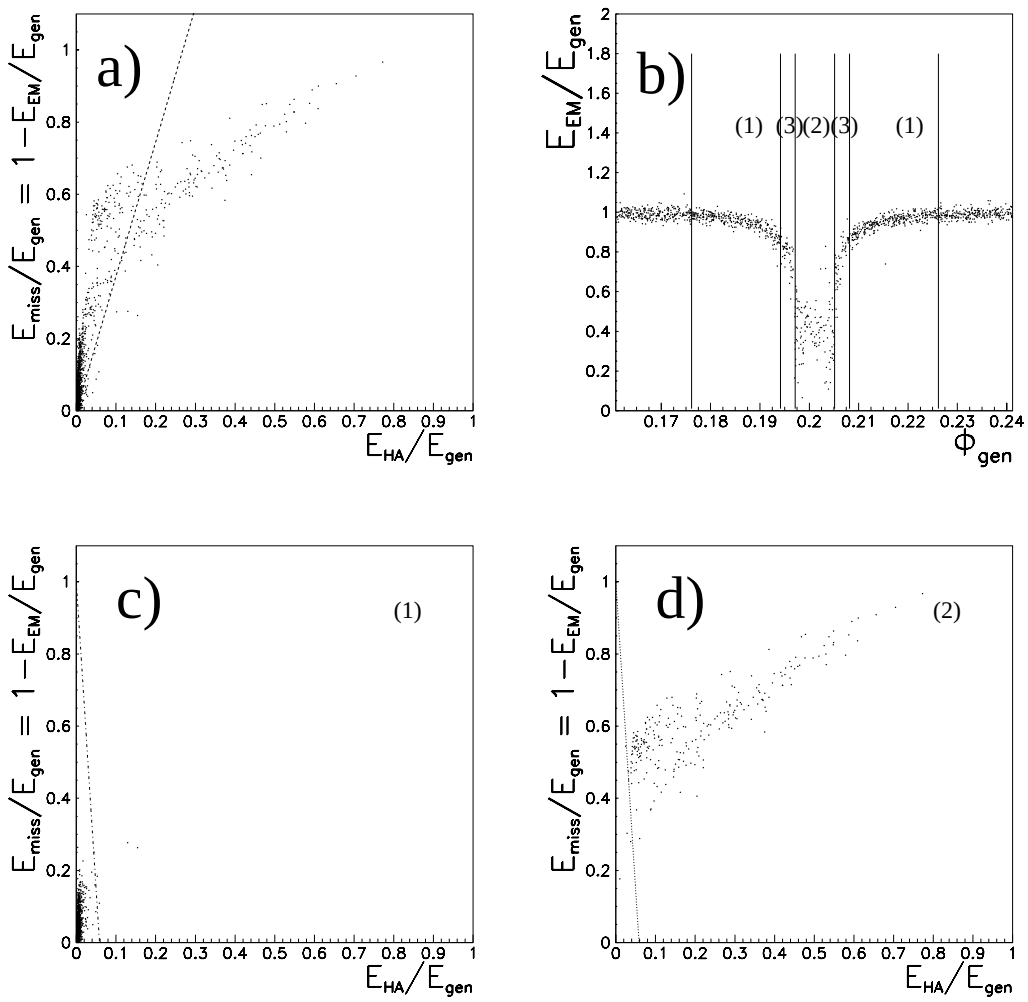

Figure 4: a) Normalized missing energy as a function of normalized hadronic energy; b) Normalized electromagnetic energy as a function of generated ϕ; c) Normalized missing energy as a function of normalized hadronic energy for events contained in the ϕ window (1) (see plot b)); d) Normalized missing energy as a function of normalized hadronic energy for events contained in the ϕ windows (2) (see plot b)).

Figures 4c and 4d show the correlation between the missing energy and the hadronic energy for both distributions. One can clearly see that most of the events from the sample $0.007 < |\Delta\phi| < 0.025$ have a small amount of missing energy, indicating that these events developed a standard shower. On an other hand, most of the events from the sample $0.004 > |\Delta\phi|$ exhibit a large amount of hadronic energy which indicate the development of a non standard shower.

We can easily separate both populations, without using the ϕ information, by applying a cut on the electromagnetic fraction of the energy $E_{EM}/(E_{EM}+E_{HA})$. The line in Figures 4c and 4d corresponds to $E_{EM}/(E_{EM}+E_{HA})=0.945$[6]. Thus most of the events with $E_{EM}/(E_{EM}+E_{HA})>0.945$ belong to the sample (1); most of the events with $E_{EM}/(E_{EM}+E_{HA})<0.945$ belong to the sample (2); events in sample (3) fall on both sides of the cut.

3.4 Energy corrections

Being able to separate both populations, we will now determine the appropriate corrections for each sample.

3.4.1 Case $E_{EM}/(E_{EM}+E_{HA})>0.945$

In this case, as can be seen in Figure 5a, the correlation between missing energy and normalized hadronic energy leads to the following correction function:

$$E_{miss}/E_{gen} = 8.4 \times E_{HA}/E_{gen}$$

and the total energy becomes:

$$\begin{aligned} E_{total} &\equiv E_{EM} + E_{miss} \\ &= E_{EM} + 8.4 \times E_{HA} \end{aligned}$$

[6] To determine this cut, one asks that the number of events of the population (1) which have $E_{EM}/(E_{EM}+E_{HA})<$ *cut* equals the number of events of the population (2) which have $E_{EM}/(E_{EM}+E_{HA})>$ *cut*.

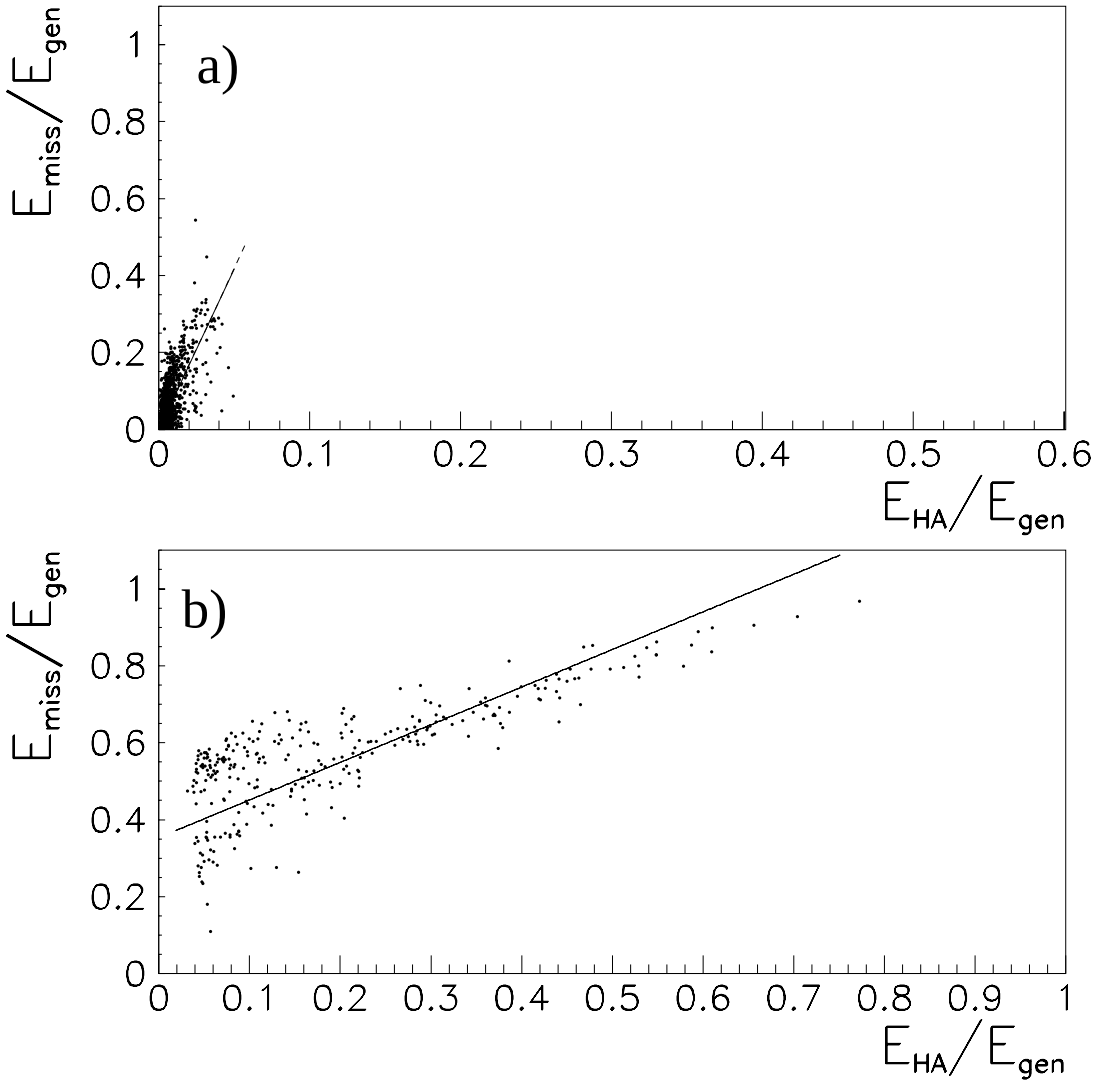

Figure 5: a) Normalized missing energy as a function of normalized hadronic energy for edge events ($0.025 > |\Delta\phi|$) with $E_{EM}/(E_{EM}+E_{HA})>0.945$; b) Normalized missing energy as a function of normalized hadronic energy for edge events ($0.025 > |\Delta\phi|$) with $E_{EM}/(E_{EM}+E_{HA})<0.945$.

3.4.2 Case $\mathbf{E}_{EM}/(\mathbf{E}_{EM}+\mathbf{E}_{HA})<0.945$

In this case, the correlation between missing energy and normalized hadronic energy can be expressed by the following formula (Figure 5b):

$$\mathrm{E}_{miss}/\mathrm{E}_{gen} = \alpha \times \mathrm{E}_{HA}/\mathrm{E}_{gen} + \beta$$

and the total energy (which we want to be equal to E_{gen}) becomes:

$$\begin{aligned} \mathrm{E}_{total} &\equiv \mathrm{E}_{EM} + \mathrm{E}_{miss} \\ &= \tfrac{1}{1-\beta}\mathrm{E}_{EM} + \tfrac{\alpha}{1-\beta}\mathrm{E}_{HA} \end{aligned}$$

Numerically, with $\alpha = 0.98$ and $\beta = 0.35$ coming from a fit to the Figure 5b data:

$$\mathrm{E}_{total} = 1.54 \times \mathrm{E}_{EM} + 1.51 \times \mathrm{E}_{HA}$$

As one can see from Figure 5b, the data distribution does not really follow a straight line. In order to reduce these fluctuations, we will use the energy correlations between the Central Preshower and Electromagnetic Calorimeter layers, and look at the events contained in the generated phi region $0.004 < |\Delta\phi| < 0.007$ (region (3) in Figures 4b and 6a) and $0.004 > |\Delta\phi|$ (region (2) in Figures 4b and 6a) separately.

Correlations:
In order to separate region (2) and region (3) event samples and to apply the appropriate correction, one can look at the fraction of the energy deposited in each layer. Figure 6b shows the fraction of the energy deposited in each layer for sample (3)[7], and Figure 6c the same distribution for sample (2); both plots are for $\mathrm{E}_{EM}/(\mathrm{E}_{EM}+\mathrm{E}_{HA})<0.945$. As we can see in these plots, the distributions are very different. Such a difference can be used to separate the populations. We use a function F defined as follow:

$$F(CPS = EM0, EM1, EM2, EM3, EM4) = \sum_{i=0}^{4} \frac{EM_i(2)}{EM_i(3)} EM_i \qquad (1)$$

where $\mathrm{EM}_i(2)$ is the layer i fraction of the energy for sample (2), $\mathrm{EM}_i(3)$ is the layer i fraction of the energy for sample (3), and EM_i is the layer i fraction

[7] layer number 0 corresponds to the Central Preshower, number 1 to the Electromagnetic Calorimeter layer 1, .., number 4 to the Electromagnetic Calorimeter layer 4, number 5 to the Hadronic Calorimeter layer 1.

of the energy for the actual event. The ratios $EM_i(2)/EM_i(3)$ are shown in Figure 6d. As it can be seen in Figure 6e, the F distribution separates both samples (sample (3) in dark dashed region; sample (2) in clear dashed region).

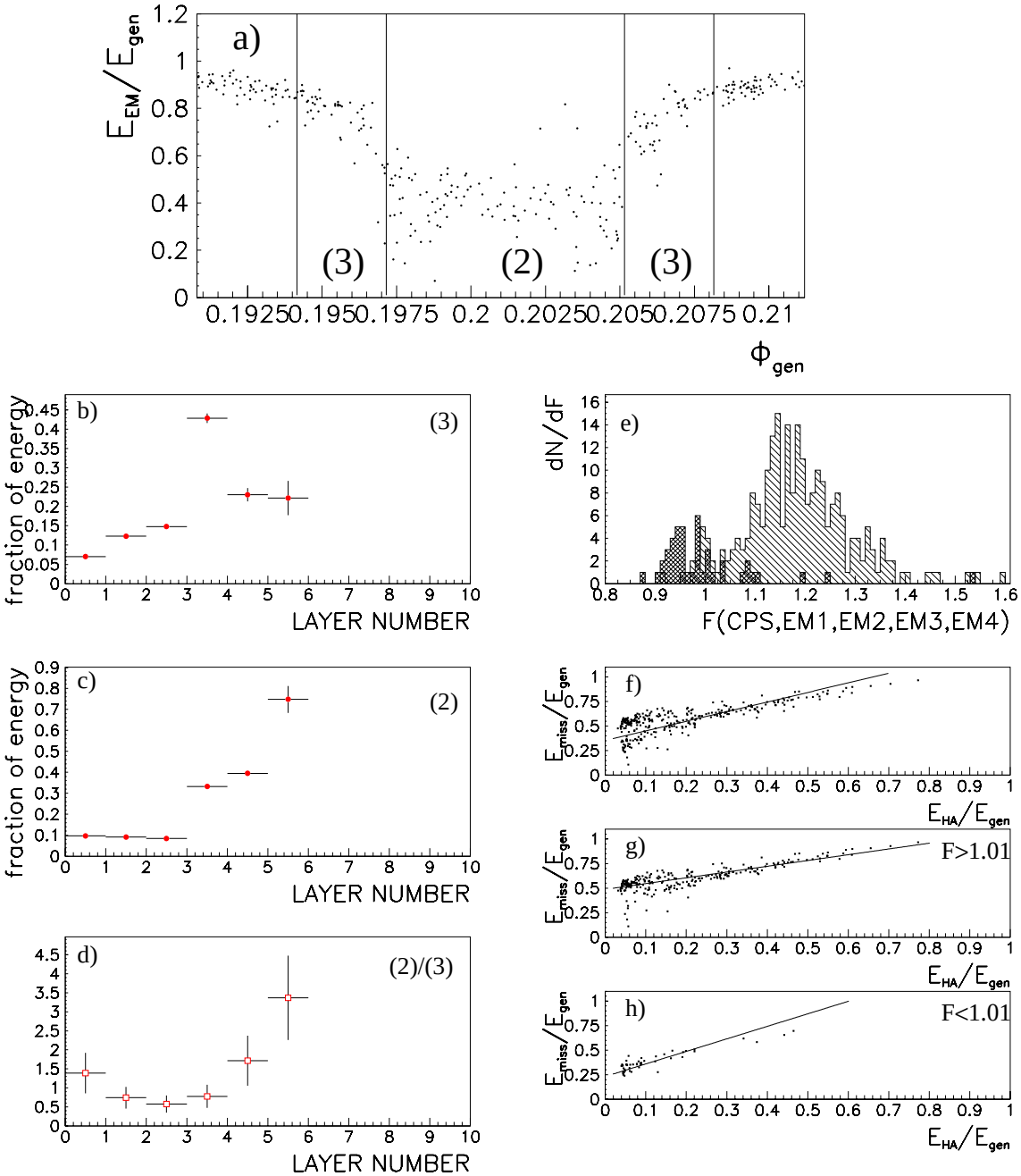

Figure 6: a) E_{EM}/E_{gen} as a function of generated ϕ; b) fraction of the energy in each layer for the sample (3); c) fraction of the energy in each layer for the sample (2); d) ratio of Figure c) to figure b); e) function F distribution; f) correlation between E_{miss}/E_{gen} and E_{HA}/E_{gen} for all events in Figure 5b; g) correlation between E_{miss}/E_{gen} and E_{HA}/E_{gen} for events in Figure 5b with F>1.01; h) correlation between E_{miss}/E_{gen} and E_{HA}/E_{gen} for events in Figure 5b with F<1.01.

Corrections:
A cut on the F value will allow us to select one or the other sample. Figure 6f shows the correlation between E_{miss}/E_{gen} and E_{HA}/E_{gen} for all the events in Figure 5b. Figure 6g shows the correlation between E_{miss}/E_{gen} and E_{HA}/E_{gen} for events in Figure 5b with F>1.01. One can see that using this cut, we get a better fit of the data[8]. For these events, the total energy becomes:

$$E_{total} = 1.95 \times E_{EM} + 1.15 \times E_{HA}$$

Figure 6h shows the correlation between E_{miss}/E_{gen} and E_{HA}/E_{gen} for events in Figure 5b with F<1.01. In that case, the total energy becomes:

$$E_{total} = 1.30 \times E_{EM} + 1.66 \times E_{HA}$$

3.5 Summary of the corrections in the correlation method

The cuts and corrections detailed in the previous section for the "correlation method", can be summarized by the following algorithm for 50 GeV electrons at η =0.05:

if $E_{EM}/(E_{EM} + E_{HA}) > 0.945$ **then** $E_{total} = E_{EM} + 8.4 \times E_{HA}$
if $E_{EM}/(E_{EM} + E_{HA}) < 0.945$ **then**
  if $F(EM0, .., EM4) < 1.01$ **then** $E_{total} = 1.30 \times E_{EM} + 1.66 \times E_{HA}$
  if $F(EM0, .., EM4) > 1.01$ **then** $E_{total} = 1.95 \times E_{EM} + 1.15 \times E_{HA}$

4 Results

In the following sections we present the results obtained with all the generated samples described in section 2.2.

4.1 Results for the 50 GeV sample

Figure 7 shows the results for the sample we have used in the previous section, namely, 50 GeV electrons generated at $\eta = 0.05$. In order to estimate the gain of the correlation method, we will compare it with the global correction method $E_{tot} = E_{EM} + 3.73 \times E_{HA}$ already presented in the section 3.2.

[8]Note that even with this new selection, one can see in Figure 6g residual fluctuations, especially for E_{HA}/E_{gen} close to 0.1.

Figure 7c shows the results after applying the correlation method (Section 3.5). Comparing to Figure 7b, which are the results after the global correction method, one can see that we are able to significantly reduce the large fluctuations in E_{total}/E_{gen}.

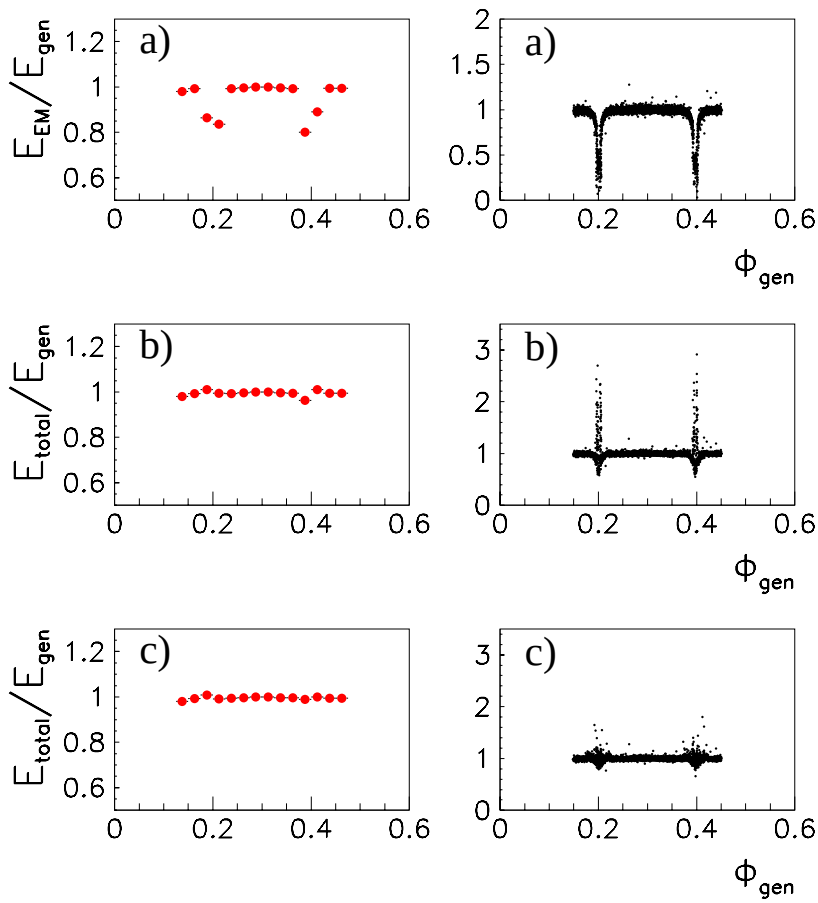

Figure 7: a) Normalised reconstructed energy E_{EM} as a function of generated ϕ; b) Normalized reconstructed energy after global correction method (E_{total}=E_{EM}+3.73×E_{EM}); c) Normalized reconstructed energy after correlation method (Section 3.5).

Quantitatively, Figures 8a, 8b, 8c, gives the energy distributions for non "edge events", "edge events" after the global correction method, and "edge events" after applying the correlation method. Comparing Figures 8b and 8c, one can observe a gain of a factor 3 on the RMS value between the global and correlation methods. The resolution (σ_E/E) is $37.2\%/\sqrt{E}$ for edge events after applying the correlation method, which is about 2.4 times worse than the $15.5\%/\sqrt{E}$ observed for the non "edge events". As a comparison, the

resolution using the central tracker system information would be close to $100\%/\sqrt{E}$ for P_T=50 GeV electrons [2] as it can be seen in Figure 9.
The same analysis has been done with 50 GeV electrons generated at η=0.05 with a smearing of the Z vertex (see table 2). We obtained the same results as the ones we got with the non Z vertex smearing sample.

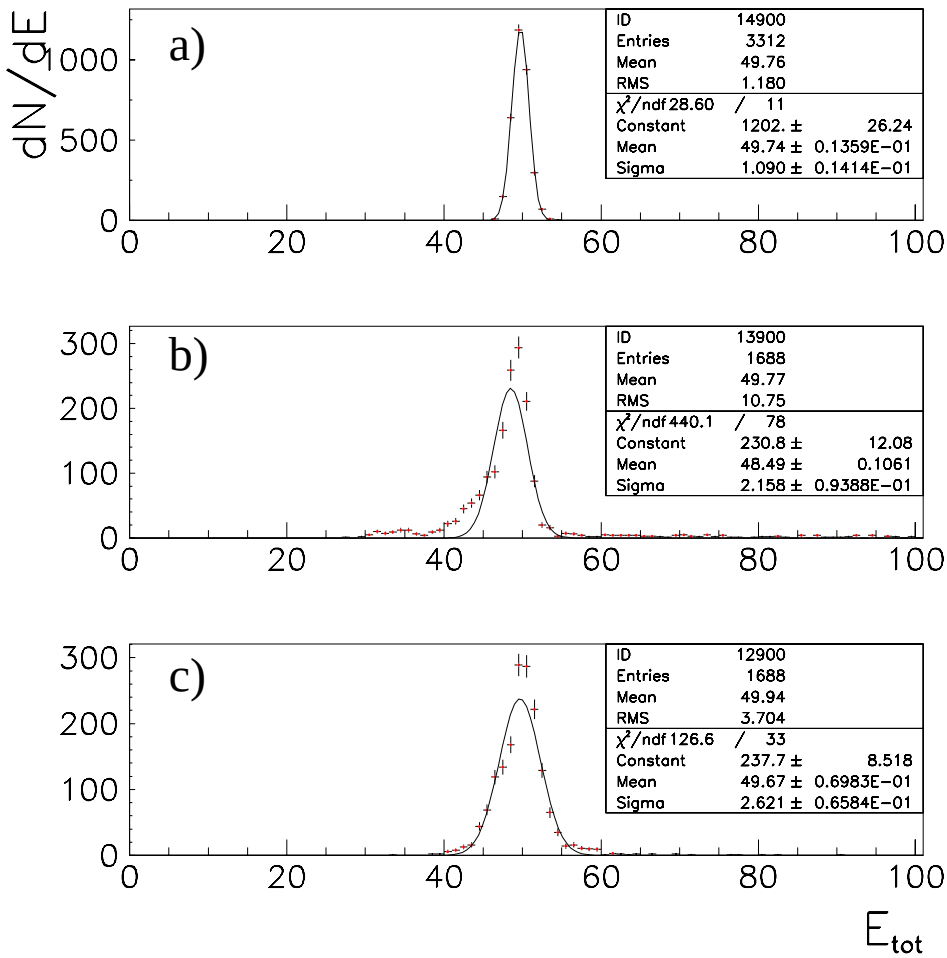

Figure 8: a) Energy distribution for non "edge events"; b) Energy distribution for "edge events" after global correction method; c) Energy distribution for "edge events" after correlation method.

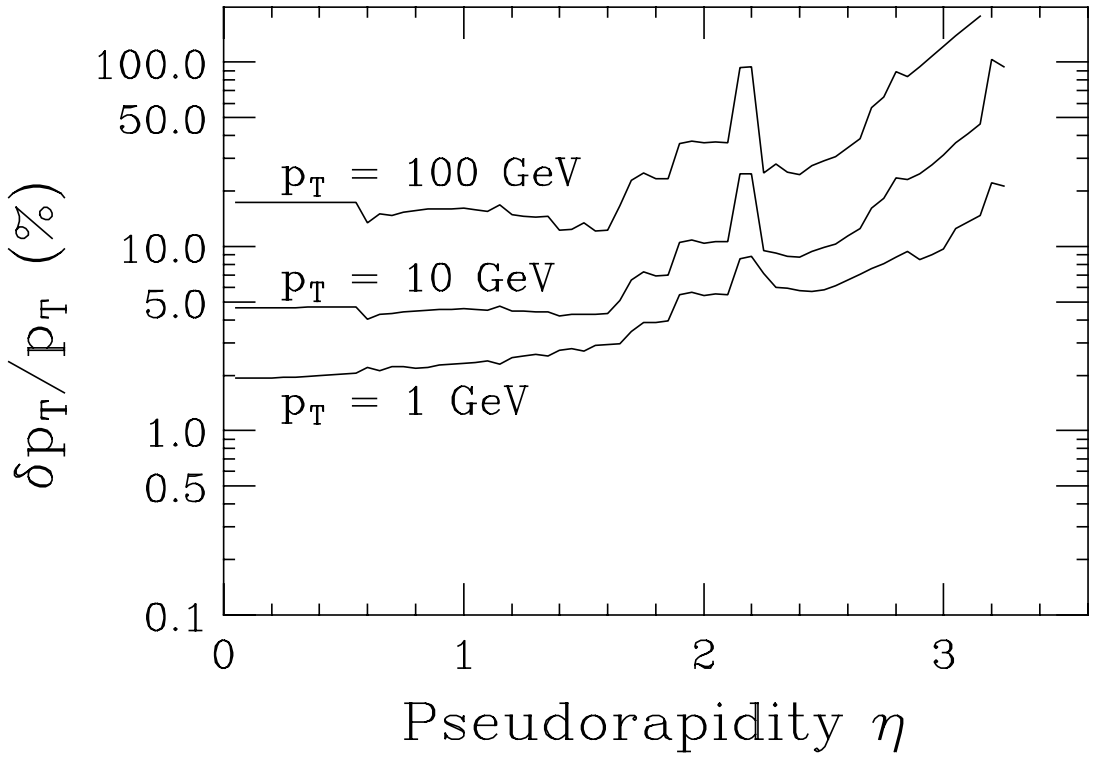

Figure 9: Charged particle momentum vs η for various P_T's [2].

4.2 Results as a function of energy

To be useful, a method for restoring lost energy must be efficient at any incident energy. We checked the quality of the method at several energy values by using the same set of parameters that was used for the 50 GeV sample. Figures 10 and 11 show the results for 20 GeV, 50 GeV, 100 GeV and 200 GeV electrons. In each case, the correlation method gives better results than the global method. Quantitatively, Figure 12 gives the resolution, the RMS and E_{total}/E_{gen} as a function of the energy. The resolution for the correlation method goes from $31\%/\sqrt{E}$ at E = 20 GeV to $83\%/\sqrt{E}$ at E = 200 GeV. At 100 GeV, we get $55\%/\sqrt{E}$, which is 4 times better than the resolution obtained by using the central tracker system information [2].

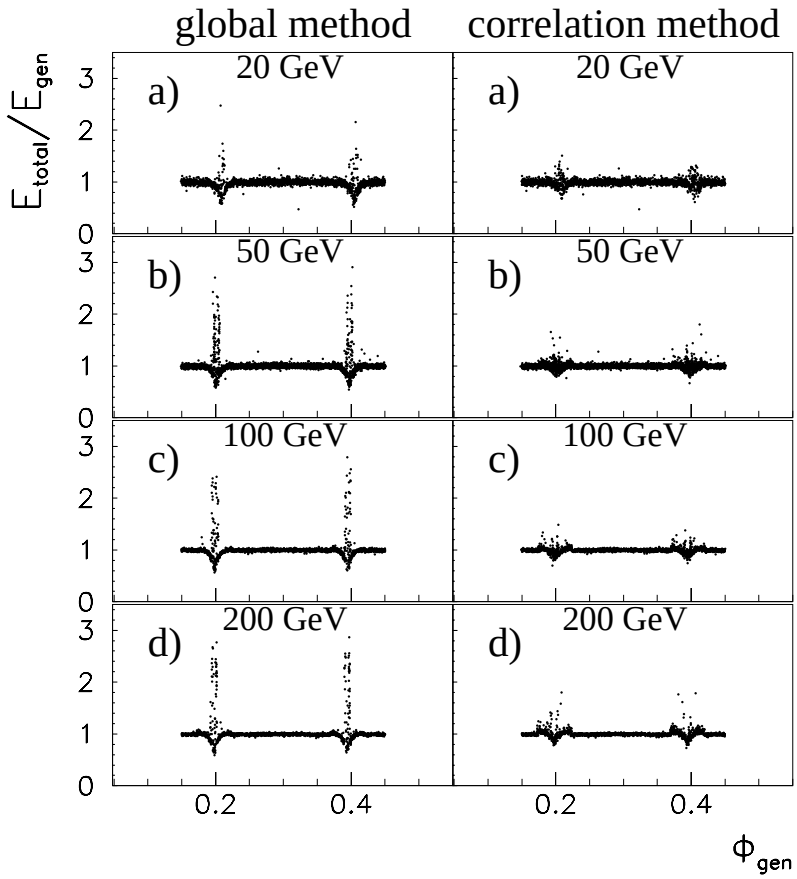

Figure 10: Left: normalized reconstructed energy after global correction method; Right: normalized reconstructed energy after correlation method; a) E = 20 GeV; b) E = 50 GeV; c) E = 100 GeV; d) E = 200 GeV;

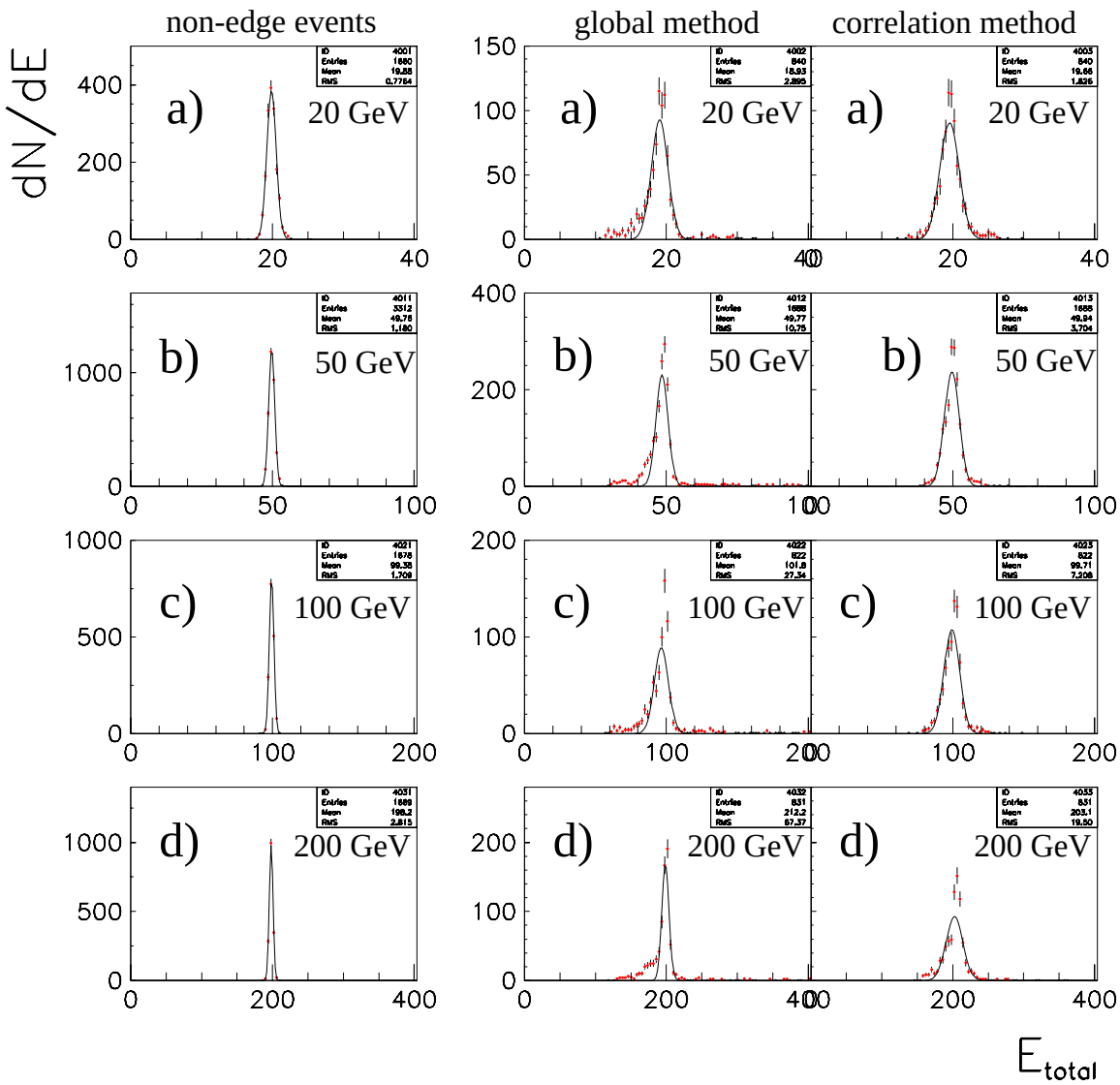

Figure 11: Left: energy distribution for non "edge events"; Middle: energy distribution for "edge events" after global correction method; Right: energy distribution for "edge events" after correlation method; a) E = 20 GeV; b) E = 50 GeV; c) E = 100 GeV; d) E = 200 GeV.

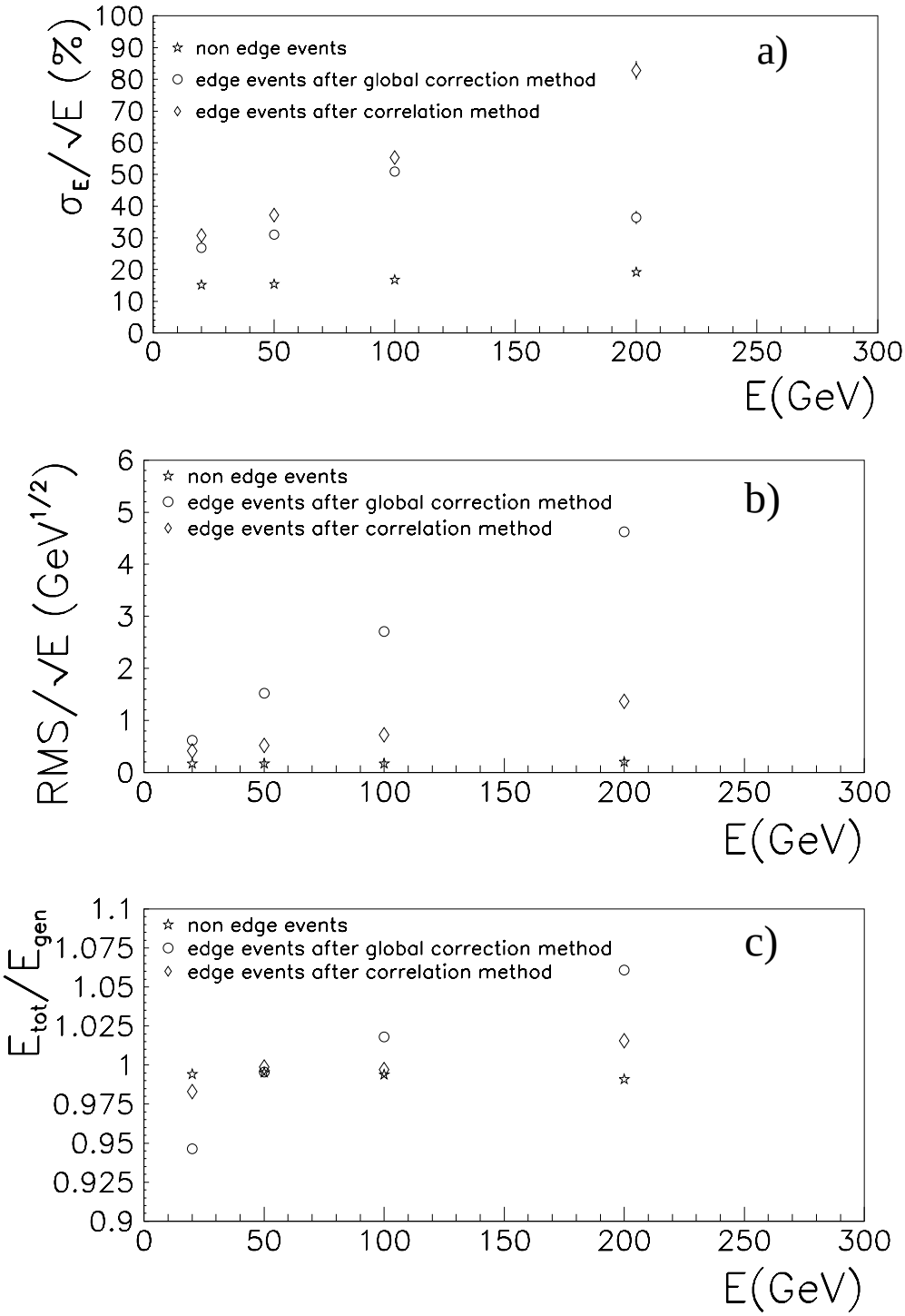

Figure 12: a) Resolution as a function of the energy (the low value at E = 200 GeV for edge events after global correction method is due to the bad quality of the fit, but is not representative of a physical effect); b) RMS as a function of the energy; c) E_{tot}/E_{gen} as a function of the energy.

4.3 Results as a function of η

In order to check the quality of the method at different rapidities, we generated 50 GeV electron samples at several η values. In each case, the parameters of the correction methods were recomputed in order to get the best results.

Figure 13 and 14 give the results obtained at $\eta = 0.05$, 0.25, 0.55, 0.75 and 0.95. In all cases, the correlation method gives a better result than the global method. Quantitatively, as can be seen from Figure 15, the resolution goes from $37\%/\sqrt{E}$ at η=0.05 to $47\%/\sqrt{E}$ at η=0.95.

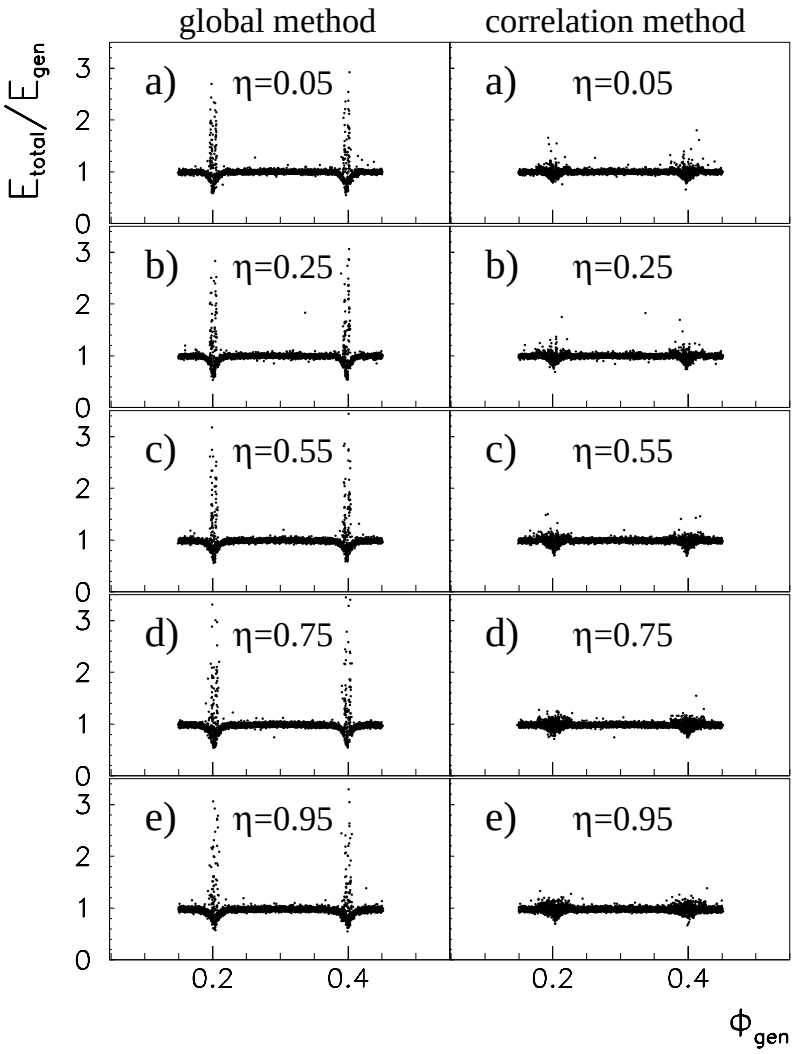

Figure 13: Left: normalized reconstructed energy after global correction method; Right: normalized reconstructed energy after correlation method; a) $\eta = 0.05$; b) $\eta = 0.25$; c) $\eta = 0.55$; d) $\eta = 0.75$; e) $\eta = 0.95$;

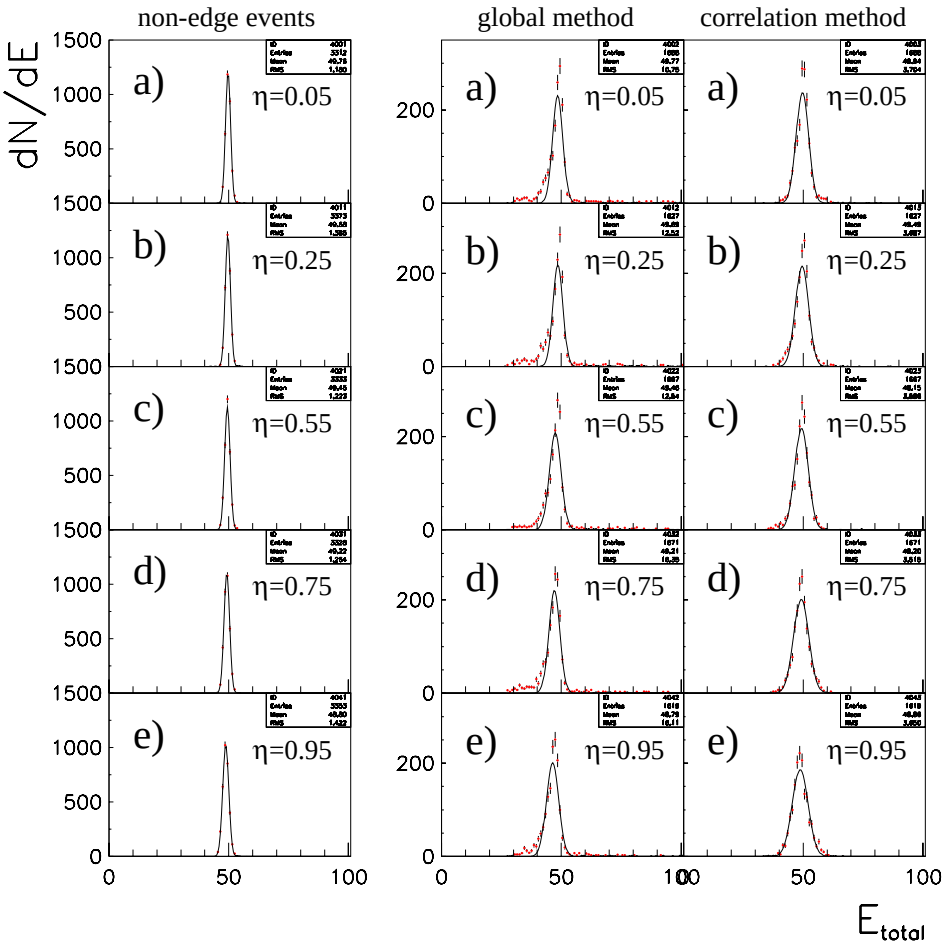

Figure 14: Left: energy distribution for non "edge events"; Middle: energy distribution for "edge events" after global correction method; Right: energy distribution for "edge events" after correlation method; a) $\eta = 0.05$; b) $\eta = 0.25$; c) $\eta = 0.55$; d) $\eta = 0.75$; e) $\eta = 0.95$.

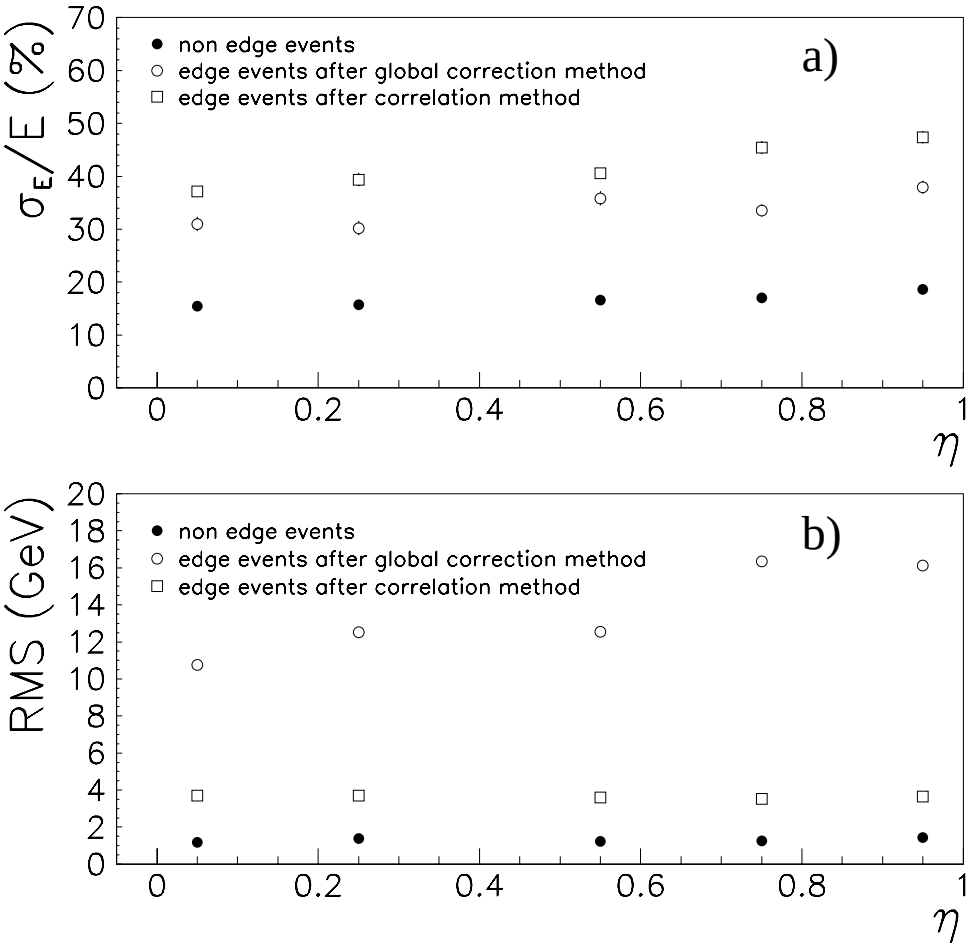

Figure 15: a) Resolution as a function of η; b) RMS as a function of η.

4.4 Remarks

The analysis and the results obtained in the previous sections have been obtained by using all the Monte-Carlo events, without any cut on the electromagnetic fraction of the total measured energy.

In this section we show the results obtained with the two global correction methods and the correlation method for 50 GeV electrons generated at η=0.05 (without any vertex smearing) which pass the cut $E_{EM} > 0.9 \times (E_{EM} + E_{HA})$.

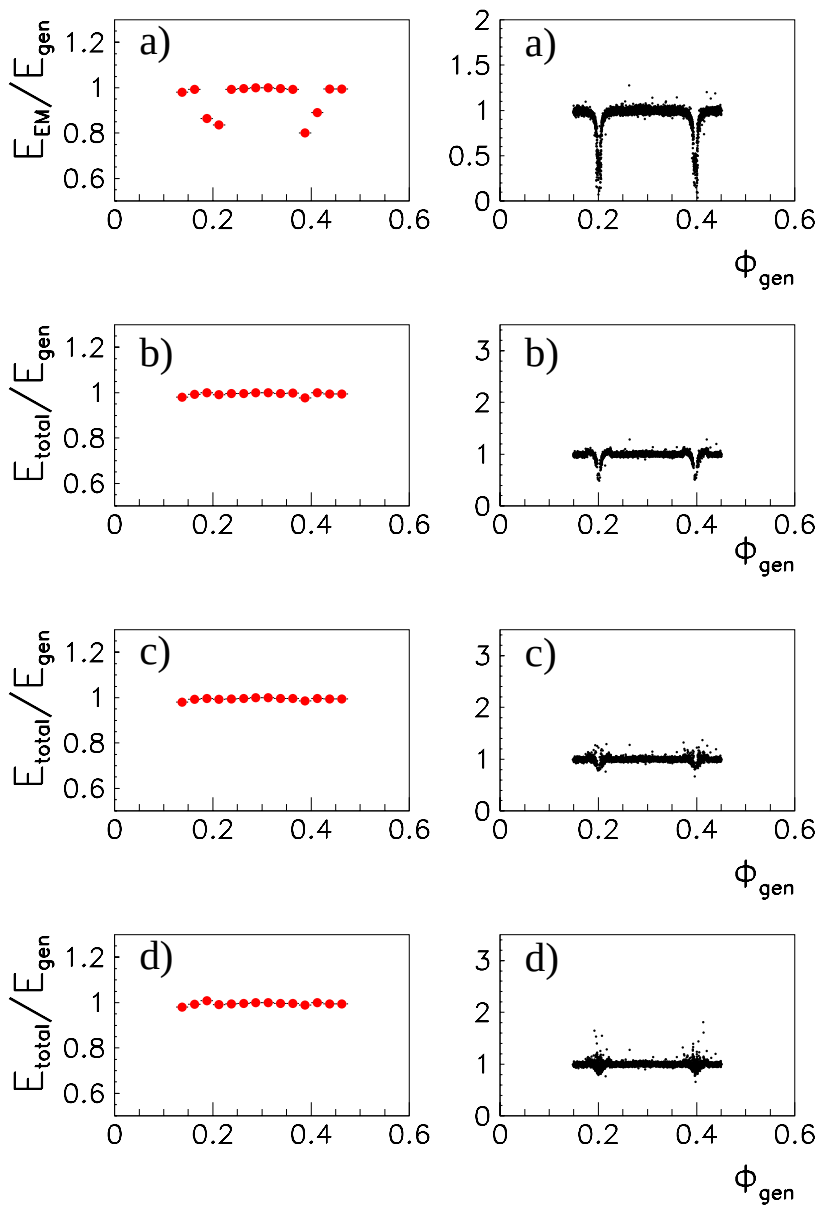

Figure 16: Normalised reconstructed energy a) E_{EM}, b) $E_{tot} = 1.07 \times (E_{EM} + E_{HA})$, c) $E_{tot} = E_{EM} + 8.33 \times E_{HA}$, d) correlation method, as a function of generated ϕ; lefts plots are profile histograms, right plots are scatter plots.

As we can see in Figure 16b, the global correction method $E_{tot} = 1.07 \times (E_{EM} + E_{HA})$ does not restore correctly the energy lost in the edge regions. On the other hand, in contrast with Section 3.2, the correction method $E_{tot} = E_{EM} + 8.33 \times E_{HA}$ gives results as good as the ones obtained with the "correlation method". This is confirmed by the results shown in Figure 17 where one can see comparable resolutions and RMS values for both methods. In fact, most of the events contained in the ϕ regions (2) and (3) of Figure

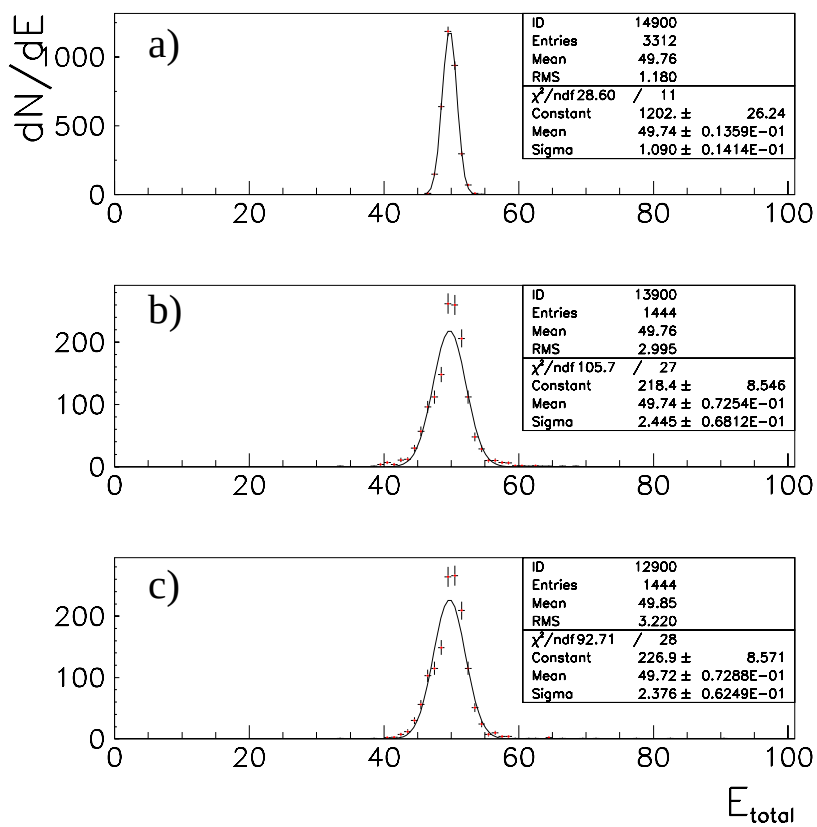

Figure 17: a) Energy distribution for non "edge events"; b) Energy distribution for "edge events" after global correction method $E_{tot} = E_{EM} + 8.33 \times E_{HA}$; c) Energy distribution for "edge events" after correlation method.

6 do not pass the cut on the electromagnetic fraction of the total energy. If one uses different calibration weights, the results might be different.

5 Conclusion

The study of edge electrons exhibits two different samples of events. The first sample contains electrons which are interacting on the border of Electromagnetic Calorimeter module, developping a standard shape shower, but depositing less energy because of non instrumented edge regions. The second sample contains electrons which are interacting between two Electromagnetic Calorimeter modules, developping a non standard shape shower.

We have shown that a cut on the electromagnetic fraction of the deposited energy can separate both populations, and, by using appropriate correlations, we are able to restore the energy lost by electrons in edge regions. The resolution for such corrected events goes from $37\%/\sqrt{E}$ to $47\%/\sqrt{E}$ for 50 GeV electrons at η=0.05 and η=0.95, and from $31\%/\sqrt{E}$ to $83\%/\sqrt{E}$ for electrons at 20 and 200 GeV at η=0.05, which is better than the one gets with the central tracker system for incident energies greater than 20-30 GeV.

Finally, we tested this method with MC events only. Considering that the detector is probably not perfectly described in the edge regions, we think that a cross-check analysis using real data (20 GeV electrons as an example) will be needed to confirm the quality of the correlation method.

Acknowledgements

I would like to thank Ron Madaras for fruitful discussions during this study and for his help in finalizing this note.

References

[1] K.M. chan, M. Zielinski, V. Zutshi, d0note 3716.

[2] The D0 upgrade, Fermilab Pub-96/357-E (Figure 16).

Low Energy Electron Identification in D0

F. Fleuret

Laboratoire de Physique Nucléaire et de Hautes Energies, Paris, FRANCE

Lawrence Berkeley National Laboratory, CA, USA

May 29, 2001

Abstract

A new method for electron identification is presented. This method is based on tracks, preshower clusters and calorimeter tower information and is used as part of the SEMReco package.

Contents

1 Introduction **2**

2 Method **2**

3 Matching criteria **3**

3.1 Samples 3

3.2 Track-PS cluster matching 3

3.3 Track-EM tower matching 6

4 Results for $Z \to b\bar{b}$ events **8**

4.1 Samples 8

4.2 Track-PS matching 9

4.3 Track-EM tower matching 11

4.3.1 With 0.5 EM fraction cut 13

4.3.2 With 0.8 EM fraction cut 14

4.3.3 With 0.99 EM fraction cut 15

4.4 Overall performance 16

4.4.1 No EM fraction cut 17

4.4.2 With 0.5 EM fraction cut 18

4.4.3 With 0.8 EM fraction cut 19

4.4.4 With 0.99 EM fraction cut 20

4.5 Performance summary 21

5 Conclusion **21**

1 Introduction

The standard electron reconstruction algorithm is based on isolated electromagnetic calorimeter cluster finding. Due to the isolation constraint, many non-isolated (mainly low energy) electrons are not found by this algorithm.

In this note, we propose a new method to find such electrons. This new method takes advantage of the new D0 tracking system and the new preshower system [1].

In the following, after having presented the principle of this new method, we define some identification *criteria* and show some results obtained with a sample of $Z \to b\overline{b}$ events.

2 Method

As mentioned in the previous section, the standard reconstruction algorithm (EMReco) proceeds in three steps:

1. find isolated electromagnetic calorimeter clusters.
2. find matching preshower cluster for each electromagnetic calorimeter cluster.
3. find matching track for each electromagnetic calorimeter cluster.

For non-isolated (mostly low energy) electrons, electromagnetic calorimeter clusters are almost never found because of the isolation *criterium*. Indeed, isolation is computed as the *ratio* $(E_{tot} - E_{core})/E_{core}$ where E_{core} is the electromagnetic tower energy in a (η, ϕ) circle of radius 0.2 and centered on the cluster's highest P_T tower, and E_{tot} is the overall (EM + hadronic) tower energy in a (η, ϕ) circle of radius 0.4 and centered on the cluster's highest P_T tower. Usually a cluster is tagged as electromagnetic if its isolation is lower than 0.2.

For non-isolated (low energy) electrons, due to the hadronic environment, E_{tot} contains energy from both electrons and surrounding hadrons; isolation thus becomes greater than 0.2 and the electron is not found.

We propose, taking advantage of the new D0 tracking system [1], starting electron identification with reconstructed tracks, to proceed in three steps, in the reverse order compared to the standard electron reconstruction algorithm, as illustrated in Figure 1:

1. find tracks.

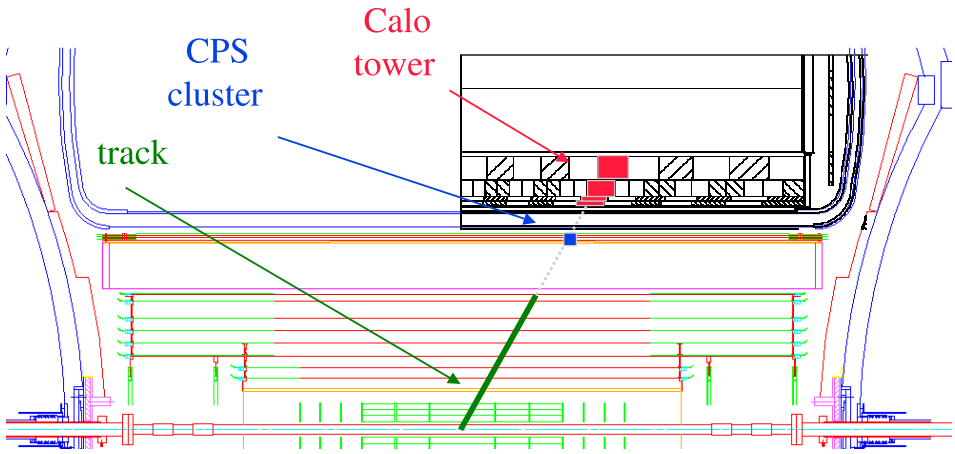

Figure 1: The D0 detector.

2. find matching preshower cluster for each track.

3. find matching calorimeter tower for each track.

The last two steps are used to reduce the amount of fake electrons. They require one to define matching *criteria*. This is done in the next section.

3 Matching criteria

3.1 Samples

In order to define matching *criteria*, we have used single electron samples generated and reconstructed within the D0 framework.

Five single electron samples (P_T = 3, 4, 5, 10 and 20 GeV) have been used, all generated in the central detector region, with vertex smearing $\sigma_x = \sigma_y = 1.0$ cm and $\sigma_z = 28.0$ cm.

3.2 Track-PS cluster matching

In order to determine the appropriate track-PS matching window we define the variables

- $\Delta\eta = \eta_{PS} - \eta_{track}$ where η_{PS} and η_{track} are respectively preshower cluster and track η positions.

- $\Delta\phi = \phi_{PS} - \phi_{track}$ where ϕ_{PS} and ϕ_{track} are respectively preshower cluster and track ϕ positions.

The goal of this section is to determine what window size should be used to match tracks with PS clusters. Before doing so, a correction must be applied to the ϕ_{track} value. Indeed, due to the 2T magnetic field inside the tracking system, the track ϕ direction at the vertex and the track ϕ direction at the preshower are different. Figure 2 shows $\Delta\phi$ distributions for the five single electron samples. In order to take this effect into account, we applied

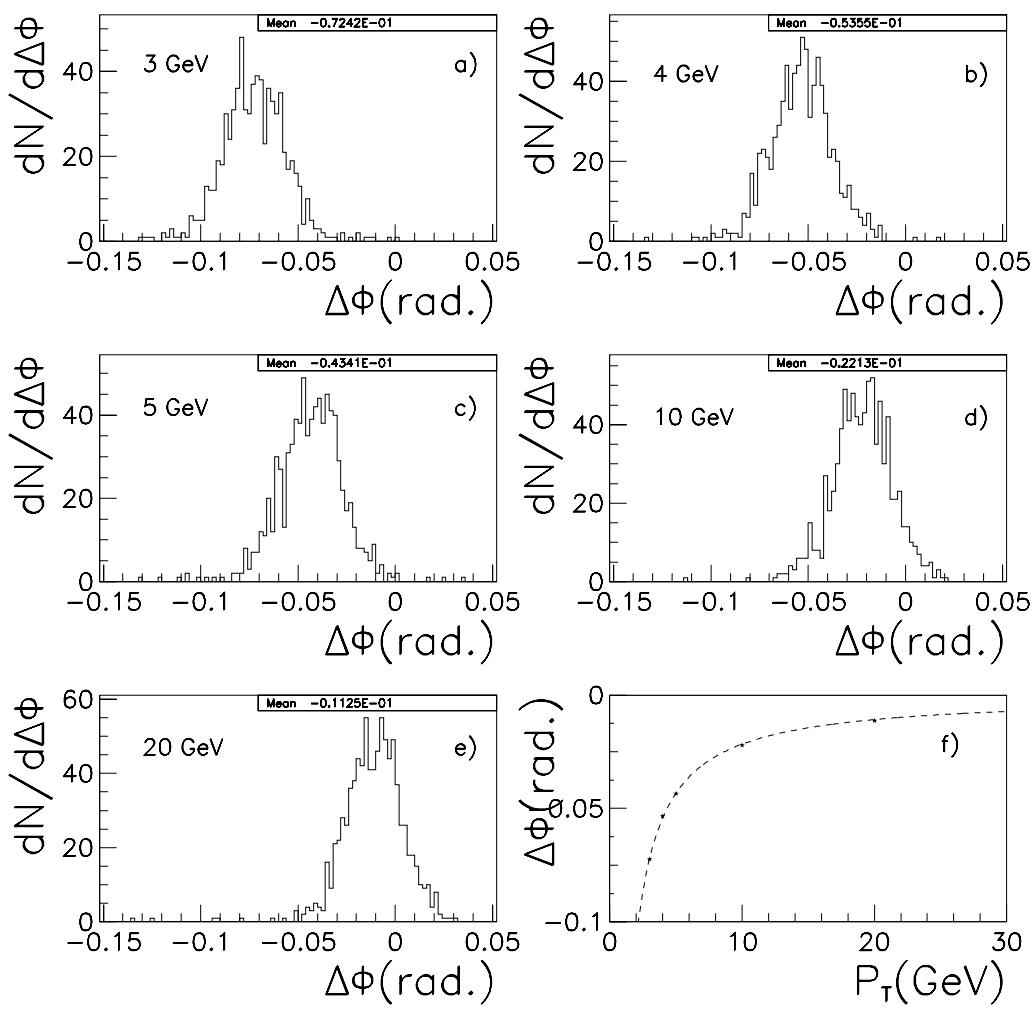

Figure 2: a) to e) $\Delta\phi$ distribution for (respectively) P_T = 3, 4, 5, 10 and 20 GeV single electrons. f) $\Delta\phi$ as a function of P_T; the fit has been obtained with equation (1).

a correction to the ϕ preshower cluster position. As shown in Figure 2, this

correction is a function of electron P_T:

$$\phi_{corrected} = \phi_{PS} - C_{PS}\frac{q}{P_T} \tag{1}$$

where q is the particle's charge and C_{PS} is the correction factor. A fit to the data gives $C_{PS} = 0.21657 \pm 0.00004$ (rad.GeV).
Figure 3 shows the $\Delta\phi \times \Delta\eta$ distributions for the 3, 4, 5, 10 and 20 GeV electrons after ϕ corrections. On average, almost 95% of the preshower clus-

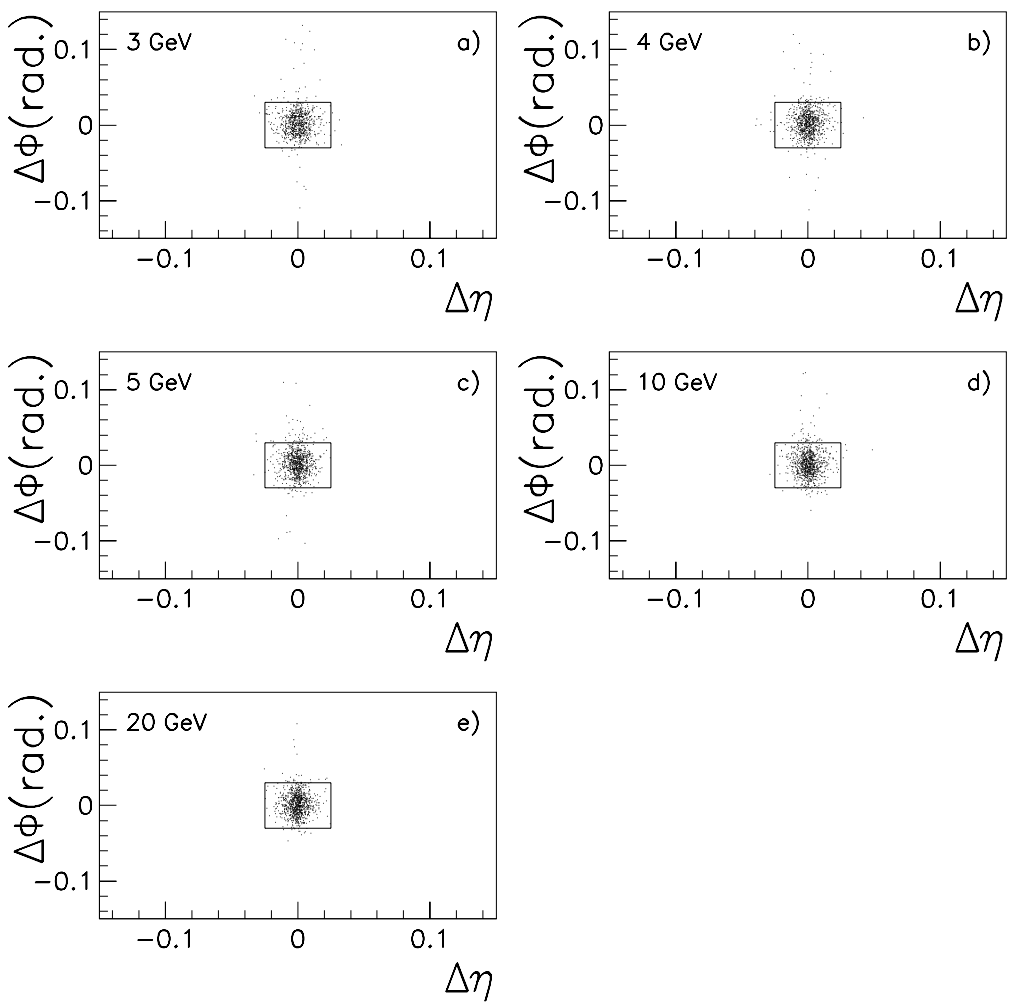

Figure 3: $\Delta\eta \times \Delta\phi$ distributions for (respectively) 3, 4, 5, 10 and 20 GeV single electrons. The window contains 94% of preshower clusters at 3 GeV, 93% at 4 GeV, 92% at 5 GeV, 93% at 10 GeV and 95% at 20 GeV.

ters match the associated track in a $\Delta\phi \times \Delta\eta = 0.03 \times 0.025$ window. This window will be used in the following to match tracks with preshower clusters.

3.3 Track-EM tower matching

The determination of the matching track-EM window follows the same pattern as in 3.2. We define $\Delta\phi = \phi_{EM} - \phi_{track}$ and $\Delta\eta = \eta_{EM} - \eta_{track}$.

As above, we first apply a ϕ correction to take the 2T magnetic field effects

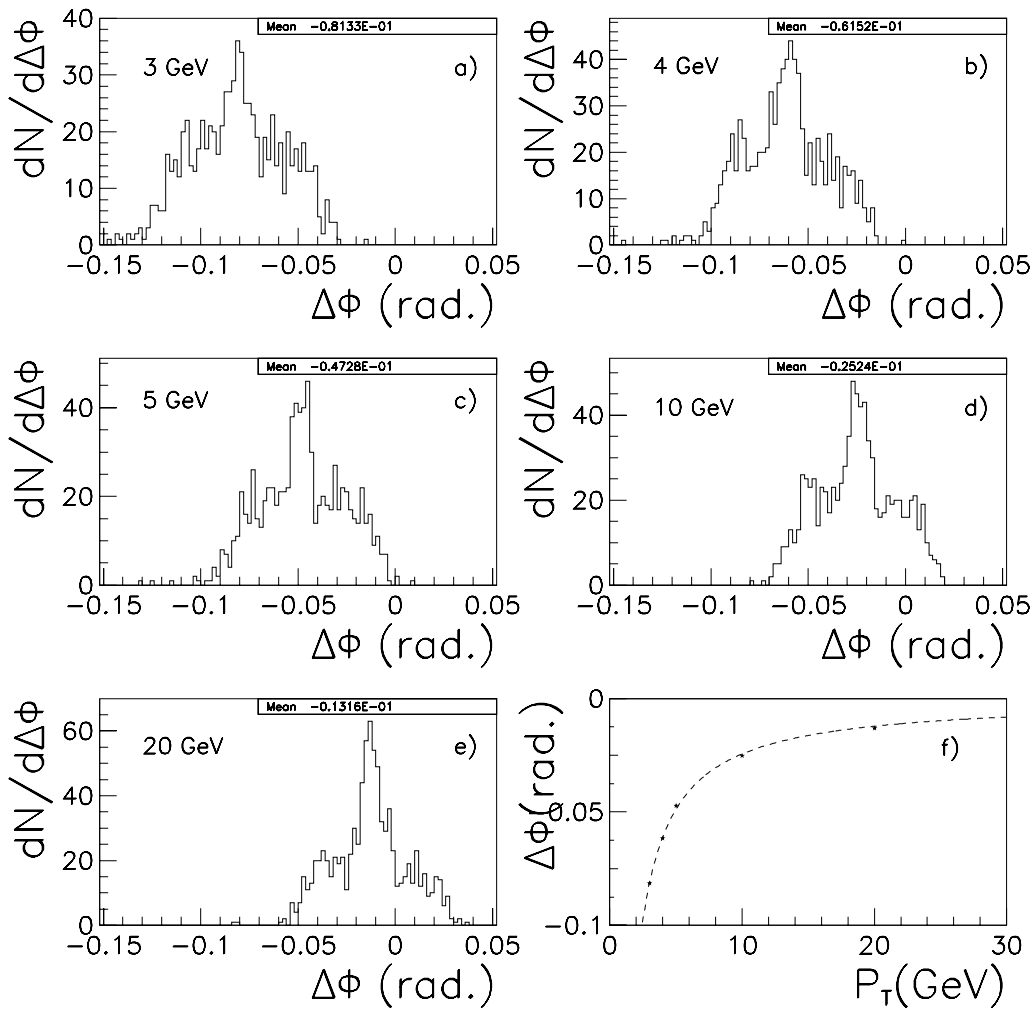

Figure 4: a) to e) $\Delta\phi$ distribution for (respectively) P_T = 3, 4, 5, 10 and 20 GeV single electrons. f) $\Delta\phi$ as a function of P_T; the fit has been obtained with equation (2).

into account. Figure 4 shows the $\Delta\phi$ distributions for the five single electron samples and exhibits shifts as a function of P_T. The correction function is in this case:

$$\phi_{corrected} = \phi_{EM} - C_{EM}\frac{q}{P_T} \tag{2}$$

where a fit to the data gives $C_{EM} = 0.24418 \pm 0.00006$ (rad.GeV). This value is slightly different than the one obtained for the track-PS matching; indeed, the calorimeter, being farther from the vertex than the preshower, requires a bigger correction even if the magnetic field effects occur in the tracking system only. Figure 5 shows the $\Delta\phi \times \Delta\eta$ distributions for 3, 4, 5, 10 and 20 GeV electrons after ϕ corrections. On average, more than 95% of the calorimeter towers match the associated track in a $\Delta\phi \times \Delta\eta = 0.045 \times 0.05$ window. This window will be used in the following to match tracks with calorimeter towers.

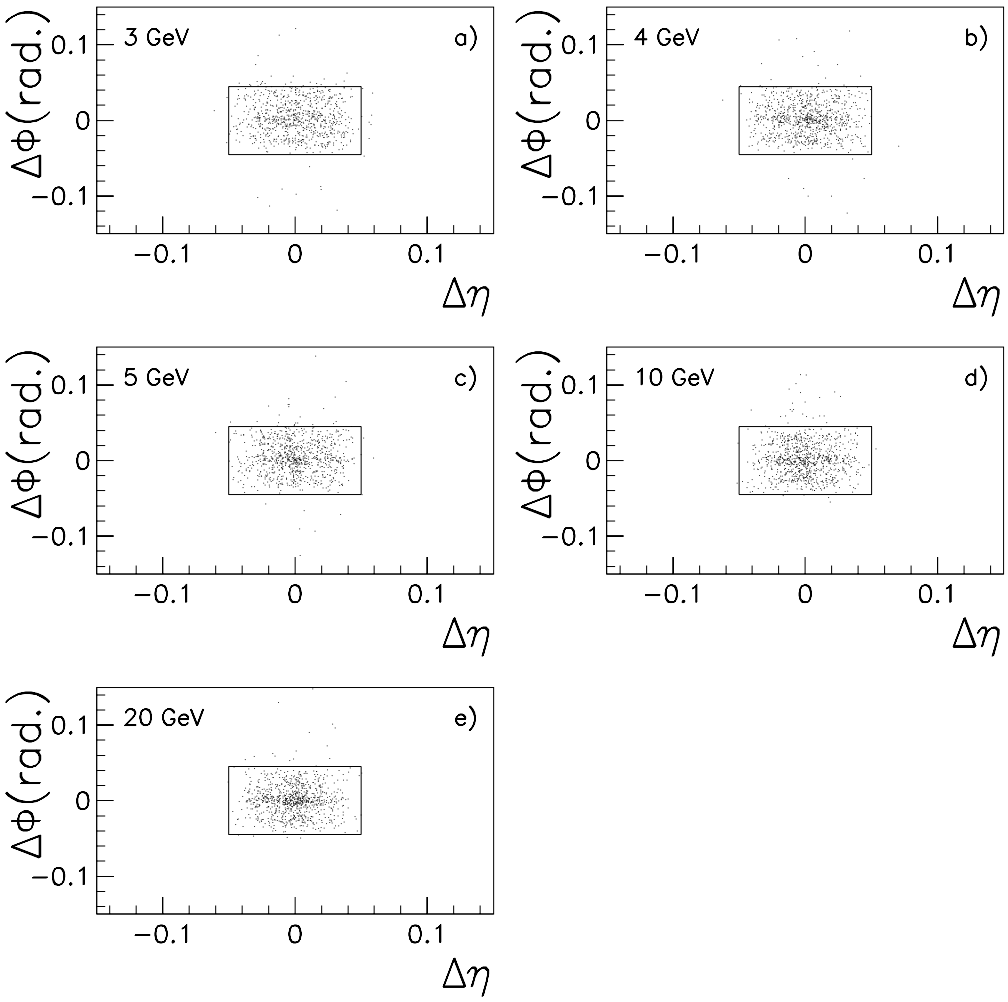

Figure 5: $\Delta\eta \times \Delta\phi$ distributions for (respectively) 3, 4, 5, 10 and 20 GeV single electrons. The window contains 95% of calorimeter towers at 3GeV, 97% at 4 GeV, 96% at 5 GeV, 96% at 10 GeV and 97% at 20 GeV.

4 Results for $Z \to b\bar{b}$ events

In this section, we'll test the matching *criteria* defined in the previous section.

4.1 Samples

In order to test the matching *criteria* we used a sample of 1600 $Z \to b\bar{b}$ events with no minimum bias events and at least one low energy electron produced per event. The events have been generated with a vertex smearing $\sigma_x = \sigma_y = 0$ cm and $\sigma_z = 28.0$ cm.

In the following we'll consider events with electrons hitting the central calorimeter only. This leads to a final number of 529 events. Figure 6 shows the P_T

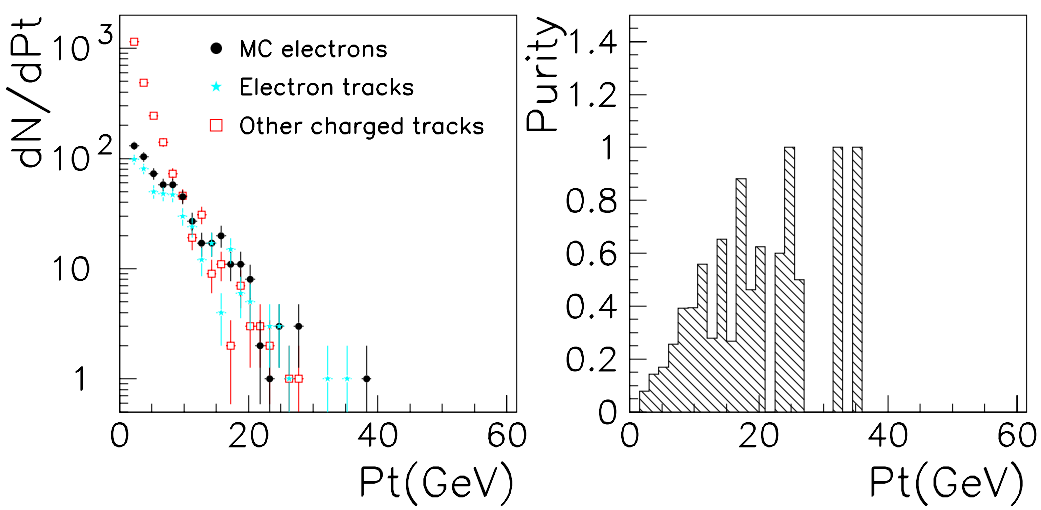

Figure 6: *Left plot:* P_T distribution of MC electrons, electron tracks (i.e. tracks matching a MC electron) and other charged particles. *Right plot:* electron identification purity as a function of P_T.

distribution (left plot) of MC electrons (dots), of tracks matching a MC electron[1] (stars), and of other tracks (squares) coming from other charged particles.

[1] In order to find the generated particle associated to a track, a match is made between reconstructed tracks and MC particle direction. The window size used is $\Delta\eta \times \Delta\phi = 0.008 \times 0.008$.

According to this, the tracking efficiency can be computed using the *ratio*:

$$\varepsilon_{track} = \frac{N_{eT}}{N_e} \tag{3}$$

where N_{eT} is the number of tracks matching a MC electron and N_e is the number of MC electrons. Numerically one finds $(76 \pm 4)\%$ efficiency for track matching.

Figure 6 also shows purity (right plot) as a function of P_T. Purity is defined as follow:

$$\Pi_{track} = \frac{N_{eT}}{N_T} \tag{4}$$

where N_T is the total number of tracks (electron tracks + other charged particles). Numerically one finds $(16.7 \pm 0.7)\%$ purity.

The goal of the next sections will be to increase the purity of the sample of candidates identified as electrons, keeping the electron finding efficiency as high as possible.

4.2 Track-PS matching

In this section we require at least one preshower cluster matching each track, as it is defined in section 3.2. We define efficiency as:

$$\varepsilon_{PS} = \frac{N_{eT+PS}}{N_{eT}} \tag{5}$$

where N_{eT+PS} is the number of electron tracks matching a preshower cluster and N_{eT} is the number of electron tracks as defined in section 4.1,

and purity as:

$$\Pi_{PS} = \frac{N_{eT+PS}}{N_{T+PS}} \tag{6}$$

where N_{T+PS} is the total number of reconstructed tracks matching a preshower cluster.

Figure 7 (upper left plot) shows the P_T distribution of electron tracks and electron tracks with PS matching. One can see that the electron tracks P_T distribution, and the electron tracks with PS matching P_T distribution, are almost the same. On average, the matching efficiency is found to be $\varepsilon_{PS} = (96 \pm^{4}_{5})\%$. The efficiency distribution as a function of P_T is also shown (lower left plot).

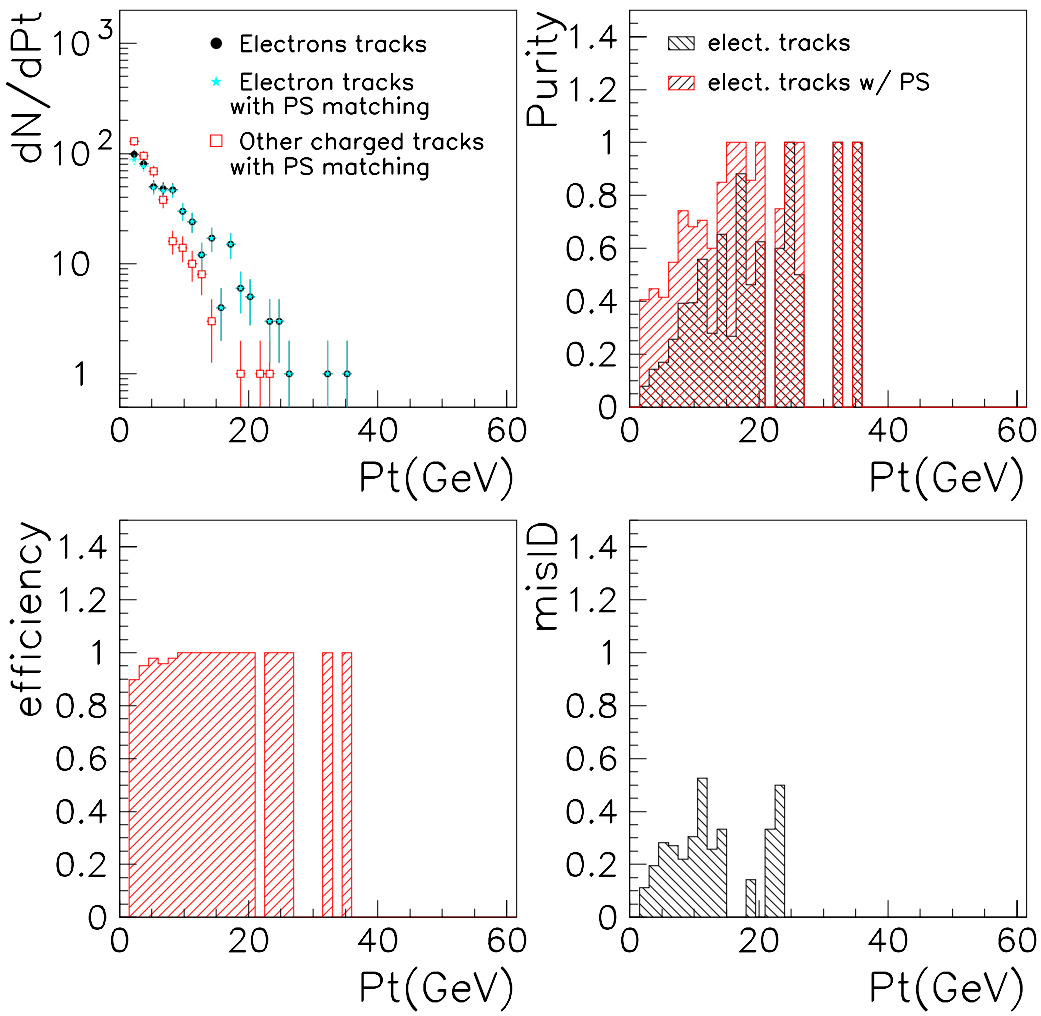

Figure 7: *Upper left:* P_T distribution of electron tracks, electron tracks with PS matching, and other charged particle (identified as non-electron) tracks with PS matching. *Upper right:* purity as a function of P_T. *lower left:* efficiency as a function of P_T. *lower right:* misidentification as a function of P_T.

In addition, Figure 7 (upper right plot) shows the purity before matching and after matching. One can see that requiring a PS cluster matching leads to a purity increase from $(16.7 \pm 0.7)\%$ for electron tracks to $(54 \pm 2)\%$ for electron tracks with PS matching (actually, the background sample is reduced by a factor 5.8, from 2229 "other charged particles" to 385 "other charged particles" with PS matching), especially in the low P_T region where the background is much bigger than the signal.
Finally, Figure 7 (lower right plot) shows the misidentification distribution as a function of P_T, where "misID" is defined as:

$$MisID_{PS} = \frac{N_{oT+PS}}{N_{oT}} \tag{7}$$

where N_{oT+PS} is the number of other charged particle (identified as non-electron) tracks matching a preshower cluster and N_{oT} is the number of other charged particles (identified as non-electron) tracks. On average, one finds misID = $(17 \pm 1)\%$.

4.3 Track-EM tower matching

In this section we require at least one calorimeter tower matching each track, as it is defined in section 3.3.

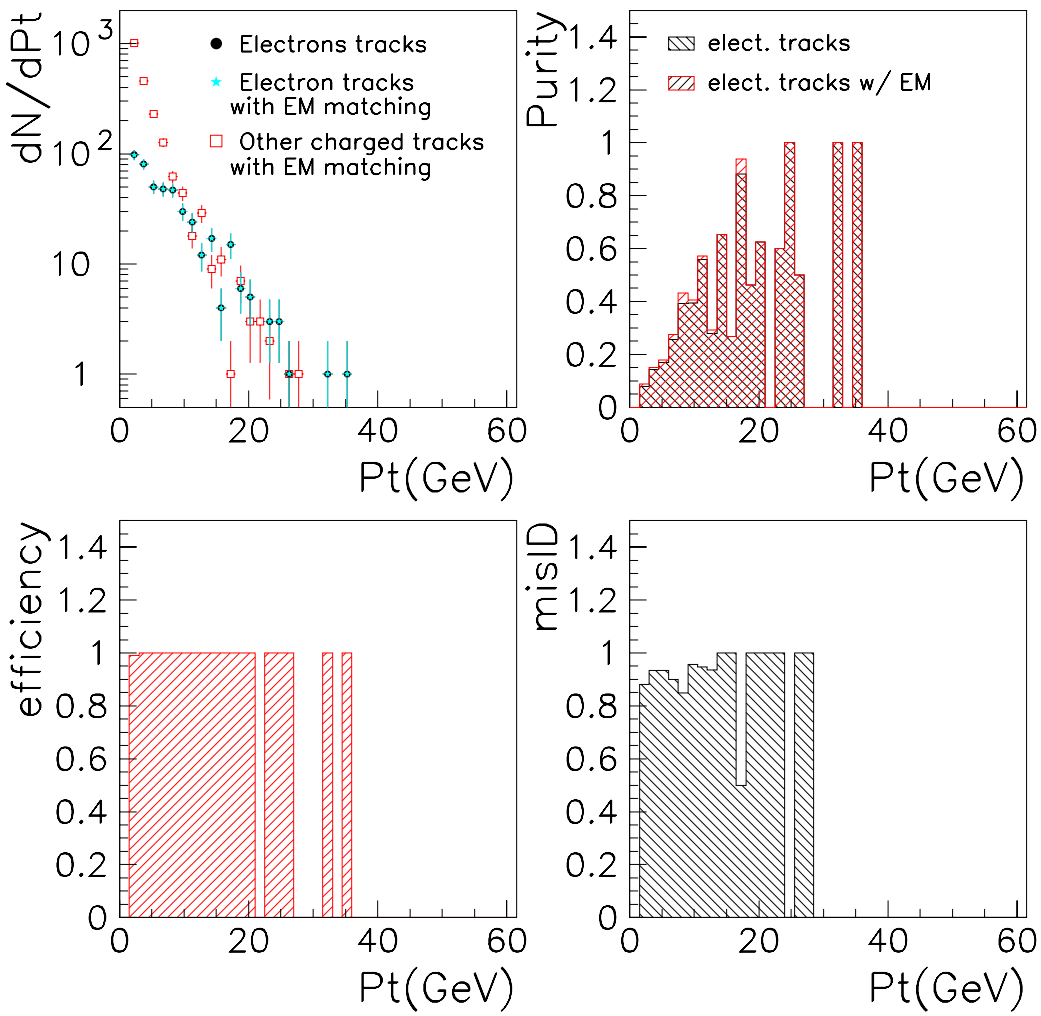

Figure 8: *Upper left:* P_T distribution of electron tracks, electron tracks with calorimeter tower matching, and other charged particle tracks with calorimeter tower matching. *Upper right:* purity as a function of P_T. *Lower left:* efficiency as a function of P_T. *Lower right:* misidentification as a function of P_T.

We define efficiency as:

$$\varepsilon_{CA} = \frac{N_{eT+CA}}{N_{eT}} \tag{8}$$

where N_{eT+CA} is the number of electron tracks matching a calorimeter tower and N_{eT} is the number of electron tracks as defined in section 4.1,

and purity as:

$$\Pi_{CA} = \frac{N_{eT+CA}}{N_{T+CA}} \tag{9}$$

where N_{T+CA} is the total number of reconstructed tracks matching a calorimeter tower.

Figure 8 (upper left plot) shows the P_T distribution of electron tracks and electron tracks with calorimeter tower matching. One can see that the electron tracks P_T distribution, and the electron tracks with calorimeter tower matching P_T distribution, are almost the same. On average, the matching efficiency is found to be $\varepsilon_{CA} = (100\pm^{0}_{5})\%$. The efficiency distribution as a function of P_T is also shown (lower left plot).
Figure 8 (upper right plot) also shows the purity before matching and after matching. One can see that requiring a calorimeter tower match does not significantly increase the purity (from $(16.7 \pm 0.7)\%$ with no matching to $(18 \pm 1)\%$ with EM matching). Finally, Figure 8 (lower right plot) shows the misidentification distribution as a function of P_T, where "misID" is defined as:

$$MisID_{CA} = \frac{N_{oT+CA}}{N_{oT}} \tag{10}$$

where N_{oT+CA} is the number of other charged particle (identified as non-electron) tracks matching a calorimeter tower. In that case, "misID" is $(90 \pm 2)\%$.

These results are not surprising since hadrons deposit energy in the hadronic calorimeter layers. In order to obtain discriminating power, one can use the tower EM fraction (the ratio of energy deposited in the electromagnetic layers to the total energy).

In the next three paragraphs we present results for electron tracks matching a calorimeter tower with the additionnal constraint that at least one matching tower has an EM fraction greater than 0.5, 0.8 or 0.99.

4.3.1 With 0.5 EM fraction cut

Figure 9 shows the results for tracks matching a calorimeter tower with the additional constraint that at least one matching tower has an EM fraction greater than 0.5. One can see that this requirement does not affect the efficiency (lower left plot) which is $\varepsilon_{CA} = (99\pm^{1}_{5})\%$, but, compared to "no EM fraction cut", slightly increases the purity (upper right plot) from $(18 \pm 1)\%$ to $(24 \pm 1)\%$, and reduces the misID to $(63 \pm 2)\%$.

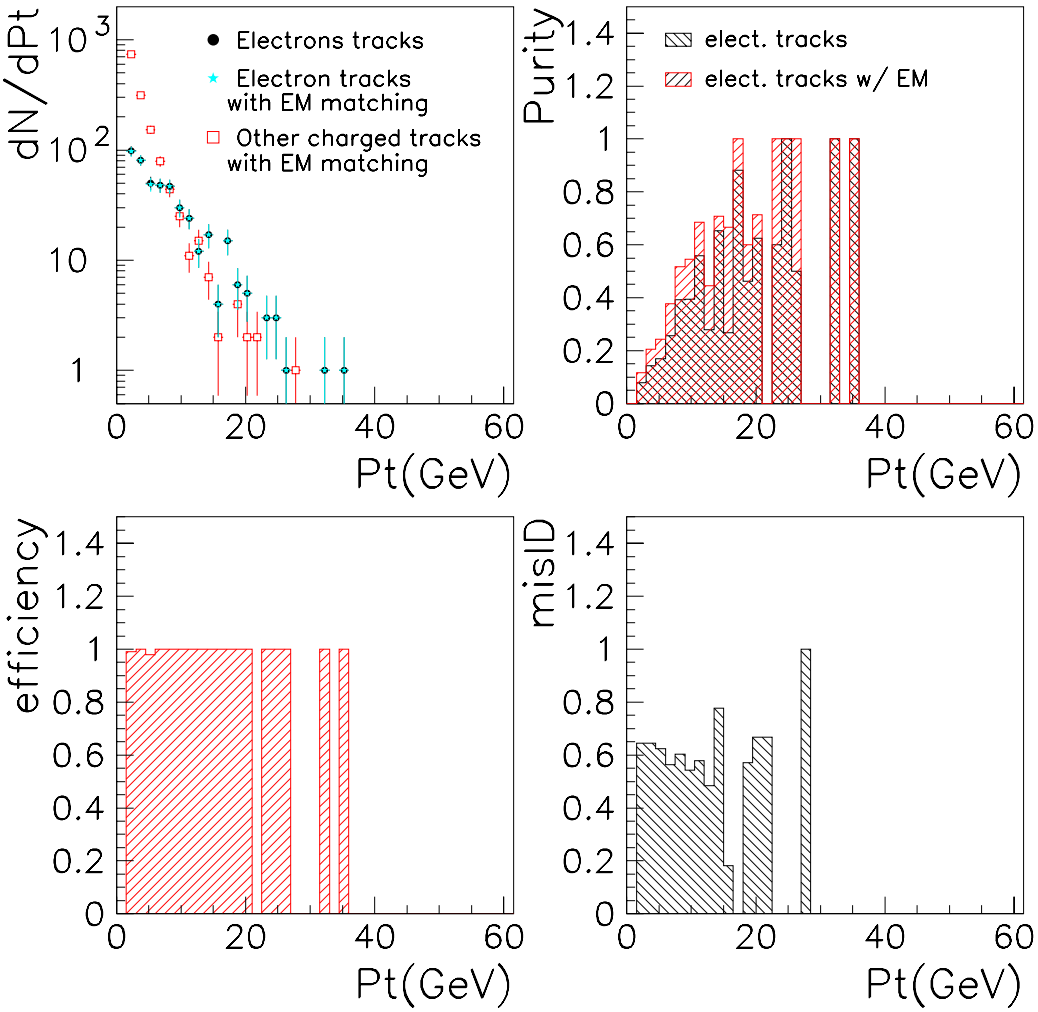

Figure 9: *Upper left:* P_T distribution of electron tracks, electron tracks with calorimeter tower matching, and other charged particle tracks with calorimeter tower matching; an EM fraction cut of greater than 0.5 is required. *Upper right:* purity as a function of P_T. *Lower left:* efficiency as a function of P_T. *Lower right:* misID as a function of P_T.

4.3.2 With 0.8 EM fraction cut

Figure 10 shows the results for tracks matching a calorimeter tower with the additional constraint that at least one matching tower has an EM fraction greater than 0.8. One can see that this requirement does not affect the efficiency (lower left plot) which is $\varepsilon_{CA} = (97\pm^{3}_{5})\%$, but, compared to "no EM fraction cut", increases the purity (upper right plot) from $(18 \pm 1)\%$ to $(30 \pm 1)\%$, and reduces the misID to $(44 \pm 1)\%$.

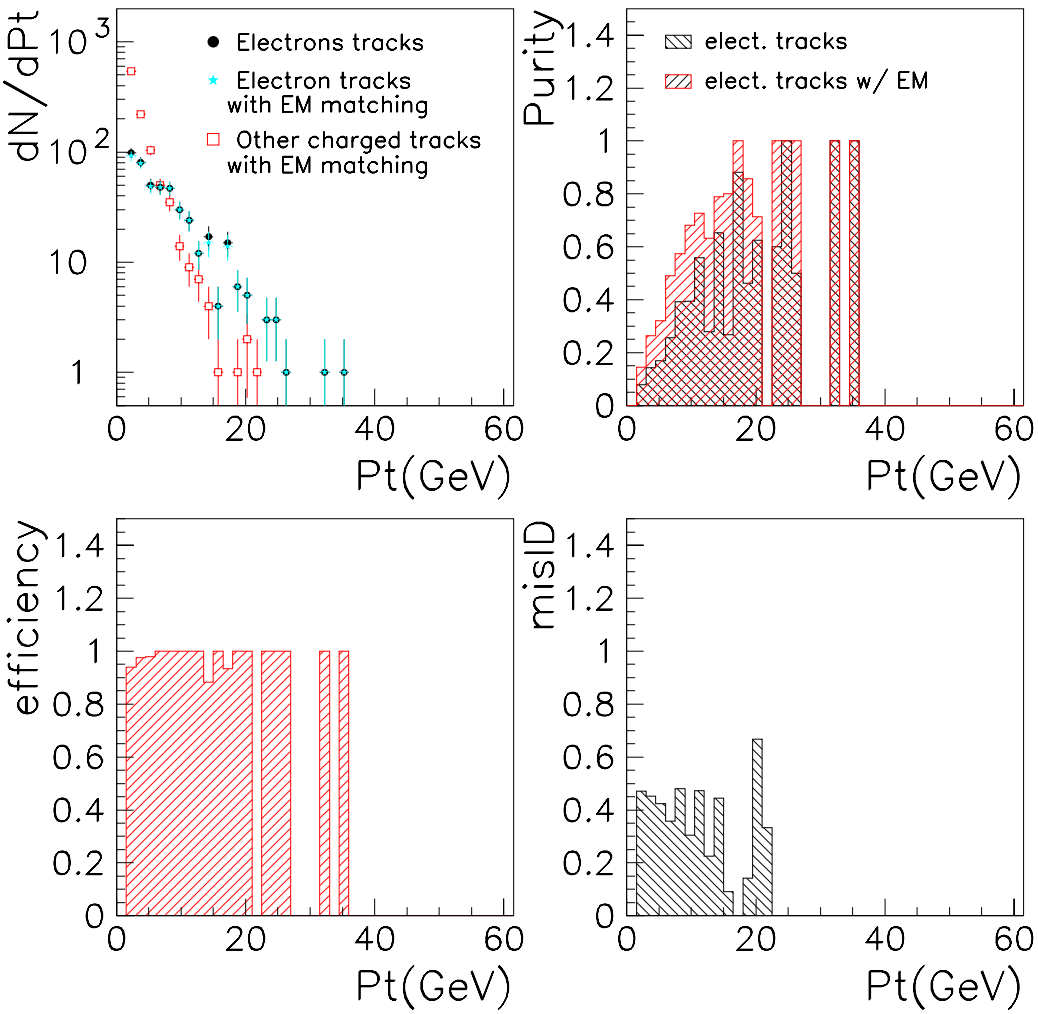

Figure 10: *Upper left:* P_T distribution of electron tracks, electron tracks with calorimeter tower matching, and other charged particle tracks with calorimeter tower matching; an EM fraction cut of greater than 0.8 is required. *Upper right:* purity as a function of P_T. *Lower left:* efficiency as a function of P_T. *Lower right:* misID as a function of P_T.

4.3.3 With 0.99 EM fraction cut

Figure 11 shows the results for tracks matching a calorimeter tower with the additional constraint that at least one matching tower has an EM fraction greater than 0.99. One can see that this requirement does reduce the efficiency (lower left plot) to $(70 \pm 4)\%$, but, on the other hand, compared to "no EM fraction cut", strongly increases the purity (upper right plot) from $(18 \pm 1)\%$ to $(52 \pm 2)\%$ and reduces the misID to $(13 \pm 1)\%$.

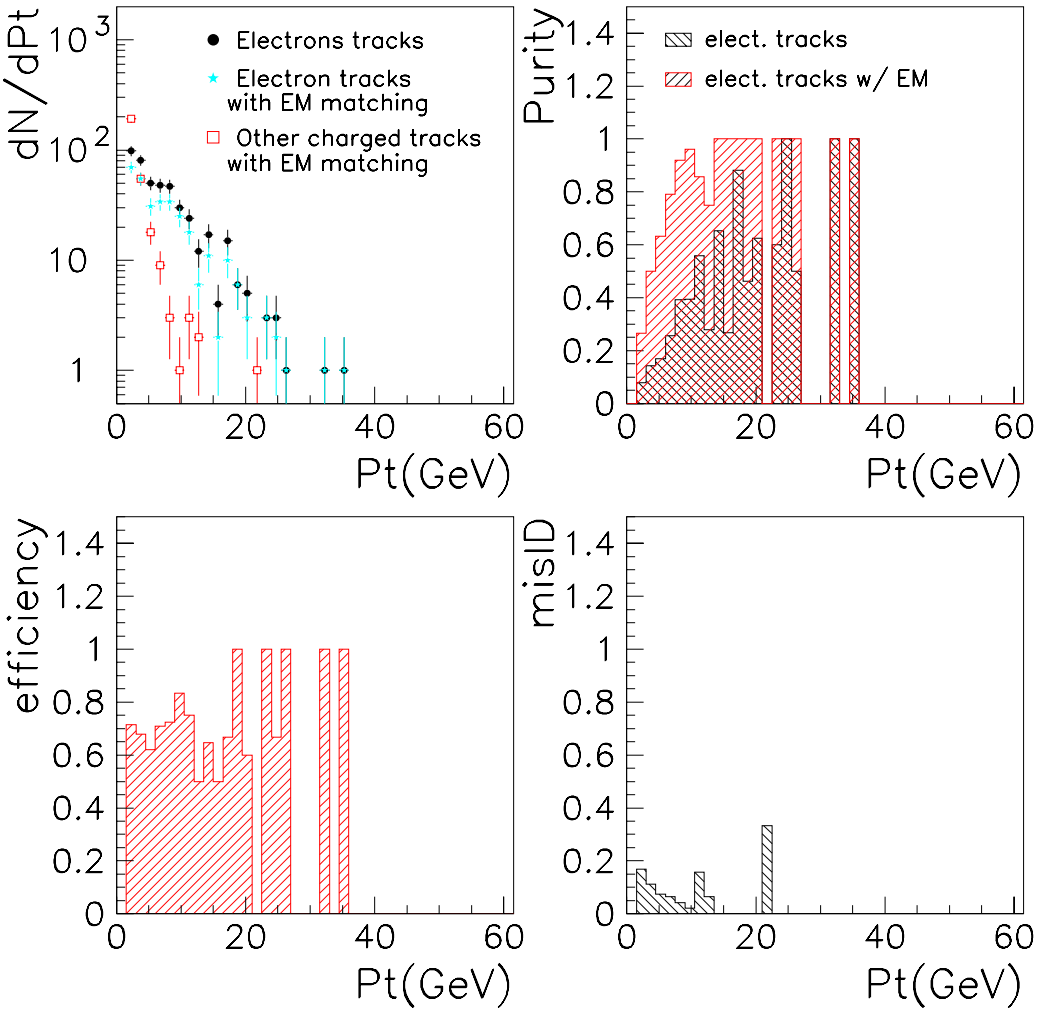

Figure 11: *Upper left:* P_T distribution of electron tracks, electron tracks with calorimeter tower matching, and other charged particle tracks with calorimeter tower matching; an EM fraction cut of greater than 0.99 is required. *Upper right:* purity as a function of P_T. *Lower left:* efficiency as a function of P_T. *Lower right:* misID as a function of P_T.

4.4 Overall performance

In the two previous section, we have shown the results obtained with the preshower cluster and calorimeter tower matching *criteria* separately. In this section, we present the overall performance obtained applying preshower cluster and calorimeter tower matching *criteria* together.

As in section 4.3 we'll apply different EM fraction cuts on the matching towers.

4.4.1 No EM fraction cut

Figure 12 shows the results for tracks matching a preshower cluster and a calorimeter tower. One can see that these requirements provide an efficiency (lower left plot) of $(96\pm^{4}_{5})\%$, and increase the purity (upper right plot) to $(55 \pm 2)\%$. The misidentification is $(16 \pm 6)\%$.

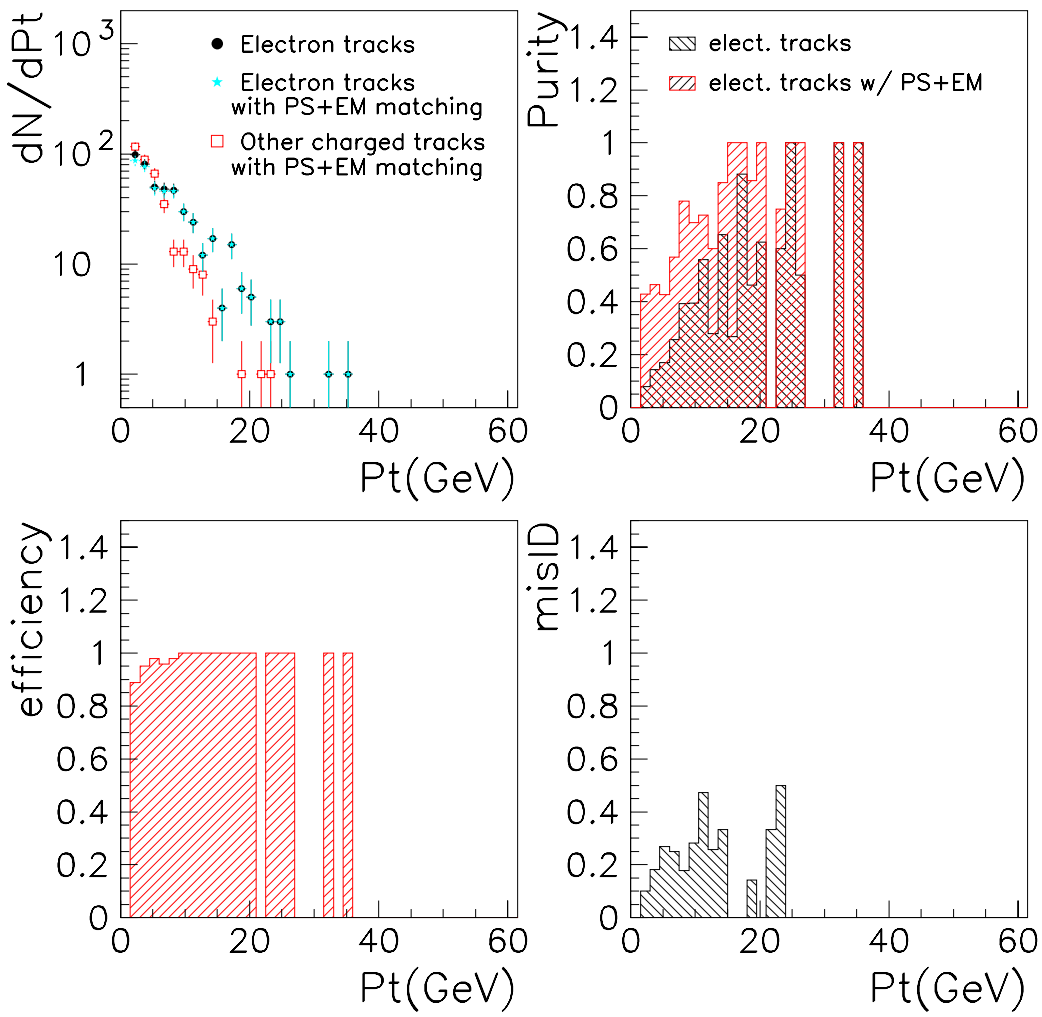

Figure 12: Overall performance with no EM fraction cut: *Upper left:* P_T distribution of electron tracks, electron tracks with preshower cluster and calorimeter tower matching, and other charged particle tracks with preshower cluster and calorimeter tower matching. *Upper right:* purity as a function of P_T. *Lower left:* efficiency as a function of P_T. *Lower right:* misidentification as a function of P_T.

4.4.2 With 0.5 EM fraction cut

Figure 13 shows the results for tracks matching a preshower cluster and a calorimeter tower, with the additional constraint that at least one matching tower has an EM fraction greater than 0.5. One can see that this requirement does not reduce the efficiency (lower left plot) which is still $(96\pm\frac{4}{5})\%$, and increases the purity (upper right plot) to $(62\pm2)\%$. The misidentification is $(12\pm1)\%$.

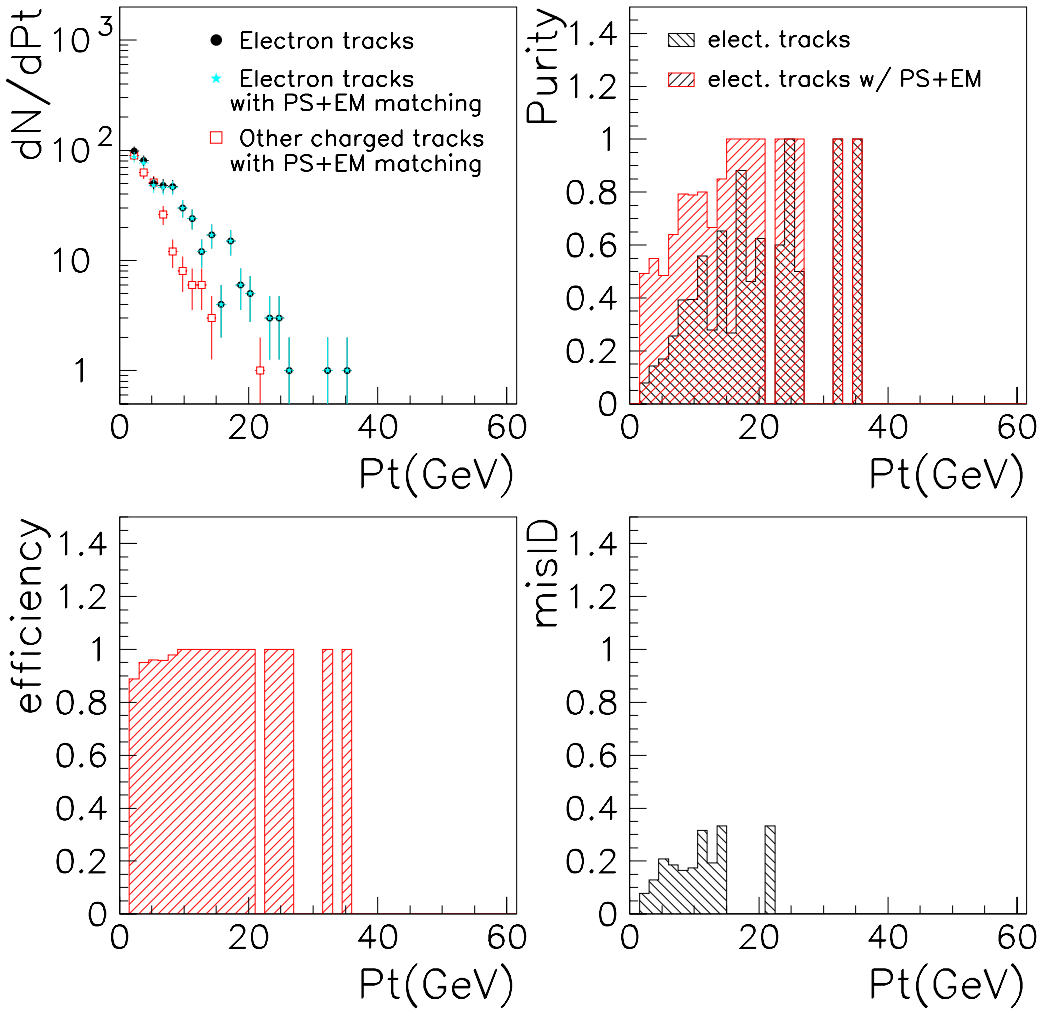

Figure 13: Overall performance with EM fraction cut = 0.5: *Upper left:* P_T distribution of electron tracks, electron tracks with preshower cluster and calorimeter tower matching, and other charged particle tracks with preshower cluster and calorimeter tower matching; an EM fraction cut of greater than 0.5 is required. *Upper right:* purity as a function of P_T. *Lower left:* efficiency as a function of P_T. *Lower right:* misidentification as a function of P_T.

4.4.3 With 0.8 EM fraction cut

Figure 14 shows the results for tracks matching a preshower cluster and a calorimeter tower, with the additional constraint that at least one matching tower has an EM fraction greater than 0.8. One can see that this requirement does not reduce the efficiency (lower left plot) which is $(94 \pm 5)\%$, and increases the purity (upper right plot) to $(68 \pm 2)\%$. The misidentification is $(9 \pm 1)\%$.

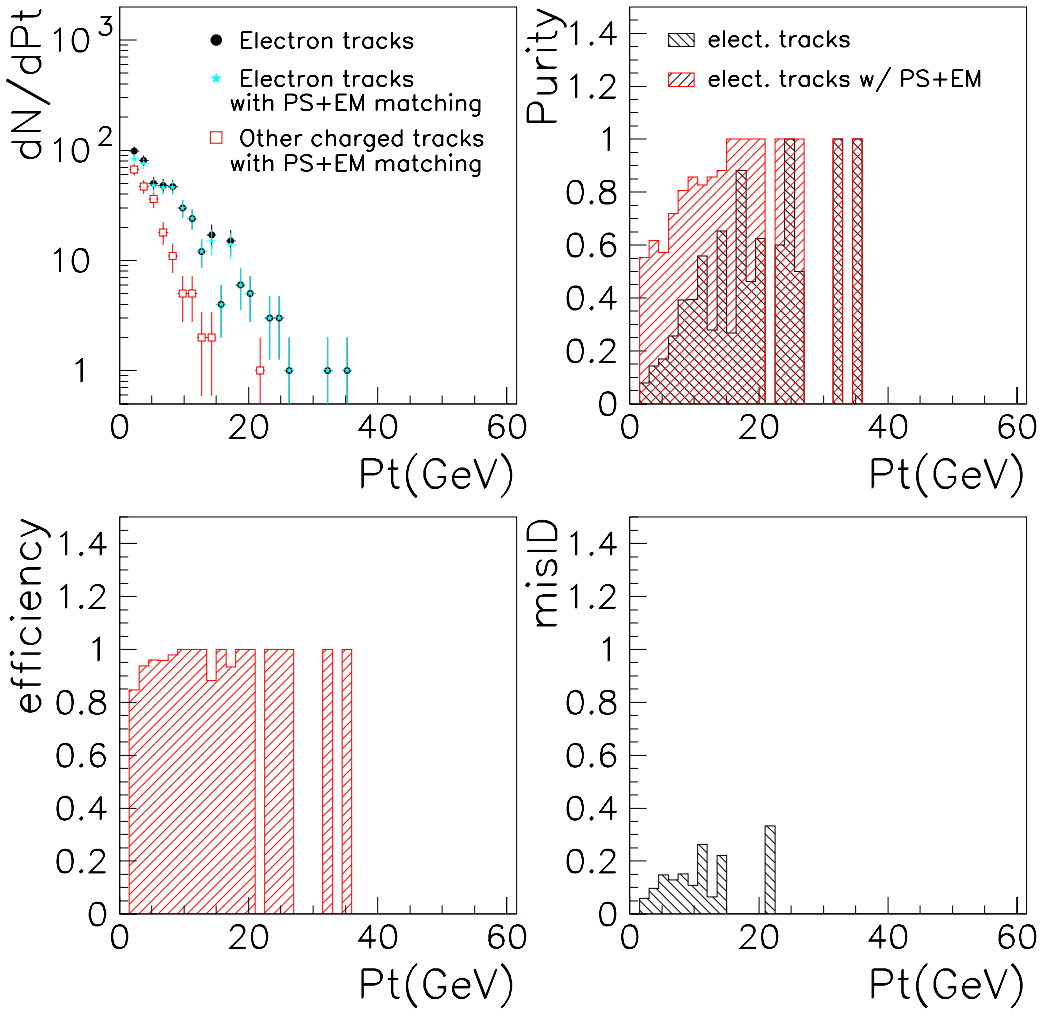

Figure 14: Overall performance with EM fraction cut = 0.8: *Upper left:* P_T distribution of electron tracks, electron tracks with preshower cluster and calorimeter tower matching, and other charged particle tracks with preshower cluster and calorimeter tower matching; an EM fraction cut of greater than 0.8 is required. *Upper right:* purity as a function of P_T. *Lower left:* efficiency as a function of P_T. *Lower right:* misidentification as a function of P_T.

4.4.4 With 0.99 EM fraction cut

Figure 15 shows the results for tracks matching a preshower cluster and a calorimeter tower, with the additional constraint that at least one matching tower has an EM fraction greater than 0.99. This requirement does reduce the efficiency (lower left plot) to $(67 \pm 4)\%$ but, on the other hand, increases the purity (upper right plot) to $(85 \pm 2)\%$ and reduces the misidentification to $(2.3 \pm 0.3)\%$.

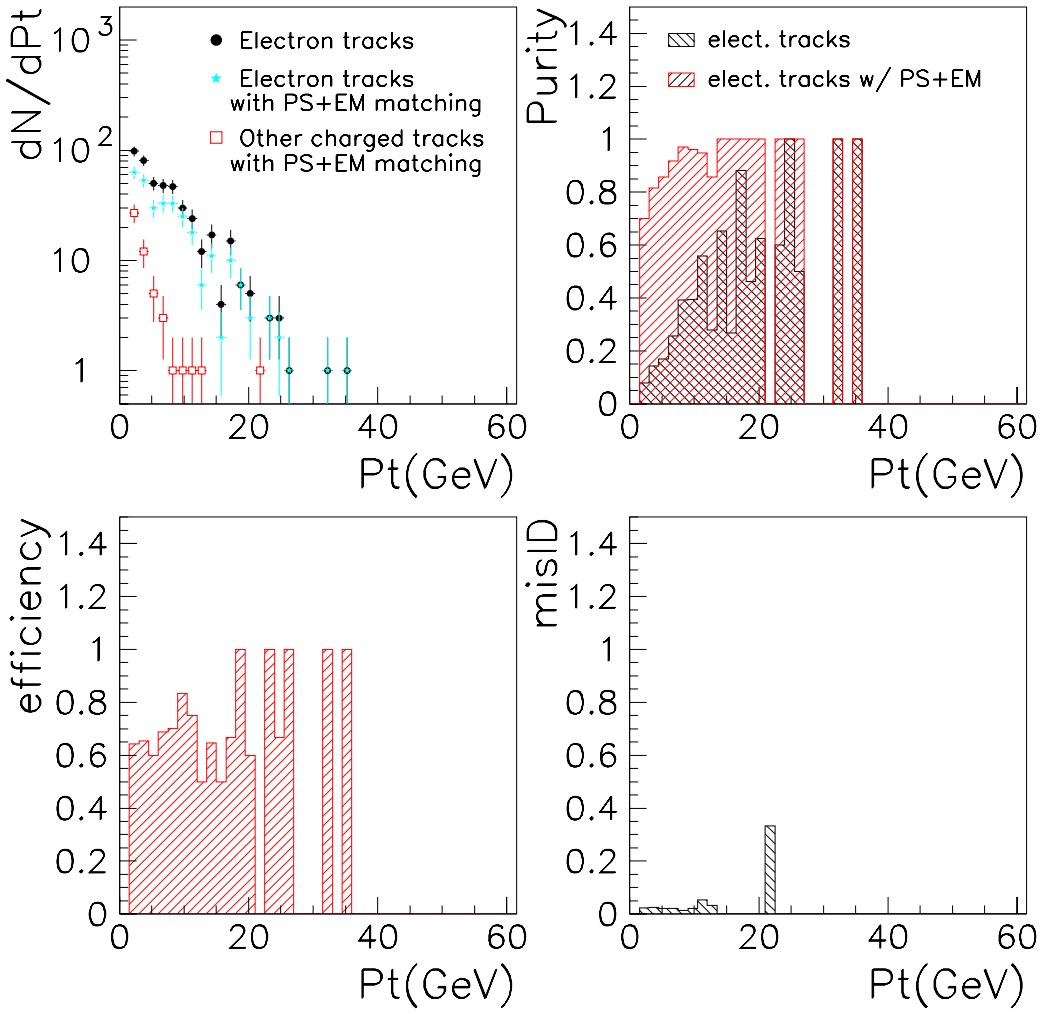

Figure 15: Overall performance with EM fraction cut = 0.99: *Upper left:* P_T distribution of electron tracks, electron tracks with preshower cluster and calorimeter tower matching, and other charged particle tracks with preshower cluster and calorimeter tower matching; an EM fraction cut of greater than 0.99 is required. *Upper right:* purity as a function of P_T. *Lower left:* efficiency as a function of P_T. *Lower right:* misidentification as a function of P_T.

4.5 Performance summary

As shown in section 4.3, efficiency, purity and misidentification strongly depend on the EM fraction cut one applies on matching calorimeter towers. The following tables summarize the results of sections 4.2, 4.3 and 4.4 for $Z \to b\bar{b}$ events.

	tracks+PS	tracks+EM no EM frac.	tracks+EM 0.5 EM frac.	tracks+EM 0.8 EM frac.	tracks+EM 0.99 EM frac.
$\varepsilon(\%)$	$96\pm^{4}_{5}$	$100\pm^{0}_{5}$	$99\pm^{1}_{5}$	$97\pm^{3}_{5}$	70 ± 4
$\Pi(\%)$	54 ± 2	18 ± 1	24 ± 1	30 ± 1	52 ± 2
$misID(\%)$	17 ± 1	90 ± 2	63 ± 2	44 ± 1	13 ± 1

Table 1: Performance summary for track-PS matching and track-EM matching

	tracks+PS+EM no EM frac.	tracks+PS+EM 0.5 EM frac.	tracks+PS+EM 0.8 EM frac.	tracks+PS+EM 0.99 EM frac.
$\varepsilon(\%)$	$96\pm^{4}_{5}$	$96\pm^{4}_{5}$	94 ± 5	67 ± 4
$\Pi(\%)$	55 ± 2	62 ± 2	68 ± 2	85 ± 2
$misID(\%)$	16 ± 6	12 ± 1	9 ± 1	2.3 ± 0.3

Table 2: Performance summary for track-PS matching and track-EM matching together

As can be seen in these tables, the higher the EM fraction cut, the lower the efficiency and the higher the purity. Note however that these efficencies do not include the tracking efficiency which is, in our case, around 75%.

5 Conclusion

A new electron tagging algorithm has been presented. This algorithm is based on reconstructed tracks instead of electromagnetic calorimeter clusters as used by the standard reconstruction algorithm.

The performance of this algorithm have been tested using a sample of $Z \to b\bar{b}$ events, and has an efficiency close to 70% if one requires a matching preshower cluster and a matching calorimeter tower with an EM fraction greater than 0.99, and about 95% for a 0.8 or 0.5 EM fraction cut. Misidentification is

less than 3% if one requires a matching preshower cluster and a matching calorimeter tower with an EM fraction greater than 0.99, and about 10% for a 0.8 or 0.5 EM fraction cut.

This algorithm has been implemented in the D0 reconstruction framework and is used within the SEMReco package [2].

Several improvements can be made to reduce the misidentification. For example, one can use E/p information, where E is the energy deposited in the calorimeter and p is the track momentum. One can also take advantage of the calorimeter granularity as shown in [3].

References

[1] The D0 upgrade, Fermilab Pub-96/357-E (Figure 16).

[2] The D0 Soft Electron Reconstruction Package SEMReco, F. Fleuret, F. Beaudette and S. Protopopescu, D0 note in preparation.

[3] b-tagging with electrons using the road method, F. Beaudette and J.-F. Grivaz, D0 note 3828.

The D0 Soft Electron Reconstruction Package SEMReco

— 05/30/2001 —

This note describes the low energy electron reconstruction package SEMReco. We first give information about the algorithm. Then, in the following parts, we discuss more detailed information about the several SEMReco classes and about the SEMparticle class which is the container of the soft electron candidate information stored in the event.

Frédéric Fleuret
Laboratoire de Physique Nucléaire et de hautes Energies, Paris
Lawrence Berkeley National Laboratory, Berkeley

Florian Beaudette
Laboratoire de l'Accélérateur Linéaire, Orsay

Serban Protopopescu
Brookhaven National Laboratory, Long Island

D0 note 3872

Contents

1 Introduction — *The SEMReco package* 3

2 SEMReco — *SEMReco Class* 6

2.1 RCP input parameters: 7

3 SEMTrackFinder — *Track Finder Class* 8

3.1 Methods: 8

3.2 RCP input parameters: 9

4 SEMEMClusFinder — *EM Calorimeter Tower Finder Class* 10

4.1 Methods: 11

4.2 RCP input parameters: 11

5 SEMPshwrClusFinder — *PS Cluster Finder Class* 13

5.1 Methods: 14

5.2 RCP input parameters: 14

6 RoadFinder — *Road finder Class* 16

6.1 Methods: 17

6.2 RCP input parameters: 18

7 SEMcandidate — *Soft electron candidate Class* 19

7.1 Methods: 19

8 SEMparticle — *Soft Electron Particle Class* 20

8.1 Interfaces required by D0PhysObj 20

8.2 Information coming from SEMEMClusFinder 21

8.3 Information coming from SEMPSClusFinder 22

8.4 Information coming from RoadFinder 22

8.5 Additional access methods 23

1 The SEMReco package: **Introduction**

In this section, we present the principle of the method.

The Soft Electron Reconstruction Package SEMReco is dedicated to the identification of low energy electrons. SEMReco proceeds in three steps [1], as shown in figure 1:

- find tracks.
- find matching calorimeter towers.
- find matching PreShower clusters.

In addition, SEMReco provides information computed with the Road Algorithm which takes advantage of the calorimeter cells granularity[2].

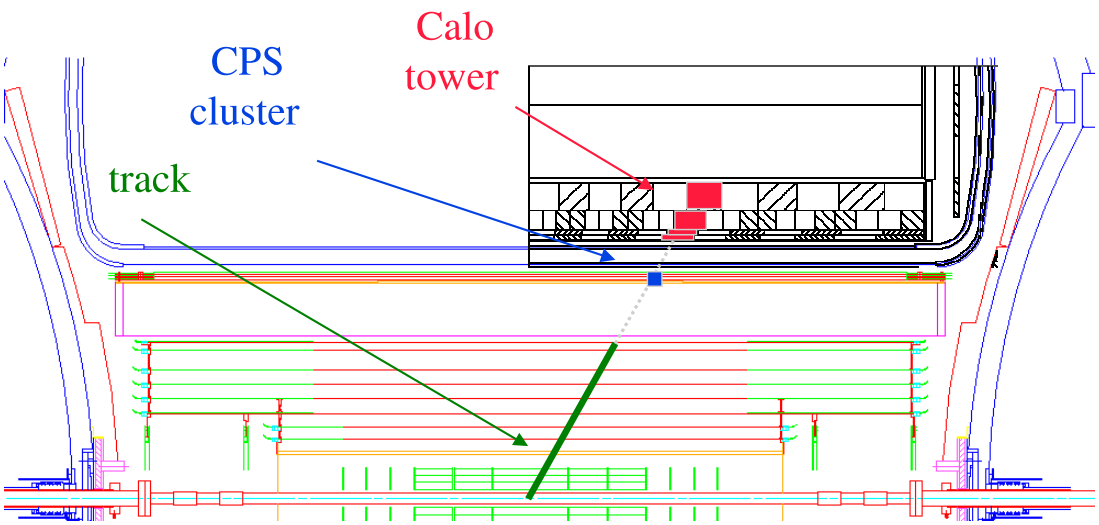

Figure 1: Information used by SEMReco to provide SEMparticle

To achieve this goal, SEMReco uses four classes, as shown in figure 2:

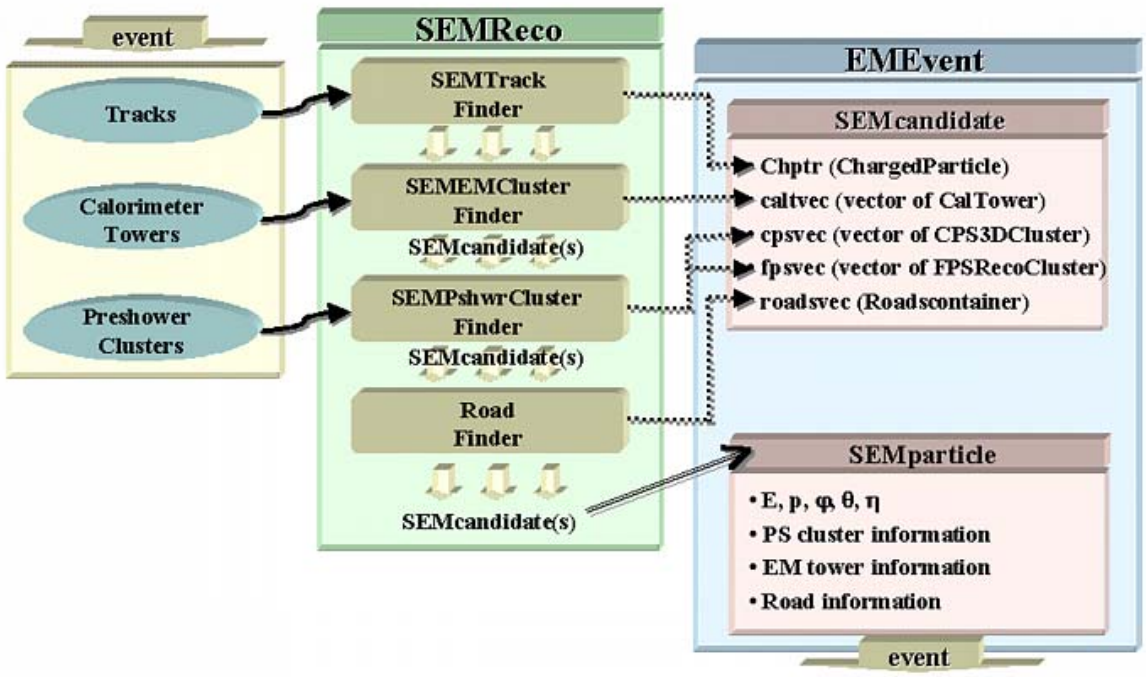

Figure 2: The SEMReco structure.

1. **SEMTrackFinder**: *find tracks*

   SEMTrackFinder uses as an input the list of ChargedParticle's coming from the event (ChargedParticleChunk) and provides the list of ChargedParticle's with $P_T > P_{T_{cut}}$ found in the event (see section 2 for more details).

   This list is used as an input of step 2.

2. **SEMEMClusFinder**: *find associated calorimeter towers*

   SEMEMClusFinder uses, as an input, the list of ChargedParticle's provided by SEMTrackFinder and the list of $P_T > P_{T_{cut}}$ calorimeter towers coming from the event (CalDataChunk).

   For each track, SEMEMClusFinder looks for at least one electromagnetic calorimeter tower (meaning a calorimeter tower with an EMfraction greater than $EMfraction_{cut}$) matching the track within a $\eta \times \phi$

window (see section 3 for more details). For each successful track (meaning matching an electromagnetic calorimeter tower) SEMEMClusFinder produces a SEMcandidate.

SEMEMClusFinder returns The list of SEMcandidate's.

3. **SEMPshwrClusFinder**: *find associated PS clusters*

   SEMPshwrClusFinder uses, as an input, the list of SEMcandidate's provided by SEMEMClusFinder, and the list of CPS3DCluster's and FPSRecoCluster's (respectively for the Central PreShower and the Forward PreShower) coming from the event (respectively CPSClusterChunk and FPSClusterChunk).
   For each SEMcandidate, SEMPshwrClusFinder looks for at least one preshower cluster matching the SEMcandidate within a $\eta \times \phi$ window (see section 4 for more details). If a match is found SEMPshwr-ClusFinder fills the preshower cluster information in SEMcandidate.

   SEMPshwrClusFinder returns the list of the SEMcandidate's (including SEMcandidate's with no PS matching).

4. **RoadFinder**: *provide road information*

   RoadFinder uses, as an input, the list of SEMcandidate's provided by SEMPshwrClusFinder and the list of calorimeter cells.

   For each SEMcandidate in the acceptance of the central calorimeter, RoadFinder computes three lists of cells along the extrapolation of the track, one for each value of the *dismerge* parameter, which controls the width of the Road ([2],[3]).

   RoadFinder returns the list of SEMcandidate's, without making any selection. The transverse energy deposits are provided at the "root-tuple" level, or using the RoadTools class, which is part of the em_analyze package.

At the end of step 4, the SEMcandidate's information is dumped into SEMparticle's objects which are stored in the SEMparticleChunk and written with the event.

References

[1] Low energy Electron Identification in D0, F. Fleuret, D0 note 3870.

[2] The road method for electron identification in jets, F. Beaudette and J.-F. Grivaz, D0 note in preparation.

[3] b-tagging with electrons using the road method, F. Beaudette and J.-F. Grivaz, D0 note 3828.

2

class **SEMReco** : public Package, public Process, public JobSummary

SEMReco Class

Inheritance

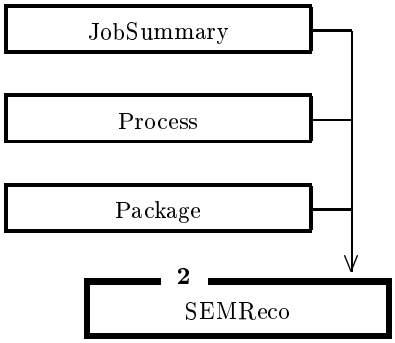

Private Members

SEMTrackFinder	**_SEMtracks**	*tracks object.*
SEMEMClusFinder	**_SEMEMClus**	*EM clusters object.*
SEMPshwrClusFinder	**_SEMPSClus**	*PS clusters object.*
RoadFinder	**_Road**	*Road object.*

2.1 **RCP input parameters:** 7

SEMReco Class.

This class has been designed to control the electron identification steps. It gets the vertex position information and then calls SEMTrackFinder, SEMEMClusFinder (vertex information is provided to this class), SEMPshwrClusFinder (vertex information is provided to this class) and RoadFinder.

2.1 RCP input parameters:

Names

bool	**_do_print**	*Printing key. The default value is set to* **false**.
bool	**_useMCvtx**	*If* **true** *and useD0vtx=false, use MC vertex.*
bool	**_useD0vtx**	*If* **true** *use reconstructed PRIMARY vertex. If useMCvtx=true (also), use MC vertex when no reconstructed PRIMARY vertex is found.*
bool	**_run_road**	*If true, run the Road algorithm.*

RCP input paramters are available in SEMReco.rcp.

3 class SEMTrackFinder

Track Finder Class

Public Members

3.1 **Methods:** 8

Private Members

3.2 **RCP input parameters:** 9

Track Finder Class.

This class has been designed to select all the $P_T > P_{T_{cut}}$ tracks contained in an event. It uses ChargedParticle (ChargedParticleChunk) as input and loops over all tracks. SEMTrackFinder returns the list of ChargedParticle's.

3.1 Methods:

Names

void **getTracks** (ErrorLog &errlog, edm::Event &event,
std::list<edm::ChunkID> &parentIDs,
std::vector<const vertex::ChargedParticle*>& chps)
Performs the track search, must be called before any other method of this class.

bool **isValid** () *Return true if the input Chunk is valid.*

3.2 RCP input parameters:

Names

bool	**_do_print**	*Printing key. The Default value is set to* **false**.
float	**_track_min_pT**	*P_T min of the tracks. The Default value is set to* **1.5 GeV.**

RCP input parameters are available in SEMReco.rcp.

4

class **SEMEMClusFinder**

EM Calorimeter Tower Finder Class

Public Members

4.1 **Methods:** 11

Private Members

4.2 **RCP input parameters:** 11

EM Calorimeter Tower Finder Class.

This class has been designed to find the calorimeter towers contained in a given $\Delta\eta \times \Delta\phi$ window around the track candidate. It uses the CalDataChunk as an input and, for each track, find matching calorimeter towers.

An EM fraction cut is applied on calorimeter towers. Only tracks with at least one matching calorimeter tower with an EM fraction greater than $emfrac_cut$ (see RCP input parameters) are stored as SEMcandidate's.

The matching between the track and the calorimeter towers is made after extrapolation of the track direction which is corrected for the magnetic field effects. Two matching methods are available:

- doing the track-EM tower match by computing the tower ϕ and η positions using the Primary vertex position.
- calculating η and ϕ of the tower crossed by the extrapolation of the track at the middle radius of EM3. The extrapolation is calculated using the parameters of the track at the Distance of Closest Approach (DCA).

By default SEMEMClusFinder uses the track's DCA to compute the tower ϕ and η positions.

4.1 Methods:

Names

void	**getSEMEMClus** (ErrorLog &errlog, edm::Event &event, float vxyz[3], std::vector<const vertex::ChargedParticle*> chps, std::list<SEMcandidate>& lsem)	*Performs the calorimeter tower matching.* **Must be called before any other method of this class.**
bool	**isValid** ()	*Return true if the input Chunk is valid.*

4.2 RCP input parameters:

Names

bool	**_do_print**	*Printing key. The Default value is set to* **false**.
float	**_pTmin**	**tower_minpT** *parameter: minimum pT of the towers. The default value is set to* **1 GeV**.
bool	**_requireEMmatch**	*EM-track matching key. The Default value is set to* **true**. *If set to* **false**, *each incoming ChargedParticle produces a SEMcandidate (no EM matching is required).*
int	**_sel_met_number**	**method_number** *parameter. If 0 use the vertex position to compute tower ϕ and η. If 1, use track DCA. The default value is set to* **1**.
float	**_corrCCphi**	*ϕ correction to apply on central track ϕ. The default values is set to* **0.24418**. *this parameter is used if method_number=0.*
float	**_corrECphi**	*ϕ correction to apply on forward track ϕ. The default value is set to* **0.36**. *this parameter is used if method_number=0.*

float	**_dphi_Etrk**	*Size of the ϕ matching window. The Default value is set to* **0.045**.
float	**_deta_Etrk**	*Size of the η matching window. The Default value is set to* **0.05**.
float	**_emfrac_cut**	*Cut on the EMfraction (EM energy/Total energy). The default value is set to* **0.80**.

RCP input parameters are available in SEMReco.rcp.

5

class **SEMPshwrClusFinder**

PS Cluster Finder Class

Public Members

5.1 **Methods:** 14

Private Members

5.2 **RCP input parameters:** 14

PS Cluster Finder Class.

This class has been designed to find the preshower clusters contained in a given $\Delta\eta \times \Delta\phi$ window around the track candidate. It uses the list of SEMcandidate's provided by SEMEMClusFinder, and the preshower clusters from CPSClusterChunk and FPSClusterChunk as inputs and, for each track, loops over all the preshower clusters to find matching ones.

For the central preshower, two methods are available:

- get the best matching CPS cluster provided in the ChargedParticle container.
- doing the track-CPS cluster match by computing the cluster ϕ and η positions using the primary vertex position. The matching is made after extrapolation of the track direction, corrected for the effects of the magnetic field.

By default, SEMPshwrClusFinder uses the matching CPS cluster provided in the ChargedParticle container.

For the forward preshower, after extrapolation of the track direction, corrected for the effects of the magnetic field, to the FPS position, the matching is done using a FPSClusterChunk method.

5.1 Methods:

Names

void	**getSEMPS** (ErrorLog &errlog, edm::Event &event, float vxtz[3], std::list<edm::ChunkID>& parentIDs, std::list<SEMcandidate>& lsem)	*Performs the CPS and FPS cluster matching, must be called before any other method of this class.*
bool	**isValidCps** ()	*Return true if the input chunk is valid.*
bool	**isValidFps** ()	*Return true if the input chunk is valid.*

5.2 RCP input parameters:

Names

bool	**_do_print**	*Printing key. The Default value is set to* **false**.
bool	**_useCPmatching**	*Use matching track-CPS cluster provided by ChargedParticle.*
float	**_corrCCphi**	**psphi_corr** *parameter: ϕ correction to apply on central track ϕ. The Default value is set to* **0.21657**.
float	**_dphi_cps**	*Size of the ϕ matching window for the CPS. The Default value is set to* **0.030**.
float	**_deta_cps**	*Size of the η matching window for the CPS. The Default value is set to* **0.025**.
float	**_corrECphi**	*ϕ correction to apply on forward track ϕ. The Default value is set to* **0.36**.
float	**_dphi_fps**	*Size of the ϕ matching window for the FPS. The Default value is set to* **0.03**.

float	**_dtheta_fps**	*Size of the θ matching window for the FPS. The Default value is set to* **0.025**.
float	**_requirePSmatch**	*PS-track matching key. the default value is set to* **false**. *If set to* **false**, *no selection is applied and matching information is stored in SEMcandidate (both SEMcandidate's with and without matching are provided).*

RCP input parameters are available in SEMReco.rcp.

6 class RoadFinder

Road finder Class

Public Members

6.1 **Methods:** 17

Private Members

6.2 **RCP input parameters:** 18

Road finder Class.

The idea of the road is to follow the extrapolation of the track and look at the transverse energy deposits in a restricted volume of the calorimeter where the shower is expected to develop.

This algorithm is defined only in the central calorimeter region (a ECRoadFinder class is under development for the forward calorimeter region). The extrapolation of the track is calculated assuming a uniform 2T magnetic field, and no magnetic field outside the coil.

All the cells which are crossed by the extrapolation of the track are included in the road. Neighbouring cells can be added to the road in order to take into account the transverse extension of the shower. This is controlled by the *dismerge* parameter.
The distance between the impact of the track in the floor and the edge of the cell is calculated in cell-width unit both in η and ϕ. If this distance is lower than *dismerge*, the neighbouring cell is included in the road. In the third floor, where the granularity is quadruple, the distance is compared to *dismerge*$\times 2$. Therefore, *dismerge* must lie between 0 (thinest road possible) and 0.25 (largest). Three roads with different dismerge values are calculated and written into the chunk.

The transverse energy deposits in each of the roads are calculated later by the RoadTools class which belongs to the em_analyze package.

6.1 Methods:

Names

void **get_roads** (std::list<SEMcandidate>& lsem)
Performs Road computation.

static void **MakeDCAParamVector** (const ChargedParticle* ptrchp, float& theta_, float& eta_, float& phi, float& pt, float par[7])
Get track DCA values.

static int **HelixCyl** (const float par[7], const float q, float parex[6])
Computes the intersection between an helix and a cylinder (radius=inner radius of the coil, length = 130 cm). The result is 1 if it is in the central region, 2 if it is in the ends. It uses the output of MakeDCAParamVector as an input.

static bool **Eta_Phi_at_radius** (float& eta, float&phi, const float& radius, const float parex[6])
Computes track η and ϕ at a given radius. It uses the output of HelixCyl as an input.

static float **Iphi_to_phi** (const int& Iphi)
Transforms ϕ tower index to ϕ value.

static int **phi_to_Iphi** (const float& phi)
Transforms ϕ value to ϕ tower index.

static int **eta_to_Ieta** (const float& d_eta)
Transforms η value to η tower index.

static float **Ieta_to_eta** (const int& Ieta)
Transforms η tower index to η value.

static TowerAddress **GetNeighbourTower** (const TowerAddress& base_tower, const int& direction, bool& status)
Get the address of the neighbouring tower. direction=1 means η+1, direction=2 means η-1, direction=3 means ϕ+1, direction=4 means ϕ-1.

6.2 RCP input parameters:

Names

float	**_dismerge_container**	*Controls the number of cells in the road. The default value is set to* **0.25**.
float	**_dismerge_road1**	*Must be lower than dismerge_container. The default value is set to* **0.125**.
float	**_dismerge_road2**	*Must be lower than dismerge_container. The default value is set to* **0.0**.

RCP input parameters are available in SEMReco.rcp.

7 class SEMcandidate

Soft electron candidate Class

Public Members

7.1 **Methods:** 19

Soft electron candidate Class.

This class holds the information about the soft electron candidates. The SEMcandidate object is for SEMReco internal use. It's not stored in the event. After all the SEMReco steps, each SEMcandidate object is dumped into a SEMparticle object which is stored in the event.

7.1 Methods:

Names

const vertex::ChargedParticle*	**chptr** ()	*Returns the ChargedParticle pointer.*
const std::vector <const CPS3DCluster*> &	**cpsvec** ()	*Returns the vector of matching CPS clusters.*
const std::vector <const FPSRecoCluster*> &	**fpsvec** ()	*Returns the vector of matching FPS clusters.*
const std::vector <const CalTower*> &	**caltvec** ()	*Returns the vector of matching calorimeter towers.*
Roadscontainer	**roadsvec** ()	*Returns the road*
bool	**hasCaltowers** ()	**true** *if the candidate has a matching tower.*
bool	**hasCPSclusters** ()	**true** *if the candidate has a matching CPS cluster.*
bool	**hasFPSclusters** ()	**true** *if the candidate has a matching FPS cluster.*

8

class **SEMparticle** : public kinem D0PhysObj

Soft Electron Particle Class

Inheritance

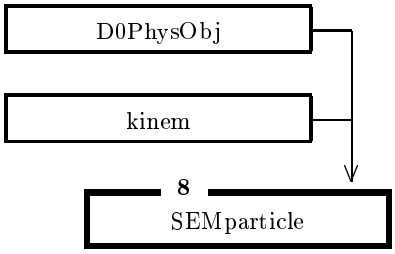

Public Members

8.1 **Interfaces required by D0PhysObj** 20
8.2 **Information coming from SEMEMClusFinder** 21
8.3 **Information coming from SEMPSClusFinder** 22
8.4 **Information coming from RoadFinder** 22
8.5 **Additional access methods** 23

Soft Electron Particle Class.

This class holds the information about the soft electron particles. A soft electron particle is defined as a track matching an EM-tower (see SEMReco.rcp for the EMfraction cut). If one wants to look at SEMparticle's with both a matching preshower cluster and a matching EM-tower, one has to require ps_matching()=true (see "Additionnal access methods").

In addition, SEMparticle holds some information about the associated PSClusters, EMtowers and Road.

8.1 Interfaces required by D0PhysObj

Names

float	**px** ()	*Return particle px*
float	**py** ()	*Return particle py*
float	**pz** ()	*Return particle pz*
float	**E** ()	*Return particle E (so far, $E = p$)*
float	**pT** ()	*Return particle pT*
float	**phi** ()	*Return particle ϕ*
float	**eta** ()	*Return particle η*
float	**theta** ()	*Return particle θ*
float	**p** ()	*Return particle p*
void	**p4vec** (float p4v[4])	*Return 4-vector (with $E = p$)*
LorentzVector	**l4vec** ()	*Return Lorentz 4-vector (with $E = p$)*
SpaceVector	**s3vec** ()	*Return the space component of Lorentz 4-vector*
float	**charge** ()	*Return object charge*

Each candidate track with a matching tower produces a SEMparticle and provides the information used to fill the SEMparticle variables.

8.2 Information coming from SEMEMClusFinder

Names

int	**nb_em** ()	*Return the number of matching EM towers.*
float	**em_E** (int i)	*Return the EM tower energy. Use the* **EM tower index** *as an input parameter.*
float	**em_emE** (int i)	*Return the EM tower EM energy. Use the* **EM tower index** *as an input parameter.*
float	**em_em1E** (int i)	*Return the EM tower layer 1 energy. Use the* **EM tower index** *as an input parameter.*
float	**em_em2E** (int i)	*Return the EM tower layer 2 energy. Use the* **EM tower index** *as an input parameter.*

float	**em_em3E** (int i)	*Return the EM tower layer 3 energy. Use the* **EM tower index** *as an input parameter.*
float	**em_em4E** (int i)	*Return the EM tower layer 4 energy. Use the* **EM tower index** *as an input parameter.*
float	**em_pT** (int i)	*Return the tower pT. Use the* **EM tower index** *as an input parameter.*
float	**em_phi** (int i)	*Return the EM tower ϕ. Use the* **EM tower index** *as an input parameter.*
float	**em_eta** (int i)	*Return the EM tower η. Use the* **EM tower index** *as an input parameter.*

8.3 Information coming from SEMPSClusFinder

Names

int	**nb_ps** ()	*Return the number of matching PS clusters.*
float	**ps_E** (int i)	*Return the PS cluster energy. Use the* **PS cluster index** *as an input parameter.*
float	**ps_phi** (int i)	*Return the PS cluster ϕ. Use the* **PS cluster index** *as an input parameter.*
float	**ps_eta** (int i)	*Return the PS cluster (detector) η. Use the* **PS cluster index** *as an input parameter.*
float	**ps_r** (int i)	*Return the PS cluster r. Use the* **PS cluster index** *as an input parameter.*
float	**ps_z** (int i)	*Return the PS cluster z. Use the* **PS cluster index** *as an input parameter.*

8.4 Information coming from RoadFinder

Names

void	**getRoads_cellvector** (std::vector<Roads_cell>& rcellvec)

		Get the Roads_cell vector.
float	**dismerge_c** ()	*Get the dismerge_container parameter (see SEMReco.rcp).*
float	**dismerge_1** ()	*Get the dismerge_road1 parameter (see SEMReco.rcp).*
float	**dismerge_2** ()	*Get the dismerge_road2 parameter (see SEMReco.rcp).*

8.5 Additional access methods

Names

bool	**ps_matching** ()	*Return true if there is a candidate PS cluster match.*
bool	**em_matching** ()	*Return true if there is a candidate EM tower match.*
void	**getVertex** (float v[3])	*Return the particle vertex in a vector.*
const ChpIndex&	**chpindex** ()	*Return ChargedParticle LinkIndex.*
const vertex::ChargedParticle*	**getPtrChp** ()	*Return pointer to the ChargedParticle.*
const CpsIndices&	**cpsindices** ()	*Return the CPS3DCluster LinkIndex vector.*
const FpsIndices&	**fpsindices** ()	*Return the FPS3DCluster LinkIndex vector.*
const CTaddress&	**toweraddress** ()	*Return the toweraddress vector.*

The D0 Electron/Photon Analysis Package EMAnalyze

— July 20, 2001 —

This note describes the electron/photon analysis package EMAnalyze. EMAnalyze provides information about EMparticle(s) and SEMparticle(s), which are the output of the EMReco and SEMReco packages. The first part gives information about electron/photon reconstruction. The following parts give more detailed information about the blocks and variables which are stored in the output ntuple (or root-tuple). This (new) version is based on the former EMAnalyze and SEMAnalyze packages. In the following, one will use GeV, cm and radian as standard units.

F. Fleuret

Laboratoire de Physique Nucléaire et de Hautes Energie, Paris

Lawrence Berkeley National Laboratory, CA

D0 note 3888

Contents

1 Introduction — *Summary of electron/photon reconstruction* 3
1.1 EMReco Initial Cluster selection 3
1.2 EMReco Final Cluster builder 5
1.3 EMReco PreShower Cluster Finder and EMReco Track Finder 6

2 EMAnalyze — *electron/photon analysis package* 8
2.1 RCP input parameters: 9
2.2 EMPART block: EMparticle information 10
2.3 EMSEM block: SEMparticle information 14

3 Analyze_CELL — *Calorimeter cells analysis class* 17
3.1 RCP input parameters: 17
3.2 EMCELL block: calorimeter cells information 17

4 Analyze_PS — *Preshower clusters analysis class* 19
4.1 RCP input parameters: 19
4.2 EMCPS block: CPS clusters information 20
4.3 EMFPS block: FPS clusters information 21

1 Introduction: **Summary of electron/photon reconstruction**

Electron/photon identification is performed both with EMReco and SEMReco, where SEMReco feeds EMReco with SEMparticle objects. In the reconstruction framework, SEMReco runs first and produces SEMparticle's (see SEMreco documentation, d0note 3872). Then, EMReco, using SEMparticle's as input, produces EMparticle's. The EMparticle list contains electron/photon candidates from both SEMReco and EMReco identification stages.

The following section describes the procedure applied in EMReco to produce the final EMparticle list, assuming that a list of SEMparticle has already been transmitted to EMReco.

1.1 EMReco Initial Cluster selection

1.1.1 Initial Cluster finder

Before the EMReco stage, an Initial Cluster builder runs and provides a list of candidate clusters to EMReco. Possible algorithms used to build these Initial Clusters are:

- Nearest Neighbors algorithm
- Simple Cone algorithm (default)
- CellNN algorithm

Using Initial Clusters and SEMparticle's as inputs, and applying several selection *criteria*, EMReco will build Final Cluster candidates and produce EMparticle's which contain information about Final Clusters and the way they were produced. The following discussion is based on Simple Cone as Initial Cluster.

1.1.2 SEMparticle-Initial Cluster matching.

The following sequence is done in emreco/EMClusFinder.

For each Initial Cluster, EMReco looks for a matching SEMparticle. The matching is made by computing $(\Delta R)^2 = (\Delta\phi)^2 + (\Delta\eta)^2$, where $\Delta\phi$ and $\Delta\eta$ are (respectively) the ϕ and η differences between Initial Cluster and SEMparticle. A SEMparticle is associated to an Initial Cluster if $(\Delta R)^2 < 0.01$.

1.1.3 First Initial Cluster selection.

The following sequence is done in emreco/EMClusFinder; parameters are set in EMReco.rcp.

Initial Cluster selection is made applying EMfraction and pT cuts or requiring a matching SEMparticle: If Initial Cluster has an associated SEMparticle, or if Initial Cluster EMfraction>**emratio** (by default 0.9) and pT>**pTmin** (by default 1.5 GeV) one proceeds. Otherwise, Initial Cluster is rejected.

1.1.4 Isolation computation and second Initial Cluster selection.

The following sequence is done in emreco/EMClusFinder; parameters are set in EMReco.rcp.

After step 1.1.3, for selected Initial Clusters, one computes isolation as follows:

1. Get the Initial cluster highest pT tower.
2. Make list LT1 of towers within a $i\eta$ x $i\phi$ circle of **LargeWindow** (default = 4) radius (for more details, see calData::towerNeighbors and TowerNeighbors::build_list). The circle is centered on the highest pT tower.
3. Loop over list LT1 and compute the overall (EM + hadronic) energy totE from towers within a η x ϕ circle of radius **isoCone** (default = 0.4). The circle is centered at the Initial cluster position.
4. In the same loop (loop over LT1) compute EM energy coreE from towers within a η x ϕ circle of radius **coreSize** (default = 0.2). The circle is centered at the Initial cluster position.
5. Compute isolation iso = (totE - coreE)/coreE. To be isolated a candidate must have iso<**isoratio** (default = 0.2).

After isolation computation, Initial Cluster selection is made applying isolation cut or requiring a matching SEMparticle: If Initial Cluster has an associated SEMparticle, or if Initial Cluster isolation iso>**isoratio** (by default 0.2), one proceeds. Otherwise, Initial Cluster is rejected.

1.1.5 Summary

Due to the flexibility of the Initial Cluster selection, different types of Initial Clusters (meaning passing different selection *criteria*) will be used as seeds to build the Final Clusters which will be stored in EMparticle objects.

In addition, EMReco will use as Final Cluster seeds all the SEMparticle's which do not match any Initial Cluster. In that case, the highest E_T calorimeter tower associated to the SEMparticle will be used as the center of a $i\eta \times i\phi = 3 \times 3$ tower window which will defined the SEMparticle associated cluster. For this cluster, isolation is computed in the same way as in 1.1.4.

Finally the different types of objects used as Final Cluster seeds are:

- Final Cluster seed = Initial Cluster; **pass EMfraction, pT and isolation** *criteria.* Doesn't have an associated SEMparticle.
- Final Cluster seed = Initial Cluster; **pass EMfraction, pT and isolation** *criteria*, **and has an associated SEMparticle.**
- Final Cluster seed = Initial Cluster; **pass isolation** *criterium* **and has an associated SEMparticle.** Doesn't pass EMfraction and pT *criteria.*
- Final Cluster seed = Initial Cluster; **pass EMfraction and pT** *criteria*, **and has an associated SEMparticle.** Doesn't pass isolation *criterium.*
- Final Cluster seed = Initial Cluster; **has an associated SEMparticle.** Doesn't pass EMfraction, pT and isolation *criteria.*
- Final Cluster seed = SEMparticle; **cluster pass isolation** *criterium.*
- Final Cluster seed = SEMparticle; cluster doesn't pass isolation *criterium.*

All these Initial Clusters will be used, as seeds, to produce Final Clusters and then EMparticle's. Note that the information about the seed characteristics is stored in EMparticle's (see EMPART block description).

1.2 EMReco Final Cluster builder

The following sequence is done in emreco/EMClusFinder; parameters are set in EMReco.rcp.

1. After selections, EMReco builds Final Clusters, using the seeds listed in 1.1.5. If the seed highest pT tower abs($i\eta$)>13 then a Forward cluster is built; Central cluster otherwise.

   Central Cluster

   (a)
   - If the candidate is isolated, loop over the above list LT1 and make list LT2 of towers within a $i\eta$ x $i\phi$ circle of **SmallWindow** (default = 2) radius (for more details, see calData::towerNeighbors and TowerNeighbors::build_list). The circle is centered on the highest pT tower.
   - If the candidate is non-isolated, make list LT2 of towers within a $i\eta$ x $i\phi$ circle of **NonIsoWindow** (default = 1[1]) radius (for more details, see calData::towerNeighbors and TowerNeighbors::build_list). The circle is centered on the highest pT tower.

   (b) From LT2, make the overall cells list LC1 and the overall EM3 cells list LC2.

[1] In this particular case (radius = 1), make list LT2 of 3x3 towers.

Forward Cluster

(a) From list LT1, take the highest pT tower and make list LT2 of towers within a $i\eta$ x $i\phi$ circle of radius=1[1] (for more details, see calData::towerNeighbors and TowerNeighbors::build_list).

(b) From list LT2, find the highest energy cell (HECell) and EM3 cell (EM3HECell).

(c) If highest pT tower $i\eta$>13 get ECS overall cells list; if highest pT tower $i\eta$<-13 get ECN overall cells list;

(d) Loop over the previous list of cells and make the overall cells list LC1 and the overall EM3 cells list LC2 within a cone of **radiusEC** (default = 10cm) radius at EM3, with its axis centered at EM3HECell and its origin at (0,0,0) [2].

2. Fill EMCluster and EMQualityInfo information with LC1 and LC2 information.

After EMClusFinder, EMreco builds, with the list of EMCluster(s), the list of EMparticle(s) and sets object indices. Note that, at this stage, EMparticle's η and ϕ are given at the reconstructed PRIMARY vertex position.

1.3 EMReco PreShower Cluster Finder and EMReco Track Finder

After having produced the EMparticle(s) list, EMReco looks for a matching preshower cluster and a matching track. These two steps are used to improve the cluster energy and position measurement.

1.3.6 Preshower Cluster Finder

The following sequence is done in emreco/PshwrClusFinder; parameters are set in EMReco.rcp.

For each EMparticle, find a matching preshower cluster:

- If the EMparticle has an associated SEMparticle, take the preshower cluster associated to the SEMparticle's ChargedParticle, if any.
- If the EMparticle doesn't have an associated SEMparticle, take the highest energy preshower cluster matching the EMparticle, within a $\eta \times \phi$=**dEtaCps**×**dPhiCps** window for the CPS (central preshower), within a $\theta \times \phi$=**dThetaFps**×**dPhiFps** window for the FPS (forward preshower), if any.

If a matching preshower cluster is found, add the preshower cluster energy to EMCluster and EMparticle and correct EMCluster's and EMparticle's positions using the preshower cluster position. Note that, at this stage, EMparticle's η and ϕ are given at the reconstructed PRIMARY vertex position.

[2] Note that if EM3HECell energy is 10 times smaller than HECell energy, HECell is used as the cone axis (instead of EM3HECell).

1.3.7 Track Finder

The following sequence is done in emreco/EMTrackFinder; parameters are set in EMReco.rcp.

for each EMparticle, find a matching track:

- If the EMparticle has an associated SEMparticle, take the ChargedParticle associated to the SEMparticle.
- If the EMparticle doesn't have an associated SEMparticle, take all the matching tracks within a $\eta \times \phi$=**trackDeltaEta**×**trackDeltaPhi** window.

If a matching track is found, set EMparticle's *momentum* using EMparticle energy and associated ChargedParticle θ and ϕ[3], and, if EMparticle doesn't have an associated SEMparticle, set EMparticle typeID=12 (resp. -12) for a negative (resp. positive) charged ChargedParticle. Note that, at this stage, EMparticle's η and ϕ don't depend anymore on the reconstructed PRIMARY vertex position, but on the associated track θ and ϕ positions.

[3] $P_x = E \times \cos(\phi_T) \times \sin(\theta_T)$, $P_y = E \times \sin(\phi_T) \times \sin(\theta_T)$, $P_z = E \times \cos(\theta_T)$, where P_x, P_y, P_z are EMparticle *momentum* projections, E is EMparticle energy and ϕ_T and θ_T are track θ and ϕ.

2

namespace emid class **EMAnalyze** : public fwk Package, public fwk Analyze, public fwk JobSummary

electron/photon analysis package

Inheritance

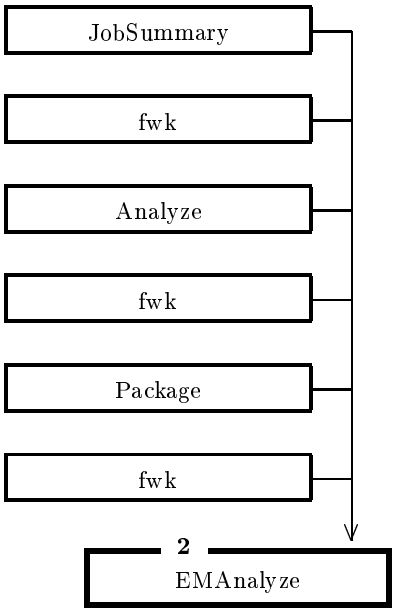

Private Members

2.1 **RCP input parameters:** 9
2.2 **EMPART block: EMparticle information** 10
2.3 **EMSEM block: SEMparticle information** 14

electron/photon analysis package.

EMAnalyze is dedicated to the electron/photon reconstruction analysis. It provides information about EMparticle, SEMparticle, calorimeter cells used to build EM clusters and matching PreShower clusters.

- EMAnalyze block structure:

  EMAnalyze produces one to five ntuple blocks, based on RCP parameters selection:

  - EMPART block provides information about EMparticle's.
  - EMSEM block provides information about SEMparticle's.
  - EMCELL block provides information about calorimeter cells (see Analyze_CELL).
  - EMCPS block provides information about CPS clusters (see Analyze_PS).
  - EMFPS block provides information about FPS clusters (see Analyze_PS).

  Each block is connected to the other *via* EMparticle index or SEMparticle index, or both.

- EMAnalyze RCP files:

  Since several EMparticleChunk's (ususally 2), corresponding to different clustering algorithms (usually Simple Cone and CellNN), can be produced by EMReco, EMAnalyze has been designed to produce several EMPART blocks, each of them corresponding to one specific clustering algorithm [4]. In order to make the difference between the several EMPART blocks, a suffix is added in their names. Usually, EMparticle's built with Simple Cone are stored in EMPART_S (see EMAnalyze-scone.rcp) and EMparticle's built with CellNN are stored in EMPART_Z (see EMAnalyze-cnn.rcp).

2.1 RCP input parameters:

Names

bool	**_do_print**	*If* **true** *print event information (can be big).*
bool	**_analyze_EM**	*If* **true** *create and fill EMPART block.*
bool	**_analyze_EM_cells**	*If* **true** *(and analyze_EM=true) create and fill EMCELL block.*
bool	**_analyze_SEM**	*If* **true** *create and fill EMSEM block.*
float	**_dismerge_container**	*1st Road parameter: Controls the number of cells in the Road. The default value is set at 0.25 (for more details, see D0 note 3872).*

[4] As an example, in runRecoAnalyze.rcp, EMAnalyze is called once with EMAnalyze-scone.rcp and once with EMAnalyze-cnn.rcp. Note that EMSEM is turned on in only one of these RCP files.

float	**_dismerge_road1**	*2nd Road parameter: Must be lower than dismerge_container. The default value is set at 0.125 (for more details, see D0 note 3872).*
float	**_dismerge_road2**	*3rd Road parameter: Must be lower than dismerge_road1. The default value is set at 0.0 (for more details, see D0 note 3872).*
float	**_EThreshold**	*Road parameter: threshold on cells taken in the road*
bool	**_removecw**	*Road parameter: if true remove CalWeights*
bool	**_analyze_PS**	*If* **true** *create and fill EMCPS and EMFPS blocks.*

The analysis is controled by RCP input parameters, which can be modified in EMAnalyze.rcp. All the parameters used to controled the particle selections are set in emreco/rcp/EMReco.rcp and semreco/rcp/SEMReco.rcp.

2.2 EMPART block: EMparticle information

Names

static const int	**_max_EM**	*Maximum allowed number of EMparticle per event. The default value is set to 20. Not filled in the ntuple.*
int	**_n_EM**	*Number of EMparticles in the event.*
std::vector <float>	**_EM_E**	*EMparticle energy.*
std::vector <float>	**_EM_pT**	*EMparticle pT (see block description).*
std::vector <float>	**_EM_pX**	*EMparticle pX (see block description).*
std::vector <float>	**_EM_pY**	*EMparticle pY (see block description).*
std::vector <float>	**_EM_pZ**	*EMparticle pZ (see block description).*
std::vector <float>		

	_EM_eta	*EMparticle eta (see block description).*
std::vector <float>	**_EM_phi**	*EMparticle phi (see block description).*
std::vector <int>	**_EM_id**	*EMparticle id (see block description).*
std::vector <float>	**_EM_iso**	*Initial Cluster isolation (see block description).*
std::vector <float>	**_EM_EisoTot**	*total energy for isolation computation (see block description).*
std::vector <float>	**_EM_EisoCore**	*EM energy for isolation computation (see block description).*
std::vector <int>	**_EM_isol**	*return 1 if the particle is isolated, i.e., usually iso<0.2*
std::vector <int>	**_EM_EMidx**	*EMparticle index*
std::vector <int>	**_EM_SEMidx**	*Associated SEMparticle index (if -1, no associated SEMparticle)*
std::vector <int>	**_EM_nb_CPS**	*number of associated CPS clusters.*
std::vector <int>	**_EM_nb_FPS**	*number of associated FPS clusters.*
int	**_EM_TRKidx** [_max_EM][3]	*Associated track's indices; if -1, no associated track (see block description).*
float	**_EM_floorE** [_max_EM][6]	*EMCluster energy in each floor (see block description).*
float	**_EM_floorX** [_max_EM][6]	*EMCluster X position in each floor (see block description).*
float	**_EM_floorY** [_max_EM][6]	*EMCluster Y position in each floor (see block description).*
float	**_EM_floorZ** [_max_EM][6]	*EMCluster Z position in each floor (see block description).*

float	**_EM_flrS1** [_max_EM][6]	*(EMCluster width)**2 in (r×ϕ) in each floor (see block description).*
float	**_EM_flrS2** [_max_EM][6]	*(EMCluster width)**2 in z (CC) or r (EC) in each floor (see block description).*
float	**_EM_flrC** [_max_EM][6]	*EMCluster correlation between the 2 sizes in each floor (see block description).*
std::vector <float>	**_EM_EMfrac**	*EMCluster EM fraction (see block description).*
std::vector <float>	**_EM_HA**	*EMCluster Total hadronic energy (see block description).*
std::vector <float>	**_EM_HMx9**	*EMQuality 9x9 Hmatrix chi2.*
std::vector <float>	**_EM_HMx41**	*EMQuality 41x41 Hmatrix chi2.*
std::vector <float>	**_EM_elk9**	*EMQuality 9x9 elike.*
std::vector <float>	**_EM_elk41**	*EMQuality 41x41 elike.*

EMparticle Variables description (see em_evt/EMparticle):

- pT, pX, pY, pZ = depending on whether or not EMparticle has an associated track (or SEMparticle), pT, pX, pY, pZ are given at the reconstructed PRIMARY vertex (if no associated track) or are computed using the matching track θ and ϕ, and the EMparticle energy as follows: $P_x = E \times \cos(\phi) \times \sin(\theta)$, $P_y = E \times \sin(\phi) \times \sin(\theta)$, $P_z = E \times \cos(\theta)$, $P_T^2 = P_x^2 + P_y^2$.
- eta = EMparticle η. Depending on whether or not EMparticle has an associated track (or SEMparticle), η is given at the reconstructed PRIMARY vertex (if no associated track) or is given by the matching track.
- phi = EMparticle ϕ. As EMparticle's η, ϕ is given at the reconstructed PRIMARY vertex (if no associated track) or is given by the matching track.
- id = EMparticle id, with (see pages 4 and 5):
  - abs(id) = 11
    - Final Cluster seed = Initial Cluster; **pass EMfraction, pT and isolation criteria; has an associated SEMparticle.**
    - Final Cluster seed = Initial Cluster; **pass isolation criterium; has an associated SEMparticle;** doesn't pass EMfraction and pT criteria.

- abs(id) = 12 (very rare)
  - Final Cluster seed = Initial Cluster; **pass EMfraction, pT and isolation criteria;** doesn't have associated SEMparticle but **does have a matching track.**
- id = 10
  - Final Cluster seed = Initial Cluster; **pass EMfraction, pT and isolation criteria;** doesn't have an associated SEMparticle.
- abs(id) = 20011
  - Final Cluster seed = Initial Cluster; **pass EMfraction and pT criteria; has an associated SEMparticle;** doesn't pass isolation criterium.
  - Final Cluster seed = Initial Cluster; **has an associated SEMparticle;** doesn't pass EMfraction, pT and isolation criteria.
- abs(id) = 10011 (very rare)
  - Final Cluster seed = SEMparticle; **3x3 cluster pass isolation criterium**.
- abs(id) = 30011
  - Final Cluster seed = SEMparticle; 3x3 cluster doesn't pass isolation criterium.

Note that id<0 (resp. id>0) if the particle charge sign is positive (resp. negative), except for id=10 for which there is no associated track or SEMparticle.

- TRKidx[_max_EM][i] = i^{th} associated track index (more than one track can match a cluster). i=0 is the preferred one. Note that if TRKidx[j][0]=-1, then TRKidx[j][1]=TRKidx[j][2]=-1.

EMCluster variables description (see em_evt/EMCluster):

- floorE[_max_EM][i] = cluster energy in layer i, where i=0,..,5 is PS, EM1, EM2, EM3, EM4, FH1.
- floorX[_max_EM][i] = cluster X position in layer i, where i=0,..,5 is PS, EM1, EM2, EM3, EM4, FH1.
- floorY[_max_EM][i] = cluster Y position in layer i, where i=0,..,5 is PS, EM1, EM2, EM3, EM4, FH1.
- floorZ[_max_EM][i] = cluster Z position in layer i, where i=0,..,5 is PS, EM1, EM2, EM3, EM4, FH1.
- flrS1[_max_EM][i] = (cluster width)**2 in r$\times\phi$ in layer i, where i=0,..,5 is PS, EM1, EM2, EM3, EM4, FH1 (for more details see em_evt/EMCluster.hpp).
- flrS2[_max_EM][i] = (cluster width)**2 in z (CC) or r (EC) in layer i, where i=0,..,5 is PS, EM1, EM2, EM3, EM4, FH1 (for more details see em_evt/EMCluster.hpp).
- flrC[_max_EM][i] = flrS1/flrS2 correlation in layer i, where i=0,..,5 is PS, EM1, EM2, EM3, EM4, FH1 (for more details see em_evt/EMCluster.hpp).
- HA = cluster energy in all hadronic layers (including FH1).
- EMfrac = cluster EMfraction
  $= \frac{PS+EM1+EM2+EM3+EM4}{PS+EM1+EM2+EM3+EM4+HA} = \frac{\sum_{i=0}^{4} floorE(i)}{HA+\sum_{i=0}^{4} floorE(i)}$

  Note that the EMfraction cut used to make the initial cluster candidate selection does not use this definition (see page 3).

- iso = isolation for cluster selection: (EisoTot - EisoCore)/EisoCore.
- EisoTot = overall (EM + hadronic) tower energy in a (η, ϕ) circle of radius = 0.4 centered on highest pT tower (see page 3). Does not include PreShower energy or energy corrections.
- EisoCore = EM tower energy in a (η, ϕ) circle of radius = 0.2 centered on highest pT tower (see page 3). Does not include PreShower energy or energy corrections.

2.3 EMSEM block: SEMparticle information

Names

static const int	**_max_SEM**	*Maximum allowed number of SEMparticle per event. The default value is set to 20. Not filled in the ntuple.*
int	**_n_SEM**	*number of SEMparticle's in the event.*
std::vector <int>	**_SEMindex**	*SEMparticle's index*
std::vector <int>	**_SEM_TRKindex**	*associated track's index*
std::vector <int>	**_SEM_nbTower**	*number of matching towers (see block description).*
float	**_SEM_TowerPhi** [_max_SEM][4]	*tower ϕ (see block description).*
float	**_SEM_TowerEta** [_max_SEM][4]	*tower η (see block description).*
float	**_SEM_TowerE** [_max_SEM][4]	*tower energy (see block description).*
float	**_SEM_TowerEM1** [_max_SEM][4]	*tower EM1 energy (see block description).*
float	**_SEM_TowerEM2** [_max_SEM][4]	*tower EM2 energy (see block description).*
float	**_SEM_TowerEM3** [_max_SEM][4]	

tower EM3 energy (see block description).

float **_SEM_TowerEM4** [_max_SEM][4]
tower EM4 energy (see block description).

float **_SEM_TowerFH1** [_max_SEM][4]
tower FH1 energy (see block description).

float **_SEM_TowerHA** [_max_SEM][4]
tower HA energy (see block description).

std::vector <int>
_SEM_nbCPS *number of matching CPS clusters.*

std::vector <int>
_SEM_nbFPS *number of matching FPS clusters.*

float **_SEM_rRC** [_max_SEM][14]
Road energy with dismerge = 0.25 in each floor (see block description).

float **_SEM_rR1** [_max_SEM][14]
Road energy with dismerge = 0.125 in each floor (see block description).

float **_SEM_rR2** [_max_SEM][14]
Road energy with dismerge = 0 in each floor (see block description).

std::vector <int>
_SEM_rcrossfl *floors crossed by the road (coded in binary).*

SEMparticle variables description (see em_evt/SEMparticle.hpp):

- nbTower = number of matching towers (after EMfraction cut). 0<nbTower<5, because of the matching window size (0.045x0.05).
- TowerPhi = 2 dimensional array; ϕ of the matching towers.
- TowerEta = 2 dimensional array; η of the matching towers.
- TowerE = 2 dimensional array; Energy of the matching towers with TowerE = TowerEM1 + TowerEM2 + TowerEM3 + TowerEM4 + TowerHA.
- TowerEM1 = 2 dimensional array; EM1 energy of the matching towers.
- TowerEM2 = 2 dimensional array; EM2 energy of the matching towers.
- TowerEM3 = 2 dimensional array; EM3 energy of the matching towers.
- TowerEM4 = 2 dimensional array; EM4 energy of the matching towers.

- TowerFH1 = 2 dimensional array; FH1 energy of the matching towers.
- TowerHA = 2 dimensional array; total HA energy (including FH1) of the matching towers.
- rRC(14) = 2 dimensional array; transverse energy in the road with dismerge = dismerge_container
- rR1(14) = 2 dimensional array; transverse energy in the road with dismerge = dismerge_road1
- rR2(14) = 2 dimensional array; transverse energy in the road with dismerge = dismerge_road2
- rcrossfl = floors crossed by the road (coded in binary). With floor number between 1 and 8.

3

namespace emid class **Analyze_CELL**

Calorimeter cells analysis class

Private Members

3.1 **RCP input parameters:** 17
3.2 **EMCELL block: calorimeter cells information** 17

Calorimeter cells analysis class.

Gives information about calorimeter cells. By default, this package is turned off in EMAnalyze.rcp; the output can be big!
EMCELL block is connected to EMPART block *via* EMparticle index.

3.1

RCP input parameters:

Names

bool	**_do_print**	*Printing key from EMAnalyze.rcp.*
float	**_cell_energy_cut**	*Cells minimum energy required for storing. The default value is set to* **0.001**.

3.2

EMCELL block: calorimeter cells information

Names

static const int	**_max_CELL**	*Maximum allowed number of cells per event. The default value is set to 1000. Not filled in the ntuple.*
int	**_n_CELL**	*Number of cells in the event.*

std::vector <int>	**_cEMidx**	*EMparticle index (see EMPART block).*
std::vector <float>	**_cE**	*Cell energy*
std::vector <float>	**_cX**	*Cell X position*
std::vector <float>	**_cY**	*Cell Y position*
std::vector <float>	**_cZ**	*Cell Z position*
std::vector <float>	**_ceta**	*Cell eta position*
std::vector <float>	**_cphi**	*Cell phi position*
std::vector <float>	**_clayer**	*Cell calorimeter layer*

EMCELL block returns cluster cell information. It's based on the former EMAnalyze package.

4

namespace emid class **Analyze_PS**

Preshower clusters analysis class

Private Members

4.1 **RCP input parameters:** 19

4.2 **EMCPS block: CPS clusters information** 20

4.3 **EMFPS block: FPS clusters information** 21

Preshower clusters analysis class.

Gives information about matching preshower clusters. By default, this package is turned off in EMAnalyze.rcp.

EMCPS and EMFPS blocks are connected to EMPART and EMSEM blocks *via* EMparticle and SEMparticle indices.

EMCPS and EMFPS blocks are filled in two steps, first looping over EMparticle's, then looping over SEMparticle's. This procedure has the disadvantage of often storing the same preshower cluster twice, but the advantage of keeping filled preshower clusters ordered in increasing EMparticle indices and then increasing SEMparticle indices.

4.1

RCP input parameters:

Names

bool	**_do_print**	*Printing key from EMAnalyze.rcp.*
float	**_CPS_eCone_detR**	*Cone radius to compute eCone energy.*

4.2 EMCPS block: CPS clusters information

Names

static const int	**_max_CPS**	*Maximum allowed number of clusters per event. The default value is set to 50. Not filled in the ntuple.*
int	**_n_CPS**	*Number of CPS clusters in the event.*
std::vector <int>	**_C_CPSidx**	*CPS3DCluster index. -1 = not a CPS cluster*
std::vector <int>	**_C_EMidx**	*Associated EMparticle index. -1 = no EMparticle associated.*
std::vector <int>	**_C_SEMidx**	*Associated SEMparticle index. -1 = no SEMparticle associated.*
std::vector <float>	**_C_E**	*PS cluster energy.*
std::vector <float>	**_C_phi**	*PS cluster ϕ position.*
std::vector <float>	**_C_dphi**	*Error on PS cluster ϕ position.*
std::vector <float>	**_C_r**	*PS cluster r position.*
std::vector <float>	**_C_dr**	*Error on PS cluster r position.*
std::vector <float>	**_C_Z**	*PS cluster Z position.*
std::vector <float>	**_C_dZ**	*Error on PS cluster Z position.*
std::vector <float>	**_C_ExSLC**	*x Single Layer Cluster (SLC) energy.*
std::vector <float>	**_C_EuSLC**	*u SLC energy.*
std::vector <float>		

	_C_EvSLC	*v SLC energy.*
std::vector <float>	**_C_CxSLC**	*x SLC centroid.*
std::vector <float>	**_C_CuSLC**	*u SLC centroid.*
std::vector <float>	**_C_CvSLC**	*v SLC centroid*
std::vector <int>	**_C_NxSLC**	*x SLC number of strips.*
std::vector <int>	**_C_NuSLC**	*u SLC number of strips.*
std::vector <int>	**_C_NvSLC**	*v SLC number of strips.*
std::vector <float>	**_C_ExStp**	*energy of highest energy x SLC strip.*
std::vector <float>	**_C_EuStp**	*energy of highest energy u SLC strip.*
std::vector <float>	**_C_EvStp**	*energy of highest energy v SLC strip.*
std::vector <float>	**_C_eCone**	*associated Cone energy.*

EMCPS block returns information about matching Central PreShower clusters for both EMparticle's and SEMparticle's.

4.3 EMFPS block: FPS clusters information

Names

static const int	**_max_FPS**	*Maximum allowed number of clusters per event. The default value is set to 50. Not filled in the ntuple.*
int	**_n_FPS**	*Number of FPS clusters in the event.*
std::vector <int>		

	_F_FPSidx	*FPSRecoCluster index. -1 = not a FPS cluster.*
std::vector <int>	**_F_EMidx**	*Associated EMparticle index. -1 = no EMparticle associated.*
std::vector <int>	**_F_SEMidx**	*Associated SEMparticle index. -1 = no SEMparticle associated.*
std::vector <float>	**_F_E**	*PS Cluster energy.*
std::vector <float>	**_F_r**	*PS Cluster r position.*
std::vector <float>	**_F_z**	*PS Cluster z position.*
std::vector <float>	**_F_phi**	*PS Cluster ϕ position.*

EMFPS block returns information about matching Forward PreShower clusters for both EMparticle's and SEMparticle's.